Inflatable Variable Stiffness Soft Robots

Stilli, Agostino

Awarding institution:
King's College London

Take down policy

If you believe that this document breaches copyright please contact librarypure@kcl.ac.uk providing details, and we will remove access to the work immediately and investigate your claim.

Inflatable
Variable Stiffness
Soft Robots

by Agostino Stilli

Primary Supervisor:

Dr. Elizabeth Sklar

Secondary Supervisor:

Prof. Kaspar Althoefer

A thesis submitted in partial fulfilment of the requirements for the degree of

'Doctor of Philosophy' in Robotics

to

King's College London

Faculty of Natural and Mathematical Sciences

Department of Informatics

September 2017

I herewith declare that I have produced this Thesis without the prohibited assistance of third parties and without making use of aids other than those specified; notions taken over directly or indirectly from other sources have been identified as such. This Thesis has not previously been presented in identical or similar form to any other British or foreign examination board.

London, September 2017

Abstract

Soft materials have opened new possibilities in robotics: the use of inherently adaptable mechanical structures allows soft robots to negotiate with uncertain and unstructured tasks. Nevertheless, their sizable elastic deformations pose a limitation to their modelling and control. Moreover, the maximum achievable stiffness is typically too low to provide performances comparable to those of their rigid-linked counterparts.

The research presented in this thesis aims at overcoming these limitations and bridging the gap between traditional and soft robotics by proposing a novel design paradigm for a Variable Stiffness System (VSS) based on soft materials with the potential to be employed in a wide range of application areas. The proposed design takes inspiration from the antagonistic stiffening mechanism of muscles in nature, in which the balancing of two opposing contractile muscle forces allows to achieve infinite stable configurations.

A combination of flexible inflatable membranes and flexible, yet inextensible fabric sleeves is used to enable fine stiffness tuning, by mean of pneumatic actuation. The conjoint use of tendon-driven actuation is proposed to enable not only stiffness controllability, but also shape-shifting and shape-locking capabilities. The use of fabric allows for significantly higher pressures to be used, thus, larger forces can be exerted on the environment, still making use of soft materials.

This has led to contributions within the areas of industrial collaborative robots, where the concept of stiffness-controllable robotic link has been explored to

enhance safety in Human-Robot Interaction (HRI); in surgical robotics where the use of the proposed antagonistic actuation mechanism has been investigated to improve the dexterity of laparoscopic tools; and in rehabilitation robotics, where the same mechanism is employed to improve the ergonomics of state-of-the-art exoskeletons for hand-rehabilitation. This thesis shows how this novel design concept can be applied to effectively improve or replace a wide range of state-of-the-art robotic systems.

Acknowledgements

I would like, first of all, to thank my main supervisor Professor Kaspar Althoefer, without whom I would not have had the chance to undertake this life-changing experience. He believed in me and in my potential from the very first email we exchanged in the summer of 2013 when I was still living in Italy, offering me the opportunity of moving to UK to kickstart my academic career. Without him, I would not have had the chance to embark, conduct and complete my PhD. I want also to thank Dr. Elizabeth Sklar and Dr. Thrishantha Nanayakkara for their support as supervisors throughout these years. I am also deeply grateful to Professor. Benedetto Allotta from the University of Florence, who guided and mentored me during my Bachelor and my Master degrees. I have been extremely lucky to meet Dr. Helge Arne Wurdemann during my first day at King's. I am very grateful for his guidance, the encouragement and the advice he has provided throughout my time as his student and colleague. Together with Dr. Angela Faragasso you have been incredibly supportive desk mates, great people to work with and became the first people in London I called friends.

I would also like to express my gratitude to Dr. Ali Shafti for his incredible support in the past four years, during which we shared every step of our PhD journey. I must also thank (soon to be Dr.) Lukas Lindenroth for supporting me throughout my research, sharing his thoughts on various technical discussions: you and Dr. Ali Shafti made my research time at King's enjoyable even during 14 hour writing days. Furthermore, I would like to thank Mr. Thomas Manwell who started and shared this PhD journey together with Dr. Ali Shafti and myself. I would also like to acknowledge Dr. Yohan Noh and Dr. Luc Marechal for making our lab at King's a great place to work and for being such good

Table of Contents

List of Figures

List of Tables

Abbreviations

ACC: Active-Active Configuration

ANSI: American National Standard Institute

APC: Active-Passive Configuration

BC1/2: Bent Configuration 1/2

CNT: Carbon Nano-Tubes

DAC: Digital-to-Analog Converter

DE: Dielectric Elastomer

DOF: Degree of Freedom

EAP: Electroactive Polymer

EMG: Electromyography

ERE: Electro-Rheological Elastomer

ERF: Electro-Rheological Fluid

ERM: Electro-Rheological Material

FEA: Fluidic Elastomeric Actuator

FSMA: Ferromagnetic Shape Memory Alloy

HRI: Human-Robot Interaction

HTSMA: High Temperature Shape Memory Alloy

IC: Integrated Circuit

IF: Impact Factor

IPMC: Ionic-Polymer-Metallic-Composite

LMPA: Low Melting Point Alloy

LMPM: Low Melting Point Material

MEMS: Micro-Electro-Mechanical System

MIS: Minimally Invasive Surgery

MLS: Multi-port Laparoscopic Surgery

MRE: Magneto-Rheological Elastomer

MRF: Magneto-Rheological Fluid

MRM: Magneto-Rheological Materials

MSMA: Magnetic Shape Memory Alloy

PAM: Pneumatic Artificial Muscle

PCB: Printed Circuit Board

PE: Pseudo-Elasticity

RIA: Robotic Industries Association

RTT: Reverse Transformation Temperature

SE: Super Elasticity

SC: Straight Configuration

SILS: Single Incision Laparoscopic Surgery

SLS: Single-Port Laparoscopic Surgery

SMA: Shape Memory Alloy

SME: Small and Medium-sized Enterprises

SMM: Shape Memory Material

SMP: Shape Memory Polymer

VSA: Variable Stiffness Actuator

VSF: Variable Stiffness Fiber

VSJ: Variable Stiffness Joint

VSL: Variable Stiffness Link

VSL V1: Variable Stiffness Link Version 1

VSL V2: Variable Stiffness Link Version 2

VSS: Variable Stiffness System

Chapter 1

1 Introduction

This chapter provides a comprehensive outline of the motivation, the aim and objectives and the main contributions of this thesis. The outline of the thesis is also presented, describing how the research is divided and presented in different chapters and how these chapters connect to each other.

1.1 **Background**

Soft robotics is regarded as one of the biggest revolutions since the dawn of robotics [1]. Soft systems are expected to play a central role in the 4th industrial revolution [2], enabling closer and safer collaboration between humans and robots. Researchers worldwide are pushing the boundaries in this novel research field where robotics meets material science. To get a measure of the entity of the research output in this field we can refer to "Soft Robotics" (Mary Ann Liebert, Inc.), the first monothematic journal on this subject, nowadays the point of reference for this ever-growing robotic community. The journal Soft Robotics was firstly launched in July 2014 [3]; in the time span of three years, thanks to the intense activity of its community and its monopolistic position, it has become the journal with the highest Impact Factor (IF) in robotics, IF: 8.649 in 2017.

The use of rubber-like materials [4], [5] opened new possibilities in terms of design, morphology and fabrication of soft systems, posing new challenges in terms of modelling and control, paving the way for a new robotics era. Silicone rubbers, scientifically known as polysiloxanes, have been widely investigated not only for their low stiffness, flexibility and stretchability, but also for their peculiar chemical-physical characteristics such as high resilience [6], extreme temperature resistance [7], low flammability [8], waterproofness [9] and remarkable environmental resistance (e.g. to ozone, UV rays, rain, snow, sleet, frost) [10]. These features make this synthetic elastomer more appealing than any other rubber-like material, both synthetic and natural, for soft robotics research. The usage of meshes [11], membranes and threads [12], has been also extensively explored: the flexibility of these materials allows for easy integration with soft robotic structures [13] or for the creation of stand-alone systems [14].

Despite the fairly recent appearance of this robotics branch, the use of soft systems has been already investigated in depth and applied widely in areas, ranging from exploration in disaster scenarios [4], rehabilitation [15], military

field service [16], minimally invasive surgery [17], sea inspection [18], to industrial robotics [19]. Soft robots have proven potential to outperform traditional robots in several, if not all, of these areas. Soft robotics research has already gone beyond academia, generating small and medium-sized enterprises (SME), such as Pneubotics Inc. [20] and attracting the interest of big robotic companies, e.g. FESTO [21], in the soft robotics quest for the future of automation. In 2014 *Big Hero 6*, a 3D computer-animated superhero-comedy film [22], was the first movie ever to introduce the concept of soft robots to the wide public, indicating soft robotics as the answer to the need for machines capable of safer human-robot interaction (HRI) [23].

Bio-inspiration has always played a central role in the soft robotics exploration of novel designs: the dexterity of natural limbs such as the trunk of the elephant [24], the tentacle of the octopus [25], [26] or the complex body motion of the snake [27], [28] have provided the role models behind the design of most of the soft robots developed so far. The human body itself inspired Joseph Laws McKibben when he developed the first pneumatic artificial muscle (PAM) in 1950 [29]. This system is regarded as the first intrinsically soft actuator. Its design, as many others in soft robotics, was the result of the search for a simpler and more adaptable robotic system to overcome the limitations of traditional rigid-linked robots; here for the delivery of rehabilitation therapy to patients affected by poliomyelitis. Since the dawn of soft robotics, pneumatics [30]–[32] and hydraulics [33], [34] have been the preferred forms of actuation, due to the possibility of seamlessly embedding chambers into soft structures, without the need for rigid components, hence maintaining their desirable properties, i.e., the softness of these structures. For the same reason tendon-driven actuation has also been largely employed in soft [25], [35], [36] and compliant robots [37], [38]. The advent of smart materials such as electroactive polymers (EAPs) [39], electro-rheological (ERM) [40], magneto-rheological (MRM) [41] materials and shape memory alloys (SMAs) [42] widened the range of actuation means

available for soft robotic applications. However, pneumatic and tendon-driven actuations are still widely preferred due to the larger forces exertable, the simplicity of their design, the inexpensiveness of the materials and the lower power consumption.

Despite the aforementioned benefits of the soft robotic approach, these systems present a number of limitations that researchers in this field are trying to overcome: soft robots are typically more complex to model and control in comparison with their rigid counterparts [43], due to the deformability of their bodies; this directly relates to what is widely considered the core challenge of soft robotics: the stiffening of soft structures [44]. In the search for the right trade-off between desired compliance and exertable force, researchers explore numerous approaches to enable on-demand stiffness tuning of soft robots [44]. These limitations are particularly evident in pneumatically and hydraulically actuated silicone-based robots. The sizable deformations exhibited in soft systems due to the inflation of embedded pneumatic/hydraulic actuators results in difficulties for modelling and control. This phenomenon, frequently referred to as *ballooning* in the soft robotics literature [45]–[47], limits not only the workspace, but also the maximum pressure these systems can operate at. As a result, the maximum stiffness achievable, as well as the maximum force that these systems can exert when interacting with the environment, are typically limited. To solve this problem researchers started to embed threads in the silicone walls of the chambers to create a braiding [12], [48], reinforcing these soft structures, thus allowing the use of higher pressures and providing only deformations in desired directions. This simple, yet effective, design adjustment significantly improved the overall performance of these systems, making it also easier to model and control their mechanical behaviour. Yet, after a certain pressure threshold is reached, the coils forming the braiding become too spaced apart to prevent undesired deformations, leading to a secondary ballooning effect in between the coils.

This thesis sets out to address these limitations proposing a novel design paradigm to enable the use of high pressure pneumatic actuation in soft robots, hence, a higher level of on-demand stiffness.

1.2 Research Motivation

Soft systems have the potential to revolutionise the robotics industry and to advance our society on a large scale. To transform this potential into real disruption, however, soft robots need to be able to deal with the tasks we are currently assigning to traditional rigid-linked robots. Although soft robots are already more dexterous than their rigid counterparts, they are still not able to achieve a comparable level of stiffness when needed. This translates into the incapability of these systems when it comes to handling the same payloads that traditional robots do. A soft robot that is not able to stiffen its body enough to guarantee the accurate positioning of a payload at the end effector, is a robot that is not ready for real word applications.

On the other hand, rigid-linked robots are unsafe by nature for HRI. Regardless of the quality of the control or design, traditional robots are still made of rigid components; hence, when it comes to interacting with soft tissues, e.g. the human skin or the mucous membrane, soft materials lend themselves more readily to creating robots that are safe in the context of HRI.

All the above limitations are directly or indirectly related to the lack of a reliable control mechanism for the stiffness of these soft structures. Bridging this gap will be important when trying to unlock the real potential of these systems. This is the main motivation behind the search for a novel Variable Stiffness System (VSS) to bridge the gap between traditional and soft robotics presented in this thesis.

1.3 Aim and Objectives

The aim of this research is the creation of a novel design paradigm to enable on-demand stiffness controllability in soft structures. Such a solution would bridge the gap between soft and traditional robots in a wide range of applications. This research therefore consists of the following objectives to achieve the described aim:

1. To create a novel VSS to be embedded in soft robots that:
    a. Works in a wide stiffness range despite being made solely of soft materials.
    b. Allows for on-demand and reversible stiffness transitions
    c. Allows for fine stiffness tuning in a continuous (non-discrete) stiffness range.
2. To create a VSS – based on (1) – that is not only stiffness-controllable, but also able of contextual shape-shifting and shape-locking capabilities.
3. To demonstrate the effectiveness of the design paradigms in (1) and (2) by using them in the creation of novel robotic systems, which outperform their state-of-the-art counterparts.

1.4 Research Contributions

The research presented within this thesis has led to the following contributions:

I. A novel active structural element that:
    o Can be continuously tuned in terms of stiffness in a wide range, achieving an infinite number of stable states;
    o Is inherently safe for human-robot interaction due to its capability of quickly switching between a rigid and a compliant/soft state and because it is made from soft materials;

o Is intrinsically able to detect collisions and interactions with the environment, acting as a distributed sensor at a much lower cost than commercially available solutions.

II. A novel anthropomorphic manipulator that uses the active structural elements proposed in (I) as robotic links to enable inherently safe HRI in collaborative scenarios.

III. A novel bio-inspired soft robotic manipulator for minimally invasive surgery (MIS) that combines pneumatic and tendon-driven actuations in an antagonistic fashion, endowed with stiffness-tuning, steering and shape-locking capabilities.

IV. A novel entirely soft assistive glove for hand rehabilitation, based on the same bio-inspired actuation principle of the system proposed in III.

1.5 Outline of the Thesis

The outline of the thesis is shown in Figure 1. Chapter 2 will provide a general background and literature review on how stiffness controllability has been addressed in soft robotics to date. Chapter 3 will describe the design, methodology, evaluation and intended application of contribution (I) and (II) in industrial robotics; background about HRI in industrial settings is also provided. Chapter 4 will then describe the design and methodology related to contribution (III). Chapter 5 will detail the use of the system in contribution (III) in surgical robotics. Chapter 6 reports on the application of the system of contribution (IV) in rehabilitation robotics. A dedicated background will be provided in each application chapter. Chapter 7 will conclude the thesis, discuss the limitations of the proposed systems and provide recommendations for future work.

1.6 Summary

This thesis explores stiffness controllability in soft robotics, a widely investigated research area where researchers are attempting to make soft robots

ready for real world applications. The lack of effective solutions served as main motivation for research into a novel stiffness-controllable structural element and a novel bio-inspired actuation system for soft robots with stiffness-tuning, shape-shifting and shape-locking capabilities. Thus, two new design paradigms for VSS will be presented. Furthermore, the use of these systems in different robotic applications, ranging from industrial (Chapter 3), to surgical (Chapter 5) and rehabilitation robotics (Chapter 6) will be explored.
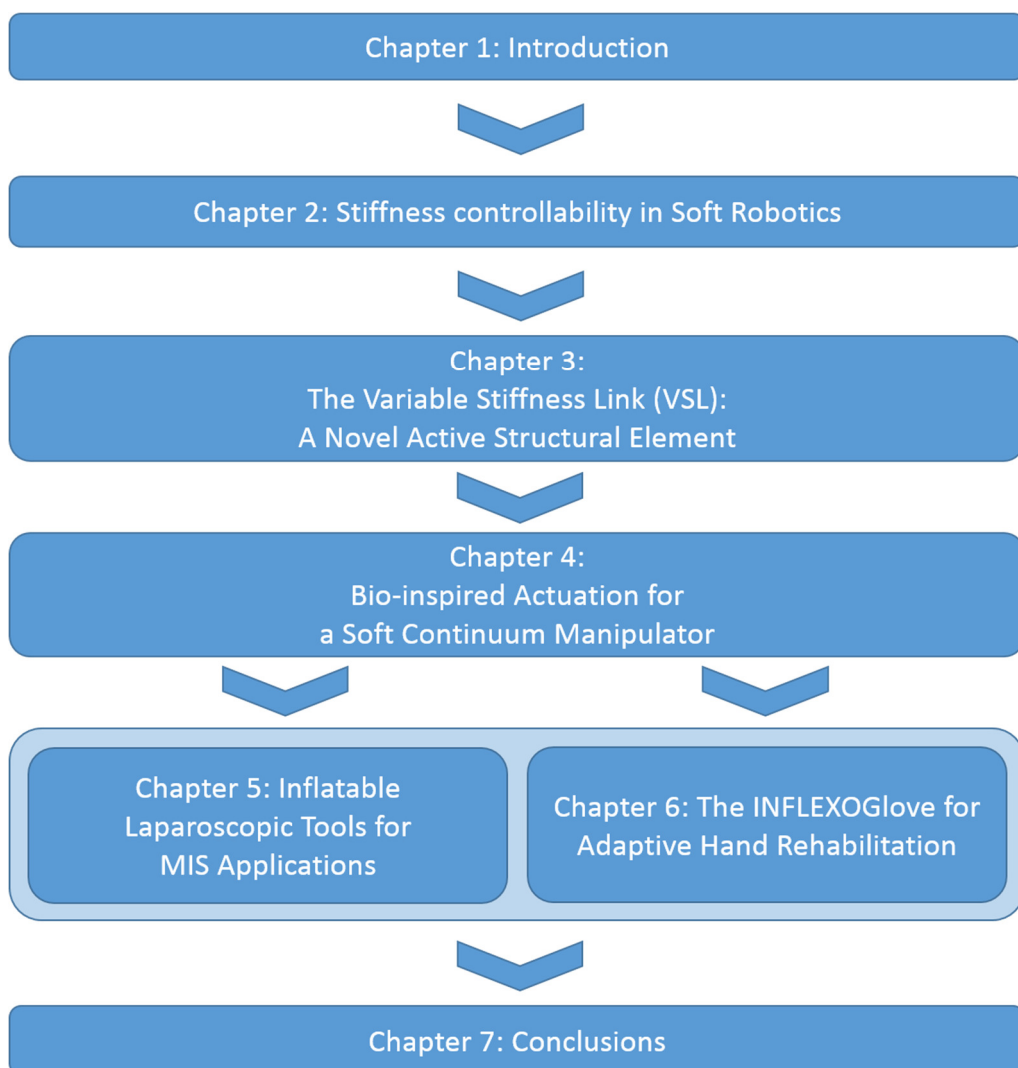
Figure 1 – Outline of the thesis.

1.7 Publications and Dissemination

The work described in this thesis has been widely presented in renowned robotic journals, such as the Soft Robotics Journal (SoRo), published by Mary Ann Liebert Inc. (IF: 8.649) and the Robotics and Automation Letters (RA-L), published by IEEE (IF to be assigned in 2018) and the British Journal of Urology (BJU), published by Wiley-Blackwell (IF: 4.439).

The work described in this thesis has been presented also on several occasions at top international robotic conferences, such as the IEEE International Conference on Robotics and Automation (ICRA), the IEEE/RSJ International Conference on Intelligent Robots and Systems (IROS) and the International Conference on Intelligent Robotics and Applications (ICIRA). Part of this thesis work will also be presented in May 2018 at the IEEE Soft Robotics Conference, the first monothematic international conference about Soft Robotics. The author presented also in international workshops, such as the Workshop on Computer /Robot Assisted Surgery (CRAS), congresses and symposiums, such as the Prostate Cancer World Congress (PCWC) and the Hamlyn Symposium on Medical Robotics (Hamlyn).

A complete list of all the publications produced by the author about the work presented in this thesis is presented here. The author also indicated to which contributions and to which thesis section each publication links to.

Journal Papers:

A. Stilli, H.A. Wurdemann, and K. Althoefer. "A Novel Concept for Safe, Stiffness-Controllable Robot Links." Soft Robotics 4, no. 1 (2017): 16-22. Contribution: I. Chapter: 3.

A. Shiva, **A. Stilli**, Y. Noh, A. Faragasso, I. De Falco, G. Gerboni, M. Cianchetti, A. Menciassi, K. Althoefer, and H.A. Wurdemann. "Tendon-based stiffening for a pneumatically actuated soft manipulator." IEEE Robotics and Automation Letters 1, no. 2 (2016): 632-637 (presented also in ICRA 2016).
Contribution: III. Chapter: 4.

K. Althoefer, H.A. Wurdemann, and **A. Stilli**. "Minimally invasive surgery employing antagonistic, inflatable robot: evaluation of positioning accuracy and motion dynamics." BJU International 116 (2015): 48-49.
Contribution: III. Chapter: 4 and 5.

Conference Papers:

A. Stilli, A. Cremoni, M. Bianchi, A. Ridolfi, F. Gerli, F. Vannetti, H.A. Wurdemann, B. Allotta and K. Althoefer. "AirExGlove - A Novel Pneumatic Exoskeleton Glove for Adaptive Hand Rehabilitation in Post-Stroke Patients", In Soft Robotics, 2018 IEEE-RAS International Conference on (RoboSoft). IEEE, 2018.
Contribution: IV. Chapter: 6.

A. Stilli, L. Grattarola, H. Feldmann, H.A. Wurdemann, and K. Althoefer. "Variable Stiffness Link (VSL): Toward Inherently Safe Robotic Manipulators." In Robotics and Automation, 2017 IEEE International Conference on (ICRA), pp. 4971-4976. IEEE, 2017.
Contribution: II. Chapter: 3.

H. Wurdemann, **A. Stilli**, and K. Althoefer, "Stiffening mechanism and stiffness-controllability of soft robots: An antagonistic actuation technique for simultaneous stiffness and position control." In International Conference on Intelligent Robotics and Applications (ICIRA), 2015.
Contribution: III. Chapter: 4.

F. Maghooa, **A. Stilli**, Y. Noh, A, K. Althoefer, and H.A. Wurdemann. "Tendon and pressure actuation for a bio-inspired manipulator based on an antagonistic principle." In Robotics and Automation, 2015 IEEE International Conference on (ICRA), pp. 2556-2561. IEEE, 2015.
Contribution: III. Chapter: 4 and 5.

A. Stilli, H.A. Wurdemann, and K. Althoefer. "Shrinkable, stiffness-controllable soft manipulator based on a bio-inspired antagonistic actuation principle." In Intelligent Robots and Systems, 2014 IEEE/RSJ International Conference on (IROS), pp. 2476-2481. IEEE, 2014.
Contribution: III. Chapter: 4.

Workshop, Symposium and Congress Papers:

A. Stilli, H.A. Wurdemann and K. Althoefer. "A Novel Flexible Endoscope for Minimally Invasive Surgery", in Annual International Conference of the IEEE Engineering in Medicine and Biology Society, 2016 (EMBC), (1 page paper).
Contribution: III. Chapter: 5.

A. Stilli, H.A. Wurdemann, and K. Althoefer, "A Novel Inflatable and Flexible Endoscope for Inherently Safe Minimally Invasive Examination", in WS on Computer /Robot Assisted Surgery, 2016 (CRAS).
Contribution: III. Chapter: 5.

A. Stilli, A. Cremoni, H.A. Wurdemann, and K. Althoefer, "A new antagonistically actuated endoscope: Towards an inherently safe minimally invasive examination", in Hamlyn Symposium on Medical Robotics, 2016 (Hamlyn).
Contribution: III. Chapter: 5.

A. Stilli, H.A. Wurdemann, and K. Althoefer, "Hybrid actuation for a bio-inspired continuum robotic manipulator for surgical applications", in Hamlyn Symposium on Medical Robotics, 2015 (Hamlyn).
Contribution: III. Chapter: 4 and 5.

K. Althoefer, H. Wurdemann, and **A. Stilli**, "Minimally invasive surgery employing antagonistic, inflatable robot: Evaluation of positioning accuracy and motion dynamics." In Prostate Cancer World Congress (PCWC), 2015.
Contribution: III. Chapter: 4 and 5.

A. Stilli, F. Maghooa, H.A. Wurdemann, and K. Althoefer, "A new bio-inspired, antagonistically actuated and stiffness controllable manipulator", in WS on Computer /Robot Assisted Surgery, 2014 (CRAS).
Contribution: III. Chapter: 4.

Chapter 2

2 Stiffness Controllability in Soft Robotics

This chapter provides an extensive background and literature review relevant to the contributions of this work. A thorough analysis of the state of the art of variable stiffness systems (VSSs) in soft robotics is provided. This chapter focuses on the approaches developed to achieve stiffness controllability in soft robotic systems. Different designs, materials and techniques are presented within this section. However, given the magnitude of the topic, previous work on the applications of the presented systems are not discussed in this chapter. A dedicated background section regarding the applications of the new system presented in this thesis, i.e., collaborative robots in industrial settings (Chapter 3), surgical applications (Chapter 5) and rehabilitation robotics (Chapter 6), is provided at the beginning of each chapter.

2.1 Introduction

This thesis focuses on the investigation of a new and innovative variable stiffness system (VSS) for soft robots. Therefore, in this section background about the research conducted within this area is provided. The VSSs for soft robots described here make use of soft means of actuation only to generate the desired change of the mechanical properties of the systems in which they are embedded. According to the recent comparative study presented in [44], VSSs for soft robots can be divided in two main groups:

I.   *Active VSSs for Soft Robots*: these VSSs provide on-demand stiffening using an antagonistic approach, i.e., the creation of stiffness by means of equilibrium between two or more forces, at least one of which is an active force.

II. *Semi-Active VSSs for Soft Robots*: these VSSs provide on-demand stiffening relying on their capability of intrinsically tuning the rigidity of the robotic structure in which they are embedded.

These two groups can be divided into sub-groups based on the soft actuation means used to achieve on-demand stiffness. The VSSs in group I are presented in Section 2.2, while group II is discussed in Section 2.3. Given the scope of this thesis, this background section focuses only on robots based on soft materials and soft actuation means, excluding flexible rigid-linked manipulators such as robots that are flexible by design. A comprehensive up-to-date literature review on flexible continuum manipulators can be found in [38]. Relevant background on the field of surgical robotics, where these systems found extensive use, will be provided in Chapter 5. Another class of mechanisms that were acknowledged by several researchers as soft robotic systems prior to the introduction of soft materials in robotics is the compliant or variable-stiffness actuators class. These actuators are not discussed in this chapter; an up-to-date exploration of these

actuators is presented in [49], [50]. Relevant background on stiffness-controllable industrial robotics will be provided in Chapter 3.

2.2 Active VSSs for Soft Robots

Active VSSs are based on active means of actuation. According to [44], Active VSSs can be divided in two primary sub-groups based on the configuration of the means of actuation used:

- *Active/Active Configuration (AAC)*: the stiffening is achieved by creating a stable equilibrium between two or more active forces that are generated by two or more active means of actuation.
- *Active/Passive Configuration (APC)*: in this scenario, only one mean of actuation is used. This mean is paired with a passive non-actuated element that provides a reactive force in response to the active force applied. The stiffening of the VSS is caused by the equilibrium between an active and a passive force.

In this section, the active means of actuation used to create Active VSSs are presented. Either of these means of actuation can be paired with any other of their kind, or with any passive system in AAC and APC configurations, respectively. In soft robotics, several, but not all, of the possible combinations between the active means of actuation listed within this section have been explored, although in theory any other combination could also be used. In addition, passive elements typically used in soft robotics in APC configurations are detailed in this section. Relevant examples of explored combinations in soft robotics are provided in this section as well.

2.2.1 Active Actuation Means

In this section, the active means of actuation used in soft robotics are presented and classified. This classification builds on the work presented in [44], providing

an extensive background in this area. The author of this thesis acknowledges this classification to be the most comprehensive proposed so far in this field; for this reason, the structure of the classification has not been altered.

Flexible Fluidic Actuators

Dating back to 1962, the flexible fluidic actuators that started the investigation into soft robotics, specifically McKibben actuators [29], are generally regarded as the first soft actuators – their introduction had considerable impact on the development of soft robotics field. However, according to the publication data presented in [51], soft robotics only became a widely recognized area of research over four decades later, into 2004. McKibben actuators have been widely investigated in the soft robotics community, and, due to the their muscle-like mechanical behaviour, are frequently referred to as pneumatic artificial muscles (PAMs) [52], [53]. PAM actuators present a simple mechanical structure composed of an air-tight internal bladder fitted inside a braided mesh shell which is made of flexible yet non-extensible threads. Once pressurised air [53] or water [54] is supplied to the bladder, due to the high longitudinal and low radial stiffness of the braiding, the actuator shortens. These actuators have a number of desirable features, including their remarkable force density per volume and mass; the McKibben actuator presented in [55], with a diameter of 15 mm and a weight of 50 g, produces up to 1,000 N at 100 kPa with radius variation of 100%. The performance of these actuators is even more impressive in the case of hydraulic actuation, as shown in [54] where a McKibben actuator that uses water pressure with an external diameter of 40 mm produces 28,000 kN at 4000 kPa.

The use of fluidic actuation to actuate soft structures has been also extensively explored in the context of elastomeric structures. Fluidic elastomeric actuators (FEAs) are a design translation of the PAM actuators, where chambers directly obtained in elastomers perform the function of the bladder and the surrounding material the role of the deformable braiding. Several designs have been explored

in this context to provide the anisomorphism necessary to generate a preferential direction of chamber expansion, analogous to the way in which the thread orientation creates a low radial and high axial stiffness in PAM actuators. These designs include non-uniform distribution of the elastomeric material by design [56], the usage of less extensible yet flexible structures embedded into the main elastomeric body [57] (typically different elastomers with considerably higher Shore hardness, i.e. the hardness scale typically used for soft materials), and the usage of fibres to braid the chambers [18] using the same principle of deformable braiding employed in PAM actuators. Additionally, the designs can include combinations of these approaches, as in the PneuFlex actuators embedded in the RBO hand presented in [58], or all of them together [13]. The modularity of these systems allows for complex and articulated designs such as those in [58] and [59]. Complex designs can be realized using embedded pneumatic networks, as demonstrated by the G.M. Whitesides group at Harvard University; such designs include the starfish-like gripper presented in [61] or the *Multigait* soft walking robot presented in [62].
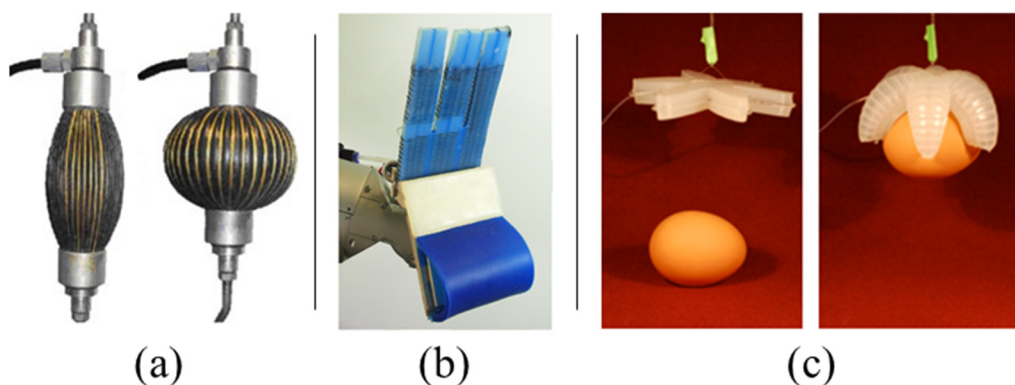
Figure 2 – Examples of soft fluidic actuated systems: (a) a PAM relaxed and contracted [52]*, (b) the RBO soft hand* [58]*, and a starfish-like gripper* [61]*.*

Shape Memory Materials

All materials capable of recovering a predefined shape that has been "memorised" during their fabrication process belong to the class known as shape

memory materials (SMMs). This controlled and invertible plastic deformation is typically induced by a phase transformation of the material. The investigation of these materials started with the work of Ölander in 1932 [63] on the metallic alloy Cd-Au (gold-cadmium). This alloy can be significantly deformed from its original shape; however, upon heating to a temperature generally referred to as the reverse transformation temperature (RTT) [64], the memorised shape is recovered. In 1941, Vernon and Vernon first introduced the term shape memory [65]. This thermoelastic behaviour associated with the martensite-austenite transformation of the alloy was reported later in 1951 by Chang et al. in [66], who already referred to this material as shape memory alloy (SMA). Another peculiar behaviour of certain SMAs is super elasticity (SE), also known as pseudo elasticity (PE); in this behaviour, at a temperature higher than the RTT, the alloy exhibits a stress-induced martensitic transformation upon loading. Once the induced load is removed, the phase transformation is inverted and the initial shape is recovered, allowing a large reversible deformation [64].

Following the discovery of these properties of the Cd-Au alloy, several other metallic alloys have been found that exhibit the same behaviour, e.g., In-Tl (Indium-Thallium), In-Cd (Indium-Cadmium) [67], Cu-Zn (Copper-Zinc) [68] and Cu-Al-Ni (Copper-Aluminium-Nickel) [69]. Despite the widespread interest of the research community, the attempt to find practical applications in industrial settings for the aforementioned alloys has been unsuccessful, largely due the high costs involved in the complex manufacturing process together with undesired mechanical properties [70]. One of the alloys that has been more extensively investigated is the binary alloy Ni-Ti (Nickel-Titanium). William J. Buehler discovered this alloy's properties in 1959 [71]; the name Nitinol combines the chemical formula and its place of discovery (Naval Ordnance Laboratory). Due to its lower cost of production and more desirable mechanical properties, Nitinol has been the first SMA to find commercial applications, including the dental, automotive, aerospace and biomedical industries [72],

starting with the CryoFit™ pipe coupler for the F-14 jet fighter built by the Grumman Aerospace Corporation in 1969 [73]. Different designs have been investigated for Nitinol-based systems, including thin films [74], springs [75] and loops [76]. Nitinol thin films are interesting as smart materials, particularly regarding to Micro-Electro-Mechanical System (MEMS) applications [77].

To improve the performance of binary SMAs in terms of operation temperature, the use of ternary metallic alloys, referred to as high temperature shape memory alloys (HTSMAs), has been investigated [78]. In contrast to their binary counterparts, which even in the case of Nitinol have a maximum temperature of operation of 100 °C, HTSMAs work in a range of 83-513 °C [73]; however, they exhibit an average strain of 1.5-4.0 %, lower than the 6-10% range of Nitinol.

Magnetic Shape Memory Alloys (MSMAs), also known as Ferromagnetic Shape Memory Alloys (FSMAs) [79], use magnetic fields to supply the necessary energy for actuation, with a similar performance in terms of strain rate to SMA but without the limitations of the long thermal transient. Consequently, it is possible to achieve higher actuation frequencies [80], even though the low operation temperature (-100.15 – 41.85 °C) [81] of MSMAs limits their use in real applications.

Shape memory polymers (SMPs), like SMAs, exhibit a thermal induced shape-memory [82] that allows these polymers to shift from a permanent to a temporary shape. In contrast to SMAs, however, the shape-shifting relates to the glass transition of the material, rather than the martensitic transformation. Composed of polymers, SMPs are easier to customise in shape, lower in cost in comparison with SMAs, and biodegradable, making them particularly suitable for soft robotics systems in bio-medical applications [83]. Another relevant characteristic of the application of certain SMPs is their self-healing capability [84]. Triple-shape polymers, i.e. SMPs with one permanent and two temporary

shapes, have been also developed [85], pairing two SMPs with diverse glass transition temperatures. An alternative approach to realising a triple-shape transition using a single SMP has been proposed in [86]. The use of a magnetic field to supply the heat required to induce the shape-changing process has been presented in [87]. Recent developments in this field have shown that the phase transition can also be induced using light rather than heat [88], or by means of a reaction with solutions [89]. On the one hand, the use of SMAs is preferred when a limited strain with a high force is required, while on the other hand SMPs can provide large strain (up to 400%, and possibly above 800%) but considerably lower forces. A comprehensive comparison between the chemical-physical properties of SMAs and SMPs is presented in tables 8 and 9 of [73]. Other materials such as ceramics have been investigated in the context of SMMs [90]; however, because these materials did not find applications in the context of soft robotics, they are not discussed further in this thesis.

Electroactive Polymers

Electroactive polymers (EAPs) are particularly conductive polymers subjected to shape-changing in response to the application of voltage. Due the nature of their behaviour, actuators based on EAPs are also referred to as "artificial muscle" in the literature [39]. Research about EAPs dates back to the 1880, when Wilhelm Röntgen first investigated the effects of the application of an electrical field on the mechanical properties of natural rubber sprayed with electric charges using needle combs at high voltage, as described in [91]. However, the first example of the synthesis of an electroactive polymer occurred a century later in 1977, when Professors H. Shirakawa, A. G. MacDiarmid and A.J. Heeger discovered polyacetylene and demonstrated that, upon doping, it exhibits conductive properties [92]. The research in this field grew slowly until the end of 2000, as reported in [93]. Following the award of the Nobel Prize for chemistry to Professors H. Shirakawa, A. G. MacDiarmid and A.J. Heeger for their findings about polyacetylene, and following the challenge to develop an

EAP-based robotic arm capable of beating a human at arm-wrestling (proposed the year before by Yoseph Bar-Cohen from the NASA Jet Propulsion Lab [39], [94]), research on EAPs sparked, reaching its peak ten years later in 2010 before slowly declining until the present day [93]. This decline is largely due to the multiple drawbacks of this technology that strongly limited its diffusion, leading to marginal commercialization.

A broad family of polymers (and elastomers) is included in the category of EAPs. These polymers can be divided in two major groups: electric and ionic. The former group is also referred as "dry" and the latter as "wet", due to their mode of use.

Electric (dry) EAPs are divided into ferroelectric polymers [95] (exhibiting both piezoelectric and pyroelectric response [96]), electrostrictive polymers [97], and Dielectric Elastomers (DEs) [98]. Electric EAPs have found wider use than ionic EAPs in traditional and soft robotic applications; this difference is due to the electric EAPs' capability of holding the shape and stiffness achieved when the application of voltage is upheld, thereby behaving as a variable capacitor. Furthermore, electric EAPs have a low power consumption and typically exhibit large strains. Lastly, they can be produced in any desired form, also being scalable as actuators. One drawback of their use, however, is that they need very high voltages to be activated.

Ionic (wet) EAPs are ionically charged polymers that have been studied as standalone systems [99] and in combination with metallic structures [100], frequently referred to as ionic-polymer-metallic-composites (IPMCs) in the literature. The actuation/stiffening principle of ionic EAPs is based on the movement of the ionic charges due to electrostatic attraction toward the metallic structure that acts as a cathode when a voltage is applied [101]. As opposed to electric EAPs, ionic EAPs require minimal voltage to be actuated (typically 1 V

-10 V [101]). They can also produce high strain [102] and be used as high sensitivity sensors [103]. However, their power consumption is significantly higher due to the movement of the ionic charges and they need to be constantly wet in order to guarantee this electric flow. Therefore, the integration of this system with robotic units has limitations, and the use of self-enclosing structures that prevent dehydration is necessary to create functional actuators [104]. In this context, the use of carbon nanotubes (CNT) has been also explored [105].

Tendon-driven Actuators

Tendon-driven actuation has been extensively investigated in robotics applications, in particular for continuum manipulators. Tendons generally exhibit minimal bending stiffness, making them suitable for soft [35], [106] and compliant [107] [37] robotics applications. Furthermore, they enable remote actuation, allowing the motors controlling the tendons to be positioned in the base of the manipulator [36], or, even further away from the actual robot structure, using Bowden-cable, which are largely employed in wearable robotics [108]. Tendon-driven system have been also investigated in combination with springs to create series-elastic actuators, such as those presented in [109]. Nowadays, thanks to the use of synthetic materials, such as nylon and polyethylene, tendons with sub-millimetre diameters can be employed to reliably transmit forces in the order of hundreds of newtons with minimal impact on the volume and weight of the system they are embedded in. The use of metallic alloys in combination with synthetic plastic has been also widely explored to customize mechanical characteristics such as tensile strength, elongation at break, flexibility, resistance to fatigue and abrasion. For these reasons, tendons have been and continue to be one of the most investigated means of actuation for traditional and soft robotic systems, in particular in applications where the size of the workspace or of its point of access is limited, e.g. in minimally invasive surgery [37].

2.2.2 Active VSSs in Active-Active Configuration

In this sub-section, relevant examples of soft robots based on the AAC configuration are presented. A comparison between the performance of these VSSs, the performance of Active VSSs in APC and those of Semi-Active VSSs is presented in section 2.4.

EAP/EAP: In [110] the use of two DEs in an antagonistic configuration is proposed to create an Active VSS. The MERbot [111], a soft walking robot that uses a 2-DOF multifunctional electro-elastomer roll as each of its six legs, uses a combination of two DEs in an antagonistic configuration to realize both motion and leg stiffening. The use of DEs in a multi-layered configuration has been explored in [112] to enable active stiffness control in orthoses for hand rehabilitation. A series of DEs is used to enable locomotion and stiffness-controllability in the annelid-inspired crawling robot presented in [113]. A comprehensive up-to-date literature review about the use of DEs in soft robotics has been presented by Anderson et al. in [114].

Fluidic/Fluidic: A soft continuum manipulator has been proposed in the recent work of Okamura et al. in [115], where a series of PAMs is radially arranged around a pneumatic backbone. Based on the same combination is the work presented in [116], where 32 micro PAMs are arranged longitudinally, radially and circumferentially to mimic the behaviour of the muscles group of an octopus tentacle. Purely fluidic actuation is used in [117] to enable crawling and rolling locomotion in addition to stiffness adjustment. A 7-m-long manipulator is presented in [118], combining three PMAs.

Tendons/Fluidic: The combination of tendon-driven (6 tendons) and pneumatic/hydraulic actuation was first explored in the KSI tentacle [25], one of the first examples of a soft continuum robotic manipulator in the 1990's. However, the accordion-shaped, non-stretchable bellow used for the body

embeds rigid ferrules along its length, introducing rigid elements into this system and therefore significantly increasing its radial stiffness. The Air-Octor [36] presents a similar design and also uses rigid elements (a long spring around the central pneumatic chamber), making this robot "soft" only in certain directions.

2.2.3 Active VSSs in Active-Passive Configuration

Fluidic/Braided chambers: The development of a multi-section variable stiffness endoscope using a series of fluidically-actuated braided silicone chambers is presented in [119], [120] for the exploration of the large intestine. Given the orientation of the fibres used for the braiding, no elongation or contraction is produced upon the application of pressure, but only stiffness tuning. The device is intended to bend passively when inserted. The design of a robotic hand using pneumatic fibre-reinforced elastomeric actuators to adjust the finger surface stiffness is presented in [121]. Kevlar threads are used to reinforce the chambers. Micro-tubes embedded in a flexible polymeric matrix composite and fluidic actuation are used in [122] to create a system with anisotropic and tunable stiffness characteristics.

SMA/Braided chambers: The combination of SMA coils and braided sleeves (commercially available, not customized) embedded in a silicone matrix has been extensively explored in the OCTOPUS project [12], [123] to enable stiffness controllability in the tentacles of a robotic octopus. The development of an 8-armed (-tentacled) robot is presented in [124]: radially- and circumferentially- [125] arranged SMA coil actuators on the inside of the tentacles mimic muscle arrangement in the octopus arm, enabling both stiffness controllability and elongation.

SMA/Flexible layers: The use of SMA spring actuators in combination with a stack of flexible layers is explored in [126] to control the bending stiffness of a beam-like system (see also 2.3.1 for layer jamming).

SMA/Elastomeric flexible layers: An SMA embedded in flexible elastomeric matrix is used to enable crawling locomotion in the soft, 3D-printed robot presented in [127]. The same combination is used in the soft actuator presented in [128], also embedding a shape retention system based on a low melting point alloy (LMPA) (see also 2.3.3 for LMPA).

EAP/Flexible layers: The use of EAPs in combination with flexible layers is explored in the work of Henke et al. [129] to enable stiffness controllability in a beam-like system. The use of pre-stretched EAP films is investigated in [130] to create variable stiffness suspensions. The recent work of Li et al., presented in [131] on a single-layer system, makes use of a DE to enable transverse curvature controllability, hence, the bending stiffness tuning. An up-to-date literature review about EAP-based grippers has been recently presented in [132]. A low-voltage ionic EAP actuator for soft robotic applications using gold nanocomposites electrodes is presented in [133].

Tendons/Braided sleeve/Spring: A new bio-inspired design for a kangaroo robot, focused on the actuation and stiffness control of the tail and combining two passive elements such as springs and braided sleeve with tendon actuation, has been recently proposed in [134]. Furthermore, a layer-jamming mechanism is integrated in the system to increase the stiffness performance (see also 2.3.1 for layer jamming).

Tendon/Fluidic (passive): A stiffness-controllable, tentacle-shaped gripper is presented in [135]. The gripper uses only two tendons to provide single-direction bending of the elastomeric conic structure where the tendons are embedded. Fluid (water) is used to fill the inner lumen of the tentacle. However, pressure is not actively controlled; once the gripper bends, due to the reduction of the internal volume, the pressure and stiffness both increase.

2.3 Semi-Active VSSs for Soft Robots

Semi-Active VSSs, in contrast to Active VSSs, allow for effectively changing mechanical properties of the material, such as elasticity and viscosity, rather than create stiffness as a result of the equilibrium of two forces. Another important difference between active and Semi-Active VSSs is that the former must embed at least one means of actuation, while the latter only enables stiffness controllability. Thus, they both must be paired with at least one soft means of actuation to create a proper soft robotic system. Examples of soft robots in which these combinations have been explored are presented at the end of each sub-section of this section.

2.3.1 Jamming-Based Systems

Jamming is a technique inspired by the well-known stiffening phenomenon observed in powder-based, vacuum-conserved foods, e.g., vacuum-packed coffee powder. The stiffening observed after vacuum pressure is applied for food preservation is due to the increased friction between the jamming media, i.e., the coffee particles. In standard pressure conditions, the coffee particles can slide against each other almost freely; consequently, they exhibit a fluid-like behaviour. However, when vacuum pressure is applied to the airtight flexible container, the differential pressure between the inside and the outside generates compression, leading to a significant increase in the friction forces between the jamming media. As soon as air is introduced again the system quickly reverts to its fluid-like state, as can be experienced by piercing or cutting a vacuum-packed coffee container. The quickness, reversibility and magnitude of this stiffness transition in conjunction with the small volume variation (less than 0.5 % in the case of powder-based systems [19]) made this technique particularly appealing for soft and compliant robotics applications. One the first commercialization attempts of a jamming-based system is found in the case of the Universal Gripper, firstly presented in [19] and developed two years later into a product by John Amend (one of the authors of [19]) under the name of Versaball ® by

Empire Robotics Inc.. The simple, yet effective gripper design consists of a bag filled with ground coffee (jamming media) to be pushed against the target object. Once the gripper interacts with the object, it deforms, enveloping the object and assuming its shape. Vacuum pressure is then applied to the internal chamber, locking the shape of the gripper, allowing for stable grasping of almost any object shape. However, as in several other robotics cases, despite the best intentions and efforts of the researchers behind this company, the translation from academia to industry was unsuccessful; this failure led to the closure of the company after 4 years at the end of 2016. This soft robotics story has been recently analysed in [136]. Nonetheless, this novel design attracted the interest of several researchers worldwide, opening the door to new applications (e.g., deep-sea sampling and manipulation [137]) and posing new interesting challenges regarding shape sensing of grasped objects using soft grippers [138]. The effect of granules hardness, size and shape on the stiffness of granular jamming systems has been investigated in [139], where a soft manipulator is presented. The STIFF-FLOP manipulator is another example of a soft robot based on pneumatic actuation and granular jamming for stiffening [60]. Not only granules have been considered as jamming media, but also layers, as in the work presented in [140] produced by researchers at MIT. One of the limitations shared by these vacuum-based jamming systems is the maximum differential pressure that is inevitably smaller than 100 kPa (typically 85 kPa – 90 kPa for good vacuum pumps). Thus, the maximum stiffness of these systems (i.e., the maximum friction between the jamming media) cannot be pushed any further, unless an external pressure, higher than the ambient pressure, is supplied.

2.3.2 Magneto- and Electro-Rheological Materials

The term rheology (from the Greek verb *rheos*, to flow) refers to the study of the mechanical property of fluid, semi-solid, molten and solid materials exhibiting predominantly a plastic and viscous behaviour. Magneto-rheological materials (MRM) and electro-rheological materials (ERM) are fluids that undergo a

modification in their rheological properties (viscosity and elasticity) when a magnetic field and electric field are applied, respectively. In both cases, the material regains its original properties once the magnetic or electric field is removed. In contrast to other VSSs described in this chapter, both ERMs and MRMs found industrial applications relatively soon after their discovery in the late 1940's by Rabinow [141], used in the automotive industry in particular to create adaptive shock absorbers [142], [143] and in rehabilitation robotics for the same purpose [144]. In the field of soft robotics, the use of magneto-rheological elastomers (MREs) has been also investigated [145], as well as the use of magneto-rheological fluids (MRFs) and electro-rheological fluids (ERFs) [146], e.g., for the soft gripper presented in [147]. However, because these fluids suspensions consist of ferromagnetic particles in most cases, these systems are particularly sensitive to particle settling. The use of MRFs in combination with absorbing foams solves this problem and allows for the use of the controllable fluids in a more cost-effective way [148]. Electro-rheological elastomers (EREs), as opposed to their magnetic counterparts, did not find widespread application in industry due to the significantly substandard performance of dampening variation that was achievable.

2.3.3 Low Melting Point Materials

The use of the state-transition from solid to liquid of some materials has also been explored to enable stiffness tuning of soft robotic systems. In particular, due the nature of the application, low melting point materials (LMPMs), i.e., materials with a low melting temperature in comparison to the ambient temperature, were considered. A surprisingly promising candidate for this material is wax, as demonstrated by the MIT research group in [149], where a 3D-printed, wax-filled polyurethane foam beam was used to create an articulated joint; a flexible, soft scaffold of the same material in both a wax-coated and non-coated version were compared, demonstrating a significant increase in stiffness in the former case. Other examples of the use of LMPMs in soft robotics are the

work of Shintake et al. presented in [150], where a metal low melting point alloy (LMPA) was used in combination with a dielectric elastomer (an EEAP) to respectively stiffen and actuate a soft gripper, or the VSS presented in [151], where a LMPA was embedded in a layer of polydimethylsiloxane. A variable stiffness fibre (VSF) based on the same metal LMPA (Cerrolow 117) has been recently presented in [152], designed to be embedded in wearable robots to provided stiffness-tuning capabilities, or to be used in combination with a silicone-based fluidic actuator.

2.3.4 Glass Transition

The glass transition is the transformation between a hard and brittle state to a rubber-like state that characterizes amorphous polymers (not crystalline polymers). It is associated with the glass temperature T_g, which defines the condition in which we find polymers at the ambient temperature T_a: rubber elastomers, e.g., polypropylene (atactic) $(T_g = -20\,°C)$ and polypropylene (isotactic) $(T_g = 0\,°C)$ [153], are polymers with a $T_g < T_a$; hence, they are normally used in a rubbery form; (amorphous) plastics, e.g. polystyrene $(T_g = 105\,°C)$ and polymethyl methacrylate $(T_g = 95\,°C)$ [153], are polymers with a $T_g > T_a$; hence, they are used in their glassy form. The glass transition is not a phase transition, even though the mechanical properties of the polymers change significantly; it is also not to be confused with the melting transition, which occurs at the melting temperature T_m and characterises crystalline polymers. However, in the case of semi-crystalline polymers (partially crystalline, partially amorphous) such as polyethylene terephthalate [154] (commonly known as PET), both transitions take place, always with $T_m > T_g$. Altering the T_g of an amorphous or semi-crystalline polymer by heating it up or cooling it down make it possible to change the polymer's stiffness on-demand. Examples of the use of this approach in soft robotics are the soft gripper made of a 3D-printed, acrylate-based thermoplastic polymer presented in [155], where a microfluidic network

is used to supply or remove heat; the approach can also be found in the work on polymer nanocomposites inspired by cucumber dermis presented in [156] and by animal whiskers presented in [157]. In all these cases, the use of the glass transition allows for a significant and reversible decrease in the elastic modulus, e.g. for the system presented in [156] by a factor of 40, from 800 to 20 MPa. One disadvantage of this transition, however, is that the time required to produce the desired transition is typically quite long, e.g. in the order of a few minutes for the system presented in [156]. Better performance, with a heating transient time in the order of seconds, can be obtained when fluid is used to supply heat [155]. A soft robotic system based on this technology is presented in [158], where the stiffness of a polycaprolactone-based grid is controlled by multiple heating elements, enabling individual stiffness tuning of each cell of the grid.

2.4 Summary

In this chapter, an extensive background and literature review on the primary purpose of this thesis, i.e., the creation of a new design paradigm to enable on-demand stiffness controllability in soft structures, has been provided. In the recent work of Manti et al. [44], published in 2016, a new and comprehensive classification of variable stiffness systems for soft robots has been introduced. The author recognises the merit and the contributions of this work; hence, based on the proposed classification, he has presented an extensive up-to-date literature review about stiffening mechanisms in soft robotics. Different VSSs and their applications in several soft robots have been discussed. As this research shows, soft materials are opening new possibilities in numerous robotic applications. A qualitative comparison between the discussed systems is presented in Table 1, based on the work presented in [44]. Up-to-date references to relevant systems are provided in the last column of the table.

Table 1 – *Qualitative comparison between VSSs for soft robotics applications, based on* [44] *(reproduction permission obtained): the modes of stiffening considered are: 1) Bending, 2) elongation/compression and 3)torsion. Different colours have been used to enhance the readability of the table.*

		ACTUATION MEANS	Speed of stiffening	Depending on	Speed of de-stiffening	Depending on	Scalability	Stiffness variation	Indep. stiffening control & eq. position	Passive deformation	# modes of stiffening	Allowed workspace	Ref.
ACTIVE VSSs	Active - Active	EAP + EAP	++	voltage amplifier	++	discharge	+	2 x	Yes	Large	1,2	Medium	[110], [112]
		McKibben + McKibben	+	fluidic inflow	O	fluidic outflow	-	10 x	Yes	Large	1,2	Large	[117], [118]
		Tendons + Fluidics	O	motors velocity and fluidic inflow	O	motors velocity and fluidic outflow	O	10^3 x	Yes	Large	1	Large	[25], [36]
	Active - Passive	Fluidics + Braided Sleeve	+	fluidic inflow	O	fluidic outflow	-	2.4 x	No	Large	1,2	Large	[119]–[121]
		SMA + Braided Sleeve	+	current limitations	-	thermal conditions	-	1.5 x	Yes	Large	1,2	Large	[12], [123], [125]
		SMA + Flexible Layers	-	current limitations	-	thermal conditions	O	14.6 x	No	Small	1,3	Small	[126]
		EAP + Flexible Layers	+	voltage amplifier	++	discharge	O	100 x	No	Medium	1,3	Medium	[129]
SEMI-ACTIVE VSSs	Jam-ming	Granular Jamming	+	vacuum pump outflow	O	vacuum pump inflow	+	40 x	Yes	Large	1,2,3	Large	[19], [60], [136]–[139]
		Layer Jamming	+	vacuum pump outflow	O	vacuum pump inflow	+	10 x	Yes	Medium	1,3	Medium	[134], [140]
	MRM/ ERM	MR - Fluids	++	magnetic field	++	magnetic field	+	37 x	Yes	Large	2	Large	[41]
		MR - Elastomers	++	magnetic field	++	magnetic field	+	5 - 16.3 x	No	Large	2	Large	[145], [148]
		ER - Elastomers	++	electric field	++	discharge	+	10 x	Yes	Large	2	Large	[40]
	LMPM	Wax	--	thermal conditions	-	heat source	++	10^3 x	Yes	Small	1,2,3	Large	[149]
		Polymers	--	thermal conditions	O	heat source	++	86 - 100 x	Yes	Medium	1,2,3	Medium	[158]
		Alloys	--	electric power	-	thermal conditions	++	25 - 10^4 x	Yes	Small	1,2,3	Large	[150]–[152]
	SMM	Polymers	-	heat source	-	thermal conditions	++	2 - 100 x	No	Small	1,2,3	Medium	[82]–[84]
		Alloys	-	current limitations	-	thermal conditions	++	8 - 10x	No	Small	1,2,3	Medium	[123]–[128]

As discussed in Section 2.1, even though several combinations of VSSs have been explored so far in soft robotics, new combinations are continuously explored by researchers, as the high number of new systems presented between the submission of this thesis and the publication of [44] demonstrates. As the data presented in Table 1 highlight, to date there is no system that can simultaneously encompass shape-shifting and shape-locking capabilities, independent control of body pose and stiffness level, a large workspace, a scalable design, high-speed stiffening and de-stiffening in a large stiffness range, inexpensive components and low-power consumptions. Certain technologies are more promising than others, but none of them address all of these factors. With the necessary background provided, the following chapters will explore the creation of a novel design paradigm for stiffness-controllable, shape-constrained, and inherently-safe soft robots.

Chapter 3

3 The Variable Stiffness Link (VSL): a Novel Active Structural Element

This chapter introduces the Variable Stiffness Link (VSL), the novel design paradigm at the foundation of the investigation presented in this thesis. The VSL is a pneumatically-actuated, stiffness-controllable structural element intended to replace rigid robotic links in traditional manipulators. The VSL presents many desirable characteristics including a large internal routing space, low weight-to-load ratio, a scalable and cost-effective design, stiffness controllability, and high stiffness using soft materials. The VSL can also act as inexpensive embedded distributed sensor for collision detection, a design feature which is particularly valuable in HRI. Traditionally, this feature has been addressed using variable stiffness actuators (VSAs) and variable stiffness joints (VSJs) to provide on-demand compliance adjustment of the overall system. However, the stiffness of the material composing these robots does not change, posing a risk for the human collaborator in case of failure of the collision detection measures that trigger the compliance adjustment, leading to potentially harmful collisions with rigid components. The VSL offers a practical solution to this problem, allowing for on-demand stiffness adjustment. A methodology is described for the fabrication of the VSL, and the stiffness of the system is evaluated experimentally. The design of an integrated anthropomorphic manipulator is presented and a collision detection algorithm is proposed and evaluated.

3.1 Introduction

When the implementation of industrial robotics first began, due to the large size and the powerful hydraulic actuation of early industrial robots as well as the lack of reliable control systems, robotic manufacturers and users decided to address safety requirements in the most radical way: humans and robots were not allowed to share the same workspace. Manipulators were usually confined to cages and separated from humans by fences. This solution was effective for the operation of robots where the intervention of humans was not required and provided a basis to start to address safety requirements in the context of industrial robotics. As reported in [159] in 1986 for the first time in USA the Robotic Industries Association (RIA) developed the R15.06 robot safety standard through the American National Standard Institute (ANSI). A few years later, Europe introduced the ISO 10218, subsequently adopted by the European Committee for Standardization as the EN 775 regulation. The fast evolution of servo-controlled electric motors in the 80's lead to a new generation of more capable robots taking over the scene in the beginning of the 90's. As a result, safety requirements changed, leading to the issuance of ANSI/RIA R15.06-1992 (USA) and ISO 10218:1992 (EN 775) (Europe), the former focused more on the integration of robots in industrial settings, the latter more on the duties of the robot manufacturer. Nevertheless, robots continued to be considered as high-risk machinery to be kept far from reach of a human operator during normal use. The 1992 regulations furtherly addressed the use of proper means of safe-guarding to guarantee the safety of the human operator. In the end of the 90's, in 1999 a task-based risk assessment methodology introduced the ANSI/RIA R15.06-1999, taking for the first time in consideration the uniqueness of each robot in relation to the assigned task, location and operation. In 2006 the ISO 10218-1 regulation was introduced to provide a comprehensive list of guidelines to develop industrial robots. Building on this regulation, in 2011 the ISO 10218-2:2011 was introduced to address safety requirements for the robotic system and its integration in industrial settings; at the same time

ISO 10218-1:2011 was published to update the 2006 version. The ISO 10218:2011 part 1 and 2 [160] have been published as harmonized standards in the European Union and these standards have been also implemented in the ANSI/RIA R15.06 in USA and in the CAN/CSA Z434 in Canada. In the past decade, robots started to be used also outside industrial settings, as a result dedicated regulations such as the ISO 13482:2014 "Robots and robotic devices - Safety requirements for personal care robots" [161] were produced to provide specific requirements and guidelines for inherently safe design, protective measures, and information for use of personal care robots. With the advancement of actuation, sensing and computing technologies, robotic industry started to move away from the caged-robot paradigm moving toward a close interaction between humans and robots. Also in this case, dedicated regulations were produced, like the ISO/TS 15066:2016 "Robots and robotic devices – Collaborative robots" [162] where the safety requirements for collaborative industrial robot systems and the work environment are specified (in addition to all the safety requirements already defined in ISO 10218:2011 part 1 and 2 for industrial robots). Requirements and guidelines have been also defined for software development in this context [163]. Extensive research has focused on the development of software and hardware that offers solutions for inherently-safe, close human-robot interactions [164], [165]. In these shared work environments, the safety of the human worker is of paramount importance and needs to be considered in the design of collaborative robots (cobots). A wide range of applications that are at present manually executed could benefit from a new generation of collaborative robots that allow safe and close interaction between the robot and the worker [166], [167]. Industrial robotic manipulators are typically heavy-payload machines, leading to a considerable robot body mass in comparison with the average body mass of a human being [168], [169]. Furthermore, they are usually capable of considerable accelerations and speeds (joints speeds up to 160°/s with angular accelerations up to $100°/s^2$ are possible [168], [169]). In case of accidental collisions with a human worker, industrial

robots can exert potentially harmful or life-threatening forces on the human body [170], [171]. The paradigm shift from the traditional heavy-duty robot operating separately from the human worker in a fenced area, to robots that work closely with humans we are witnessing nowadays represents one of the transitions envisioned by researchers worldwide in the so-called 4th industrial revolution [2]. This trend moves towards lightweight robots; examples include the Universal Robots UR3/UR5/UR10 [172], the lightweight robots from KUKA [168], FerRobotics [173], Franka [174], and the Sawyer and the Baxter Robots from Rethink Robotics Inc. [175]. These robotic manipulators claim to be safe due to integrated, stiffness-controllable actuators that can adapt their stiffness based on software tools that rely on sensory information. In some cases, e.g. for the Baxter and the Sawyer, the use of series-elastic actuators [176] in the joints is also exploited to provide additional hardware compliance.

In an attempt to make robots safer for interaction with humans, one of the first approaches explored was the development of variable stiffness actuators (VSA) [49], [177], given the rigid components of traditional manipulators. The electrical current and voltage responses of electro-mechanical actuators to mechanical load variations enable these systems to be used as intrinsic sensors within robotic manipulators [178], allowing for faster and safer motion control that maximizes motion speed while limiting risks of injury. A number of studies have confirmed that variable stiffness plays a key role in the creation of safe high-performance systems [177], [179]. Nowadays, the safe human-robot interaction problem is typically addressed using variable stiffness joints (VSJ) [180]–[182]. The primary goal of the control systems developed based on this joint class is to minimize the probability of injuries due to unexpected collision with humans by taking advantage of the natural flexibility of the joints, absorbing potential impacts on the rigid components of the robot.

Sensing-based safety approaches have also been investigated, such as the use of distributed sensors on the external surface of the robot body [183]. These range from robot skins that provide contact recognition capabilities such as a pneumatic network [184] or capacitive sensors [185], to vision-based systems developed to avoid and detect collisions [186]. However, despite their accuracy in detecting the location and measuring the intensity of collision, these solutions all require additional hardware, a fact which can increase the price of the manipulator or limit its motion.

Although much has been done to improve sensor and actuator performance for faster, safer and more accurate collision detection, limited effort has been made to improve the intrinsic level of safety of manipulator links. Passive solutions like the AirSkin® from Blue Danube Robotics [187], an add-on inflatable skin, have been developed and commercialized to provide a softer contact surface in case of accidental collisions. However, the materials used to construct links of these "lightweight" robots have rigid properties. Metallic alloys and rigid polymers are used to build the core structure. Any collisions between a manipulator made of these materials and a human worker could still result in serious trauma [188].

One of the questions this thesis seeks to answer, is whether the use of soft materials could help in finding more effective design solutions to this issue so as to guarantee a safer HRI. In the past decades, the introduction of soft robotics has redefined the limits of what a robot can accomplish. A number of soft manipulators have proven capable of achieving complex body poses [12]. As pointed out in the background chapter, many silicone-based robotic systems make use of fluidic actuation; in this method, a number of chambers that are independently actuated [60] or connected in a network [30] are directly embedded in the silicone body of the robot. The controlled expansion or contraction of the pressurised chambers leads to a deformation and therefore

movement of the overall structure [62]. The main limitation of this type of actuation is the maximum acceptable deformation of the robot body and fluidic (pneumatic or hydraulic) pressure that its silicone structure is able to withstand without bulging or blowing up. As a consequence of these mechanical limitations, the maximum force exertable by such robotic systems is typically limited [12]. A deformation of the same relative order of magnitude can be observed in the legs of the walking soft robot proposed in [62] once its pneumatic network is pressurised to perform a movement. As mentioned in Section 1.1, this phenomenon is widely known as ballooning. These volume variations are generally difficult to model and thus difficult to predict, creating a significant control problem.

The investigation presented in this thesis is inspired by the EU FP7 Project STIFF-FLOP (Grant n. 287728), where the use of silicone to develop bio-inspired soft robotic surgical tools [189], [190] was explored for the first time. The proposed modular manipulator in STIFF-FLOP was made out of silicone. Each module was comprised of three equally-spaced, pneumatically-actuated chambers in parallel with the longitudinal axis [191]. The STIFF-FLOP manipulator has embedded sensors such as force/torque (F/T) and bending sensors to estimate the robot's tip pose [190], [192]–[194]. To limit the lateral inflation of the modules, i.e., to solve the ballooning problem characteristic of silicone-based systems described previously, each chamber was individually fibre-reinforced [195], significantly improving the performance compared to externally-braided robots [60]. A similar approach has been investigated in [196], where the combination of different braiding angles was explored to achieve a desired bending behaviour for the robot. The use of braiding for soft robotic fingers has been explored by researchers in [48], [197]. A modular design for stiffness-controllable, passively-bent, thread-braided silicone links is presented in [119], [120].

To overcome the issue of large deformations associated with the pneumatic actuation of silicone-based robotic systems, the author of this thesis proposes and investigates a new type of stiffness-controllable, silicone-based system which uses pneumatic actuation and a combination of silicone, plastic meshes and fabric. The work presented in this thesis follows the overall idea of creating inherently-safe robots that can be used in different robotic applications, attempting to provide solutions for safe human-robot interaction. In this chapter, the author introduces the Variable Stiffness Link (VSL), an Active-Passive VSS for robotic manipulators and for industrial cobots in particular. Using VSLs in place of traditional rigid links, it is possible to effectively change and actively control the level of stiffness of robotic manipulators.

In section 3.2, the use of meshes in place of braiding in silicone-based system is investigated. The development of the VSL – Version 1 is presented, including its design, working principle and fabrication process. Multiple prototypes of this version which make use of different meshes have been tested in terms of stiffness.

In section 3.3, the VSL – Version 2 is presented. Here the mesh-silicone structure of the VSL – Version 1 is reinforced, making use of an external fabric sleeve to widen the pressure range of operation, i.e., the stiffness range. The overall system design and fabrication process are detailed in this section.

In section 3.4, an integrated, small-scale anthropomorphic manipulator embedding two instances of VSL – Version 2 is presented. In this proof-of-concept system, traditional rotational joints are combined with pneumatically-actuated VSLs. In one of the first attempts to merge soft and traditional robotic elements, thereby bridging the current gap between the two, the author proposes a new hybrid manipulator intended to increase safety in human-robot interaction while ensuring high stiffness when required. As a result,

not only can this manipulator be tuned from a completely soft to a rigid state according to the requirements of the task at hand, but collisions can also be detected without the need for additional sensors by using the VSL as an embedded distributed sensor. A range of experiments have been conducted to evaluate both the workspace of the two VSLs system and the collision detection algorithm developed, which are presented along with the relative results.

Section 3.5 summarizes the achievements of the work related to the VSL, its limitations and presents future works.

3.2 The VSL Version 1: from Threads to Plastic Meshes

The use of threads helicoidally embedded in the chamber walls of silicone-based robots has been extensively explored in soft robotics in an attempt to minimize the lateral inflation of these systems and enable the use of higher pressures, resulting in higher forces and therefore higher levels of stiffness. In the STIFF-FLOP manipulator [60] or in the soft bending actuator presented in [196], as in many others cases, researchers have used this improved design to reinforce the actuation chambers embedded in the silicone bodies of these systems. The braiding increases the radial stiffness of the cylindrical chambers, which becomes significantly higher than the axial stiffness thereof. Therefore, once pressurized, the chambers tend to elongate rather than inflate laterally. However, even if braided systems largely outperform non-braided soft robots in terms of maximum force and stiffness, this approach also presents a limitation. To understand this limitation, the sequence of section views of a braided chamber shown in Figure 3 can be referenced: at the beginning (a) when pressurized fluid is supplied, the lateral walls of the cylindrical chamber deform in the desired direction (longitudinally), generating the desired motion. The more the pressure increases, the wider apart the coils of the braiding are spaced (b). Increasing the pressure over a certain system-specific threshold leads to further spacing (c) of the coils, causing a secondary ballooning effect. As a result, even if this approach solves the issue of ballooning at low pressures for exclusively silicone-based systems, at high pressures the ballooning problem returns.
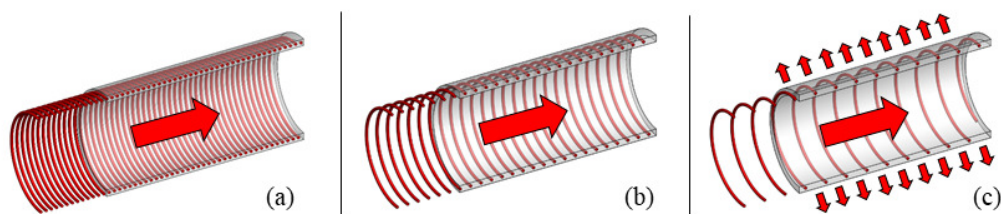
Figure 3 – Mechanism of the secondary ballooning in fluidic actuated silicone-based robots with braided chambers: the red arrows indicate the direction of deformation of the silicone walls when pressures is applied inside the chamber.

The same issue is present in systems with multiple threads and braiding angles [196], leading to ballooning in each cell created by the overlapping of two pairs of threads. In an attempt to overcome the limitations of traditional braided silicone-based actuators, the use of plastic meshes is investigated in this section. Plastic meshes, like braids, are composed of multiple threads and present a pattern with differently-shaped cells. However, in contrast to braids, no relative movements between the threads delimiting a cell is allowed, because at each point where two or more plastic threads meet, the threads are soldered together. The idea behind the proposed design is to prevent the spacing of threads, i.e., the secondary ballooning. It is important to note, in the context of the research presented in this chapter the author investigates a silicone-based VSS, i.e. a system that has been designed to act as a stiffness controllable structural element. Hence, the proposed system does not bend, elongate nor shrink as a standard silicone-based fluidic actuator. However, pre-shaped elastic meshes with non-deformable cells can be employed in the same manner to prevent ballooning in silicone-based and in general rubber-like-material-based fluidic actuators. In this section, the author describes the design, working principle, fabrication process and stiffness analysis of the VSL – Version 1, hereafter referred to as VSL-V1. This section begins by detailing VSL-V1's design and working principle (**Error! Reference source not found.**); next, the section investigates the silicone materials and meshes necessary to achieve adequate behaviour for the main states of these links, both soft and stiff, as well as outlining the fabrication process (3.3.2). In subsection 3.2.3, the experimental setup for stiffness evaluation is described and the results are presented. Subsection 3.2.6 summarises the achievements and limitations of the VSL-V1, linking to the next section and the VSL – Version 2. The results presented in this section are also published in A. Stilli, H.A. Wurdemann, and K. Althoefer. "A Novel Concept for Safe, Stiffness-Controllable Robot Links." Soft Robotics 4, no. 1 (2017): 16-22 [198], published in the Soft Robotics journal by Mary Ann Liebert Inc., a key point of reference for the soft robotics community worldwide.
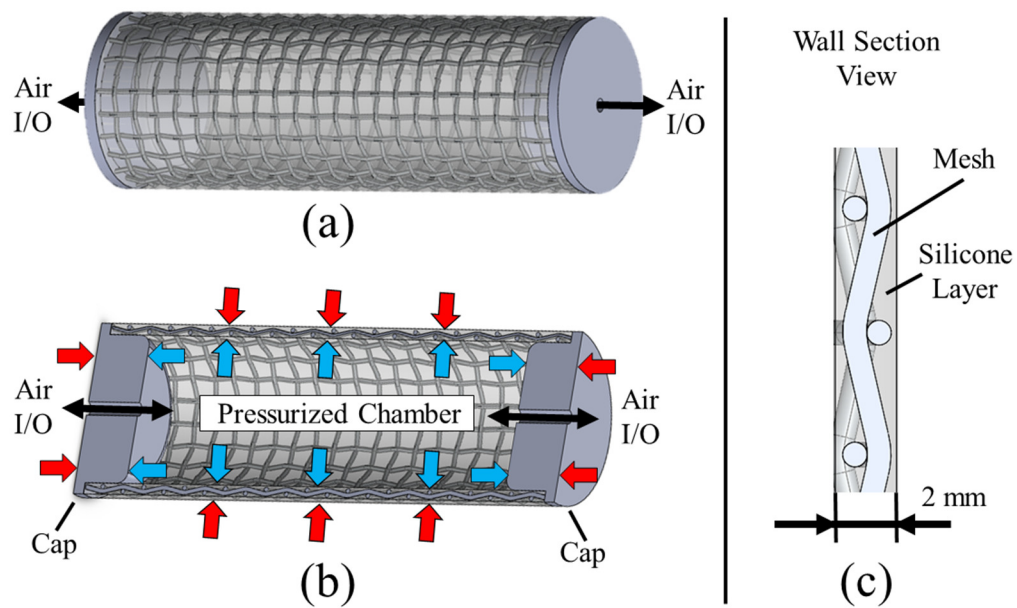
Figure 4 – CAD drawings of the VSL - V1 - Design and working principle: overview of the link assembly (a), longitudinal section view of the link (b) showing the I/O channel for pressurized air, with azure arrows showing the force distribution of the pressurized air inside the internal chamber and red arrows the force distribution of the reaction forces of the link. (c) shows a longitudinal magnified section of the wall link, showing the mesh embedded in a 2-mm silicone layer.

3.2.1 Design and Methodology

The design of the c is presented in Figure 4 (a). The VSL-V1 is composed of two main structural elements: a plastic mesh which is embedded inside a layer of silicone in the shape of a hollow cylinder, as shown in the wall section view in Figure 4 (c). When both ends of this cylindrical structure are closed with caps, the created airtight chamber can be pressurised using the channels in the caps, as shown in the section view in Figure 4 (b). The same pressure line can be used to control a chain of links, or several channels can be passed through a link to individually control the pressure of each link in a chain. The mesh not only prevents the ballooning of the system, but also gives the VSL its cylindrical shape and prevents it from collapsing when it is in a low-pressure state. To explore the influence of this type of link on stiffness, different silicone materials and plastic meshes were investigated at different pressure levels. Figure 4 (b) also shows the force distribution inside the link: the pressurized air (azure

arrows) pushes from the inside to expand the link; this action is counterbalanced by the reaction force (red arrows) of the mesh and silicone walls, keeping the cylindrical shape unaltered. The balance between these forces allows the stiffness of the VSL to be tuned. As opposed to other soft actuators, the VSL neither changes its shape nor twists or bends, but only varies its stiffness. The use of plastic meshes rather than threads, which creates non-deformable plastic cells, allows for higher pressures to be realised in the chamber. The VSL is designed to be:

- Stiffness-controllable and inherently safe

- Easy to manufacture and inexpensive

- Made of soft material, but capable of behaving like a traditional rigid link

- Hollow, to maximise the housing space inside the link body

- Lightweight, being hollow and pressurised with air.

3.2.2 Materials and Fabrication

To select a suitable mesh for the VSL, parameters such as the shape and aperture size of the cell patterns, as well as the thread material, were considered. Different meshes were tested (see Figure 5). Polypropylene (PP) among other common plastics, e.g. Polytetrafluoroethylene (PTFE), was chosen as it is durable and does not react chemically with silicone-based materials. In addition, the surface of this mesh type is smooth, which significantly reduce the risk of perforation of the silicone membrane. The low cost (less than 1 £/sqm) of these meshes allows the creation of inexpensive but robust and lightweight robotic links. Furthermore, any link diameter can easily be realised using the proposed fabrication process starting with a flat, square piece of mesh. A diamond-shaped aperture pattern is chosen for this application. This mesh aperture geometry has been chosen instead of other commercially available meshes with different patterns due to its isotropic mechanical behaviour along the axis of symmetry of the cell.
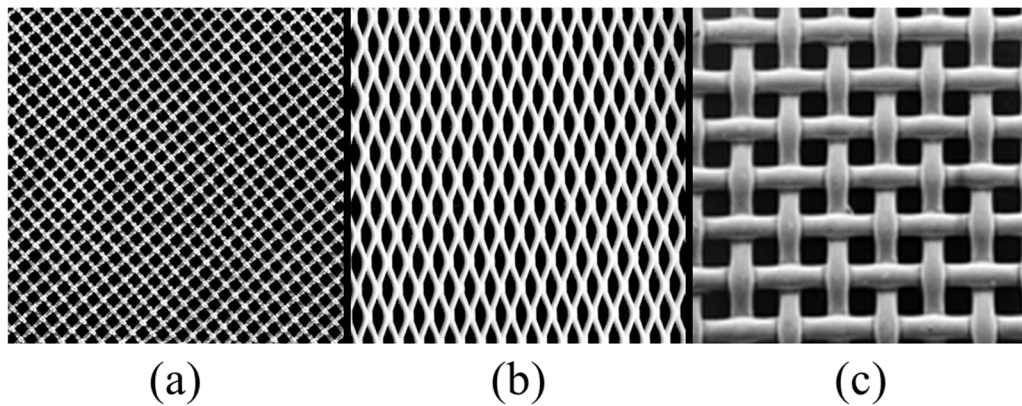
Figure 5 – Plastic meshes tested: (a) diamond-shaped polypropylene (PP) mesh, (b) eye-shaped Polytetrafluoroethylene (PTFE) mesh, (c) woven Polyester mesh.

These features match the system requirements in terms of non-deformability of the link along longitudinal and radial directions. Based on these considerations, four different PP meshes from Normesh Ltd. [199] with diamond patterns and different aperture sizes and thread diameters have been selected as follows (aperture size/thread diameter): sample (a) 105 μm/106 μm, sample (b) 150 μm/110 μm, sample (c) 250 μm/215 μm, sample (d) 420 μm/340 μm. In selecting an appropriate silicone material, different silicone types from Smooth-On Inc. [200], such as Dragon Skin® (described as high-performance silicone rubber by the supplier), Oomoo® and Ecoflex® (described as super-soft silicone rubber by the supplier), were evaluated concerning their stiffness, chemical stability and castability. In particular, Dragon Skin® 20A and 30A, Oomoo® 25 and 30, and Ecoflex® 0030 and 0050 silicones were preliminarily tested using small samples in the shape of small stripes 100 mm in length and 2 mm in thickness, which is the desired thickness of the VSL walls. A comparison between these silicone types obtained from the producer's website [200] is available in Appendix I. Based on this preliminary analysis, Dragon Skin® was selected as the most suitable for this application, exhibiting a high level of elasticity and shape retention and low long-term shrinkage, less than 0.001 mm/mm. Aiming to achieve a good trade-off between softness of the material, needed to ensure a safe HRI, and the mechanical rigidity of the cylindrical structure, needed to

guarantee the robustness of the system, Dragon Skin® 20A was selected from among the Dragon Skin® family. The 20A in the name refers to the Shore hardness of the material. The Shore scale, developed by Alfred Ferdinand Shore in the 1920's [201], is a stiffness scale typically used for rubber and plastic materials. A rubber marked as 20 on the Shore scale A is considered a soft rubber, in the same range as a rubber band.

The fabrication process for the VSL-V1 is as follows: rectangular sheets of the selected PP meshes of dimensions of 15 cm × 8.5 cm were hand-sewn into the shape of cylinders with a length of 15 cm and a diameter of 2.5 cm to create the link prototypes. Nylon threads were used to sew the longitudinal mesh sides together (with an overlap of 7 mm) to form the cylindrical structures, as shown in Figure 6. The meshes were cut and sewn in such a way that the main diagonal of the diamond apertures was aligned with the longitudinal axis of the link. A mould consisting of three components was created to allow each cylindrical mesh to be enclosed within the silicone material (Dragon Skin® 20 A). The mould parts I, II and III (see Figure 6 [b]) were created by a Stratasys Dimension SST 768 rapid prototyping machine.
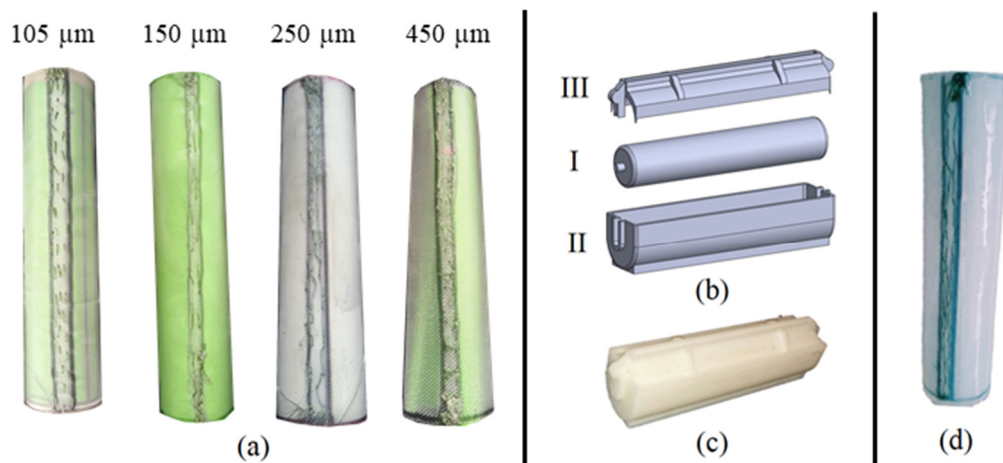
Figure 6 – Fabrication stages of the VSL-V1: mesh sewn in the shape of a cylinder (a), mould components (I, II and III (b)) and mould assembled (c). Figure (d) shows the link after demoulding and removing of the silicone excess.

The moulding process proceeded as follows: the sewn PP mesh was slipped over the cylindrical mould component I. Then, the mixture (1:1 ratio) of the two components of Dragon Skin® 20A silicone was prepared and degassed in a vacuum chamber at a vacuum pressure of – 0.85 kPa. Part of the silicone mixture was then poured into the base part of the mould (II), filling the mould to half of its capacity. Part I of the mould with the mesh was then inserted from the top into part II. More silicone was added after inserting part I into part II, to ensure that enough material was present to form a complete and continuous link wall. Part III was then inserted into part II as demonstrated in Figure 6 (b); excess silicone escaped from the long aperture located at the top of part III. The silicone was then allowed to cure at room temperature for 8 hours. Figure 6 (c) presents the mould in its assembled state, while Figure 6 (d) displays the link after the moulds and any excess silicone have been removed. The whole procedure was repeated to create four samples employing the four different meshes. The mould was specifically designed to generate silicone-mesh walls of the same thickness for all four samples, i.e., 2 mm, regardless of the thickness of the mesh used.

3.2.3 Test Rig for Stiffness Analysis

The mechanical properties of the systems presented in this thesis are strongly influenced by the pressure level applied. Different approaches have been investigated in the past to assess the mechanical behaviour of inflated structures: in [202] the bending behaviour of inflated fabric tubes is thoroughly investigated and the case of cantilever beam loaded at the tip is analysed proposing a robust model for this scenario. Timoshenko's beam theory is preferred to Bernoulli beam theory to describe the kinematics of these systems. Here, a purely fabric-based system is considered and even in this simpler case a number of assumptions are needed to simplify an otherwise complex non-linear problem. Similarly in the work presented in [203] the behaviour of inflated beams composed of thin films is investigated. To the best knowledge of the author, none of the proposed models in the literature is considering the case of a multi-

material system as the one described in this work. Given the use of multiple materials in all of the systems presented in this thesis and in light of the fact that the main aim of this thesis work is not the development of an accurate mechanical model for the proposed system, the author decided to investigate the stiffness behaviour using a "black-box" approach rather than a classical mechanical characterization based on the Young's modulus of the materials used. A test rig was prepared to evaluate the bending and axial stiffness of the prototypes according to different levels of applied pressure in the internal chamber. This investigation strove to determine which mesh property had the most significant effect on the mechanical behaviour of the system, the aperture size or the diameter of the thread used.
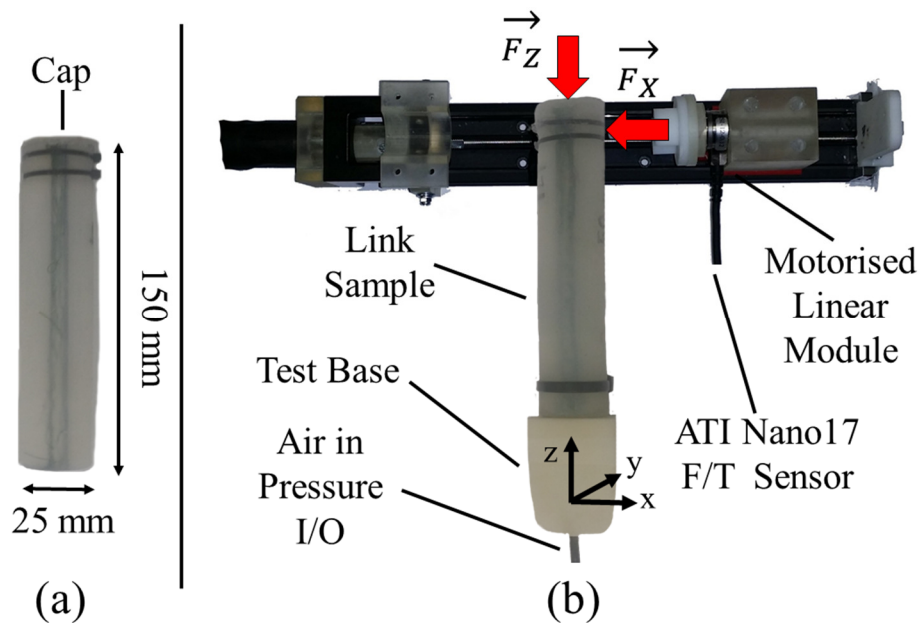
Figure 7 – VSL-V1 sample with 3D printed cap embedded for stiffness test (a) and setup for the bending and axial stiffness tests at the tip (b): direction of the lateral force F_x and of the longitudinal force F_z applied during the tests are marked.

In order to pressurise and test the samples, one of the two circular openings in the base of the cylinder was sealed using a customized 3D-printed cap. The cap was inserted and secured in place with cable ties and silicone glue to guarantee

that the internal chamber was air-tight. Figure 7 (a) illustrates one of the samples ready for testing. After closing the tip with the cap, the open end of the sample was attached to a customised 3D-printed test base. A pressure line was embedded in the base and connected to a pressure regulator (SMC Pneumatics [204], SMC ITV0010-3BS-Q, see Appendix II for the data sheet). This configuration allowed for control of the pressure level inside the link. Figure 7 (b) displays the experimental setup of the system for a lateral tip stiffness test. Cable ties and silicone glue were used on the base side as well to ensure that the only air inlet or outlet was via the pressure line. The pressure regulator was controlled by LabVIEW software. The level of stiffness of the samples was evaluated at the tip, where the displacement generated by an external applied force is maximal. Tests were performed pushing an ATI Nano17 Force/Torque sensor (resolution: 0.0031185147 N, normal force range: ± 17 N) connected to a linear module towards the tip as shown in Figure 7 (b), laterally along the x-axis and longitudinally at the front of the tip along the z-axis. To measure F_x, a linear slide was rotated counter-clockwise by 90° in comparison with the pose shown in Figure 7 (b), so that the linear module with the mounted F/T sensor exerted force along the z-axis. Both test scenarios were performed applying four different pressure levels: 15 kPa, 30 kPa, 45 kPa and 60 kPa. Each experiment started with the ATI Nano17 Force/Torque sensor 0.5 mm away from the silicone surface of the sample. The bending stiffness tests consisted of load and unload cycles applying the force at 13.5 cm from the base, achieving a deflection of 15 mm. For the axial stiffness tests, a smaller displacement of 5 mm was achieved, sufficient to show buckling phenomena, which took place for all the samples in the displacement range 3.5 mm – 4.5 mm. Each loading and unloading cycle was performed five times to compute the variance of the measurements. It is important to note that no significant radius or length variations occurred after pressurising and depressurising the samples, even after tens of cycles, further proving the effectiveness of this design in limiting undesirable deformations of the silicone-based system.

3.2.4 Stiffness Analysis – Bending Stiffness at the Tip

For each of the four VSL-V1 samples, the lateral tip test was performed applying four different pressure levels. Each loading and unloading cycle was repeated five times. The results of these tests are illustrated in Figure 8, with the lateral force F_x plotted against the deflection displacement d_x. Here the average values of the five force reading cycles are plotted with the corresponding error bars for each pressure level P in separate graphs, with numeric values of the standard deviations listed in the caption.
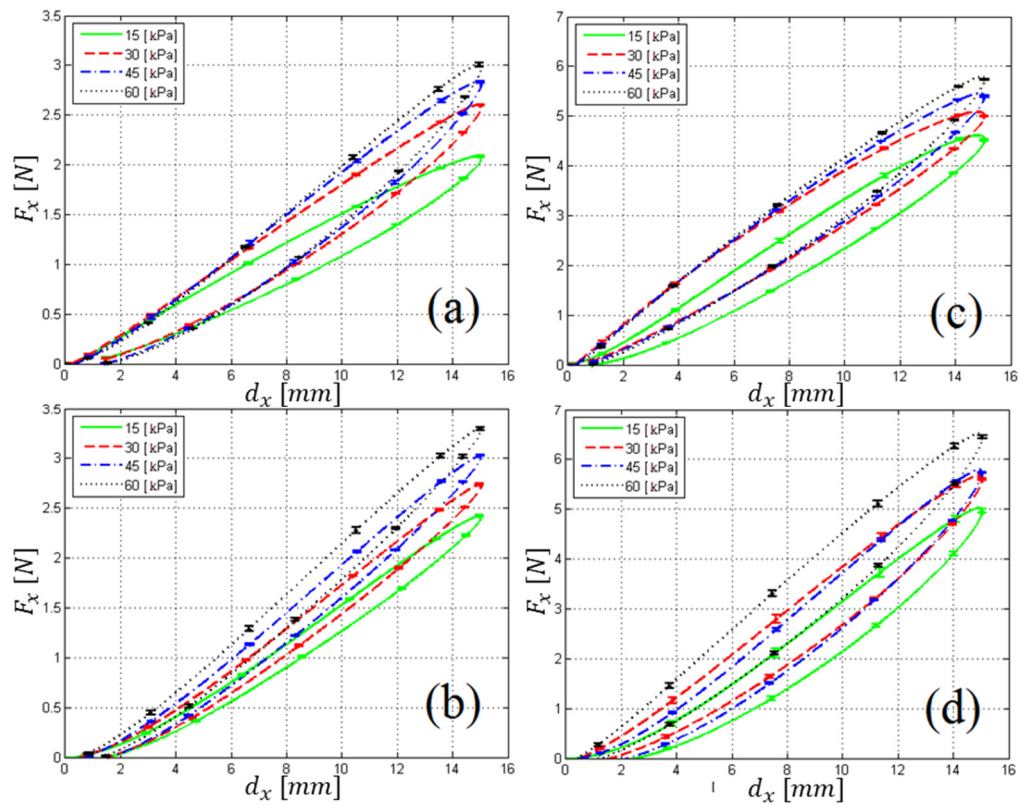
Figure 8 – Force F_x [N] at the link tip against displacement along x-axis d_x [mm] for samples (a), (b), (c) and (d) at 15 kPa, 30 kPa, 45 kPa and 60 kPa. Standard deviation values ordered by increasing pressure level: (a) 0.007, 0.006, 0.0144, 0.009; (b) 0.009, 0.008, 0.008, 0.018; (c) 0.018, 0.016, 0.013, 0.016; (d) 0.041, 0.039, 0.017, 0.036.

As shown in Figure 8 (a), the load-unload curves have an overall linear trend and some hysteresis. The measurements show small standard deviation values, hence, tight error bars. The maximum force at 15 kPa is 2.09 N. Increasing the

pressure to 30 kPa, 45 kPa and 60 kPa, the force increases to 2.61 N, 2.85 N and 3.01 N, respectively. As expected, applying a larger pressure leads to an increase in stiffness of the inflated link and, therefore, an increase of the reaction force offered by the VSL. Comparing the four graph sets of Figure 8 displaying the readings obtained from experiments with different mesh-silicone combinations, it can be inferred that the larger the thread diameter and the aperture sizes, the stiffer the inflated link. For instance, the mesh used in Figure 8 (a) at 60 kPa exerts a lateral force of 3.01 N, whereas the one used in Figure 8 (d) with the same pressure can exert more than double the amount of force at 6.55 N with the same displacement. The bending stiffness of a beam is defined as its resistance against a bending deformation [205]. The bending stiffness can be calculated starting from the general definition of the stiffness of a system, typically indicated as k, i.e. the resistance of offered to a deformation. This is calculated as the ratio between the module of the force F causing the deformation, and the system deflection d along the force direction, as seen in the following general expression:

$$k = \frac{F\ [N]}{d\ [mm]} \tag{1}$$

Hence, the bending stiffness S_x can be derived considering the force F_x applied laterally at the tip of the link and the displacement d_x of the system in the point of application of the force F_x. Based on the data collected regarding displacement of the tip, the bending stiffness S_x at the tip of the VSL-V1 can be calculated in function of the pressure. Hence, the bending stiffness S_x of each sample for each pressure level P is calculated averaging the ratio between the measured force $F_x\ [N]$ and the measured displacement $d_x\ [mm]$ values over the load-unload cycle in the range 10 mm – 15 mm, to neglect any nonlinearity in the right neighbourhood of the origin, as per the following formula (2):

$$S_x(P) = \langle \frac{F_x(j)}{d_x(j)} \rangle \, for \, j = [1,2,\dots,n], for \, d_x(j) \in [10,15] \qquad (2)$$

These data are then averaged again over the five cycles to add statistical significance to the presented results. The stiffness data are presented in the graph of Figure 9. As shown by the collected data, there is a clear linear dependence between pressure and stiffness for all the samples and, as expected, the pressure level defines the bending stiffness of the system. It is worth noting that the lines related to the linear approximations of stiffness data for the four samples have almost the same angular coefficient with different offsets from the horizontal axis, suggesting that the type of mesh used defines the intrinsic stiffness of the sample when the pressure is zero and the relative stiffness increment provided by the pressurized air similarly affects all the samples.
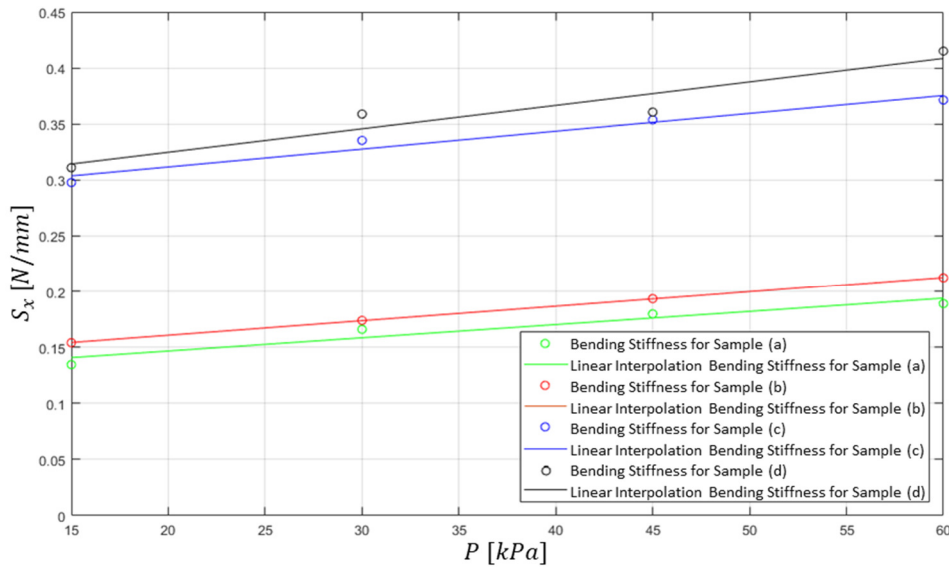
Figure 9 – Bending stiffness S_x [N/mm] against pressure P [kPa]) for sample (a) in green, sample (b) in red, sample (c) in blue and sample (d) in black. The circles are values calculated as average on the load/unload cycles and the continuous lines the linear interpolation of the samples.

To get a better understanding of how the stiffness values here presented compare with those of other materials we can compare the proposed cantilever system

with a rigid elastic cantilever beam of the same geometrical parameters composed of a material of known Young's Modulus E. Hence, we consider a beam of the following dimensions: external diameter D= $25\ mm$, length $L = 150\ mm$ and circular section. As well known from classic mechanics, the bending stiffness of a cantilever beam laterally loaded at the tip can be expressed as:

$$S_x = \frac{F}{d_x} = \frac{3EI}{L^3} = \frac{[N]}{[mm]} \tag{3}$$

Where E is the Young's modulus of the material composing the beam, I is the moment of inertia calculated along the axis of symmetry of the beam on the section and L is the beam length. For a circular section, in the case of a solid beam of homogeneous material, the moment of inertia can be calculated as follows:

$$I_{Solid\ Beam} = \frac{\pi D^4}{64} = [mm^4] \tag{4}$$

Hence, the bending stiffness $S_{x\ Solid\ Beam}$ of a cylindrical cantilever beam laterally loaded at the tip of a generic material of Young's modulus E, with $D = 25\ mm, L = 150\ mm$ can be expressed as follows:

$$S_{x\ Solid\ Beam} = \frac{3E\pi D^4}{64L^3} = 0.0170442309 * E = \frac{[N]}{[mm]} \tag{5}$$

It is useful also to compare our system with a hollow beam with the same wall thickness of our system, i.e. $2\ mm$. In this case, the moment of inertia should be calculated as follows:

$$I_{Hollow\ Beam} = \frac{\pi(D^4 - d^4)}{64} = [mm^4] \qquad (6)$$

For the proposed system the internal diameter $d = 21\ mm$. Hence, the bending stiffness $S_{x\_Hollow\_Beam}$ of a cylindrical hollow cantilever beam laterally loaded at the tip of a generic material of Young's modulus E, with external diameter $D = 25\ mm$, internal diameter $d = 21\ mm$ and length $L = 150\ mm$ can be expressed as follows:

$$S_{x\ Hollow\ Beam} = \frac{3E\pi(D^4 - d^4)}{64L^3} = 0.0085583965 * E = \frac{[N]}{[mm]} \qquad (7)$$

We can consider now some common materials to better understand how the stiffness of the proposed VSS compare with traditional rigid elastic beams. The results of this evaluation are shown in the table here under and the Young's Modulus have been retrieved from [206]:

Table 2 - Bending Stiffness of a solid cylindrical beam (Solid case: external diameter $D = 25\ mm$, length $L = 150\ mm$. Hollow case: external diameter $D = 25\ mm$, internal diameter $d = 21\ mm$ and length $L = 150\ mm$) laterally loaded at the tip: examples of some common materials.

Material	$E\ [N/mm^2]$	$S_{x\ Solid\ Beam}\ [N/mm]$	$S_{x\ Hollow\ Beam}\ [N/mm]$
Rubber	10	0.170442309	0.085583965
Polyethylene	110	1.874865399	0.941423615
Polypropylene	1500	25.56634635	12.83759475
Nylon	2000	34.0884618	17.116793

Comparing the bending stiffness data of the VSL-V1 (see Figure 9) with the data in Table 2 , the VSL-V1 exhibits a behaviour comparable to a solid rubber beam or to a hollow plastic beam.
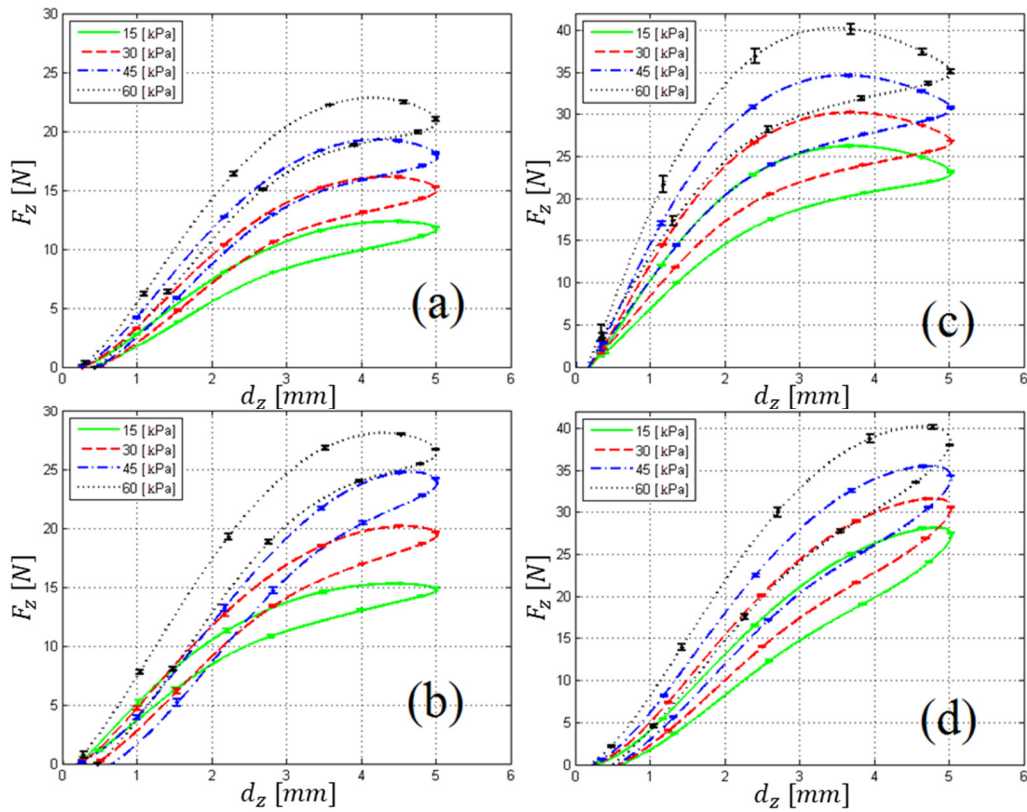
Figure 10 – Force F_z [N] at the link tip against displacement along z-axis d_z [mm] for samples (a), (b), (c) and (d) at 15kPa, 30kPa, 45kPa and 60kPa. Standard deviation values ordered by increasing pressure level: (a) 0.051, 0.080, 0.089, 0.153; (b) 0.150, 0.136, 0.178, 0.179; (c) 0.133, 0.123, 0.206, 0.536; (d) 0.095, 0.100, 0.121, 0.255.

3.2.5 Stiffness Analysis – Axial Stiffness

For each of the four VSL-V1 samples, the axial stiffness test was performed at the tip, applying the same four pressure levels considered for the evaluation of the bending stiffness. Each loading and unloading cycle was repeated five times. The results of these tests are shown in Figure 10, with the axial force F_z plotted against the deflection displacement d_z. Here the average values of the five force-reading cycles are plotted with the corresponding error bars for each pressure level P in separate graphs, with numeric values of the standard deviations listed in the caption. Comparing the graphs in Figure 9 and Figure 10, the forces measured at a displacement of 5 mm for the longitudinal tip stiffness tests consistently exceeded the corresponding measurements of the bending

stiffness tests. For instance, sample (a) at 15 kPa produced a maximum reaction force of 2.09 N, if stressed laterally, with a displacement of 15 mm. However, the same link sample leads to a peak reaction force of 11.90 N and an associated displacement of only 4.2 mm when the force is applied longitudinally (see Figure 10 [a]). Consequently, the sample behaves similarly to a cantilever beam with a circular section. The mechanical properties of this soft robotic link structure make the modelling significantly simpler when compared to the typical silicone-based robot manipulators. Significantly, the peak force values during a load-unload cycle are reached for the axial tests before the displacement of 5 mm is reached. This outcome can also be explained considering the boundary conditions of the system (cantilever beam) and the buckling generated by the applied compression axial force at the tip after a deformation of 3.5 mm – 4.5 mm; the beginning of the buckling corresponds to the trend inversion in the exerted force. Also in this case, the obtained force readings for the four samples display a continuous increase as pressure increases, as indicated in Figure 10.
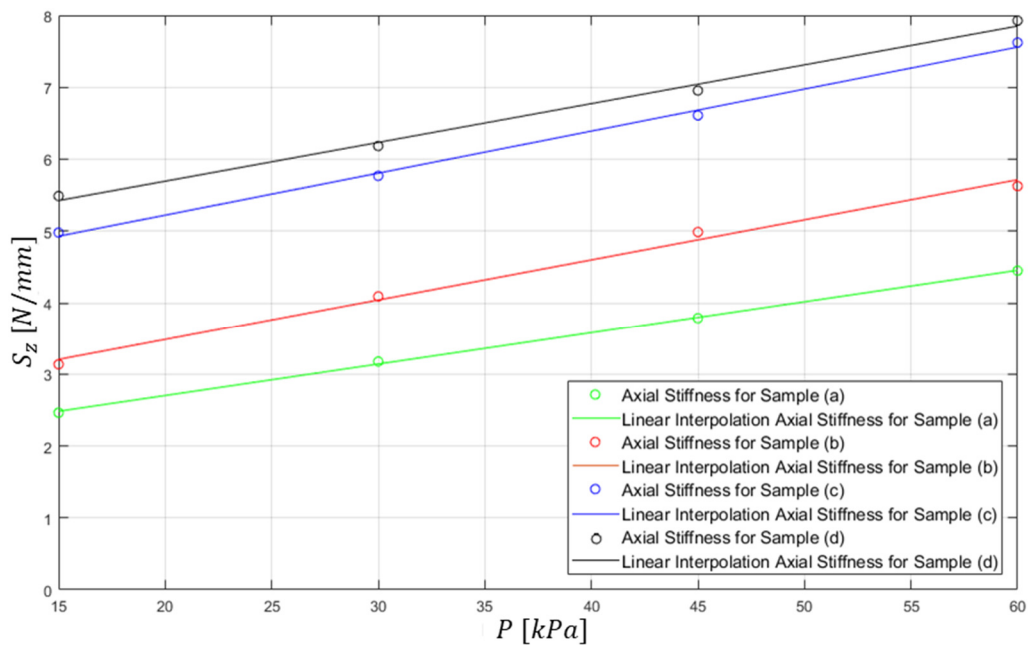
Figure 11 – Axial stiffness S_z [N/mm] against pressure P [kPa]) for sample (a) in green, sample (b) in red, sample (c) in blue and sample (d) in black. The circles are values calculated as average on the load/unload cycles and the continuous lines the linear interpolation of the samples.

The samples using meshes with larger threads and aperture sizes exhibit a stiffer behaviour. Based on the data collected in terms of displacement of the tip the axial stiffness S_z at the tip is calculated as a function of pressure. The axial stiffness S_z of each sample, as the bending stiffness, is calculated by averaging the ratio between the measured force F_z $[N]$ and the measured displacement d_z $[mm]$ values over the load-unload cycle in the range 3 mm – 5 mm, to neglect any nonlinearity in the right neighbourhood of the origin, as seen in the formula below (8).

$$S_z(P) \ = \langle\frac{F_z(j)}{d_z(j)}\rangle \, for \, j = [1,2, \dots, n], for \, d_z(j) \ \in [3,5] \qquad (8)$$

In this case, the data are then averaged over the five cycles to add statistical significance to the presented results. The stiffness data are presented in the graph in Figure 11. As indicated by the collected data, in the axial case there is also a linear dependence between the pressure and the stiffness for all the samples.

3.2.6 Discussion

A comparison between the collected data's peak forces for the four samples is presented in Table 3. As displayed in this table, the peak force, hence, the stiffness, increases with the thread diameter and with the opening of the cells of the mesh. Observing these data and the stiffness data presented in Figure 9 and Figure 11, it is clear that the mesh plays a critical role in the stiffness of the link, especially at low pressures, enabling the use of the VSL as a structural element. The VSL-V1, in terms of applicable pressure, outperformed several purely silicone-based ([5] 25 kPa, [61] 28 kPa, [62] 48 kPa) and silicone-based, thread-braided systems ([56] 55 kPa), exhibiting similar performance when compared with fibre- or inextensible-layer-reinforced soft-bending actuators such as those presented in [207].

Table 3 – Comparison of peak force values at different pressure levels for the four samples analysed in the bending and axial stiffness test. Colour gradients show force trends in relation to pressure levels and meshes geometrical characteristics.

Stiffness Test		Sample	Peak Forces [N]			
			15 kPa	30 kPa	45 kPa	60 kPa
Bending	Thread Diameter → Aperture Size	(a)	2.09	2.61	2.85	3.01
		(b)	2.42	2.73	3.03	3.30
		(c)	4.55	5.00	5.40	5.83
		(d)	5.04	5.71	5.81	6.55
Axial	Thread Diameter → Aperture Size	(a)	11.90	15.10	17.90	20.90
		(b)	14.90	19.50	23.70	26.50
		(c)	23.50	27.20	31.50	35.80
		(d)	27.80	31.10	34.70	39.10

The VSL-V1 has pressure and stiffness performance comparable with externally-braided systems such as the modular system presented in [60]; however, it has a considerably lower weight and inertia thanks to its allowed design, being easier and cheaper to fabricate and providing an ample lumen for cable routing. Furthermore, the use of plastic meshes rather than threads allows for higher stiffness at low or zero pressure. Nonetheless, the maximum applicable pressure with this design is still limited. The author successfully applied up to 100 kPa to all the samples without any visible deformation occurring. However, once this threshold is exceeded, the mesh can no longer hold the shape of the link and radial deformations take place. Increasing the pressure further led to laceration of the mesh in the first instance and subsequently of the silicone. Using a working pressure under this threshold allows for stiffness levels sufficient for low-payload applications that use short links. Nonetheless, the combination of meshes and silicone allows for the creation of new structural elements that are otherwise unachievable. Building on this design, the author further investigated ways to improve this system to overcome the pressure limitations. The results of this investigation are detailed in the next section, where the VSL Version 2 (VSL-V2) is presented.

3.3 The VSL Version 2: from Meshes to Fabric

In order to improve the working pressure range of the VSL, the use of fabric as external constrain has been explored. As suggested by the work of Galloway et al. presented in [13], the combination of braiding and fabric sleeves in silicone-based bending actuators allows for higher pressures to be used (up to 400 kPa for the presented system). The same idea can be applied to the proposed mesh-reinforced structural element presented in this thesis to widen its working pressure range. This section reports on the development of the Version 2 of the VSL (VSL-V2) and the analysis of its mechanical behaviour. The design of the VSL-V2 builds on the design of the VSL-V1, proposing a number of design and fabrication improvements. The stiffness of this new system is extensively analysed and a model is proposed. The application of the VSL-V2 in a real robotic manipulator is explored in the subsequent section. Some of the results presented in this and the following section are also published and have been presented in: A. Stilli, L. Grattarola, H. Feldmann, H.A. Wurdemann, and K. Althoefer. "Variable Stiffness Link (VSL): Toward Inherently Safe Robotic Manipulators." in Robotics and Automation, 2017 IEEE International Conference on (ICRA), pp. 4971-4976. IEEE, 2017 [208].

3.3.1 Design and Methodology

The working principle and design of the VSL-V2 are illustrated in Figure 12. The VSL-V2, in respect to the VSL-V1, presents a double layer of silicone (see the detail of the section of the wall in Figure 12 [b]) rather than a single one, ensuring that the plastic mesh is firmly bonded to the silicone layer. Furthermore, the outer fabric layer, being flexible, yet inextensible, significantly reinforces the link structure, preventing lateral inflation and structural damage even at high pressures. Therefore, higher pressures lead to greater forces and thus greater stiffness of the link. At low pressure, the plastic mesh adds structural strength and prevents the link from collapsing. As per the VSL-V1, the application of a positive pressure to the chamber (as indicated by the double white arrow in

Figure 12 [a]) results in the VSL-V2 varying its stiffness as illustrated by the light blue arrows indicating the direction of the air pressure force on the lateral walls of the cylinder and the red arrows showing the reaction forces of the walls of the cylinder. The VSL-V2 also presents an ample lumen to house cables and tendons, allowing routing of these elements inside the manipulator body to power motors and tools on the end effector. The design proposed here maximises the space for cable housing inside the link body, providing a large percentage of the link's external volume. The internal volume V_i of the link can be expressed as function of the external one, V_e, as follows (refer to Figure 12 for d_e, d_i and d_w):

$$V_i = V_e * \frac{d_i^2}{d_e^2} = V_e * \frac{(d_e - d_w)^2}{d_e^2} \tag{9}$$

For $d_e \gg d_w$, the ratio d_i^2/d_e^2 tends to 1; hence, the internal volume of the link tends toward 100% of the external. In the VSL-V2 samples presented here, $d_e = 30\ mm$, $d_i = 25\ mm$; therefore, a 69.4% of the external volume is available.
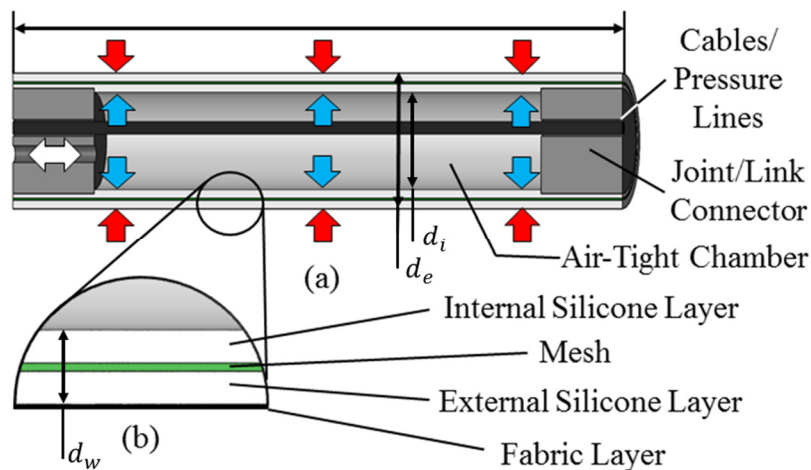
Figure 12 – VSL V2 working principle and design: (a) CAD drawings showing a longitudinal section view of the VSL illustrating the I/O channel for pressurized air (double headed white arrow), the force distribution of the pressurized air inside the internal chamber (azure arrows) and the force distribution of the reaction forces of the link walls (red arrows); (b) subfigure shows a magnified longitudinal section, highlighting the layers composing the wall link.

However, it is important to note that the wall thickness d_w only defines the stiffness at low pressures; consequently, d_w can be the same for small or large d_e, making this percentage significantly higher for larger links.

3.3.2   Materials and Fabrication

Based on previous investigations regarding the material choice of the VSL-V1, the following components were selected for the VSL-V2: Dragon Skin® 20A silicone by Smooth-On Inc. (US), and a polypropylene (PP) plastic mesh (400 µm thickness, OBI-Italia) (Figure 13 [a], I) with a diamond-shaped texture.
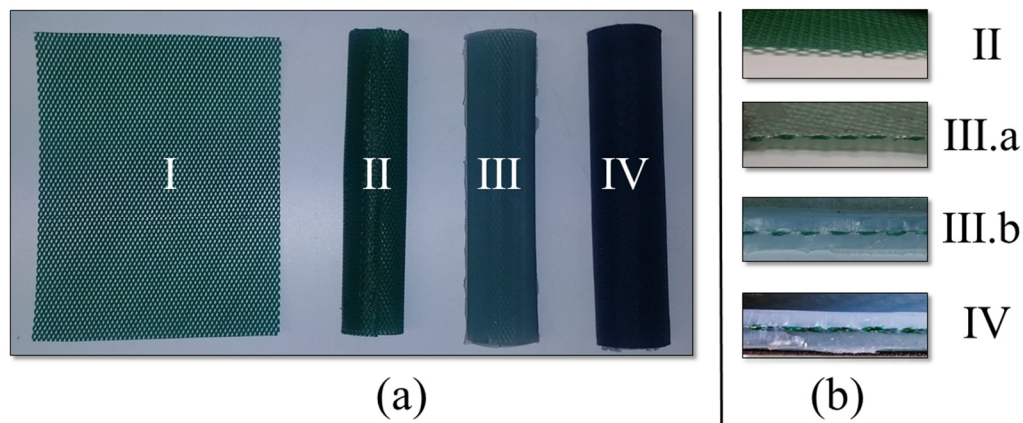
Figure 13 – Fabrication stage of the VSL-V2: subfigure (a) shows how the VSL V2 looks from the outside and subfigure (b) shows how the wall section looks like during the assembly process. I is the mesh before being formed in the shape of a cylinder, II is the mesh soldered and closed in the shape of cylinder, III is the link after the casting of the external silicone layer (III.a) and after casting of the internal layer (III.b) and IV is the finished VSL-V2.

The multiple stages of the fabrication process are demonstrated in Figure 13. Initially, a rectangular sheet of mesh (Figure 13 [a], I) was cut from a larger layer. The longer side was 140 mm in length, which was equivalent to the length of the link. The height of the sheet was 80 mm that was approximately 10 mm longer than the circumference of the cylindrical links. The additional 10 mm of material was needed in order to provide a 5-mm overlap between the two long sides when the mesh was closed in the shape of a cylinder. This overlap allowed for the creation of the soldering needed to form the rectangular mesh into a

cylindrical shape. To create a more robust bond between the two edges of the mesh, low-temperature sealing is used in place of hand-sewing. The overlap is kept to a minimum in order to minimise the thickness increase after sealing, keeping the mesh as isomorphic as possible. By using a commercially-available heat sealer, a 2-mm width sealing line was produced on the rolled-up rectangular mesh, forming the mesh into the shape of a cylinder (see Figure 13 (a), II). In the second stage of the fabrication process, the plastic mesh was embedded into a layer of silicone. A two-phase moulding process was applied to cast the silicone on the mesh into a cylindrical shape.
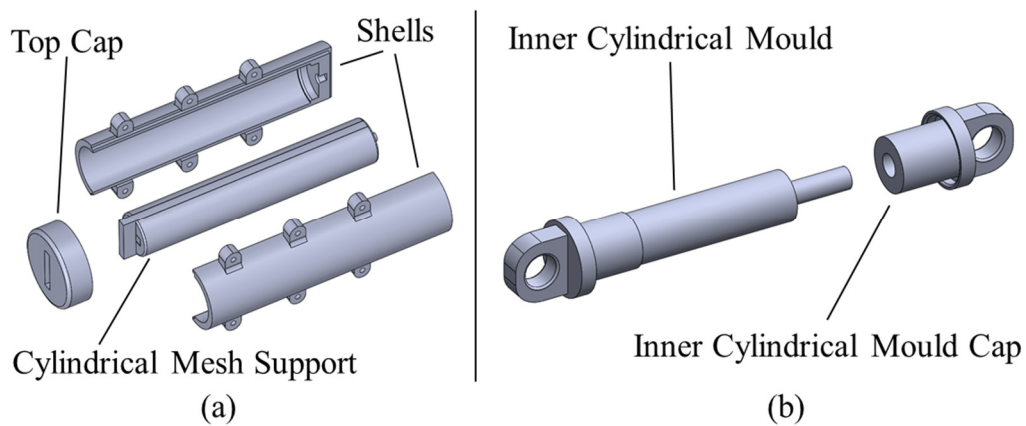
Figure 14 – CAD drawings of the moulds to form the external (a) and the external (b) silicone layers of the lateral walls of the VSL-V2.

Figure 14 (a) shows the components of the first mould used to create the external silicone layer. The cylindrical mesh (Figure 13 (a), II) was slipped over the cylindrical mesh support. The two shells of the mould were then assembled, forming a hollow cylinder. Dragon Skin® 20A silicone was mixed, degassed and poured in the outer cylindrical mould. The rolled mesh and its support were inserted into the assembled shells, which were filled with silicone that filled the interstice between the internal and external walls. The entire moulding system was composed of several parts in order to ensure a smooth de-moulding process. Figure 13 (b), III.a illustrates a section view of the wall of the resulting mesh in a cylindrical shape and with an outer layer of silicone. Next, an internal layer of

silicone was added, utilizing the mould illustrated in Figure 14 (b). Silicone was poured into the partially-formed link and the inner mould components were inserted from the two sides. This process finally resulted in the mesh being embedded between two layers of silicone (see the wall section view in Figure 13 [b], III.b): the internal layer had a thickness of 1 mm, whereas the external thickness was about 1.5 mm. A rectangular sheet of finely-woven nylon fabric was cut and machine-sewn into the shape of a cylinder and slipped on the outside of the cast link, as indicated in Figure 13 (a), IV.

3.3.3 Stiffness Analysis – Bending Stiffness

A test rig analogue to the one presented in Figure 7 for the VSL-V1 was prepared to evaluate the bending stiffness of the VSL-V2 prototype according to different levels of pressure applied. A wider pressure range was explored because the new design of the VSL-V2 was aimed at increasing the working pressure range. With this investigation, the author sought to evaluate the effects of the fabric layer addition on the overall stiffness system. Furthermore, in order to better understand the mechanical behaviour of the proposed soft system and its similarities and differences from a rigid cantilever beam, a more extensive stiffness analysis was conducted, collecting data for the bending stiffness at multiple points that are different distances from the base.

The bending stiffness tests were performed by applying six different pressure levels, 0 kPa (no pressure applied), 30 kPa, 60 kPa, 100 kPa, 150 kPa and 200 kPa. The no-pressure case was considered to provide data about the intrinsic stiffness of the system, which was not considered during the previous analysis on the VSL-V1. Each loading and unloading cycle was repeated five times. A significantly smaller displacement (2 mm rather than 15 mm) was considered in this case, given the considerably higher stiffness exhibited by this system and the maximum force safely measurable by the ATI Nano17 Force/Torque sensor used.
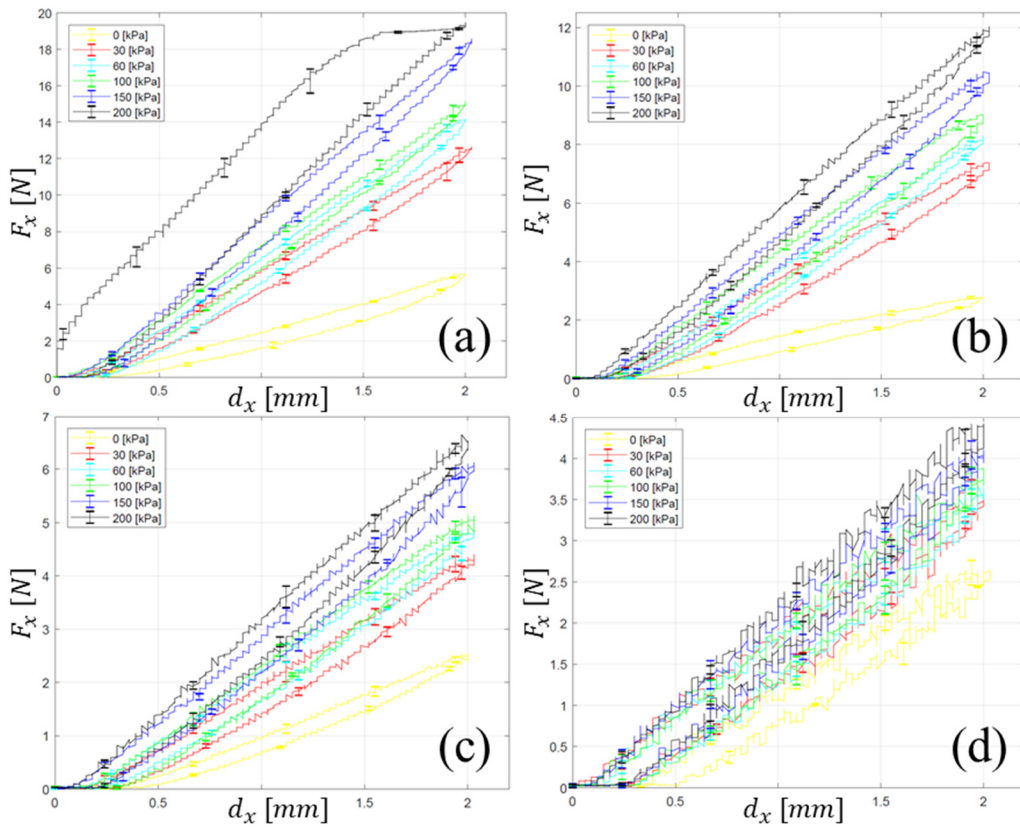
Figure 15 – Force F_x [N] at the link tip against displacement along x-axis d_x [mm] for the VSL V2 sample at 4.187 cm (a), 7 cm (b), 9.812 cm (c) and 12.625 cm (d) from the base at 0 kPa, 30 kPa, 60 kPa, 100 kPa, 150 kPa and 200 kPa. Standard deviation values ordered by increasing pressure level: (a) 0.046, 0.196, 0.097, 0.095, 0.146, 0.269; (b) 0.034, 0.140, 0.077, 0.124, 0.123, 0.131; (c) 0.040, 0.098, 0.060, 0.086, 0.083, 0.086; (d) 0.168, 0.243, 0.225, 0.262, 0.277, 0.290.

The results of these tests are shown in Figure 15, with the lateral force F_x plotted against the displacement d_x along the x-axis for four different distances from the base of the link: 4.187 cm (a), 7 cm (b), 9.812 cm (c) and 12.625 cm (d) , with numeric values of the standard deviations listed in the caption. The average values of the five force-reading cycles are plotted with the corresponding error bars for each pressure level in separate graphs. The same overall linear trend reported for the VSL-V1 is observable, as well as the hysteresis. To compare the performance of the VSL-V1 and V2 given the same boundary conditions (bending stiffness at the tip, cantilever beam), the force data presented in graph (d) in Figure 8 for the pressure level 60 kPa for 2 mm of displacement and the force data presented in the graph (d) in Figure 15 for the same pressure level and

displacement were considered; in the former case this value was $F_x = 0.67$ N, while in the latter case it was $F_x = 3.56$ N. Using this comparison, the effect of the fabric sleeve on the stiffness of the VSL became clear. To better quantify this effect, the stiffness of the system was calculated for the different pressure levels and distances from the base. Based on the force and displacement data, the bending stiffness S_x at different distances from the base was calculated in relation to the pressure. The stiffness data are presented in the graph of Figure 16. The bending stiffness S_x for the four distances from the base for each pressure level P was calculated as described in 3.2.4 by equation (2), averaging the ratio between the measured force F_x [N] and the measured displacement d_x [mm] values over the load-unload cycle and over the five cycles in the range 1 mm – 2 mm, to neglect any nonlinearity in the right neighbourhood of the origin. In this case, there is also a clear linear trend between the stiffness and the pressure for all considered distances from the base.
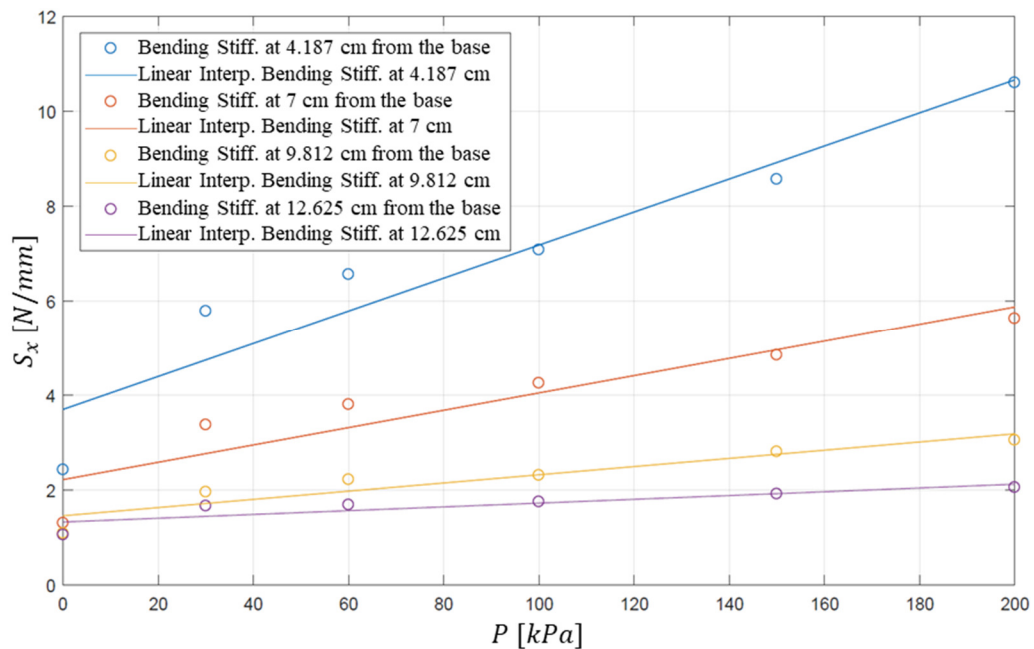
Figure 16 – Bending stiffness S_x [N/mm] against pressure P [kPa]) at 4.1876 cm (azure), at 7 cm (magenta), at 9.812 cm (yellow) and 12.625 cm (purple) from the base for the VSL V2 sample. The circles are values calculated as average on the corresponding load/unload cycles and the continuous lines the linear interpolation of the samples.

It is worth noting that even when the VSL-V2 is not pressurised, it exhibits a stiffness of 1.051 N/mm at 12.625 cm from the base and 2.423 N/mm at 4.187 cm from the base, making it remarkably stiffer than the VSL-V1. By comparison, the bending stiffness of the VSL-V1 sample (d) (which is stiffer and more similar to VSL-V2) at 60 kPa at the tip (13.5 cm from the base) is only 0.3143 N/mm, illustrating once more how fabric plays a critical role in the bending stiffness of the system. This bending stiffness values can also be compared with those presented in Table 2 to get a better understanding of the mechanical behaviour of the proposed system.

As discussed in 3.2.4 in the case of a rigid cantilever beam, assuming the beam to be homogenous and of constant section along its whole length, given a transversal force applied at distance from the base (d_{base}) the bending stiffness independently from the force module, can be calculated as follows:

$$S\,(d_{base}) = \frac{3EI}{{d_{base}}^3} \tag{10}$$

In this equation, E as the elastic module and I as the moment of inertia of the beam along the longitudinal axis are constant. As a result, for rigid beams $S\,(d_{base})$ is inversely proportional to the third power of the distance d_{base} between the applied force and the base. Here, the bending stiffness of the VSL-V2 using the same boundary (clamped at the base, open at the end see) was evaluated. The collected data were analyzed to compare the stiffness model for rigid beams with the stiffness model of the VSL-V2. The author purposely analysed only small deflections (< 2 mm for a minimum distance of 4.187 cm from the base to the measurement point) to make negligible the rotation of the system and consider the measured displacement as pure deflection along the direction of the applied force. Given the boundary conditions (cantilever beam), the bending stiffness can be considered infinite in the base.
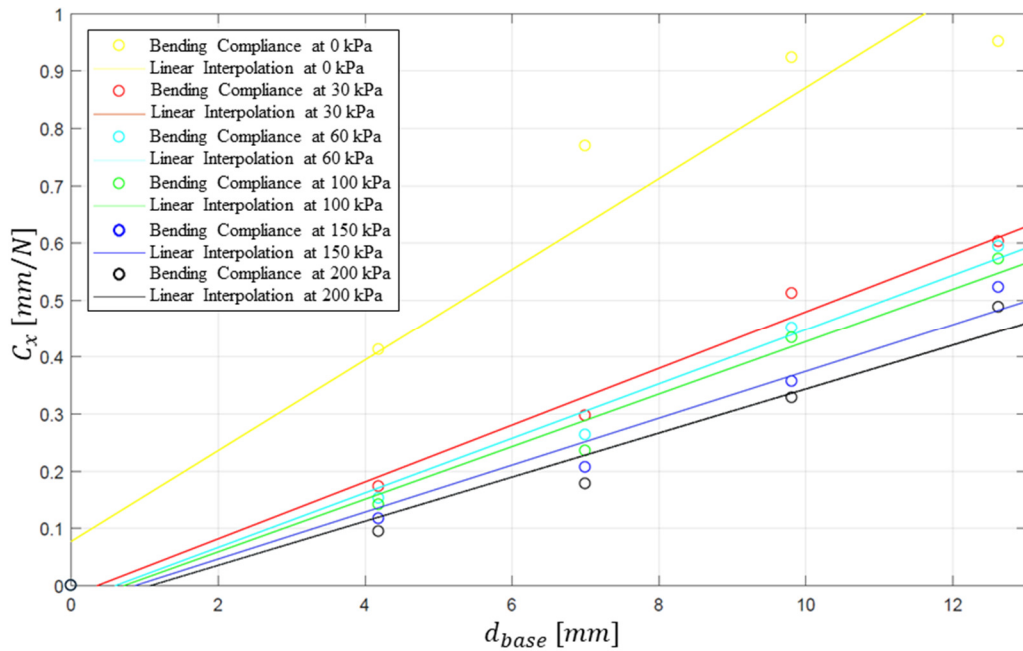
Figure 17 – Bending compliance [mm/N] along the x-axis versus distance from the manipulator base [mm] for the VSL V2 sample when measured at 0 kPa (yellow), 30 kPa (red), 60 kPa (cyan), 100 kPa (green), 150 kPa (blue) and 200 kPa (black). Bending compliance of the manipulator in the base is assumed to be 0 during these tests, given the boundary condition of a cantilever beam (clamped base).

Consequently, instead of considering the bending stiffness as a function of the distance from the base, a function that presents an infinite in zero, the inverse of the stiffness, the bending compliance C_x (d$_{\text{base}}$), were considered. Therefore, if $S_x (0) = \infty$, then $C_x (0) = 0$. The bending stiffness values presented in Figure 16 are used to calculate the respective bending compliance values. The graphs for each pressure level of the compliance C_x (d$_{\text{base}}$) against the distance from the base d_{base} are shown in Figure 17. The C_x (d$_{\text{base}}$) value for $d_{base} = 0$ is considered zero based on the discussed assumptions. It is worth mentioning that the behaviour of the system at $P = 0\ kPa$ is significantly less linear than in all the other cases considered. The lack of a straightening effect of the pressure reduces the elasticity of the system, introducing more plastic non-linear behaviours. For this reason, even though the stiffness in the base has been considered also here infinite, hence, a zero compliance, the linear interpolation line does not fit well the measurements. Thus, a significant offset from the origin

as clearly visible in the left side of Figure 17. If, on the one hand, the data in Figure 16 clearly indicate that the bending stiffness increases with the pressure and decreases with the distance from the base, on the other hand the data in Figure 17 demonstrate that a linear relation between the distance from the base and the compliance of the VSL-V2. Thus, the data show that the bending stiffness, being the inverse of the bending compliance, is proportional to $1/d_{base}$, rather than to $1/d_{base}{}^3$, as in the case of rigid beams, described by equation (10). Also for this reason, despite the similarities between the mechanical behavior of the VSL-V2 and a rigid beam, equation (10) cannot be used to calculate an equivalent elastic modulus E for this system. A discussion related to the results presented in this section is presented in section 3.3.5.

3.3.4 Stiffness Analysis – Axial Stiffness

The same test rig was used to evaluate the axial stiffness of the VSL-V2.
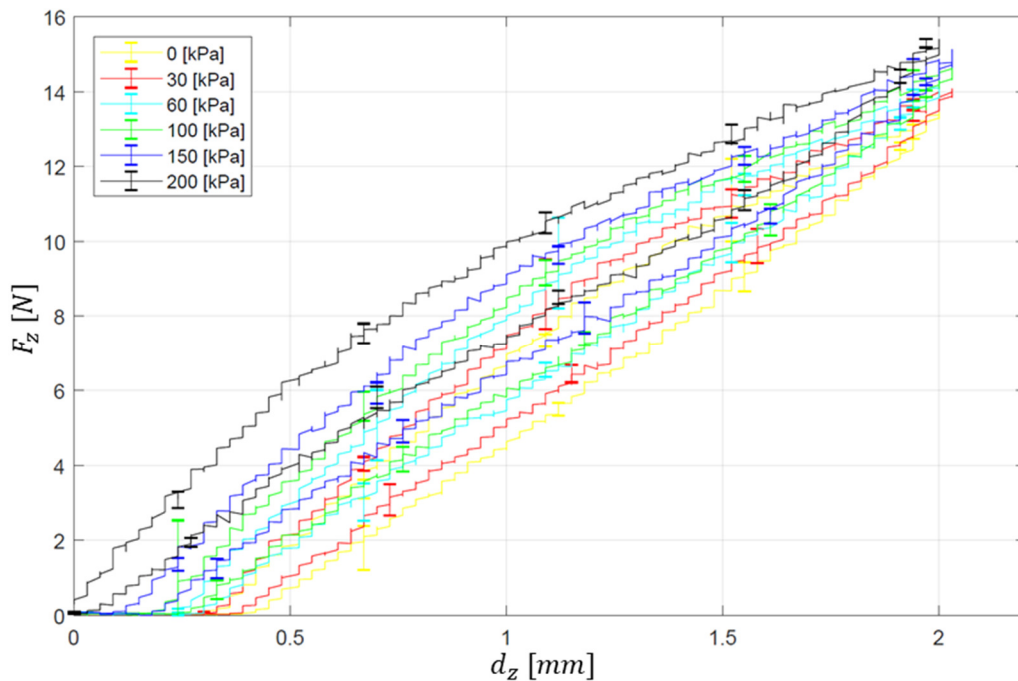
Figure 18 – Force F_z [N] at the link tip against displacement along z-axis d_z [mm] for the VSL V2 sample at 0 kPa, 30 kPa, 60 kPa, 100 kPa, 150 kPa and 200 kPa. Standard deviation values ordered by increasing pressure level: 0.271, 0.277, 0.289, 0.302, 0.335, 0.349.

The axial stiffness test was performed at the tip, applying the same six pressure levels considered for the bending stiffness evaluation. Each loading and unloading cycle was repeated five times. The results of these tests are illustrated in Figure 18 with the axial force F_z plotted against the deflection displacement d_z, with numeric values of the standard deviations listed in the caption. The same displacement (2 mm) considered for the bending stiffness tests was also considered for the axial stiffness tests. As in the case of the VSL-V1, the axial stiffness was considerably higher than the bending stiffness. However, in contrast to the VSL-V1, the axial stiffness was significantly less affected by the pressure in the internal chamber. As demonstrated by the graphs in Figure 18, the curves of the load-unload cycles were almost overlapping in comparison to the curves for the VSL-V1 presented in Figure 10 (d). To better quantify this result, the axial stiffness data were calculated from the force and displacement data. In this case, the axial stiffness S_z for each pressure level P were also calculated, averaging the ratio between the measured force F_z [N] and the measured displacement d_z [mm] values over the five cycles in the range 1 mm – 2 mm to neglect any nonlinearity in the right neighbourhood of the origin. The calculated axial stiffness data are plotted against the pressure in the graph shown in Figure 19 together with their linear interpolation. The axial stiffness data in Figure 11 for sample (d) of the VSL-V1 and the same data for the sample of VSL-V2 of Figure 19 were then evaluated by comparing the equations of the line of their linear approximations. The former is described by the equation (6) and the latter by the equation (12).

$$S_{VSL\,V1\,(d)\,axial}(P) = 0.053912 * P[kPa] + 4.6162 = \frac{[N]}{[mm]} \quad (11)$$

$$S_{VSL\,V2\,axial}(P) = 0.0068499 * P[kPa] + 6.4632 = \frac{[N]}{[mm]} \quad (12)$$

The VSL-V2 was intrinsically stiffer than the VSL-V1. In addition, concerning the axial stiffness for the zero-pressure case and given the higher stiffness of the system, the effects of pressure on this system are less evident, as demonstrate by the difference in the order of magnitude between the angular coefficients of the two lines (0.053912 and 0.0068499). It is also noteworthy that in the case of VSL-V2, no buckling was detected for the displacement range explored, as indicated by the data in Figure 18 (peak force corresponds to the maximum displacement). However, to properly compare the performance of the VSL-V2 with the VSL-V1, an extended displacement range for the axial case was explored without collecting force data, due to limitations of the ATI Nano17 Force/Torque sensor used (normal force range: ± 17 N), but only by visually assessing the buckling. No buckling was detected in the extended displacement range 0 mm – 5 mm. As per the bending stiffness, in the case of the axial stiffness the fabric has proven to significantly improve the mechanical behaviour of the system.
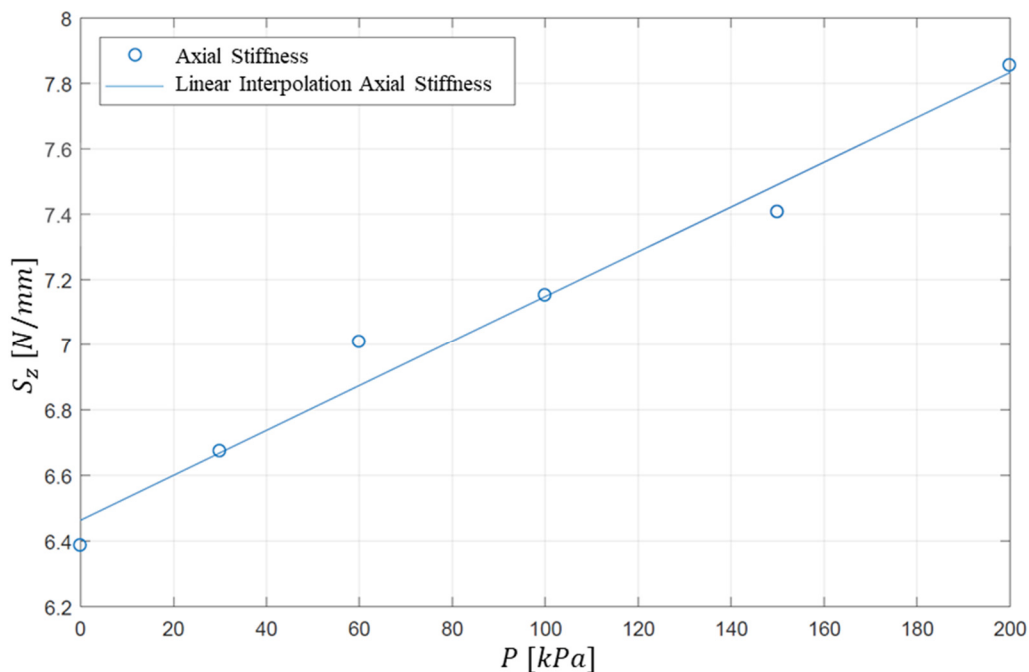
Figure 19 – Axial stiffness S_z [N/mm] against pressure P [kPa]) of the VSL V2 sample. The circles are values calculated as average on the load/unload cycles and the continuous lines the linear interpolation of the samples.

3.3.5 Discussion

As the data presented in this chapter has demonstrated, the use of an external fabric sleeve on top of the silicone-mesh structure used in the VSL-V1, significantly enhances both the bending and axial stiffness of the VSL-V2. This design modification allows for significantly higher pressures to be used: at a safety distance of three meters, using protective glasses, the system has been tested with pressures up to 300 kPa. No leakages were detected, even after several pressurization and depressurization cycles, reaching the same working pressure of car tyres. As a result, thanks to this design improvement, higher forces can be exerted during interaction with the environment. In the next section, the integration of the VSL-V2 as a structural element of a robotic system is explored.

3.4 The VSL Robot: A Novel Hybrid Design for Cobots

Inflatable elements have been investigated in the last three decades in the field of space robotics [209], however the main motivation behind their development has always been the payload reduction for space vectors. Nowadays, lighter and higher-performance materials are available for space robotic systems, hence, the research interest in this direction has declined, even though inflatable systems are still widely used as components of deployable space structures. More recently, in the past two decades, inflatable robotic systems started to be considered in the context of service, assistive and collaborative robotics because of their intrinsic safety in HRI, as for the robotic arm from proposed in [210]. This design approach, completely based on soft materials, which has also been investigated by company such as Pneubotics Inc. [20], despite being optimal for a safe HRI, it is limited by the maximum stiffness, hence accuracy that can be achieved during manipulation tasks e.g. when controlling the position of a load at the end-effector. In one of the first attempts to combine soft and traditional robotic elements, to overcome the limitations of fully soft inflatable robotic systems and to bridge the current gap between the two in industrial robots, the

author proposes a new hybrid manipulator intended to increase safety in human-robot interaction while also being able to ensure high stiffness, accuracy and precision when required. As a result, not only can this manipulator be tuned from a completely soft to a rigid state according to the requirements of the task at hand, but collisions can also be detected without the need for additional sensors. In this section, the first integrated robotic system that makes use of the VSLs is presented. The anthropomorphic manipulator based on the VSL described here is able to tune on-demand the link's stiffness to provide a safe HRI in collaborative applications, and to act as a distributed sensor for collision detection. In the proof of concept presented in this section, traditional rotational joints (3) are combined with pneumatically-actuated VSLs (2) based on the VSL-V2 design presented in the previous section. Sub-section 3.4.1 presents the overall robot design and actuation architecture. Sub-section 3.4.2 presents the results of the experiments conducted to evaluate the workspace of the two-links system. The collision detection algorithm developed is presented in sub-section 3.4.3.

3.4.1 The VSL Robot Design

In the work presented here, the manipulator shown in Figure 20 was assembled. The anthropomorphic robot is composed of two VSL and three rotational joints. The joints are actuated by one high torque 360° stepper motor in the base (distributed by RobotShop [211], SY57ST76/0686B, see Appendix III, indicated as J1), and by 180° servo motors (HiTech [212], HS-7954SH, see Appendix IV indicated as J2 (shoulder) and J3 (elbow)). The motors were chosen in order to guarantee a payload on the end effector of 3N in addition to the weight of the two VSL-based links, the servo motors and additional 3D-printed components. Servomotors were preferred to stepper motors for J2 and J3 due to their relatively low weight for the torque they provide. Furthermore, the torque required on J1 is more than twice the torque required on J3. Hence, a high torque stepper motor was selected for J1 and a lightweight servomotor was selected for J3. All other

components of the manipulator have been designed and 3D-printed using professional 3D printed machines: a Stratasys Dimension SST 768 and a ProJet® HD 3000+. The former of these machines was used to fabricate high-resolution components, while the latter was employed for the remaining elements. To guarantee the air-tightness of the VSL chambers, the connections between the joint bases and link extremities was sealed with silicone glue and reinforced with metal cable ties, as demonstrated in Figure 20. Concerning the hardware of the motor and pressure control, an Arduino Uno board has been used. The schematic of the control scheme is shown in the bottom of Figure 20.
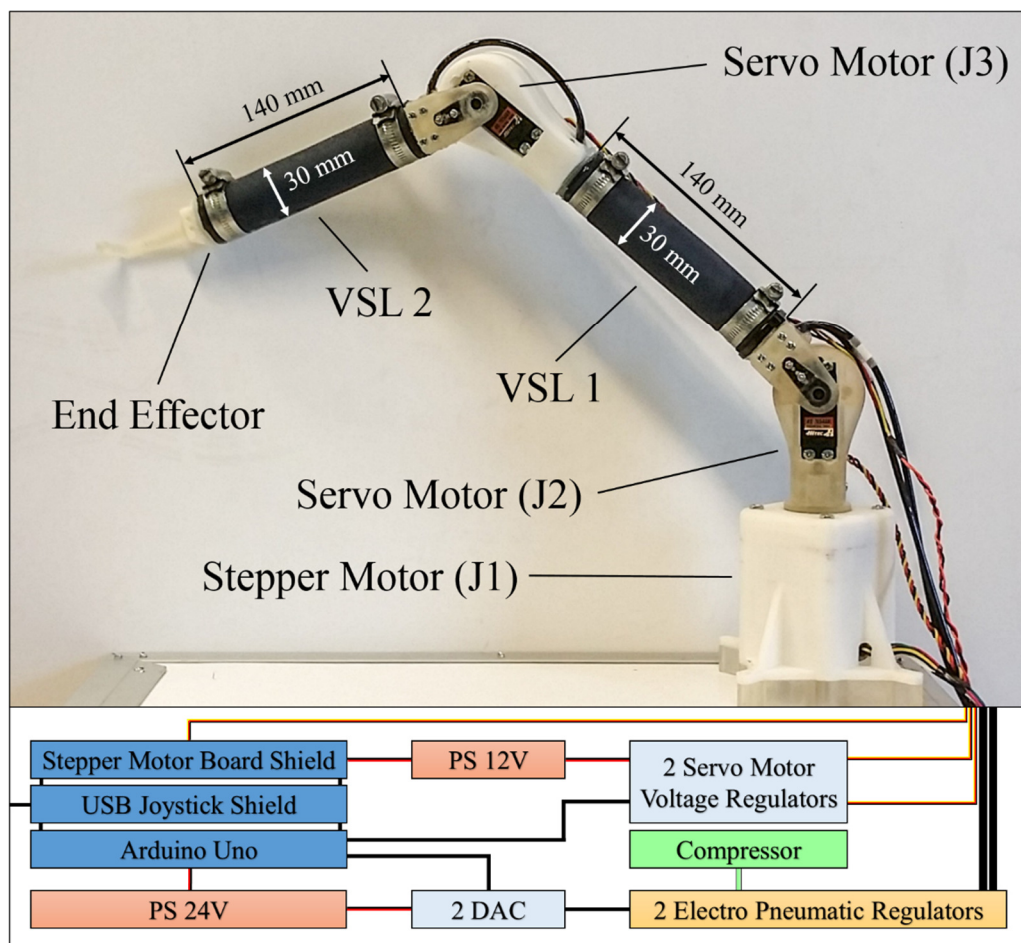
Figure 20 – Conceptual architecture of the VSL Robot, an anthropomorphic manipulator developed to assess the performance of the VSL.

While the servo motors were controlled directly, an additional board was needed to control the stepper motor; therefore, an Adafruit motor shield V2 was added to the Arduino Uno. Two electro-pneumatic regulators (SMC Pneumatics [204], SMC ITV0030-3BS-Q, see Appendix II for the data sheet – output pressure range 0 kPa – 500 kPa) were used to independently control the pressure level of the two VSLs in the links. A commercially-available compressor was used as pressure source. Two Digital-to-Analog Converters (DACs) were employed to provide the desired pressure value to the regulators and feedback the pressure reading. The circuit diagram is shown in Appendix V.

3.4.2 Workspace Evaluation

In this sub-section, the deformation of the VSLs is assessed in a dynamic case when different loads and pressures are applied. The aim of these experiments is to demonstrate how the chain of two VSLs can be approximated as a traditional link chain, simplifying the modelling and the control of the VSL-based manipulator. To evaluate the stiffness-versus-load effects on the workspace of the VSL manipulator, a series of experiments were conducted. The end effector was loaded using a series of weights (0 N, 0.5 N, 1 N, 1.5 N and 2 N). Each experiment was repeated at three different pressure levels (from 0 kPa, 100 kPa, and 200 kPa). Then, J3 was actuated from 0 to 180°, where 90° meant the VSL2 was parallel to VSL1. In order to accurately evaluate the position of the end effector, an Aurora Electromagnetic Tracking System (Northern Digital Inc., Waterloo, Ontario, Canada [213]) was used. This system was composed of two elements: a field generator that emits a low intensity electromagnetic field, and multiple magnetic trackers to be collocated inside the field generator's workspace. One tracker was mounted on the manipulator's end effector and another in correspondence with the rotational axis of J2. The results are illustrated in the graphs of Figure 21. Even though the elongation of the VSLs was measured in the full range of motion of J3 (0° to 180°), the graphs indicate the positions of the end effector in the 1st quadrant only.
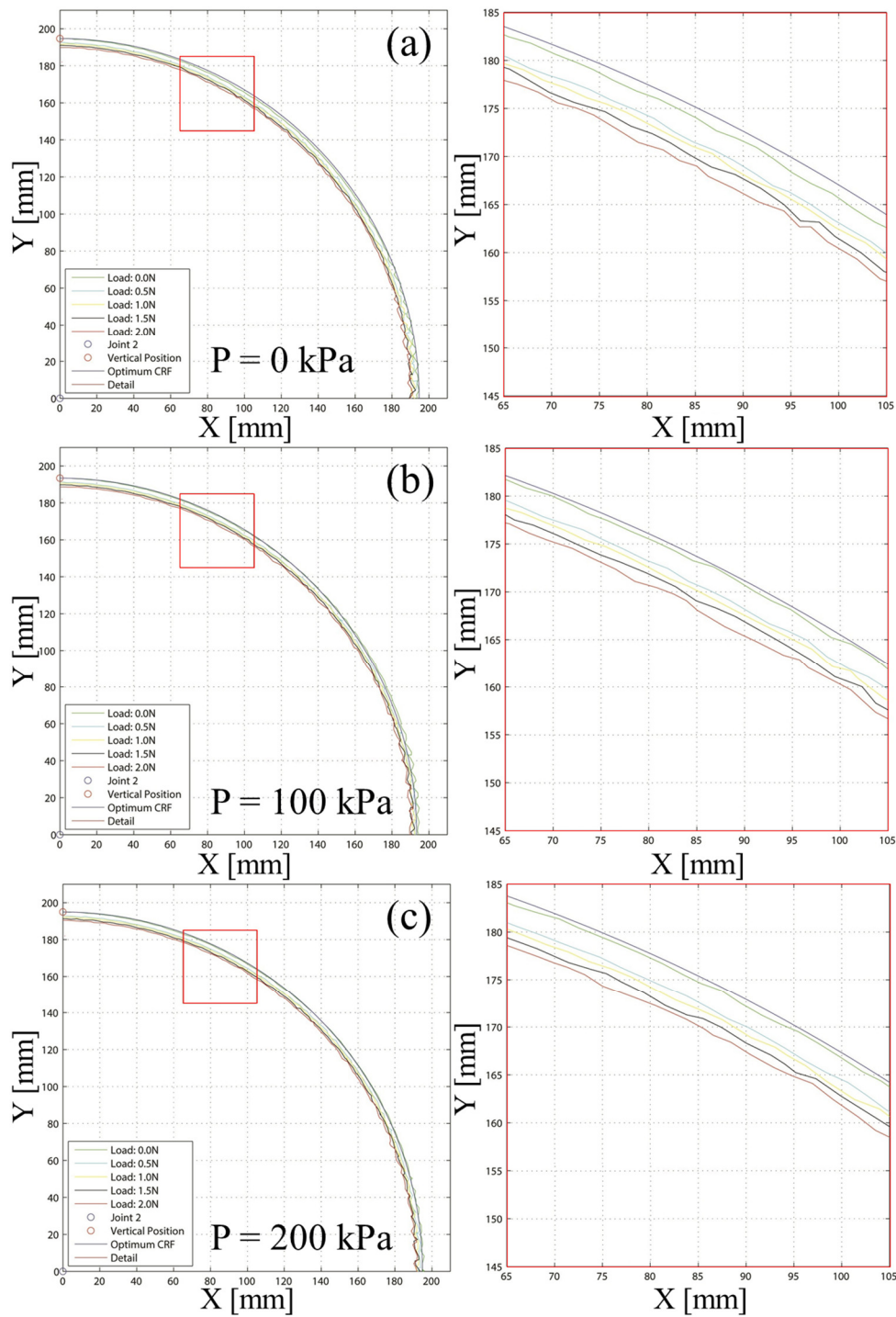
Figure 21 – End effector position in the XY plane (defined as best fit plane for the sequential position of the end effector) when actuating J3 from 0° to 90° (left graphs) when the pressure inside the VSLs are (a) 0 kPa, (b) 100 kPa and (c) 200 kPa. In all graphs, the data is plotted for different load levels at the end effector (0N, 0.5N, 1N, 1.5N and 2N). The reference system is centred in J3. During the experiments, the VSL1 is kept in vertical position; The pressure level of VSL1 and VSL2 is identical. J3 is actuated at a speed of 30°/s. A magnified view of each of the graph on the left is presented in the graphs on the right, showing the content of the red squares.

This is because a clear symmetry in the results of these experiments is verified for the 2nd quadrant. A magnified view is also provided to enhance the readability of the results. In each sub-figure of Figure 21, the pressure is fixed (0 kPa in Figure 21 [a], 100 kPa in Figure 21 [b] and 200 kPa in Figure 21 [c]) while the load varies, as indicated by the labels. The blue circumference in the three graphs is the ideal circumference that has as its radius the distance between the magnetic markers placed in the end effector and its centre J3, when the robot is not loaded and the VSLs are at the pressure used respectively in the three set of experiments. As the graphs illustrate, the overall behaviour of the system at the different pressure levels is consistent: the higher the load, the higher the deformation. Considering an effective length of 140 mm for the VSL 2 (the 183-mm distance given in the graphs for the reference circumference takes into account the rigid connectors of the VSL 2 mounted on the extremities), a maximum length variation of 5 mm for all the given pressures is detected, hence, a maximum percentage variation of 3.57 %. This value decreases slightly with the increase in pressure, which is directly related to the stiffness of the VSL as shown in section 3.3. Furthermore, the higher the pressure, the less the system is affected by vibrations due the stiffness increase and the consequent more-rigid behaviour of the VSL. It is worth mentioning that thanks to the multi-layer design of the VSL and the structural support of the mesh, even the combination of low pressures and high loads in horizontal positions does not result in the VSL collapsing.

3.4.3 The VSL as Distributed Sensor for Collision Detection

To use the VSLs as distributed sensors to detect collisions, the instant pressure values that are normally measured and used for the internal loop of the pressure regulators of each VSL must be fed back to the Arduino board. The proposed approach reads the pressure level inside the VSL and identifies a collision by detecting a sudden change in pressure values. A simple algorithm has been implemented and the pseudocode is presented in Figure 22 (the full code is

available in Appendix VI). The average pressure is measured over period T and stored as reference value for the manipulator behaviour when it is not involved in a collision. The idea behind the proposed algorithm is to detect a collision when at least two samples in an experimentally defined time span (y) are above a certain threshold, calculated as a percentage (x) of the average pressure inside the VSL. More elaborated algorithms can be used to implement the desired reaction; however, for the purpose of this work, the presented algorithm suffices.

```
for (T=1 ms; T++)
  SumPressure[T] += ReadValueFrom(VSL_2)
  AveragePressure =SumPressure[T]/T
  Threshold = x% (AveragePressure)
  InstantPressure = ReadValueFrom(VSL_2);

  if (InstantPressure >= AveragePressure + Threshold)
      for (y ms)
          Pressure = ReadValueFrom(VSL_2);
          if (Pressure >= Threshold)
                CollisionDetected();
          end if
      end for
end for
```

Figure 22 – Pseudocode for the collision detection algorithm for the two VSLs anthropomorphic manipulator: in case of collisions on the VSL 2 the manipulator stop, moves away from the point of collision and reduce the pressure of the VSL 2 to guarantee a safe interaction.

One important aspect to evaluate in the context of collaborative robots in industrial settings as also highlighted in ISO TS 15066:2016 "Robots and robotic devices – Collaborative robots" [162] is the magnitude of the interaction force in case of collision between a robot and a human operator in its workspace. In this field another important document that provides directives and guidelines to define force thresholds in human-machine interactions is the *Euro NCAP assessment protocol and biomechanical limits* [214] which has been used in crash-test studies as the one presented in [215] produced by Haddadin et al, one of the pioneers in the field stiffness controllable robots. As highlighted in this and other works [170], [216], factors likes force magnitude and duration should

be considered to decide whether a collision has to be considered harmful or life-threatening for a human collaborator. Hence, to assess the performance of the proposed system, the experimental setup shown in Figure 23 has been used.

In order to simulate a collision inside the workspace of the manipulator on the more distal side of the link, the VSL1 was kept in a vertical position with J3 moving from 0° to 180°. At an angle of approximately 135°, a rigid object, i.e., a 3D printed disc, was positioned on the trajectory of the VSL 2. In order to collect force data at the point of collision, an ATI Nano17 Force/Torque sensor was embedded in the disc as indicated in Figure 23. Tests were conducted simulating a collision with the point of physical contact in both the middle of the VSL (as in Figure 23) and at the end effector.
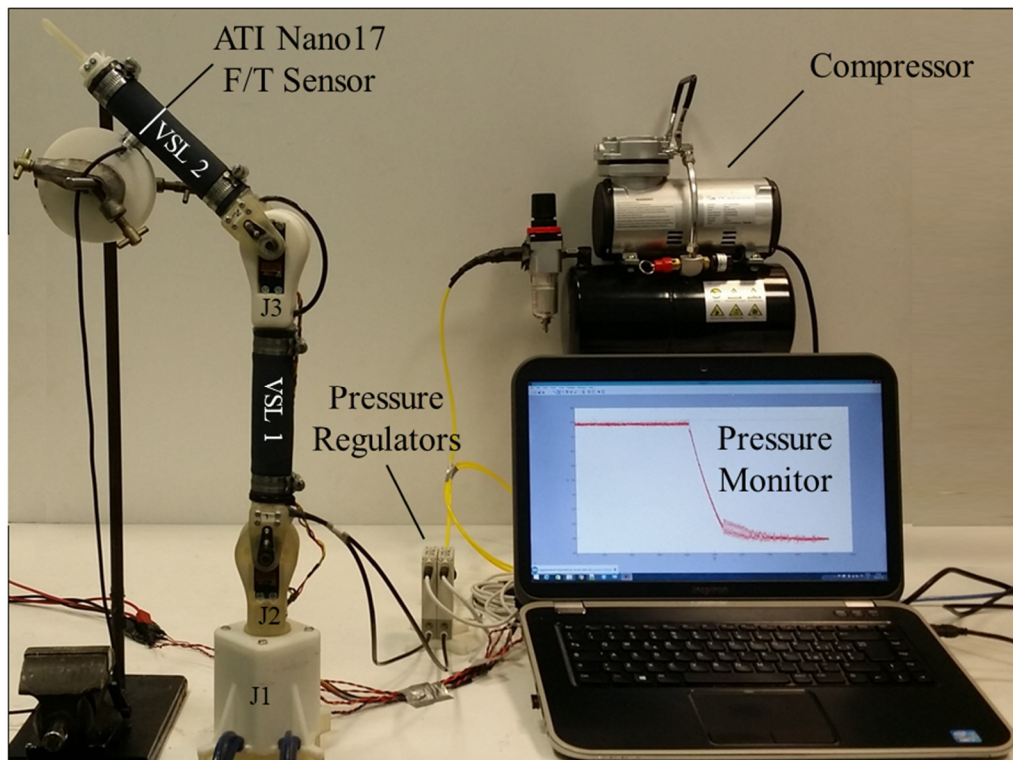
Figure 23 – Overview of the experimental setup for the testing of the collision detection algorithm: the VSL Robot VSL 2 is moved against a rigid object (3D printed disc) where a ATI Nano17 F/T sensor is embedded to measure the interaction force. Pressure data are contextually recorded from the pressure regulators through the Arduino board using a laptop.

Both tests were performed with the same angular speed of J3, hence, at different linear speeds at the point of collision. Both sets of experiments have been repeated ten times in order to evaluate the success rate of the algorithm. A pressure of 140 kPa was selected to be used in these tests. This value can be considered the average initial pressure level inside the VSL 2, even though the algorithm updates this value in real time to provide a more accurate measure. The pressure readings were collected from the pressure regulators by the Arduino board at 2.4 kHz, with a sample period of 0.48 ms. Experimentally, a time span y = 8.4 ms and a percentage threshold x = 1.4 % were defined for the algorithm. Once the collision occurs, two parallel reactions were implemented to minimise the interaction force at the point of collision: the link stops and then moves away from the collision point. Simultaneously, the pressure is lowered (to 50 kPa) to significantly reduce stiffness, providing a softer and safer interaction. In a larger-scale robotic system intended for industrial settings, the combination of these two behaviours could prevent an otherwise harmful or deadly collision between a robot and an operator in the robot's workspace. Table 4 presents the results obtained from the two sets of the experiments proposed in this section, calculating the values averaging the results of ten sets of experiments for each of the two tests proposed.

Table 4 – Collision detection data for a collision taking place in the middle of VSL 2 and at the end effector when VSL 2 is moving and the VSL 1 is vertical: linear speed at the point of collision, peak force detected and reaction times of the system are reported as average on ten trials for each case.

	Link Middle	End Effector
Linear Speed in the Point of Collision [cm/s]	6.65	8.56
Peak Collision Force [N]	5.25	3.43
Detection Time [ms]	110	80
Motion Reaction Time [ms]	120	120
Pressure Reaction Time [ms]	480	480
Total Motion Reaction Time [ms]	230	200
Total Pressure Reaction Time [ms]	590	560

The graph in Figure 24 (a) illustrates the force and time values listed in the table and presents the raw data collected during one of the ten experiments. The total motion and pressure reaction times are the sums of the motion reaction and pressure times and the detection times, respectively. Based on the results presented in Table 4, it can be inferred that the collision detection algorithm performs more effectively at a higher linear speed. Not only is a decrement of 34.67% on the peak force of impact measured, but the time of detection also decreases by 27.28% from the case of the collision in the middle of the link to the case of the collision in correspondence of the end effector.
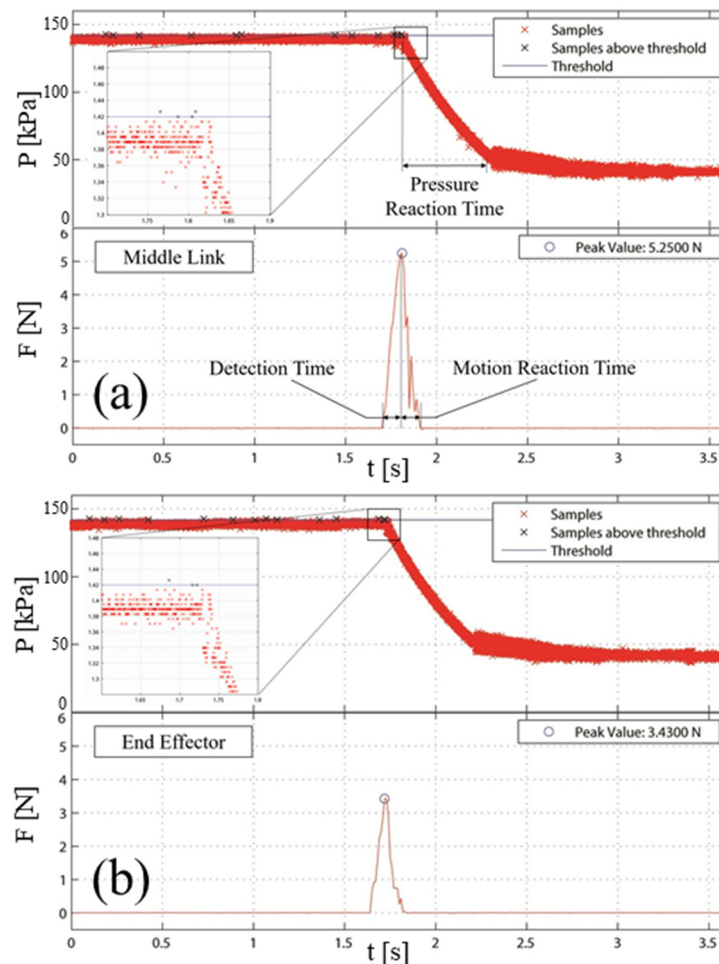
Figure 24 – Collision detection data for different point of impacts: the middle point of the VSL 2 (a) and the end effector (b). Pressure values collected from the pressure regulator controlling the VSL 2 and force value collected from the ATI Nano17 F/T sensor. Force data collected relate to the normal direction as shown in Figure 23.

Due to the higher linear velocity of the impact at the end effector, the variation of pressure recorded inside the VSL 2 shows a more rapid pressure change compared to the middle link case. Therefore, as expected, a greater number of samples overcome the threshold consecutively and less time is needed by the system in order to identify the collision, as shown in the magnified views of Figure 24 (a) and (b). With the current system, both in the case of collision in the middle of the link and at the end effector, more than 500 ms are needed to depressurize the link to a low stiffness level from the moment of the collision. This time also accounts for the communication limitations of the pressure regulators. Nonetheless, the response time of the overall system as a sensor is just 110 ms in the worst case, providing a prompt collision detection considering the performance of the microcontroller used to analyse the data. Furthermore, even though the servomotors used are inexpensive motors for modelling, they allow the system to react to the collision in just over 200 ms. The system showed promising results, with interaction forces well under the thresholds defined by the regulation [162] previously discussed. However, given the size, the speed and the mass of the prototype system presented in this work, this result was expected. To properly assess the safety performance of this design a full scale robotic arm is needed; with such a system, tests comparable to those presented in [215] could be conducted. The performance of the implemented collision detection algorithm is demonstrated in the video available for download and streaming at the following link: https://youtu.be/wZXxv2mFGBg, where an overview of the system and the VSL Robot performing a pick-and-place task are also included.

3.5 Summary

In this section, the author proposed the Variable Stiffness Link (VSL), a stiffness-controllable, active structural element to create soft robotic manipulators and to enhance traditional robotic manipulators. The stiffness controllability of the proposed system has been extensively investigated and tested and its mechanical behaviour analysed. Two design iterations of the proposed system have been investigated and compared in terms of stiffness performance. In addition to the fast on-demand stiffness tuning, the author demonstrated a number of other desirable features of the VSL, including a large internal lumen (almost 70 % of its external volume in the presented samples), a low weight-to-load ratio, and an inexpensive scalable design that becomes even more cost-effective for large diameters.

In light of this investigation, the author envisions a new generation of collaborative robots made of VSLs. A proof-of-concept robot has been presented and the testing that was conducted has produced promising results. The use of Version 2 of the VSL allows for the stiffness to be varied rapidly and reliably over a wide range, offering an innovative solution for close, inherently safe interaction with humans. At the same time, low pressure values result in a compliant robot structure with minimal impact to a human in case of collisions. The author has also demonstrated how the VSL can be utilized as an embedded distributed sensor to detect collisions. Pressure sensor information of the pressure regulators is monitored; rapid change in the pressure sensory data suggest a collision which will then result in immediate stiffness adjustment. This detection is possible without the need for expensive distributed sensors such as tactile skins. The limitations of this system as well as future work are discussed in Chapter 7. In the next chapter the author will explore how the proposed design can be modified to provide not only stiffness-controllability, but also shape-shifting and shape-locking capabilities in inflatable robotic systems.

Chapter 4

4 Bio-inspired Actuation for a Soft Continuum Manipulator

Starting from the work on stiffness-controllable inflatable systems presented in the previous chapter, the author introduces here a new design for a soft continuum robotic manipulator that combines pneumatic and tendon-driven actuation in a bio-inspired antagonistic fashion. This work is especially inspired by the octopus, which uses the longitudinal and transversal muscles in its arms to achieve varied motion patterns; activating both sets of muscles, the octopus can control its arm stiffness over a wide range. The approach presented here mimics this behaviour and achieves comparable motion patterns, including bending, elongation and stiffening. The proposed method combines the advantages of tendon-driven and pneumatic actuated systems and goes beyond what current soft, flexible robots can achieve; because the new robot structure is effectively an inflatable sleeve, it can be pumped up to its fully-inflated volume and also deflated completely. Since, in the deflated state, it is comprised of just its outer "skin" and tendons, this robot can be compressed to a very small size, many times smaller than its fully-inflated state. This chapter describes the mechanical structure of this system. Proof-of-concept experiments are presented that focus on the robot's ability to bend, to morph from completely deflated to entirely inflated and to vary its stiffness.

4.1 Introduction

Traditional robots inspired by human limbs are composed of discrete rigid links connected by low degrees of freedom (DOFs) joints. Over the past decades, researchers, taking inspiration from the limbs of animals such as the tentacles of the octopus or the trunk of the elephant, have created several continuum robotic manipulator types that can be categorized into three main classes: discrete, serpentine and continuum robots [217]. Continuum robots, in contrast to traditional robots, theoretically have an infinite number of DOFs. The actual DOF depends to a large extent also on the actuation method employed. Based on their actuation mechanisms, Walker in [218] classifies continuum robotic manipulators into the following categories: intrinsic, where the actuators are located inside the body of the manipulator; and extrinsic, where the actuators are located outside, and hybrid actuation approaches.

The most common extrinsically-actuated continuum robots are based on tendons that drive the joints of a manipulator. Thin tendons or cables are guided along the robot and fixed at the tip and at intermediate points. Externally-placed motors control the length of each cable as seen, for instance, in the KSI tentacle robot [25]. For tendon-driven systems, the effective number of DOFs depends on the number of integrated tendons and the number of fixed points along the manipulator [219]. Other examples of bio-inspired continuum manipulators that use tendon-based actuation are a robotic trunk for liquid material transportation [24], the tentacle presented in [220] and the Tubot robot [221]. The use of extrinsic actuation in tendon-driven manipulators like the Air-Octor [36] enables not only bending but also extension of the structure in longitudinal direction. Another recent approach to continuum manipulators inspired by the body of the snake is based on extrinsically-actuated concentric tubes to create active cannulas for applications in the field of minimally invasive surgery (MIS) [222], [223]. Hollow, pre-curved and flexible cannulas are longitudinally moved inside each other and hence gradually extend the manipulator. Applying a rotational

motion to one or multiple segments results in a variation of the robot's shape. Taking inspiration from the octopus, a number of intrinsically-actuated manipulators have been created; the Octarm manipulator, for example, is equipped with a set of pneumatic artificial muscles (PAMs) arranged in series [224]. A bio-inspired, universal-joint-based flexible robot for MIS was developed in [225]. The articulated sections are actuated by seven embedded micro-motors, allowing for the development of a miniaturized structure with a diameter of 12mm. In the OCTOPUS project, a flexible, octopus-like arm was fabricated from a series of shape-memory alloy, active-spring actuators mimicking the contraction and elongation behaviour of the biological counterpart [42]. Whereas the OCTOPUS robot was developed with the intention to be as natural as possible, the STIFF-FLOP project investigates how the features of an octopus can be exploited to create surgical devices [226]. Sensor integration was also an important aspect of STIFF-FLOP [189], [190], [193]. The latest STIFF-FLOP robot prototype consisted of a silicone body with three equally-spaced hollow chambers embedded within and arranged in a radial fashion along the longitudinal axis; the chambers are pneumatically actuated [60]. Stiffness control is achieved using granular jamming inside an additional chamber within silicone structure [227]. In [31], researchers proposed the use of polymeric artificial muscles to actuate a robot manipulator. This type of actuation mechanism was extended by incorporating granular-jamming compartments capable of actuating, softening and stiffening the joints along the length of the manipulator [139]. Purely intrinsic pneumatic actuation is used instead in the anteater-inspired walking robot called Ant-Roach by OtherLabs® [228]. The combination of two types of actuation principles often leads to enhanced manipulation capabilities when compared to a single actuation principle [218], including the improved control of the robot's configuration, stiffness and compliance. An example of a hybrid bio-inspired actuation can be found in [25], where extrinsically (tendon-driven) and intrinsically (pneumatic) actuation mechanisms were fused. This combination of pneumatic and

tendon-driven actuation was then further investigated in [229]; each module consists of a pressurisable, non-stretchable hose inside an outer hose and a set of tendons that are connected to rigid supports at the top and bottom of each module.

In this chapter, the author proposes a new, entirely-soft robot called the Inflatable Arm, inspired by the design of the VSL, in which a hybrid of tendon-driven and pneumatic actuation is used to provide not only stiffening, but also steering and shape-locking capabilities. The active variable stiffness system of the Inflatable Arm, according to the classification proposed in [44], works in active/active configuration, rather than in the active/passive as per the case of the VSL. The hybrid actuation approach employs pneumatic and tendon-driven actuation mechanisms to realize a new type of robotic manipulator that can elongate along its longitudinal axis over a wide range, bend in all directions away from the longitudinal axis and change its stiffness. The Inflatable Arm is entirely soft, consisting of modules that are constructed of an internal stretchable, air-tight bladder integrated with an outer, non-stretchable polyester fabric sleeve that prevents ballooning. Tendons connected to the distal ends of the robot modules run along the outer sleeve, allowing each module to bend.

This chapter is organized as follows: Section 4.2 explores the natural example of an octopus's tentacle and the way in which the tentacle translates into the design of the Inflatable Arm; in addition, this section highlights the main contributions and new features of this system. Section 4.3 presents the design of the manipulator, the working principle behind its antagonistic actuation, and the control architecture. The experimental studies related to the mechanical behaviour of the Inflatable Arm are presented in Section 4.4 and a summary of this chapter in Section 4.5. The applications of the Inflatable Arm in minimally invasive surgery (MIS) and of its actuation principle in exoskeletons for hand rehabilitation are presented in Chapters 5 and 6 respectively.

4.2 The Inflatable Arm – Bio-inspiration

The design of the Inflatable Arm is inspired by biology, and the inspiration for this research comes from the limbs of the octopus. Specifically, the proposed actuation and variable stiffness mechanism (Active VSS in Active-Active configuration) is antagonistic in nature as is the case with the above animals, as well as with many other animals and humans. Two sets of muscles "collaborate" in opposing ways to actuate and stiffen a link or link segment, such as an arm. The octopus has longitudinal and transversal muscles in its tentacles and, by activating both sets of muscles, they can be stiffened [26], [230]. In Figure 25 (reproduced from [231]), a section view (schematic drawing in [a] and histological picture in [b]) of the octopus arm is given, illustrating the muscle structure and the antagonistic arrangement of oblique (O), transverse (T) and longitudinal (L) muscles around the nerve cord (N). In octopus arms, biologists speak about the connective tissue that keeps the muscles of the octopus arms in place, avoiding bulging and allowing the animal to achieve stiffness in its arms (comparable to a tube inside a bicycle tire). A similar behaviour is achieved with the design presented here. The proposed hybrid actuation mechanism combines the advantages of tendon-driven (extrinsic) and pneumatic (intrinsic) actuation mechanisms. It has been demonstrated that, due to their thin structure and high tensile strength, tendons can be employed to operate large manipulators [224] as well as miniaturized robots [37].
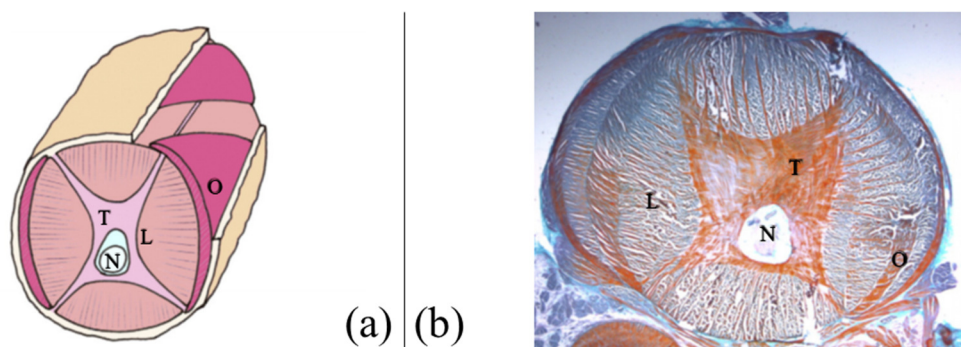
Figure 25 – Anatomic muscle structure of an octopus arm [231]*: (O) oblique, (T) transverse, and (L) longitudinal muscles; (N) nerve cord.*

Fairly accurate position control can be achieved using tendons. The motors used to control the length of the tendons or cables are most commonly placed outside the robot's main structure; hence, the maximum forces that can be applied depend on the tensile strength of the tendons and the maximum force that can be generated by the motors. On the other hand, the main advantage of pneumatic-actuated robots is their capability to be compliant, which makes them particularly suited for use in the vicinity of humans. Combining these two actuation principles, the design concept proposed in this chapter has the following characteristics:

1) The Inflatable Arm is able to morph between the extreme states of being entirely shrunk and completely elongated. As the structure consists only of tendons, an internal latex bladder and an outer sleeve made of fabric, an extension of factor 20 or more is possible.

2) By inflating the outward-moving manipulator and tightening the tendons at the same time, stiffness controllability and shape-locking can be achieved.

3) Due to the Inflatable Arm's structure that functions without a backbone or an external skeleton, the manipulator can be squeezed through narrow openings while remaining fully functional.

4) The manipulator is fundamentally a simple structure which lends itself to miniaturization. It is noted that in addition to the above considerations, for the design of the manipulator prototype described here, only materials that do not affect the homogeneity of magnetic resonance (MR) images, hence, non-magnetic materials, have been used for the whole body of the robot (the actuation system can be remotely located at safe distance); as a result, the proposed robot is MR-safe and lends itself to be used during MR-guided MIS. This particular application, as mentioned before, will be discussed in the next chapter.

4.3 The Inflatable Arm – Design and Methodology

In this section, the design of the first prototype of the Inflatable Arm, its actuation principle and its control system are described. The system described here has been presented in A. Stilli, H. A. Wurdemann, and K. Althoefer, "Shrinkable, stiffness-controllable soft manipulator based on a bio-inspired antagonistic actuation principle," in *IEEE International Conference on Intelligent Robots and Systems*, 2014, pp. 2476–2481 [232], which is to date the most cited publication of the author of this thesis (39 citations), as well as in H. A. Wurdemann, A. Stilli, and K. Althoefer, "Lecture notes in computer science: An antagonistic actuation technique for simultaneous stiffness and position control," in *International Conference on Intelligent Robotics and Applications*, 2015, pp. 164–174 [233] and in A. Stilli, F. Maghooa, H. Wurdemann, and K. Althoefer, "A new bio-inspired, antagonistically actuated and stiffness controllable manipulator," in *Workshop on Computer/Robot Assisted Surgery (CRAS)*, 2014 [234]. In the beginning of 2017 the actuation system of the Inflatable Arm has been completely redesigned to provide real-time measurements of the tendon forces in order to achieve a better understanding of the mechanical behaviour of this system, investigating the relationship between internal and external forces. Building on the data presented in this thesis, a piecewise beam-mechanics-based model of this system has been investigated.

4.3.1 Design and Actuation Principle

The first prototype of the Inflatable Arm is shown in Figure 26 and is comprised of three main elements: an internal airtight, yet expandable, latex bladder; an external, non-expandable, but collapsible and foldable polyester sleeve; and nylon tendons (six) attached to the outer fabric for bending the inflated structure in different directions. As latex bladder, a commercially available party balloon has been used. The six tendons are arranged in two sets of three: three attached at the arm tip, distributed around the arm's perimeter at 120 degrees intervals; and three attached to the outer fabric halfway between base and tip, spaced in

the same way as the first set (Figure 27). The area between the base and the mid-point will be referred to as the proximal section and the area above the mid-point as the distal section, as shown in Figure 26. Figure 27 (b) illustrates the different forces produced by the two actuation means and their interplay inside the body. The pushing force of the pressurized air inflates the manipulator and provides a straitening momentum, while the pulling force of the tendons steer the manipulator in the desired direction.
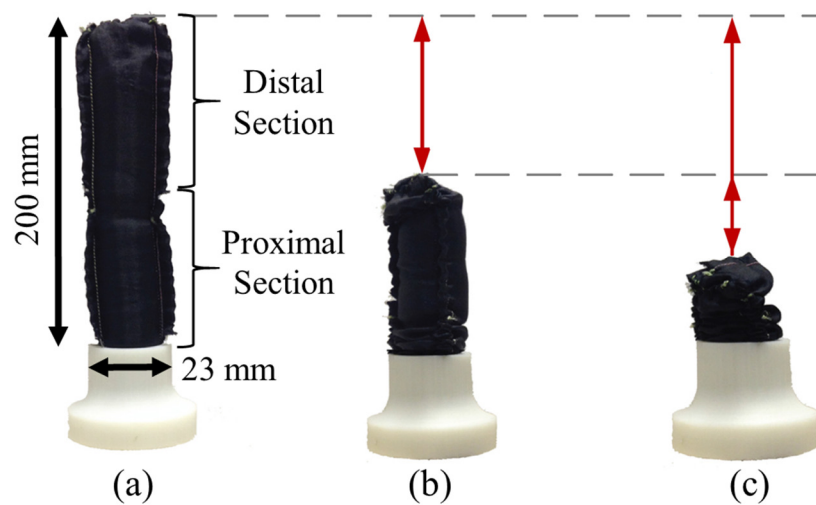
Figure 26 – Elongation manifold of the first prototype of the Inflatable Arm in the (a) elongated state, (b) with the proximal section collapsed and the distal section inflated, and (c) in the shrunk state.

This interplay forms a bio-inspired, antagonistic push-and-pull stage. The equilibrium between the internal pressure, the ambient pressure and the sleeve reaction force defines the level of stiffness, while the equilibrium between the straightening momentum generated by pressurized air and the bending momentum generated by the tendons defines the shape. The proposed system presents the same actuation mechanism of the Air-Octor [36] from Clemson University, employing both tendon-driven and pneumatic actuation. However, differently from its predecessor, where a loose metal spring is employed to provide the chambers with structural support laterally, here no rigid nor semi-rigid elements of any kind are embedded in the body of the manipulator, thus

allowing complete "shrinkability", not only longitudinally, but also radially. Employing two sets of three tendons (one set per section), the two sections composing the manipulator can be independently controlled to achieve complex configurations, including those that have an "S-shape", as shown in Figure 27. The proposed design allows to achieve the same number of DOFs of the Air-Octor [36] using a single pneumatic chamber, rather than two, thus furtherly simplifying its manufacturing. The maximum achievable volume of the proposed structure is defined by the size of the non-expandable fabric (here, a cylindrical structure that is defined by the fabric's surface area); the Inflatable Arm prototype, when inflated, can expand to a maximum length of 200 mm and a diameter of 23 mm (see Figure 26). Retracting the tendons will shorten the overall length of the manipulator; appropriately regulating the air pressure at the same time will allow the stiffness to be adjusted. The nylon tendons (1 mm diameter, nylon 6.6, 20 kg minimum breaking load) are embedded along the outer length of the manipulator sleeve within channels formed by folding and sewing the fabric layer. Figure 28 shows the differences between the kinematics of the manipulator when only one tendon in the middle (a) or at the tip (b) is actuated. The distal section in the former scenario is kept straight by the pushing force of the air, regardless of the bending occurring in the proximal section.
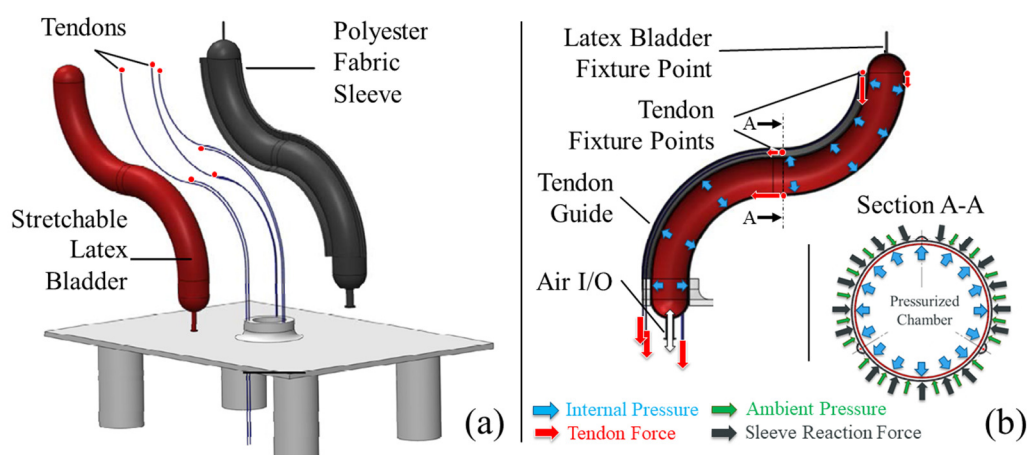
Figure 27 – CAD drawings of the first prototype of the Inflatable Arm: (a) Exploded view showing the arm components and (b) section view showing the tendon routing and their fixture points, the force distribution due to the pressurized air, the reaction force of the sleeve and the tendon pulling force.
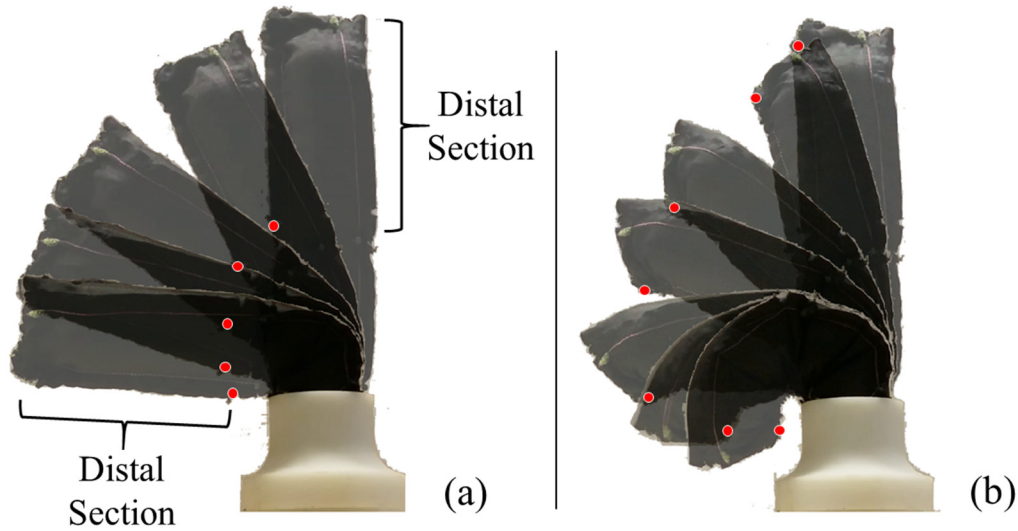
Figure 28 – Kinematics of the single tendon actuation for proximal tendon actuation (a) and distal tendon actuation (b). Red dots are the sequential positions of the fixture of the actuated tendon.

4.3.2 Control System

Figure 29 displays an overview of the control architecture of the entire system. The internal latex bladder can be inflated or deflated through a pressure regulator (SMC Pneumatics [204], SMC ITV0010-3BS-Q, see Appendix II for the data sheet) to which it is connected. The regulator is able to adjust the air pressure in a range from 0.001MPa to 0.1 MPa. An air compressor (BAMBI MD Range Model 150/500) ensures that the supply maintains sufficient pressure, depending on the maximum pressure the regulators can handle. The six tendons are joined by a pulley with a 13.85-mm radius to six stepper DC motors (distributed by RobotShop [211], Soyo SY57ST56-0606B Unipolar Stepper Motor). By using micro-stepping, the motors are able to produce a holding torque of 0.6 Nm, which allows a resolution of 0.1125° (1.8°/step, $1/16^{th}$ of step accuracy) with a precision of ±5%. The radius of the pulley is known, the pulley is directly mounted on the motor shaft with no gearbox. Thus, the maximum pulling/holding force of a single tendon can be calculated according to Equation (8).

$$F_{Max} = \frac{0.6\ [N*m]}{0.01385\ [m]} = 43.32\ [N] \tag{13}$$

The DC motors and pressure regulators are interfaced via a data acquisition card (NI USB-6211) connected to a computer. LabVIEW software (running on the computer) is used to acquire and process signals as well as send actuation commands. A joystick (Logic 3 JS282 PC Joystick) is used to steer the robot arm; the main joystick controls the tendon motors and an additional button is configured to regulate the pressure. It is possible to steer the manipulator by using the tendons and regulating the pressure at the same time. This allows constant pressure to be maintained when the manipulator shrinks, extends or bends. It also allows for stiffness control, increasing the pressure in the latex bladder, when pulling all tendons simultaneously. The described motion control architecture was used to conduct all the experiments described in the next section.
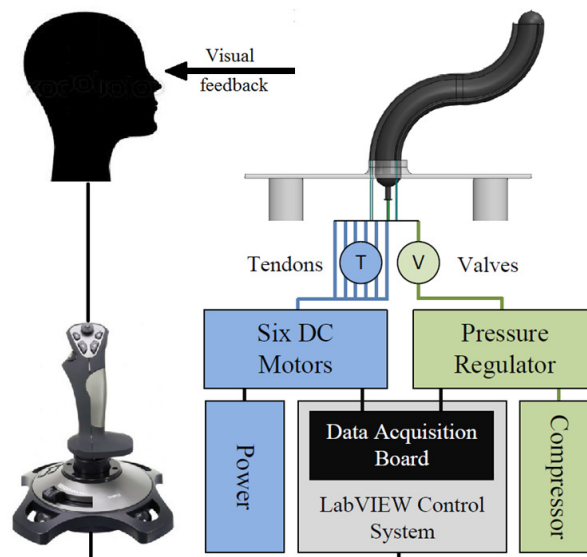
Figure 29 – Schematic of the control architecture of the first prototype of the Inflatable Arm, including DC motors for tendon actuation and pressure regulator for pneumatic actuation.

4.4 The Inflatable Arm – Stiffness Analysis

A number of tests have been performed to investigate the stiffness of the Inflatable Arm and its performance when interacting with the environment. The proposed analysis investigates the relationship between the stiffness (bending and axial) of the system, accounting for the level of pressure, the tendon arrangement on the manipulator section and the body pose. The test rig used for the stiffness evaluation is the same one used to assess the stiffness of the VSL-V1 and V2 presented in subsection 3.2.3. In contrast to the case of the VSL where no actuation was available to steer the system, in this case the stiffness behaviour of the system in different body poses can be evaluated. Therefore, three different configurations are considered and displayed using CAD drawings in Figure 30, and referenced in this chapter as follows: straight configuration (SC), in which the manipulator is in a straight configuration and fully elongated; bent configuration 1 (BC1), in which the manipulator is bent by 90° pulling a single tip tendon; and bent configuration 2 (BC2), in which the manipulator is bent by 90° pulling two tip tendons. The red arrows in Figure 30 indicate where and in which direction the stiffness was evaluated, i.e., at which point of the body of the manipulator the reaction forces were measured: at the tip in lateral direction (I, II, VI, VII, VIII, IX), in the middle in lateral direction (IV, III), and at the tip in longitudinal direction (V, X, XI). In all the tests performed, the stiffness was evaluated in the plane α, i.e., the plane where the bending takes place as Figure 30 indicates. Both BC1 and BC2 were tested, rather than only one of the two, in order to better understand the role that tendons play on the overall stiffness of the system. In test VI, for example, the F/T sensor interacts with the manipulator to evaluate the stiffness pushing on a single tendon; in contrast to test IX, which presents a symmetrical configuration, this interaction takes place between two tendons. In all the tests conducted, a force was applied that caused the robot arm to displace, with displacements of up to 15 mm both for the lateral and axial cases. As with the VSL, only small deflections were considered in order to render the system's rotation negligible, which allowed the

measured displacement to be considered pure deflection along the direction of the applied force. During the stiffness tests, the ATI Nano17 Force/Torque sensor was moved toward the manipulator according to the direction indicated by the red arrow in Figure 30; this movement was accomplished by a motorized linear slide endowed with an encoder, which allowed for a contextual measure of the displacement. These tests can be considered static because the manipulator reacts only to the external forces applied to it; no tendon actuation takes place during these tests, and the tendons are locked in position once the desired body pose is achieved. No tendon displacement takes place, nor is permitted, and the tendon elastic and plastic deformations are both negligible, given the mechanical properties of the selected tendons. Four different pressure levels were analysed: 15 kPa, 30 kPa, 45 kPa and 60 kPa. These levels are the same ones used for the investigation into the VSL-V1. The pressure levels considered for the VSL-V2 were not considered here for two reasons: firstly, the system is intended to be used at lower stiffness levels in the intended application described in the next chapter, and secondly, at high pressures the actuation system cannot produce the necessary force to steer the manipulator.
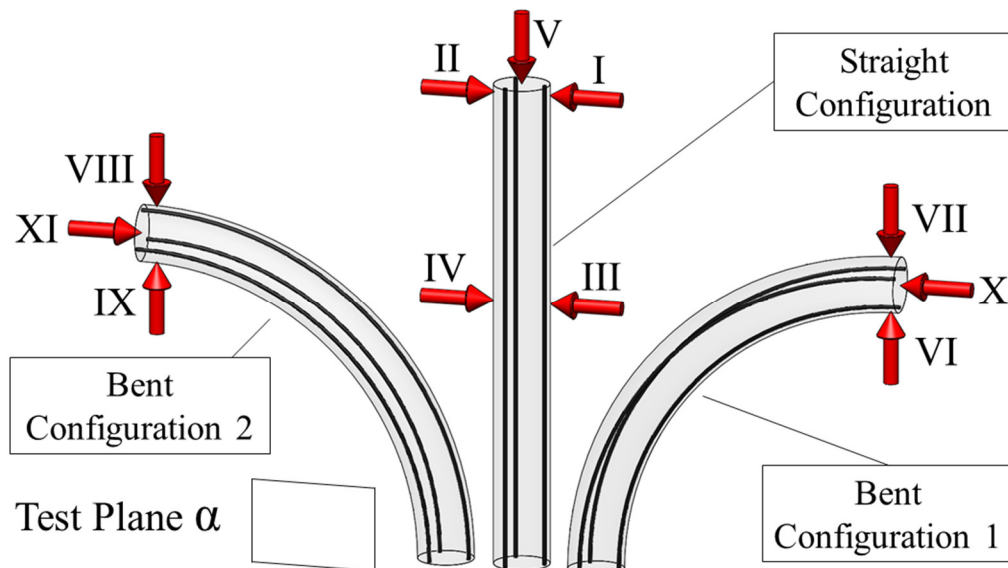
Figure 30 – The three manipulator configurations analysed and the stiffness tests performed. The points where the forces are measured to compute the stiffness are indicated with red arrows.

Nonetheless, the system has been stress-tested up to 120 kPa without actuating the tendons, and neither the fabric sleeve nor the latex bladder were damaged. The speed of the linear module used was set to a low value (0.25 mm/s) in order to perform quasi-static experiments; this speed also rendered negligible the dynamic components of the forces resulting from the interaction between the sensor and the manipulator. Also in this case, each stiffness test was performed loading and unloading the manipulator five times for each of the four pressure levels considered, with the average values of the five force-reading cycles plotted with the corresponding sparse error bars for each pressure level P in separate graphs. A schematic depicted in each of the force/displacement graphs in Figure 31 to Figure 40 recalls which pose the manipulator assumed and the direction in which the forces were applied for each experiment.

4.4.1 Stiffness Analysis in Straight Configuration

Bending Stiffness

The first set of experiments evaluated the bending stiffness of the Inflatable Arm in SC. The same methodology applied during the stiffness analysis of the VSL-V2 in sub-section 3.3.3 was also applied to the Inflatable Arm. In Figure 31, the force data collected during stiffness tests I and II are shown.

Figure 31 – Force F_x [N] against displacement along x-axis d_x [mm] of the Inflatable Arm in Straight Configuration (see Figure 30) on the tendon (I) and in between two tendons (II) at 15 kPa, 30 kPa, 45 kPa and 60 kPa.

The measured reaction force F_x [N] is plotted against the displacement d_x [mm]. The manipulator exhibits similar behaviour for both sides, with a peak force of 2.27 N on the single tip tendon side (I) and 2.48 N when measured in between two tendons on the opposite side (II), evaluated at 60 kPa. The same overall trends observed in the case of the VSL-V1 in Figure 8 can also be observed here, i.e., an overall linear trend with a certain level of hysteresis, in line with the experimental results collected during the bending stiffness analysis of the VSL-V1 and VSL-V2 presented in Figure 8 and Figure 15 respectively. It is worth to note that also in this case the load curve (the highest half of the hysteresis loop) present a significantly more linear behaviour in comparison with the unload one. To enhance the readability of the results relative to the same experiment, the two opposite sides of the manipulator (i.e., measurement on the tendon and in between two tendons) are plotted together with the same scale for the y-axis. In Figure 32, the force and displacement data for the middle section are illustrated. The peak reaction force in this case is roughly double the force evaluated laterally at the tip, resulting in 5.24 N on the single tendon side (III) and 5.53 N when measured in between two tendons on the opposite side (IV), evaluated again at 60 kPa.

Figure 32 – Force F_x [N] against displacement along x-axis d_x [mm] of the Inflatable Arm in Straight Configuration (see Figure 30) on the tendon (III) and in between two tendons (IV) at 15 kPa, 30 kPa, 45 kPa and 60 kPa.

Using the same methodology used for the VSL-V2 in sub-section 3.3.3, force data have been used to calculate the bending stiffness as function of the pressure for each of the stiffness tests presented in Figure 31 and Figure 32. In this case, the range 10 mm – 15 mm is also considered for the calculation of the stiffness to neglect any nonlinearity in the right neighbourhood of the origin (2):

$$S_x(P) = \langle \frac{F_x(j)}{d_x(j)} \rangle \, for \, j = [1,2,\dots,n], for \, d_x(j) \in [10,15] \quad (14)$$

The bending stiffness data for the sides of the manipulator and for the two points (tip and mid-point) are presented in the graph of Figure 33. In contrast to the case of the VSL, the zero-pressure case is not considered here due to the impossibility of measuring the stiffness of the uninflated system. However, it can be theoretically approximated as zero as the intercept of the lines suggests. Consistent with the bending stiffness data of the VSL, a clear linear dependence between the pressure and the stiffness for all samples is measured. The data show similar stiffness trends for tests I and II as well as for tests III and IV, indicating that in this configuration the bending stiffness of the system is not strongly
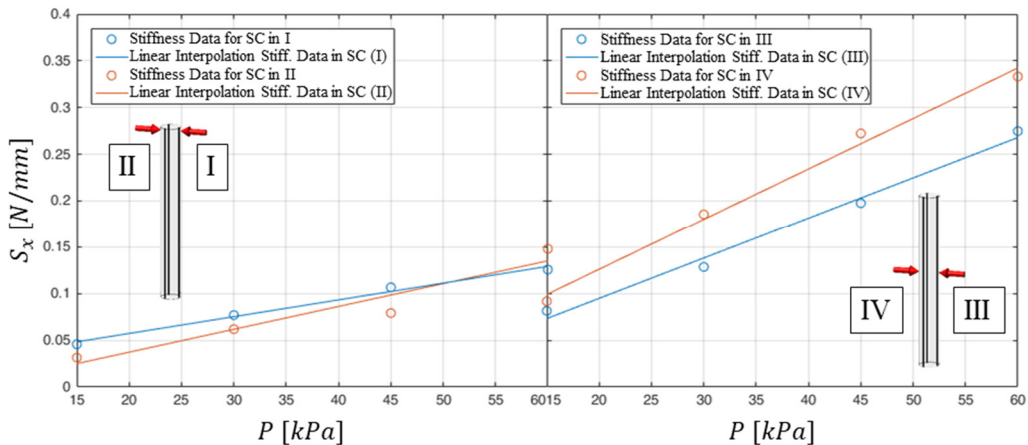
Figure 33 – Bending stiffness S_x [N/mm] against pressure P [kPa]) of the Inflatable Arm in Straight Configuration (see Figure 30) at the tip (left graph) for test I (azure) and test II (magenta) and in the middle (right graph) for test III (azure) and test IV (magenta). The circles are the values calculated as average on the corresponding load/unload cycles and the continuous lines the linear interpolation of the samples.
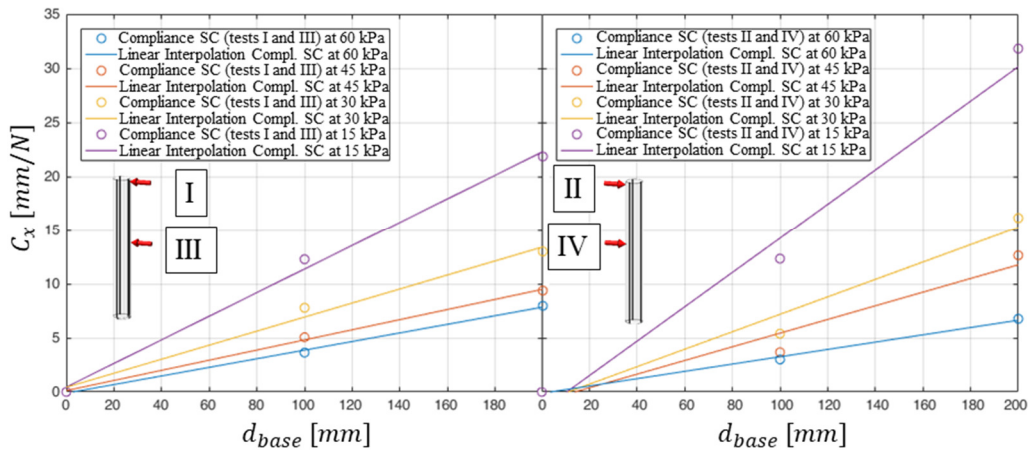
Figure 34 – Bending compliance [mm/N] along the x-axis versus distance from the manipulator base [mm] for the Inflatable Arm in Straight Configuration (see Figure 30) for tests I and III (left graph) and for tests II and IV (right graph) when measured at 15 kPa (purple), 30 kPa (yellow), 45 kPa (red), 60 kPa (cyan). Bending compliance of the manipulator in the base it is assumed to be 0 during these tests, given the boundary condition of cantilever beam (clamped base).

related to the point of application of the force in respect to the tendons position in the manipulator section. What instead appears to be relevant in this case is the distance between the point of force application and the base of the manipulator. As with the beam-like behaviour of the manipulator previously highlighted in 3.3.3 for the VSL-V2, the bending stiffness is assumed to be inversely proportional to the distance from the base and tends toward infinite in the base. Given the same boundary conditions, the bending compliance C_x (d_{base}), is considered in order to verify this assumption. The bending stiffness values presented in Figure 33 are used to calculate the respective bending compliance values. The graphs of the compliance C_x (d_{base}) for each pressure level are plotted against the distance from the base d_{base} and illustrated in Figure 34. The data indicate that there is a clear linear relation between the distance from the base and the compliance of the Inflatable Arm. Hence, the previous assumptions about the behavior of the system are validated. Thus, also in the case of the Inflatable Arm, the bending stiffness results being proportional to $1/d_{base}$, rather than to $1/d_{base}^{3}$ as in the case of rigid beams, described by equation (10). It can be argued that the compliance values measured on the single tendon side

(tests I and III) are lower overall in respect to the values measured between two tendons (tests II and IV), because the local deformations in the former are smaller than in the latter. In both cases the bending stiffness is inversely proportional to the distance from the base, according to the following function:

$$S_x(P, d_{base}) = \frac{1}{m(P) * d_{base}} \qquad (15)$$

Here $m(P)$ is the coefficient of the compliance lines in Figure 34 that are a function of the pressure.

Axial Stiffness

The axial stiffness test has been performed at the tip, applying the same four pressure levels considered for the evaluation of the bending stiffness, using the same methodology described at the beginning of this sub-section. The results of these tests are illustrated in Figure 35 (left graph), with the axial force F_z plotted against the deflection displacement d_z. The same displacement (15 mm) considered for the bending stiffness tests is also considered for the axial stiffness tests. As in the case of the VSL-V1 and V2, the forces measured here are considerably higher than those related to the bending stiffness evaluation, with a peak force of 16.51 N at 60 kPa. A displacement of 15 mm was observed, but no buckling was detected. A stiffness of 1.002 N/mm at 60 kPa was measured. Additionally, there was a linear relation between the pressure and the stiffness. As seen in the case of the VSL-V1, the axial stiffness is strongly affected by the pressure variation. The axial stiffness data are calculated from the force and displacement data, using the same methodology described in 3.3.4. As per the case of the bending stiffness, only the range 10 mm – 15 mm is considered, to neglect any nonlinearity in the right neighbourhood of the origin. The calculated axial stiffness data are plotted against the pressure in the graph displayed in Figure 35 (right graph), together with their linear interpolation.
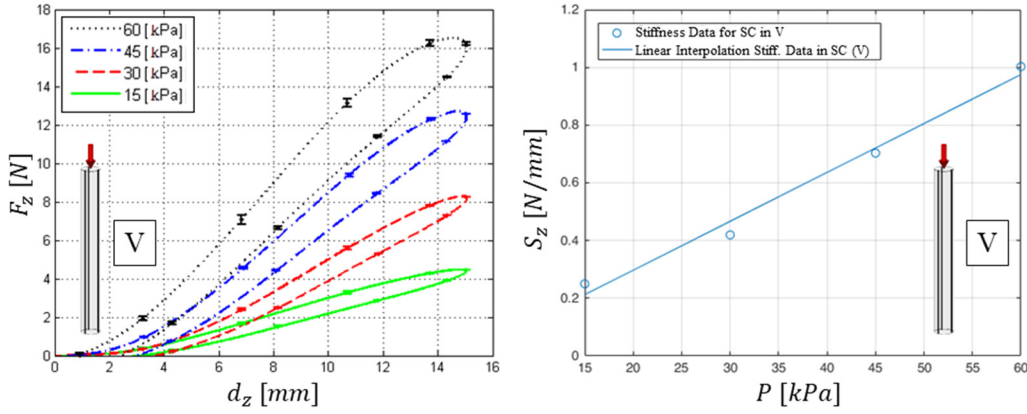
Figure 35 – Force F_z [N] against displacement along z-axis d_z [mm] of the Inflatable Arm in Straight Configuration (see Figure 30) at the tip (V) (left graph) at 15 kPa, 30 kPa, 45 kPa and 60 kPa and Axial stiffness S_z [N/mm] against pressure P [kPa]) (right graph). The circles are the values calculated as average on the corresponding load/unload cycles and the continuous lines the linear interpolation of the samples.

The equation of the line is described by the following relation:

$$S_{IA\_SC\ axial}(P) = 0.016947 * P[kPa] + 0.041776 = \frac{[N]}{[mm]} \quad (16)$$

Thus, the system exhibits minimal stiffness when no pressure is applied and a relative stiffness increase proportional to the pressure in between the stiffness values of the VSL-V2 and VSL-V1, as can be demonstrated by comparing the first order coefficient of the linear interpolation line for the axial stiffness in (16) with the same coefficients for the VSL-V1 in (11) and the VSL-V2 in (12).

4.4.2 Stiffness Analysis in Bent Configuration 1 and 2

Bending Stiffness

The set of experiments presented in this sub-section evaluated the bending stiffness of the Inflatable Arm in BC1 and BC2, with the same methodology applied during the stiffness analysis of the VSL-V2 that was presented in sub-section 3.3.3. In Figure 36 and in Figure 37, the force data collected during the bending stiffness tests in BC1 (VI and VII in Figure 30) and the bending

stiffness tests in BC2 (VII and VIII in Figure 30) are revealed. The measured reaction force F_x [N] is plotted against the displacement d_x [mm] for the four pressure levels previously considered. Consistent with the reduction in length of the lever arm of the applied force, both in BC1 and BC2, the system exhibits higher reaction forces when compared to the straight case. This result can also be verified by comparing the bending stiffness data at the tip in the straight configuration presented in Figure 33 (left graph) with the bending stiffness data for BC1 and BC2 presented in Figure 38 (left and right graphs, respectively).
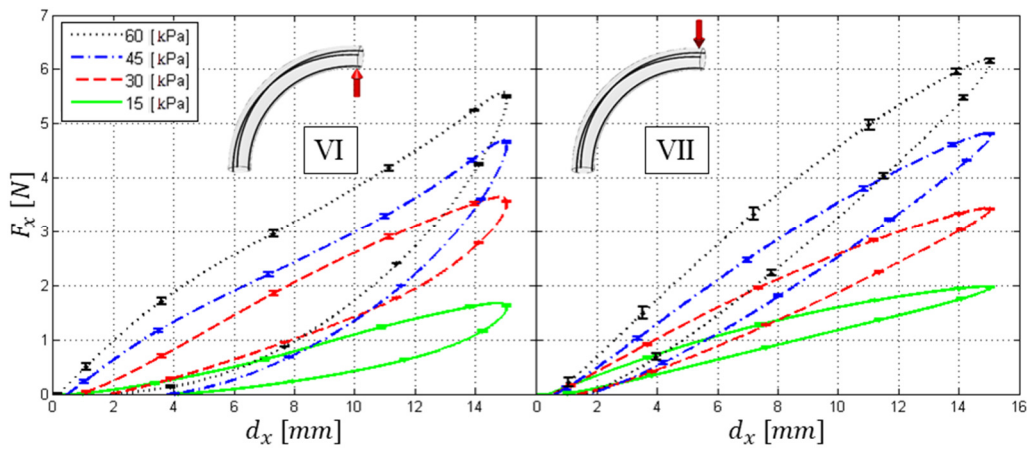
Figure 36 – Force F_x [N] against displacement along x-axis d_x [mm] of the Inflatable Arm in Bent Configuration 1 (see Figure 30) on the tendon (VIII) and in between two tendons (IX) at 15 kPa, 30 kPa, 45 kPa and 60 kPa.
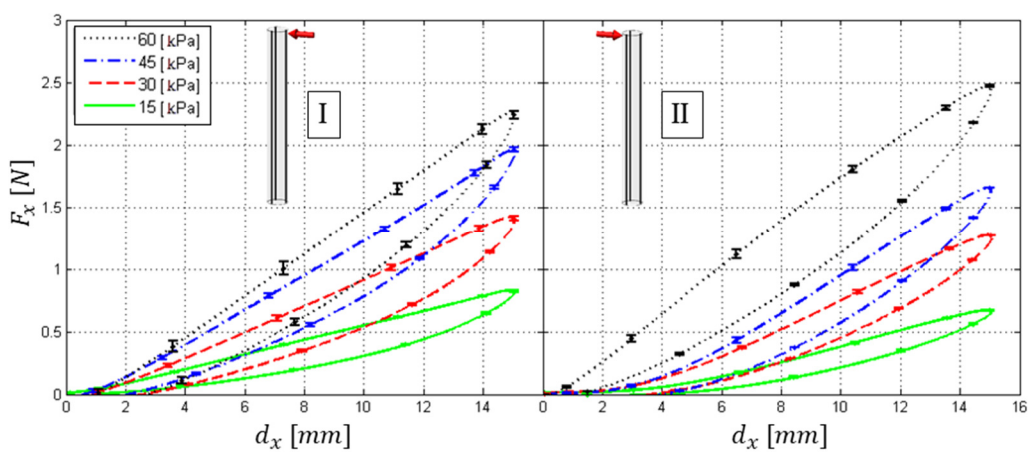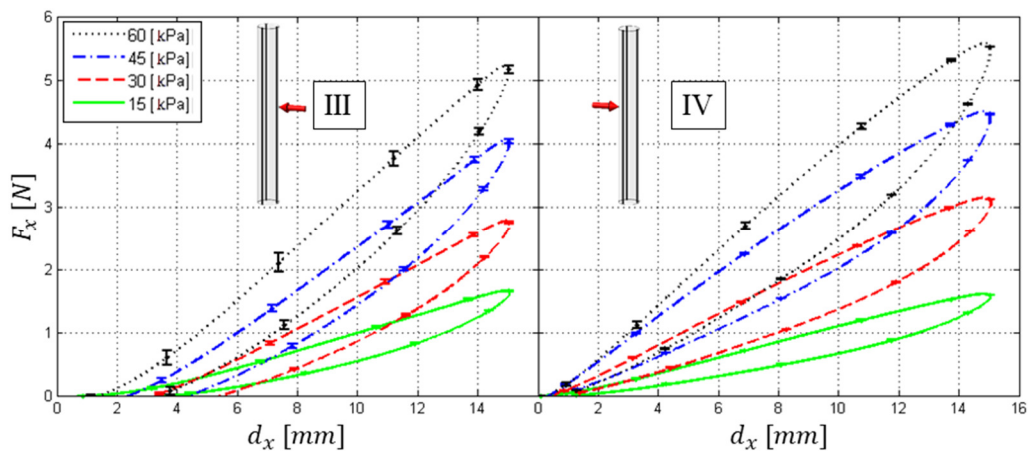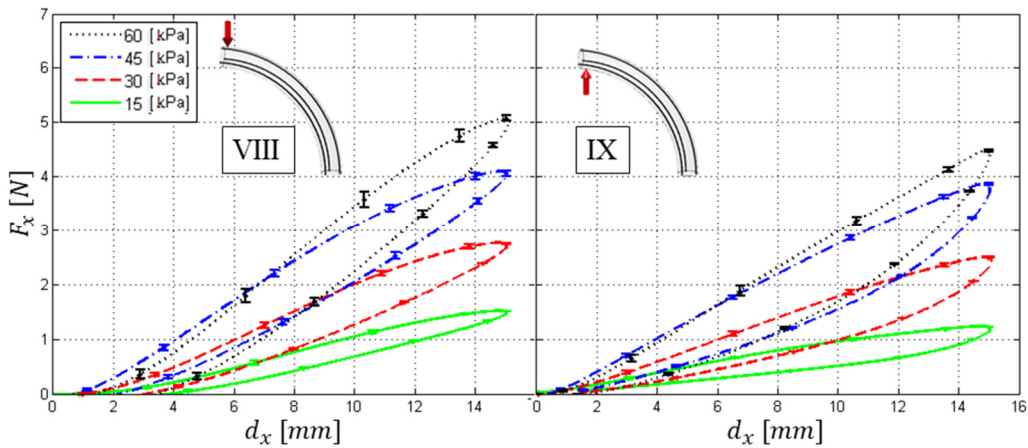

Figure 37 – Force F_x [N] against displacement along x-axis d_x [mm] of the Inflatable Arm in Bent Configuration 2 (see Figure 30) on the tendon (VIII) and in between two tendons (IX) at 15 kPa, 30 kPa, 45 kPa and 60 kPa.

Stiffness data have been calculated with the same methodology described in 3.3.4, again considering the displacement range 10 – 15 mm. Comparison of the two bent configurations observe that the stiffness levels are lower on average in the BC1 in respect to BC2. As a result, the mechanical behaviour of the manipulator when bent is significantly more dependent on the body pose and tendon disposition than in straight configuration. It can be argued that this dependency is contingent upon the number of tendons under tension to achieve the bent body pose, i.e., one in BC1 and two in BC2. To give a measure of the distance between the mechanical behaviour of the Inflatable Arm in BC1 and BC2 in terms of bending stiffness, the stiffness measured for 60 kPa in case VII and IX can be examined: the former is 0.3896 N/mm, the latter 0.2493 N/mm; hence, the former is 56.27% higher than the latter. The angular coefficients of the linear interpolation lines associated with case VII and IX indicate that the lines for higher pressure values diverge, making this gap even larger and the behaviour of the system even more anisotropic.
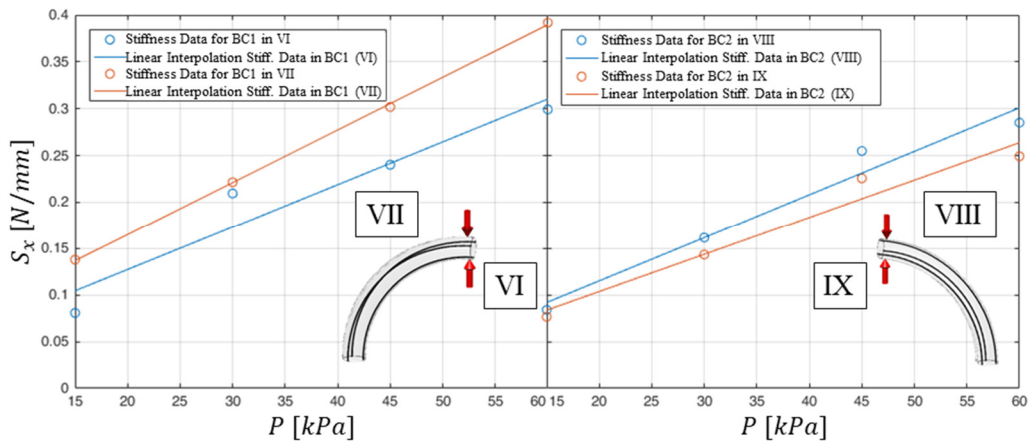
Figure 38 – Bending stiffness S_x [N/mm] against pressure P [kPa]) of the Inflatable Arm in Bent Configuration 1 (left graph) and Bent Configuration 2 (right graph) (see Figure 30) at the tip for test VI and VIII (azure) and for tests VII and IX (magenta). The circles are the values calculated as average on the corresponding load/unload cycles and the continuous lines the linear interpolation of the samples.

Axial Stiffness

In this last set of experiments, the axial stiffness of the Inflatable Arm when in BC1 and BC2 is evaluated with the same methodology applied during the stiffness analysis of the VSL-V2, presented in sub-section 3.3.3. In Figure 39, the force data collected during the axial stiffness tests in BC1 (X in Figure 30) and the bending stiffness tests in BC2 (XI in Figure 30) are illustrated in the left and the right graph, respectively.
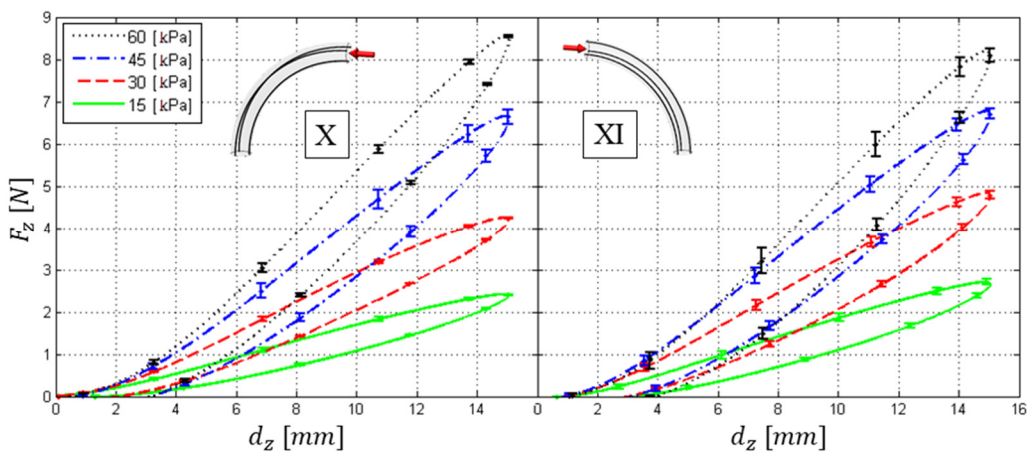
Figure 39 – Force F_z [N] against displacement along z-axis d_z [mm] of the Inflatable Arm in Bent Configuration 1 (left graph) and in Bent Configuration 2 (right graph) (see Figure 30) at the tip (tests V,XI) at 15 kPa, 30 kPa, 45 kPa and 60 kPa.
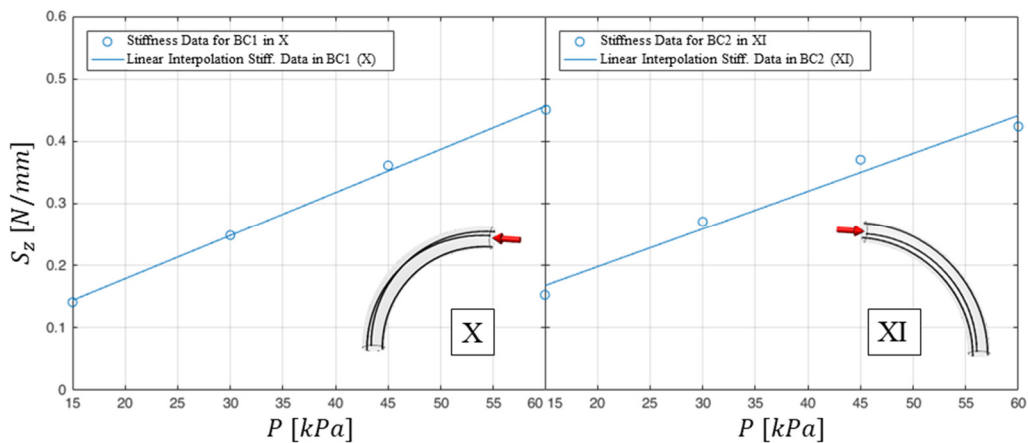
Figure 40 – Axial stiffness S_z [N/mm] against pressure P [kPa]) of the Inflatable Arm in Bent Configuration 1 (left graph) and in Bent Configuration 2 (right graph) (see Figure 30) at the tip (tests X and XI). The circles are the values calculated as average on the corresponding load/unload cycles and the continuous lines the linear interpolation of the samples.

The forces measured in BC1 and BC2 are similar, with peak forces of 8.50 N and 8.21 N at 60 kPa, respectively, almost half of the peak force measured for the straight case (16.51 N, see Figure 35). The axial stiffness data are calculated from the force and displacement data using the same methodology described in 3.3.4. As per the case of the bending stiffness, only the range 10 mm – 15 mm is considered. The calculated axial stiffness data are plotted against the pressure in the graph shown in Figure 40, for BC1 in the left graph and for BC2 in the right. The mechanical behaviour of the Inflatable Arm is similar in terms of axial stiffness to BC1 and BC2, having the two linear interpolation lines at almost the same angular coefficient as demonstrated in equations (17) and (18), which describing the axial stiffness for and BC1 and BC2.

$$S_{IA\_BC1\ axial}(P) = 0.006950 * P[kPa] + 0.039687 = \frac{[N]}{[mm]} \quad (17)$$

$$S_{IA\_BC2\ axial}(P) = 0.006085 * P[kPa] + 0.076243 = \frac{[N]}{[mm]} \quad (18)$$

It is worth noting the difference between the axial stiffness in BC1/BC2 and in the SC, comparing equations (17) and (18) with equation (16). The axial stiffness in the SC is remarkably higher than in both BC1 and BC2. This difference is due to the force and momentum exerted by air pressure, which produces a straightening effect on the manipulator. Therefore, when the manipulator is axially compressed in a straight configuration, the air pressure exerts a reaction force on the sensor and the manipulator base, with no or minimal straightening momentum component. On the other hand, when the manipulator is bent, the stiffness level is reduced by the torque component produced by the straightening effect of the pressurized air.

4.5 Summary

In this chapter, the author proposed a novel soft robotic system called the Inflatable Arm, inspired by the design of the VSL which was presented in Chapter 3. Though the proposed system shares some design features with other continuum robotic manipulators, it is the first of its kind to be completely made of soft materials. The Inflatable Arm not only can be controlled in terms of stiffness, but it is also endowed with shape-shifting and shape-locking capabilities. The stiffness controllability of the proposed system has been extensively investigated and tested and its mechanical behaviour analysed. The collected data indicate that the proposed system behaves similarly to a cantilever beam with a fixed base; however, the Inflatable Arm's bending stiffness is inversely proportional to the first power of the distance from the base, rather than to the third power as is the case for rigid beams. The higher the pressure in the inner chamber, the higher the bending stiffness. The tests highlighted that the bending stiffness is influenced also by the position of the measurement point in respect to the tendons. When the measurement is performed in correspondence to a tendon, the local level of stiffness is higher, on the other hand is lower when measured in between two adjacent tendons. Consequently, the bending stiffness is affected by the local stiffening of the tendons and the more the manipulator is bent, the more pronounced is this effect. A higher number of tendons could potentially minimize this slightly anisotropic behaviour. The data collected show a negligible variance in the body pose during the load/unload cycle; therefore, the system behaviour can be predicted with high accuracy. Lastly, the system has been proven to be tunable in stiffness over a wide range without affecting its controllability, even though in this sense a more systematic approach and testing is needed. The stiffness analysis presented in this chapter gives a good understanding of the mechanical behaviour of the proof of concept system presented. However, in order to generalise this analysis for any size, the relationship between the stiffness and the geometric parameters of the system, such as the section diameter and the length, as well as the number of tendons

(i.e., their tendon spacing), require further investigation. This investigation will allow the development of a comprehensive parametric model of the system, capturing the geometrical parameters, the number of tendons, the pressure level and the body pose, allowing for accurate open-loop control of the system. It is worth mentioning that in light of the recent advancements of machine learning techniques and software tools, as well as the significant improvements in terms of computational power generally available, a model-free learning-based approach could provide better and more general results in a shorter time-frame in comparison to the development of a complex multi-parametric model. The same approach could also be considered in the case of the VSL, even though there is a clear difference between the level of complexity of its model and the model of the Inflatable Arm, making this learning approach especially convenient for the latter.

In the next chapter, the application of the Inflatable Arm in surgical scenarios, particularly for multi-port laparoscopic surgery (MLS) and single-port laparoscopic surgery (SLS) will be discussed. Two adaptations of the design discussed in this chapter will be presented and the system miniaturization will be evaluated to match the diameter requirements typical of minimally-invasive surgery applications (i.e., allowing the robot to fit through a standard trocar port in the MLS scenario). In order to achieve the workspace of typical laparoscopic tools, an inflated length of 200-250 mm is desirable; designs with longer shapes are considered to provide the right fit for the application. The design features of the proposed system such as the intrinsic capability to adjust its stiffness, to bend and elongate, as well as to squeeze through narrow openings, make the Inflatable Arm a suitable candidate for surgical applications. Thanks to an internal structure that is naturally empty, the manipulator is light-weight and can easily house the wiring and other electro-mechanical connections necessary to power a gripper, a camera or a number of sensors.

Chapter 5

5 Inflatable Laparoscopic Tools for MIS Applications

This chapter is the first of two chapters dedicated to the applications of the bio-inspired antagonistic system presented in Chapter 4. Here the author introduces two new designs of the Inflatable Arm specifically conceived for MIS applications: a conic-shaped, robotically-actuated, 12-tendon, 3-section version (the Inflatable Tentacle), and a cylindrical-shaped, manually-actuated, 4-tendon, single-section version (the Inflatable Laparoscopic Camera); the former was conceived for single-port laparoscopic surgery (SLS), and the latter for multi-port laparoscopic surgery (MLS). This chapter focuses on the design optimization of the Inflatable Arm, rather than on the stiffness analysis that has been extensively investigated in the previous chapter. Proof-of-concept systems are evaluated in terms of workspace, dexterity and applicability using a 1:1 scale facsimile of the human abdomen for testing.

5.1 Introduction

Laparoscopic surgery, also known as minimally-invasive surgery (MIS), has been practised since the beginning of the 1900s. Professor Hans Christian Jacobaeus (1879 - 1937) from the Karolinska Institutet in Stockholm is regarded as the father of laparoscopic surgery; when he was an internist in 1910, he performed the first laparoscopic surgical procedure on humans [235]. Even though this procedure is regarded as the first attempt on humans, ten years earlier Georg Kelling, a German surgeon from Dresden who also claimed to have invented this procedure, performed several laparoscopic examinations on dogs [236]. However, Kelling did not see the potential in this procedure and as a result did not publish his work, leaving the primary authorship of this procedure to Jacobeus. Jacobeus enthusiastically published and presented worldwide about the procedure, strongly believing in this promising new alternative to open surgery [237]. Nevertheless, this technique was not incorporated into standard medical practice until the end of the first World War [238]. Laparoscopic procedures and tools did not significantly evolve after their introduction in the 1940s until the 1990s, when the potential role of robotics in the surgical field was recognized by the scientific community and the industry [239], almost 70 years after the development of the first robotic systems. The first robotically-assisted surgical procedure dates back to the 1985 when a PUMA 560, an industrial robotic arm, was used to accurately position a needle for a brain biopsy [240]. Later in 1988 Professor Brian Davies and his team at Imperial College London developed the PROBOT, the world first special-purpose robot [241], designed for prostatic surgery. In 1992 the ROBODOC system [242] was introduced by Integrated Surgical Systems for femoral bone drilling, using a total automated active modality. Several years later, the Computer Assisted Surgical Planning And Robotics (CASPAR) system by OrtoMaquet (then URS) was introduced as an alternative active automated solution [243]. The first robotic assisted endoscope (also referred to as the camera-holder robot) approved by the FDA was the Aesop 3000 by Computer Motion Inc., introduced in 1994 [244].

Inspired by the research on the PROBOT system, the same team explored the concept of active constraints in bone-cutting surgical procedures, referring to this control modality as hands-on [245]. Believing that this hybrid approach was preferable for surgeons, the team translated the research into products, leading to the creation of the spin-off robotic company ACROBOT, founded in 1999 and acquired 10 years later by Stanmore Implants Worldwide, another medical robotic company. In 2000, the da Vinci Surgical System® from Intuitive Surgical Inc. was the first multi-arm robotic platform for abdominal laparoscopic procedures to be FDA approved. Almost contextually, the multi-arm robotic platform ZEUS also developed by Computer Motion Inc., was FDA approved in 2001. The fierce competition between Computer Motion Inc. and Intuitive Surgical Inc. resulted in a years-long patent litigation. In 2003, the two companies merged, keeping the Intuitive Surgical Inc. name and discontinuing the ZEUS system in the same year, paving the way for Intuitive Surgical Inc. to become the world leader in general laparoscopic robotic surgery. The da Vinci Surgical System (called da Vinci Xi® in the current generation launched in 2014) is usually regarded as the golden standard in terms of robotic-assisted laparoscopic surgery. To provide additional dexterity to the robot-held laparoscopic tools, the da Vinci System embeds in each of them a 7-DOF mechanism at the tip, called the EndoWrist®. However, this system still relies on a rigid design employing straight-line instruments with clear workspace limitations.

Flexible laparoscopic tools and endoscopes have been investigated to enhance the capabilities of their traditional, both robotic- and human-held, counterparts. Flexible scopes can be inserted via small incisions in the skin during MIS, or through natural openings such as the mouth, urethra, or anus. To reduce the invasiveness of today's abdominal operations, Natural Orifice Transluminal Endoscopic Surgery (NOTES) has been also introduced; flexible scopes and surgical instruments are passed through natural orifices and then guided into the

abdominal area through an internal incision made in, for example, the stomach or bladder [246], [247]. Nowadays, these tools are widely used in colonoscopic procedures, entering through the anus to visually inspect the colon in order to detect early signs of colorectal cancer [38]. Compared to rigid scopes (used in laparoscopy), flexible scopes offer enhanced dexterity when moving inside the human body and around organs. Flexible scopes used in today's medical interventions have a continuous structure made of a sequence of small rigid and/or semi-flexible links and joints [248], [249]. The operating handle includes either a manual or robotic tendon-based control system to steer and manoeuvre the endoscope tip around organs, while at the same time maintaining a safe distance between the scope and the internal anatomy. These robotic tools are typically constructed to exhibit a certain flexibility (i.e., adapting the endoscope's shape to the anatomy), but also to have sufficient stiffness to be pushed forward through narrow openings towards a desired target without bending excessively. Typically, the stiffness of standard endoscopes cannot be varied. A different solution is proposed by Edmundowicz et al. [250], where the flexibility of the probe gradually varies throughout its length due to changes in the material of the outer tube. In this case, the level of compliance of the device can be regulated by means of compressing and extending a specific coil attached to the tip of the probe. A number of manipulators recently developed, such as those presented in [251]–[253], have been constructed with a three-section structure: a proximal actuation segment, a flexible multiple joints segment for the movement of the probe inside the human body and a distal rigid segment for the camera orientation. The most common manner used to control the bending of the flexible section is tendon-driven actuation. Another similar approach is proposed in [254], where the flexibility of the probe can be regulated by means of a knob; the handle-rotation in one direction causes the internal flexible part to be exposed and therefore the endoscope to be bendable, whilst rotating in the opposite direction pulls a sleeve back, restoring the initial body pose. Even though these steerable devices have been designed to be compliant, their

components are usually fairly rigid; as a result, the interaction between the device and the human body is not guaranteed to be without risk of injury. Indeed, any impact of the probe on the tissue surrounding the operative area can cause damages to the body and pain to the patient. Two of the first authors addressing these safety issues were HJ Chiel [255] and B Ju in [256]; although the their probes had different characteristics, Chiel's being based on soft McKibben actuators and Ju's on tendon-driven actuation, scope-tissue interactions proved safer with their designs. However, both approaches could not avoid the use of rigid elements for the connection of the different flexible parts. Another approach is described in [257], where a flexible laparoscopic camera is able to switch between being rigid and pliable using vacuum pressure.

In this chapter, two new systems based on the Inflatable Arm design are presented, envisioning their use in abdominal MIS procedures. Tendon-based actuation has been selected because it minimizes the encumbrance of the means of actuation and allows the actuators to be placed outside the articulated structure; this placement, in turn, considerably decreases the structure's diameter and makes the proposed devices suitable for minimally-invasive interventions. The proposed system, being able to vary its structural stiffness level, allows for high pliability during insertion and investigation procedures and a firm pose when one becomes necessary. The first design derivation of the Inflatable Arm, the Inflatable Tentacle, is presented in Section 5.2. This system is conceived for Single-port Laparoscopic Surgery (SLS) applications. The second derivation, the Inflatable Endoscope, is presented in Section 5.3 and designed for Multi-port Laparoscopic Surgery MLS applications. In Section 5.4, the conclusions related to this chapter are presented.

5.2 The Inflatable Tentacle

In this section, the design of the Inflatable Tentacle, a design iteration of the Inflatable Arm, and its application in MIS applications, particularly SLS, are described. The system described here has been firstly presented in – F. Maghooa, A. Stilli, Y. Noh, K. Althoefer, and H. A. Wurdemann, "Tendon and pressure actuation for a bio-inspired manipulator based on an antagonistic principle," *Robotics and Automation (ICRA), 2015 IEEE International Conference on*. pp. 2556–2561, 2015 [258], which is to date the second most-cited publication of the author of this thesis, with 31 citations. In addition, the work on this system was presented in the form of a poster at the Prostate Cancer World Congress 2015 in Cairns, Queensland, Australia (K. Althoefer, H. Wurdemann, and A. Stilli, "Minimally invasive surgery employing antagonistic, inflatable robot: Evaluation of positioning accuracy and motion dynamics." In Prostate Cancer World Congress (PCWC), 2015). This system was also extensively used for lab demonstrations on multiple occasions in the Mechatronics Lab at King's College London.

5.2.1 Design and Methodology

The antagonistic actuation of the Inflatable Arm that combines extrinsic (tendon-driven) and intrinsic (pneumatic) actuation is used here to actuate a conic-shaped inflatable manipulator. The design of the Inflatable Tentacle and the benchmark setup used are presented in Figure 41. As opposed to the case of the Inflatable Arm, in this case the testing is conducted with the manipulator hanging from the top of a dome to better understand the mechanical behaviour of the system in the context of the envisioned application, i.e., SLS abdominal surgery.
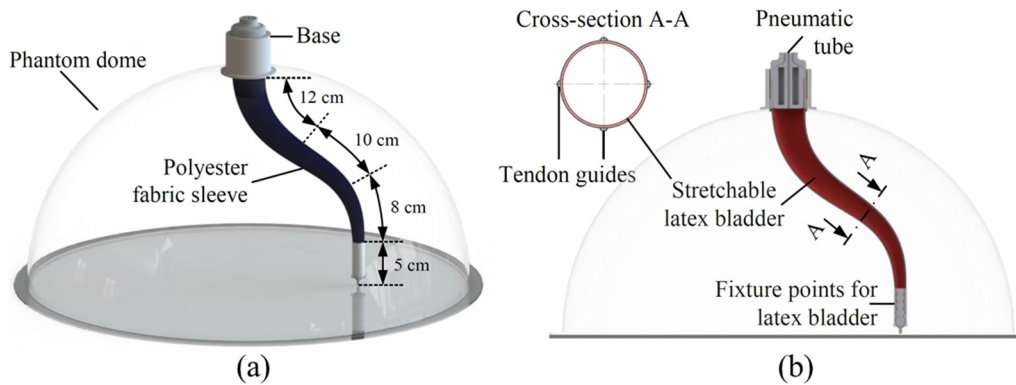
Figure 41 – CAD drawings of the Inflatable Tentacle inside the Plexiglas dome used to test the manipulator in a hung configuration to simulate the scenario of SLS abdominal surgery: in (a) the dimension of the rhee sections are indicated, in (b) a longitudinal section is presented.

A Plexiglas dome is employed for this purpose, as illustrated in Figure 41. The manipulator presented here is composed of three sections and actuated by four tendons, spaced by 90° in each section. The diameter of the manipulator is 40 mm at the base and narrows down to 10 mm at the tip, resembling the shape of an octopus arm. Analogous to the Inflatable Arm, the Inflatable Tentacle is composed of an inner air-tight and stretchable latex bladder, and an outer, non-stretchable (but foldable) double-layer polyester fabric sleeve in which the nylon tendons are embedded. The stretchable latex bladder is inserted into the polyester sleeve. The outer sleeve is 30cm in length when fully inflated. As the fabric material is non-stretchable, the outer sleeve prevents any ballooning of the inner bladder in a radial direction beyond the maximum diameter. The stiffness of the arm can be controlled in the same way it is controlled in the case of the Inflatable Arm; the tip of the latex bladder is mounted to the tip of the outer sleeve to prevent the latex sleeve from twisting inside the manipulator when actuated. A noteworthy design and fabrication improvement from the initial design of the Inflatable Arm to the design of the Inflatable Tentacle involves the use of a double layer of fabric rather than a single layer. In fact, in the former system only one layer is used for the body of the manipulator, creating the tendon channels by folding this layer and hand-sewing the tendons fixtures afterward. This fabrication method limits the maximum air pressure that can be used: at

high pressure levels, the seam of the tendon lines cannot withstand the circumferential stress and breaks, leaving the tendons in contact with the latex membrane. Furthermore, the hand-sewn fixture of the tendons is generally less robust than its machine-sewn counterpart. The use of two layers of fabric allows for the creation of the channels for the tendons by mean of two parallel, machine-sewn seams, as well as the machine-sewn tendon's fixtures. The use of two seam lines and two fabric layers makes the system significantly more robust, because, regardless of the pressure level and the circumferential forces applied, the seams of the tendon channels cannot be damaged. In this three-section prototype, four tendons are fixed at the end of the proximal section of the manipulator and another two sets of four tendons are attached to the end of the middle and the proximal section, respectively.
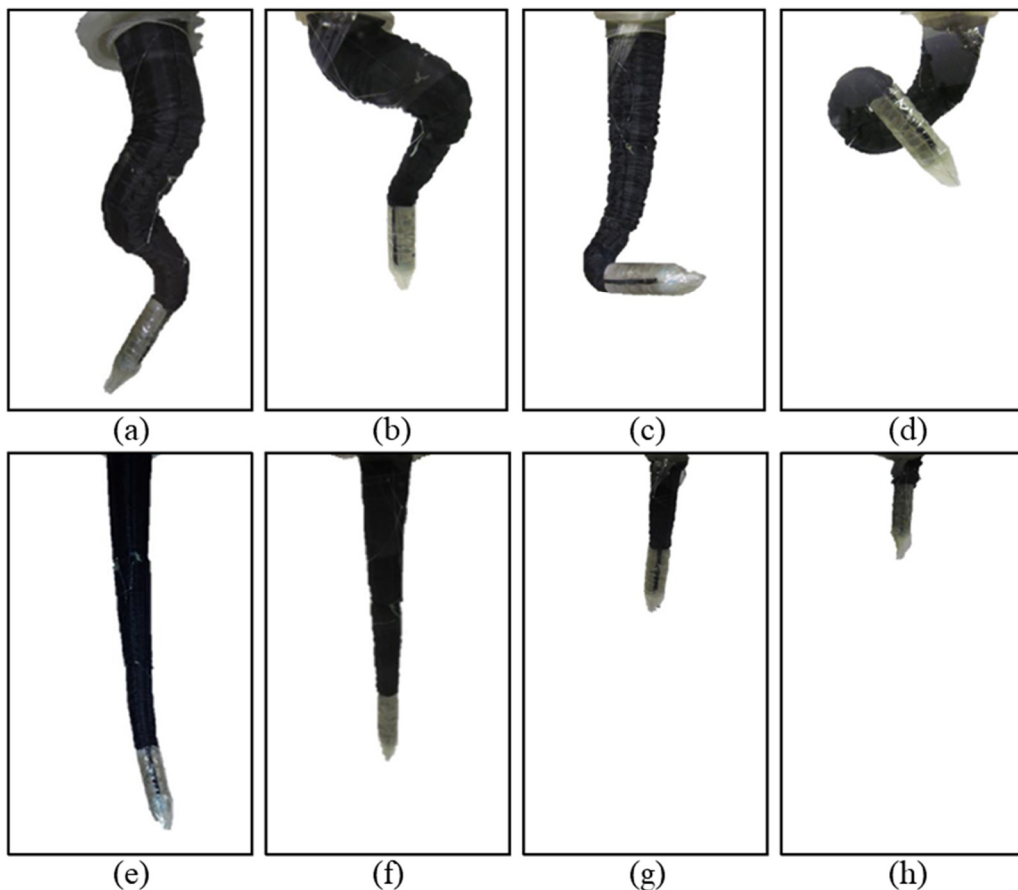
Figure 42 – The Inflatable Tentacle: Examples of possible configurations – single tendon actuation of (a) the middle and distal sections, (b) the proximal and middle sections, (c) the distal section, (d) all sections, and multi-tendon actuation (e)-(h) to show elongation/shrinkage capability.

The proximal section is 12 cm in length, the middle section 10 cm, and the distal section is 8 cm. A rigid tip 5 cm in length and 10 mm in diameter is connected to the distal section as shown in Figure 41(a). The robot's three sections can be independently controlled, allowing for more complex body poses to be achieved, in comparison with the 2-sections system presented in the previous chapter. In Figure 42, the dexterity of the Inflatable Tentacle is demonstrated. Figures (a) to (d) illustrate several of the possible configurations of the manipulator when a single tendon is actuated on the middle and the distal section (a), on the proximal and the middle sections (b), on the distal section only (c) and on all the sections (d). As configuration (a) demonstrates, the Inflatable Tentacle can bend around obstacles, offering one degree of redundancy (DOR). As the body pose shown in (c) demonstrates, the manipulator can be kept straight for configuration in the proximal and middle sections, bending only the distal section, despite the tendons of the distal section running along the whole manipulator body and being pulled from the base. In Figure 42 (e-h), the elongation and shrinkage capabilities of the manipulator are demonstrated; in (e) all the tendons are not displaced and the system is fully inflated, while in (f) the four tendons of the proximal sections are displaced minimizing the section length, without altering the shape of the middle and distal sections. The same parameters apply for (g) and (h), where the four tendons of the middle section and the distal sections are displaced, respectively. One the tentacle is fully deflated, the inflatable body can be compressed in less than 1 cm. The conic shape makes the folding and unfolding process more organized and mono-directional in comparison with cylindrical case of the Inflatable Arm. The result is a mechanical behaviour resembling the one exhibited by the octopus tentacle during elongation.

5.2.2 Mathematical Approximation

The Inflatable Tentacle is composed of three sections which can be configured independently. Figure 42 illustrates the experimental results of the bending behaviour of the base section in the case of single-tendon actuation. Multiple

bending angles are achieved by keeping the pressure constant at 60 kPa. The bending behaviour of the proximal section demonstrated in the (a) to (d) actuation sequence can be approximated with circles of increasing diameter. As a result, the diameter length is inversely proportional to the displacement of the actuated tendon and the manipulator meets the constant curvature condition. According to [259], where Webster and Jones presented the kinematics description of this type of continuum manipulator, the constant curvature model can be applied. The geometry can be modelled using the three arc parameters l, ϕ and γ, where l is the arc length, ϕ is the angle defining the plane containing the arc (see also Figure 44 [a]) and γ is the curvature of the arc. According to this model, the motion of the robotic sections can be separated into a rotation of angle ϕ around the z-axis and a rotation around the direction normal to the arc plane.
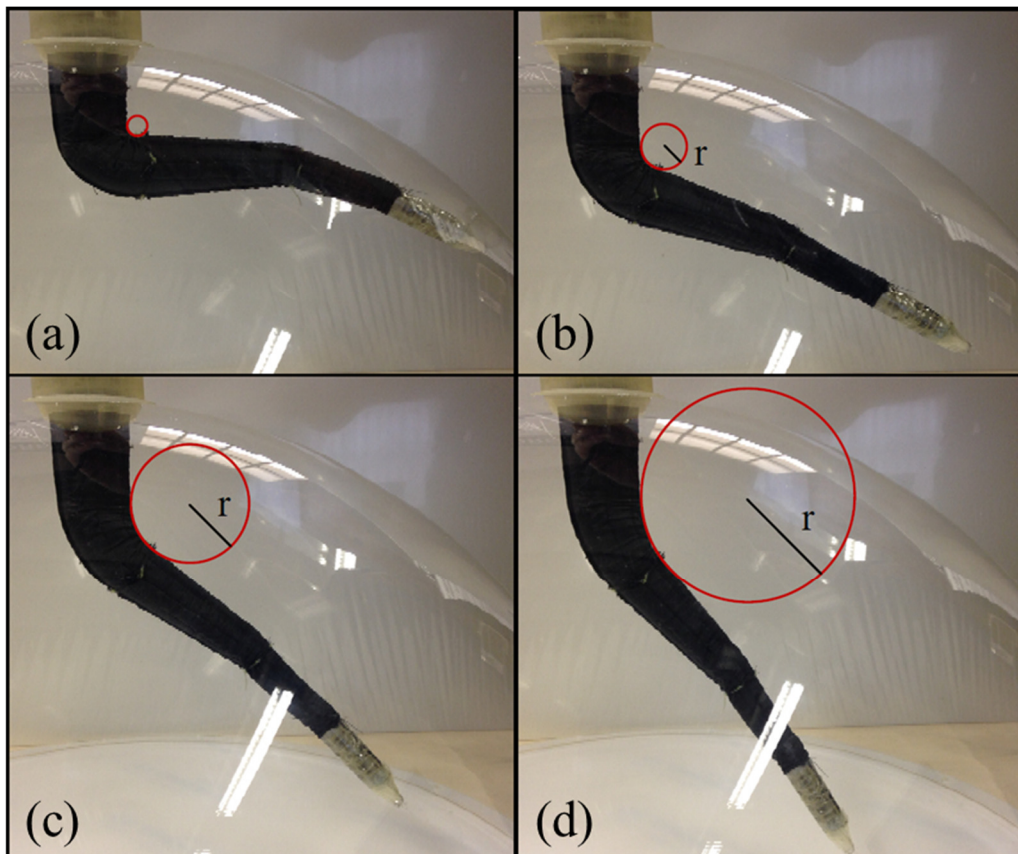
Figure 43 – Bending behaviour of the proximal section in one plane actuating a single tendon at the end of the proximal section.

As per [259], the transformation matrix T from the global to the tip frame is:

$$T = \begin{pmatrix} \cos\phi\cos\gamma l & -\sin\phi & \cos\phi\sin\gamma l & \dfrac{\cos\phi(1-\cos\gamma l)}{\gamma} \\[2mm] \sin\phi\cos\gamma l & \cos\phi & \sin\phi\sin\gamma l & \dfrac{\sin\phi(1-\cos\gamma l)}{\gamma} \\[2mm] -\sin\gamma l & 0 & \cos\gamma l & \dfrac{\sin\gamma l}{\gamma} \\[2mm] 0 & 0 & 0 & 1 \end{pmatrix} \quad (19)$$
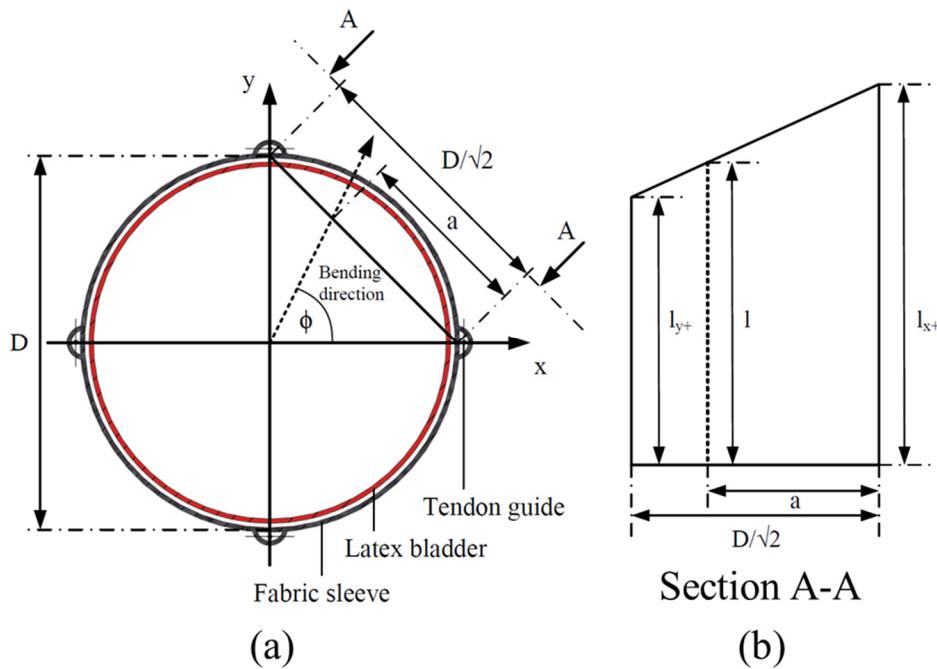
Figure 44 – Cross-section view (a) and section view A-A (b) along the central axis of the manipulator when bending in direction ϕ.

This model is used to implement a Cartesian control of the tip: as it is able to regulate tendon length and measure tendon displacement, the Inflatable Tentacle can be tele-operated. In Figure 43, the single-tendon-actuation bending case is presented; the bending direction angle ϕ in this case can only be either 0 or $\pi/2, \pi \ and \ 3\pi/2$ for the individual actuation of the four tendons. However, when actuating two adjacent tendons, any value for the bending angle ϕ can be achieved. As demonstrated in the cross-section of Figure 44 (a), each section of the manipulator is connected to four tendons, spaced at 90° around its central

axis where the bending direction is indicated. The length of each tendon can be determined by the geometry of the manipulator, and the displacement can be measured. The bending direction, characterized by the angle ϕ when two adjacent tendons are displaced, can be determined by considering the geometrical relationship shown in Figure 44 (b), where l_{y+} and l_{x+} are the displaced length of the tendons in correspondence with the positive semi-axis x^+ and y^+. In the case represented in Figure 44, l_{y+} is smaller than l_{x+}; therefore, the tendon in y^+ is more displaced than the tendon in x^+ and the bending direction is closer to the y^+ semi-axis. Due to the symmetrical arrangement of the tendons, the following description refers to bending angles within the interval $\phi = [0, \pi/2[$. Using trigonometry, ϕ can be calculated as a function of a and D (which are the geometric parameters displayed in Figure 44 [a]) as follows:

$$\phi = arctan\left(-\frac{1}{1 - \dfrac{D}{a\sqrt{2}}}\right) \qquad (20)$$

The input device used for the manipulation of the robot relies on position data along the x and y-axis, the corresponding component of which can be expressed by the bending angle ϕ; hence, a relation between the length of the tendons and the bending angle is established. When bending, the section view along the central axis of the manipulator can be approximated by a trapezium, as indicated in Figure 44 (b). Consequently, l can be calculated as the following:

$$l = max\left(l_{x+}, l_{y+}\right) - \frac{a\sqrt{2}\left|l_{x+} - l_{y+}\right|}{D} \qquad (21)$$

Implementing equations (20) and (21), it is possible to tele-operate each section of the manipulator in any desired direction. However, this approximation of the

manipulator's curvature holds only for single-section actuation using one or two adjacent tendons; for multi-section actuation, more advanced models are required. However, this kind of system modelling is not crucial to the investigation presented in this paper. The model described in this section has been used to implement a Cartesian control for the end effector of the manipulator in the actuation cases listed before. A model-free controller in the joint (section) space has been also implemented to test more complex actuation scenarios.

5.2.3 Actuation and Software Architecture

Figure 45 illustrates the setup of the overall system. The soft manipulator is mounted inside a phantom dome. The 12 tendons that are connected to the three sections are fed through Bowden cables before being wound around a pulley system with a 14-mm radius. Each pulley is fixed onto the shaft of a stepper motor (distributed by RobotShop [211], Soyo SY57ST56-0606B Unipolar Stepper Motor, see Appendix III for the data sheet). The motors are able to produce a holding torque of 0.6 Nm, with a resolution of 1.8°/step.
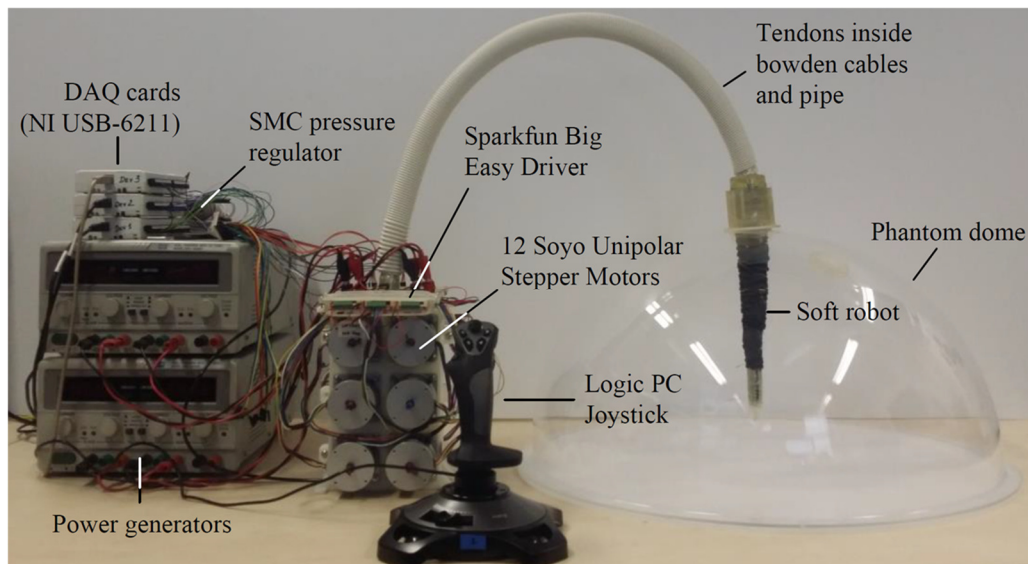
Figure 45 – Setup of the overall system: robotic manipulator inside a phantom dome, stepper motors pack, pressure regulator, stepper motors driver, joystick and NI DAQ cards.

This has been reduced to 1/10 of a step using micro-stepping control) and a precision of ±5%. By controlling the angular position of the pulley system, it is possible to vary the length of each tendon separately and, therefore, the bending of the manipulator. The stepper motors are connected to bi-polar micro-stepping drivers (Sparkfun Big Easy Driver ROB-11876, for datasheet see [260]). The inner latex bladder is connected to one pressure regulator (SMC Pneumatics [204], SMC ITV0010-3BS-Q, see Appendix II for the data sheet). The regulator is able to control the air pressure from 1 kPa to 100 kPa, and is capable of inflating and deflating the inner bladder of the robot. A built-in pressure sensor ensures that the desired pressure inside the bladder is maintained. An air compressor (BAMBI MD Range Model 150/500) ensures the supply, with sufficient pressure limited to the maximum pressure the regulators can cope with. The motor drivers and pressure regulator are interfaced via three DAQ cards (NI USB-6211) to LabVIEW software. A joystick (Logic 3 JS282 PC Joystick) is utilized as an input device for the operator in order to remotely control the position and configuration of the manipulator. The conceptual system architecture is presented in Figure 46. A human operator will send commands via a joystick (Logic 3 JS282 PC Joystick) and receive visual feedback.
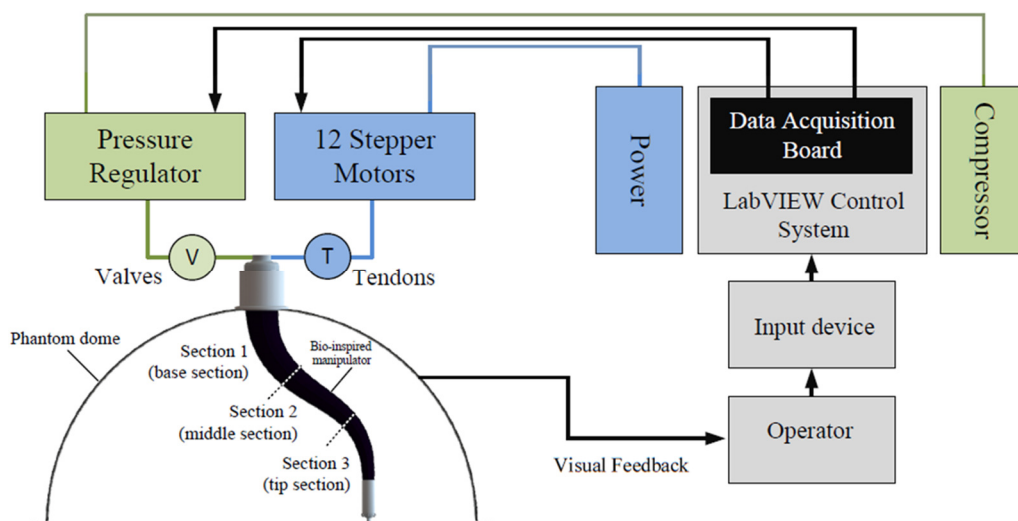
Figure 46 – Conceptual system architecture of the Inflatable Tentacle with three sections and a combination of tendon-driven and pneumatic actuation.

LabVIEW software has been used to create the control scheme that enables the key motion features envisioned for the Inflatable Tentacle; these features include bending, elongation, shrinking and stiffness adjustment. An open loop control strategy, based on the mathematical approximation presented in 5.2.2, is described here in order to achieve tendon and pressure actuation; this strategy also fuses both actuation principles to obtain the antagonistic behaviour that allows for control of the pose and the arm's stiffness. Based on the equations described in 5.2.2, tendon actuation is implemented. The length of the tendons is calculated by using the feedback obtained from the 12 stepper motors, with a radius of 14 mm for each pulley. As a result, each section of the manipulator can be independently bent in two directions and has two DOFs. An additional DOF is added when all tendons of a section are actuated at the same time, applying the same displacement, and the manipulator elongates or retracts. The pressure is constant during the tendon-actuated mode and adapts due to feedback from the built-in sensors of the pressure regulators. The internal pressure of the latex bladder can be increased or decreased in the range of the regulator. Current data from the pressure sensors can also be used for feedback; the same collision detection principle based on pressure feedback proposed in 3.4.3 can also be employed in this case. In any configuration of the manipulator's sections, the pressure can be changed. Therefore, the stiffness of the manipulator can be controlled analogously to the Inflatable Arm presented in the previous chapter. A preliminary investigation of the stiffness of this system has been presented in [258], uncovering results consistent with those obtained during the stiffness analysis of the Inflatable Arm.

5.2.4 Workspace Evaluation

Figure 47 illustrates the simulated workspace of the manipulator. The robot is placed upside down, consistent with the setup presented in Figure 41. Three different scenarios were simulated and compared with their experimental counterparts: 1) all sections were elongated and the proximal section actuated;

2) the proximal section was entirely deflated and the middle section actuated; 3) both the proximal and middle sections were entirely deflated and the distal section actuated. A discrete number of bending angles in each of the three cases were plotted. The results illustrate the volume of the workspace, which is limited by the outer hull of a semi-ellipsoid in all the three cases analysed. Any point belonging to the volume between the surface defined by the point cloud in cases 1 and 3 can be reached by the manipulator, thanks to the combination of pneumatic and tendon actuation.
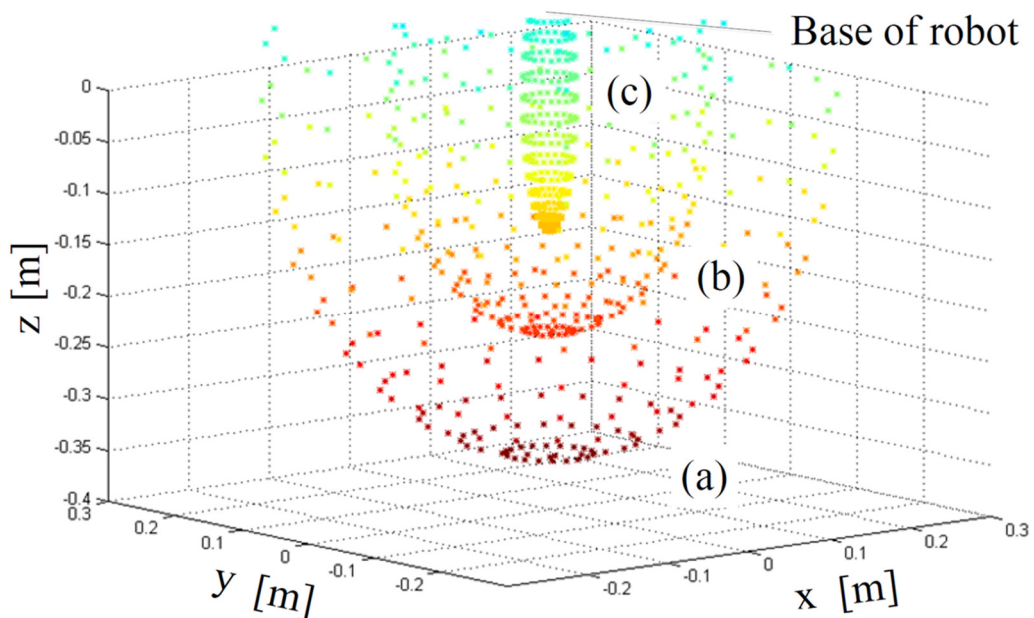
Figure 47 – Simulated workspace of the manipulator with (a) all sections elongated and section 1 actuated, (b) sections 2 and 3 elongated and section 2 actuated, and (c) section 3 elongated and actuated.

The data in these simulations demonstrate a significant degree of similarity to the data collected from analogous experiments. Nonetheless, as previously mentioned, this approach for modelling and open-loop control for the end effector in the Cartesian space is reliable only when a maximum of two adjacent tendons are actuated on a single section.

5.2.5 The Inflatable Tentacle in SLS Applications

Single-port laparoscopic surgery (SLS) is an alternative MIS approach to traditional invasive open surgery and multi-port laparoscopic surgery (MLS). In SLS, a single multi-channel trocar port (20 - 30 mm in diameter) is placed just above the navel as a unique access point to the abdominal cavity, as shown in Figure 48 (c).

Figure 48 – Abdominal surgery incisions for: (a) traditional open surgery, (b) Multi-port Laparoscopic Surgery (MLS) and (c) Single-port Laparoscopic Surgery (SLS) [267].

A comparison with the abdominal incisions in the MLS case (b) and the open surgery case (a) is also presented in Figure 48. To maximise the workspace when performing abdominal surgery, the abdomen of the patient is inflated using CO_2, with the pressure constantly controlled during the procedure. Consequently, a dedicated channel for pressure control is typically embedded in these systems. Customized flexible laparoscopic tools, as well as endoscopes or other probes (e.g., ultrasound probes), are all passed through the channels of the port. Generally, this approach has a minimal long-term cosmetic effect on the patient, as well as minimal internal scaring and port-site associated morbidity [261]. SLS has also a reduced risk of infection and blood loss due to vessel injury, as well as shorter hospitalization when compared both with open surgery and MLS. However, despite these numerous benefits on the patient side, these systems present several limitations on the user side. Due to the single point of entry, the smaller workspace, the reduced dexterity and the need for specialised articulated laparoscopic instruments, only highly trained surgeons can properly perform abdominal surgery using these single-port multi-channel systems, for which there is a long learning curve [262]. A number of single port systems have been

developed and commercialized thus far; certain examples are given in Figure 49. The use of a single point of access pairs with the use of flexible tools. Examples of customized instruments for the ports presented in Figure 49 are presented in Figure 50. The scenario for these systems, once the port is placed and the instruments inserted, is presented in Figure 51. The robotic approach can be particularly beneficial in SLS, making the learning curve steeper and the user experience more intuitive, as indicated by the recent trials with the last generation of SLS tools for the daVinci system; these tools, named the Single Site® tools, were presented in [263] and FDA-approved in 2016.

(a)   (b)   (c)   (d)   (e)

Figure 49 – Single-port multi-channel systems: the Uni-x [261] (Pnavel Systems, Morganville, New Jersey, USA), the X-Cone and the Endo-Cone [268] (Karl Storz, Tuttlingen, Germany, the SILS Port (Covidien, Norwalk, Connecticut, USA, subsidiary of Medtronic Inc, Minneapolis, Minnesota, USA) and the TriPort+ [305] (Advanced Surgical Concepts, Bray, Ireland).

(a)   (b)   (c)
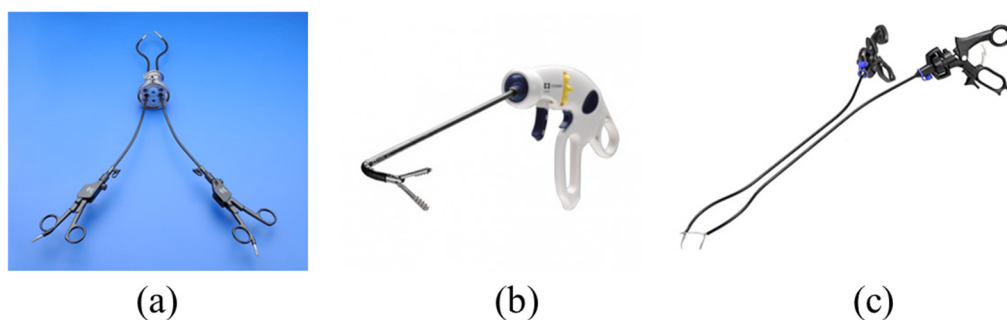
Figure 50 – Flexible laparoscopic tools for SLS: (a) the Cuschieri Coaxial Deviating Instruments for the Endo-Cone [268] (Karl Storz, Tuttlingen, Germany); (b) the SILS Hand Instrument for the SILS Port [306] (Covidien, Norwalk, Connecticut, USA, subsidiary of Medtronic Inc, Minneapolis, Minnesota, USA); (c) the HiQ LS [267] (Olympus Corporation, Shinjuku, Tokyo, Japan sole distributor of Advanced Surgical Concepts since 2011) for the TriPort+ [305] (Advanced Surgical Concepts, Bray, Ireland).
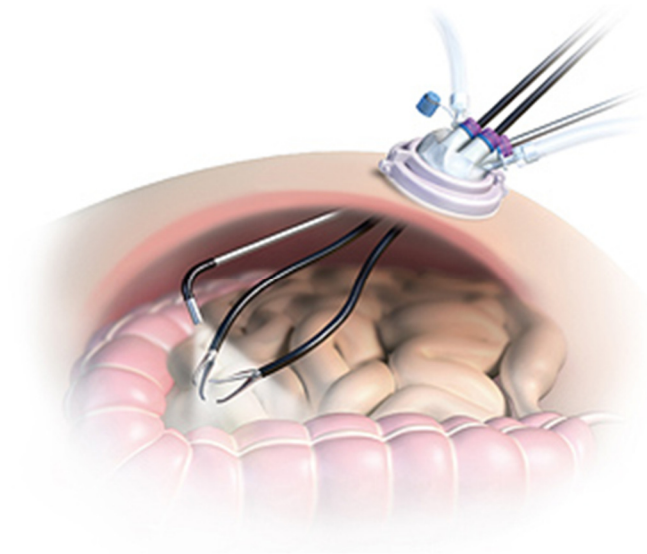
Figure 51 – Single-port Laparoscopic Surgery: two flexible laparoscopic tools and flexible endoscope inserted through a TriPort+ [267].

The Inflatable Tentacle has been conceived as an integrated robotic platform for the SLS scenario. In contrast to the single-port, multi-channel approach used in commercially-available SLS ports, the idea behind the design proposed here is to insert a single tentacle through a single trocar port placed in the proximity of the navel.
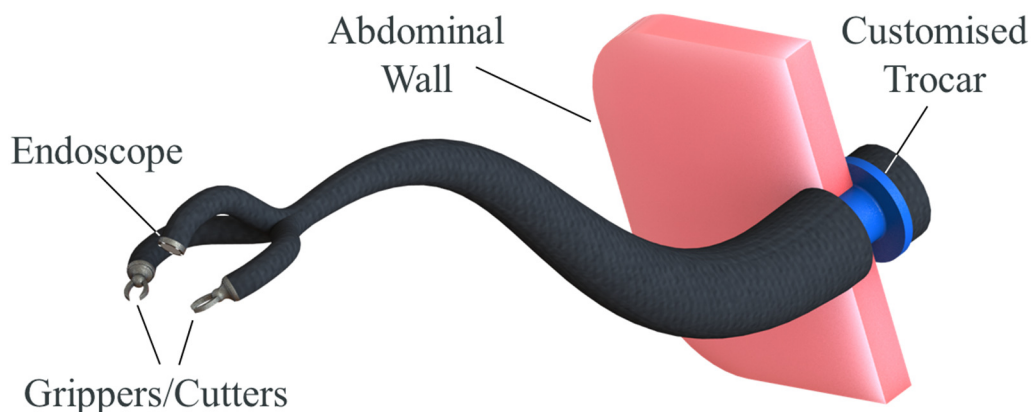
Figure 52 – Envisioned design of the multi-head Inflatable Tentacle for abdominal Single-site Laparoscopic Surgery.

The first two sections of the Inflatable Tentacle (proximal and middle) can be used to navigate the end effector in the proximity of the surgical area and adjust its orientation, while the distal section can be used for fine position adjustment during manipulation tasks. The proof-of-concept system presented in this section embeds only a single end effector; however, thanks to its customizable design, multiple distal sections can be potentially embedded on the middle section to enable double-gripper grasping and endoscopic imaging, as depicted in Figure 52. Thanks to its foldable design, the port diameter can be even smaller than that used in SLS; the system can be squeezed through a narrow opening and subsequently without affecting its functionality. Furthermore, once the system is inflated, the larger diameter of the areas of the base section inflated before and after the port stabilise the system, preventing undesired translation along its axis, as shown in Figure 52. Future work on this system will focus on the implementation and testing of this design, as well as the implementation of an intuitive user interface for navigation and grasping.

5.3 The Inflatable Endoscope

In this section the design of the Inflatable Endoscope, a design iteration of the Inflatable Arm, and its application in MIS applications and MLS in particular are described. The system described here has been firstly presented in – A. Stilli, H. A. Wurdemann, and K. Althoefer, "A Novel Flexible Endoscope for Minimally Invasive Surgery (1 page paper)," in *Annual International Conference of the IEEE Engineering in Medicine and Biology Society (EMBC)*, 2016 [264]. The work on this system has been also presented in similar form at the Hamlyn Symposium on Medical Robotics in 2016 (A. Stilli, A. Cremoni, H. A. Wurdemann, and K. Althoefer, "A new antagonistically actuated endoscope: Towards an inherently safe minimally invasive examination," in *Hamlyn Symposium on Medical Robotics*, 2016) [265] and at the annual Workshop on Computer/Robot Assisted Surgery (CRAS) [266] in 2016 (A. Stilli, H. A. Wurdemann, and K. Althoefer, "A Novel Inflatable and Flexible Endoscope for

Inherently Safe Minimally Invasive Examination," in *Workshop on Computer/Robot Assisted Surgery (CRAS)*, 2016).

5.3.1 Design and Methodology

A number of implementations of the Inflatable Arm as a flexible laparoscopic tool to be used in the MLS scenario were considered: a camera embedded to create an endoscope; a tendon-driven forceps mechanism to create a gripper or a cutter; a pipe to create an aspirator/irrigator; or an electrode to create an ablation tool, as indicated in Figure 53. For the proof of concept system presented in this section, a commercially available inexpensive USB camera was chosen to create the inherently safe, soft, hand-held, laparoscopic system known as the Inflatable Endoscope. As with the case of the Inflatable Arm, the Inflatable Endoscope is able to vary its structural stiffness level, allowing it to have a high pliability during insertion and investigation procedures and a firm pose when a stable camera image at the site of interest is needed. In contrast to the case of the Inflatable Tentacle, for the Inflatable Endoscope the author focuses on the design of a manually-operated system, as found in traditional laparoscopic tools used in standard surgical procedures, rather than on robotic-assisted procedures. For this reason, a single-section system is considered here rather than a multi-section one.

Figure 53 – Possible implementation of the Inflatable Arm as flexible laparoscopic tool: (a) endoscope, (b) gripper or cutter, (c) aspirator/irrigator, (d) RF ablation tool.
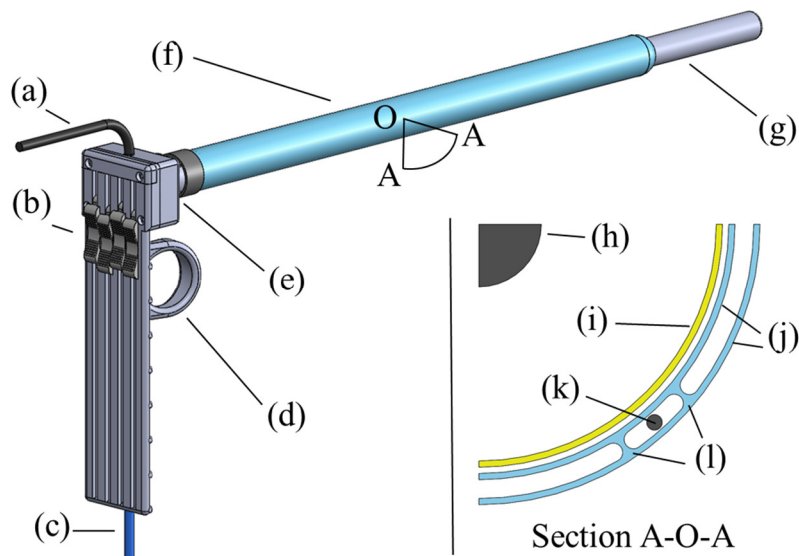
Figure 54 – CAD drawing of the assembly of the Inflatable Endoscope with partial radial section view A-O-A: (a) USB camera cable, (b) manual tendon sliders, (c) pressure line (I/O), (d) ergonomic handle, (e) base connector, (f) fabric polyester sleeve, (g) camera housing, (h) USB camera cable section, (i) latex bladder, (j) fabric layers, (k) nylon tendon and (l) sewing lines.

The design of the Inflatable Endoscope is presented in Figure 54. The device is composed of five main elements:

1. A customized sleeve (f), machine-sewn in the shape of a cylinder with a length of 250 mm and a diameter of 18 mm, composed of two layers (j) of polyester fabric;

2. An air-tight bladder (i) made of flexible material (latex), fitted inside the sleeve and pressurised through a 4-mm diameter pressure line (c);

3. Four nylon tendons (k), spaced 90° apart along the perimeter of the sleeve and attached on one side to the base of the housing structure of the camera (g) and on the other side with four individual sliders (b). The tendons have been embedded between the two layers of the fabric (j) that compose the outer sleeve;

4. A commercially available endoscopic USB camera (a) with a diameter of 8.5 mm and a length of 45 mm (Flylinktech® USB Endoscope);

5. A 3D printed ergonomic handle (d) to hold the endoscope, with a system of four tendon sliders (b) to be actuated using the thumb.

On one end, four individual tendons are attached at the scope's tip where the camera is housed (g) and guided through narrow sheaths inside the fabric wall (f) along the length of the endoscope to its base (e). On the other end, the tendons are connected to four sliders (b), respectively. This actuation provides steering capability to the system, allowing the user to exert a longitudinal pulling force on each tendon. Moving one slider downwards pulls one tendon and bends the inflated structure towards the tendon being pulled. Two adjacent sliders can be pulled, allowing the structure to bend in all directions away from the longitudinal axis. When all tendons are pulled simultaneously, the length of the manipulator can be adjusted. By changing the pressure inside the bladder, the stiffness of the endoscope can be tuned. Among all the systems developed in relation to the Inflatable Arm, the scope presented here has the highest miniaturization level: the housing structure (g) of the camera has a diameter at the tip of 11.8 mm, making it suitable to be inserted through a standard 12-mm trocar port, which is typically used in MLS abdominal procedures. Significant investigation has been dedicated to the fabrication process; to maximize robustness, the distal tips of the tendons have been directly sewn between the two layers of fabric that compose the outer sleeve, as well as to the rigid support of the camera embedded with four eyelets in correspondence to each tendon. To guarantee the air-tightness of the chamber, a combination of silicone glue and heat-shrink pipes has been employed in the base Figure 54 (e). The lightweight design of this system allows straightening against gravity with very low air pressure; to horizontally withstand the weight of the camera, 20 kPa (20% of the highest pressure tested) is sufficient to deploy the endoscope. A visual side-by-side comparison between the prototype of the Inflatable Endoscope and a commercially-available rigid endoscope (ENDOCAM System – Richard Wolf GMBH, Knittlingen, Germany) is presented in Figure 55. The two instruments have a similar length; however, the dexterity of the Inflatable Endoscope provides a significantly larger workspace in comparison with its rigid counterpart.
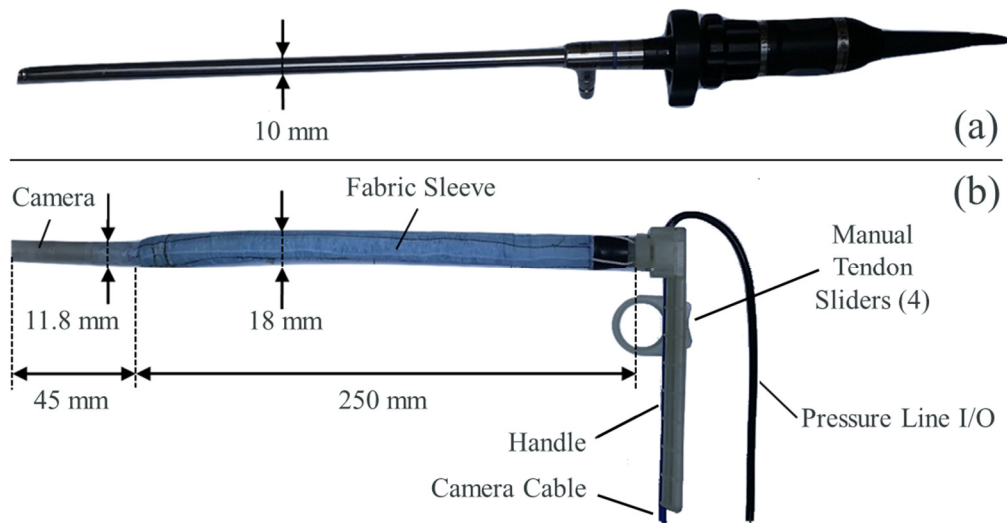
Figure 55 – Size comparison between a state-of-the-art endoscope – ENDOCAM System by Richard Wolf GMBH (Knittlingen, Germany) and the Inflatable Endoscope.

Furthermore, its larger diameter (18 mm rather than 10 mm) notwithstanding, the Inflatable Endoscope can be easily squeezed through a trocar port of a smaller diameter when no or low pressure is applied, and, following insertion, can be pressurised with a higher pressure in order to navigate without its functionalities being altered. The camera cable and the pressure line cannot be compressed beyond their nominal diameter, however, even when paired, their size does not exceed 7 mm, hence, they are not affected by the trocar port restriction. This newly-proposed endoscope is designed to outperform traditional rigid and flexible endoscopes, through the following characteristics:

- A lightweight design: being made of fabric and latex membranes and a few rigid plastic components, the prototype weighs 25 g without the handle, and 85 g with the handle, improving usability and ergonomics on the user side, in comparison with traditional rigid laparoscopes typically weighting between 200 g and 400 g depending on the optics [267], [268];
- Dexterous actuation maximizing the workspace of the manipulator and, consequently, the field of view of the user;

- Inexpensive design, since the proposed system is composed of commercially-available, low-cost components and small 3D-printed parts;

- The use of soft materials, making the proposed system inherently safe when it comes to physical interaction with soft tissues inside the human body.

5.3.2 Mathematical Model and Workspace Analysis

The Inflatable Endoscope proposed in this section is composed of a single air chamber and a set of four tendons, which are connected to the base of the camera integrated into the tip of the endoscope. The performance comparison between the Inflatable Arm presented in Section 4.3 (two sections, three tendons per section) and the Inflatable Tentacle presented in Section 5.2 (three sections, four tendons per section) suggested the choice of a four-tendon system for this hand-actuated device. Since the four tendons are arranged in the periphery of the central axis of the manipulator with a radial displacement of 90°, the movements of the end effector, i.e., the camera, are decoupled along the axis of the Cartesian space allowing intuitive manoeuvring. Alternatively, the use of coupled mechanical mechanisms in the handle could be also considered, rendering the choice of a four-tendon over a three-tendon system irrelevant. However, the focus of this work is on the system and its intrinsic dexterity, rather than on its actuation; hence, a decoupled solution has been preferred. As with the case of the Inflatable Tentacle, the behaviour of the Inflatable Endoscope has been investigated in the context of the envisioned application, i.e., MLS. Therefore, the Inflatable Endoscope has been also tested when passed through a trocar port, to understand how interaction with the port affects the workspace. Figure 56 illustrates a number of experimental results when the endoscope is passed through a standard trocar port and actuated by pulling one tendon (achieving a planar bending motion).
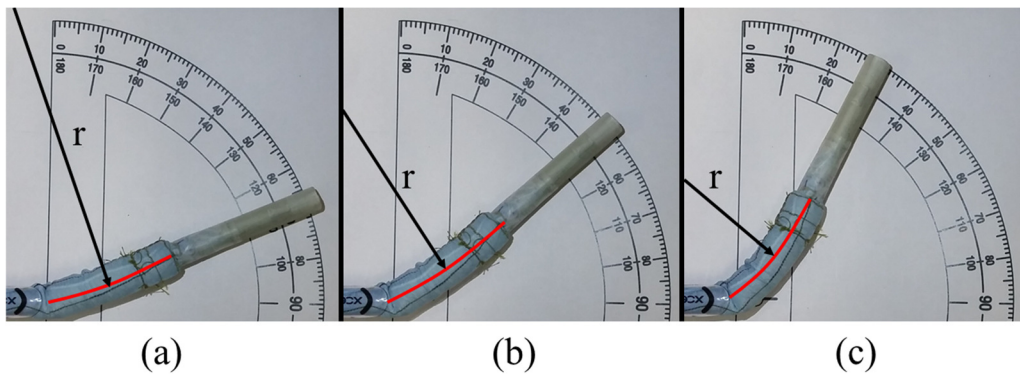
Figure 56 – Bending behaviour of the flexible endoscope in one plane actuated by a single tendon after the insertion through a trocar port of 12 mm diameter.

The red arcs and black vectors demonstrate that the constant curvature approximation considered in 5.2.2 also holds true for this system. The curvature radius is inversely proportional to the displacement of the tendon causing the deformation; the more the tendon is pulled, the smaller the curvature radius of the circumference that better fits the curvature of the longitudinal axis of the manipulator body. This model-based approach is even more robust in this case due to the use of a single-section actuation. It is important to note that in this scenario, when the scope is passed through the trocar port, the bending radius is not only a function of the tendon(s) displacement, but also of the length of the portion of the manipulator that protrudes from the end of the port, making the portion inside and before the port non-influential. Both these parameters can potentially be calculated based on encoder measurements in a robotic-operated version of the proposed device, given the trocar port length. A human operator instead makes use of visual and tactile feedback to control this system. Different bending angles are illustrated in Figure 57: these sequences of body poses were achieved by pulling a single tendon successively in two opposing directions at 20 kPa. In order to measure the workspace of the endoscope, a magnetic tracking system has been employed to track the position of the endoscope tip during single- and double-tendon actuation.
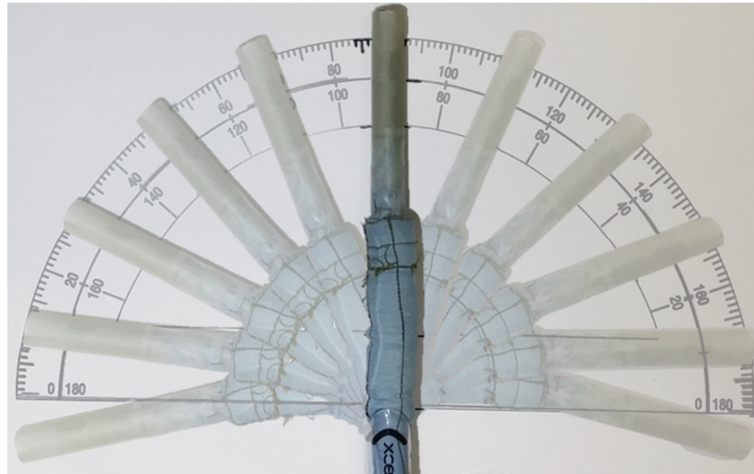
Figure 57 – Range of motion of the Inflatable Endoscope inserted through a 12 mm Ø trocar port in one plane actuating sequentially a pair of diametrically opposed tendons.

Figure 58 shows the experimental setup used to conduct these experiments; an Aurora Electromagnetic Tracking System (Northern Digital Inc., Waterloo, Ontario, Canada [213]) was used to detect a magnetic tracker embedded in the tip of the endoscope, i.e., in its most distal part, where the camera lens is located.
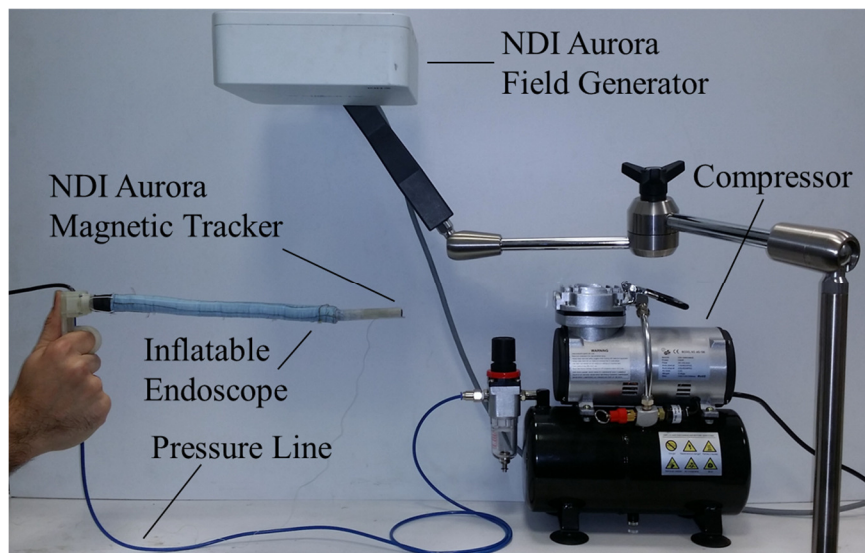
Figure 58 – Experimental setup for the workspace evaluation of the inflatable endoscope using a magnetic field generator and a magnetic tracker. The pressure source is a compressor AS186K.
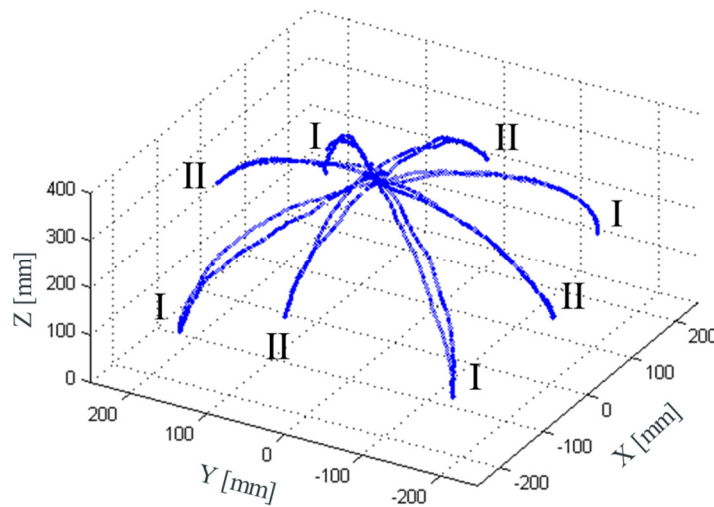
Figure 59 – Workspace of the flexible endoscope. Single (I) and double (II) tendon actuation for the four tendons. Data collected using an Aurora Electromagnetic Tracking System (Northern Digital Inc., Waterloo, Ontario, Canada). A single magnetic tracker is embedded next to the camera lens.

The collected data are displayed in the 3D graph of Figure 59. The pressure level was kept constant at 0.2 bar for the whole duration of the experiment. The Roman numbers indicate when single-tendon actuation (I) was applied and when two tendons spaced 90° apart (II) were actuated. Though a robotic-assisted actuation could improve the accuracy of the control, the manual actuation realized by means of the sliders provided promising results in terms of quality and intuitiveness of the position control of the end effector. The two sets of trajectories belong to the outer hull of two ellipsoids. The experimental results reveal a significantly wider workspace in comparison with the one of a rigid endoscope of the same length, making it unnecessary for the clinician to rotate the whole body of the scope, pivoting around the point of entrance of the trocar port, to adjust the point of view, resulting in a better user experience. The endoscope exhibits a fairly predictable and repeatable behaviour.

5.3.3 The Inflatable Endoscope in MLS Applications

The Inflatable Endoscope has been developed to investigate the applicability of the Inflatable Arm in the MLS scenario. The typical incisions made in order to access the abdominal cavity using this approach are illustrated in Figure 48 (b).
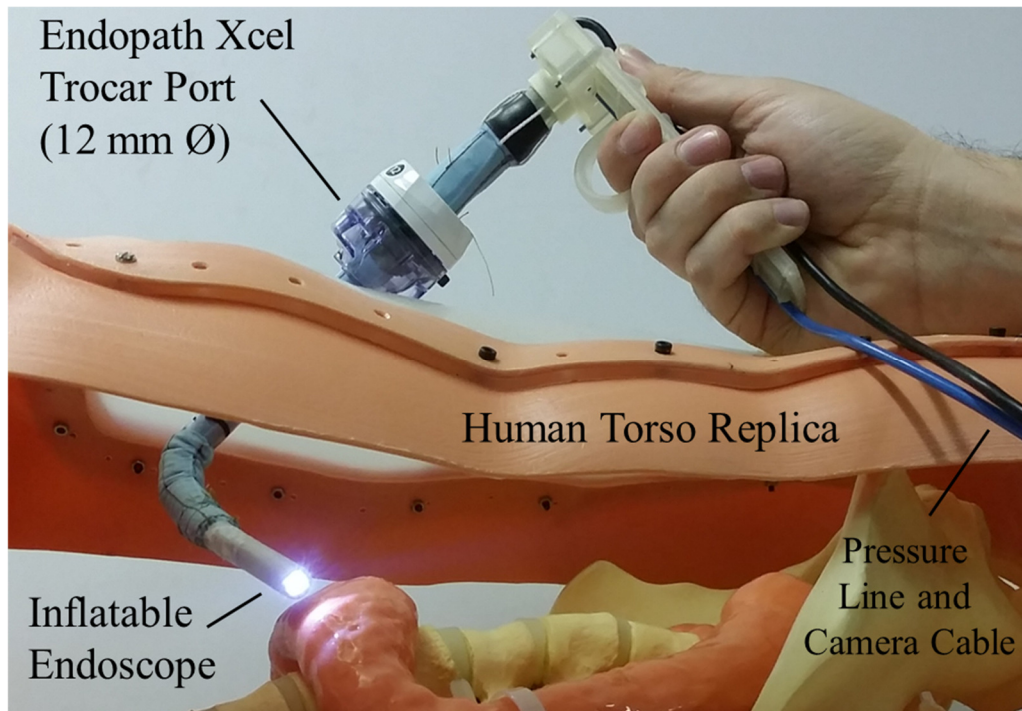
Figure 60 – The inflatable endoscope accessing the abdominal cavity of a human torso replica through a standard trocar port (Endopath Xcel, 12 mm Ø) bent by 90° after insertion, pressurised at 30 kPa.

To properly test the developed system, a 1:1 scale human torso replica has been used, as indicated in Figure 60. The replica presents a replaceable hard rubber translucent 3-mm layer on the chest side; a 15-mm longitudinal incision has been made to place a 12-mm standard trocar port, the Endopath Xcel® (Ethicon, Sommerville, New Jersey, USA, subsidiary of Johnson & Johnson, New Brunswick, New Jersey, USA). The Inflatable Endoscope is inserted through the trocar port, pressurised at 30 kPa and steered by 90° after the insertion. This setup has been used to perform extensive testing to assess the dexterity of the proposed system in a realistic scenario. Different insertion lengths and pressures were tested to evaluate the system behaviour. These qualitative tests showed

promising results, demonstrating ease of use and fast adjustment of the field of view of the camera with minimal movement of the handle, even for non-clinician.

5.4 Summary

In this chapter, the author proposed two design iterations of the Inflatable Arm, the bio-inspired system presented in Chapter 4: The Inflatable Tentacle and the Inflatable Endoscope. The envisioned application of the former system is single-port laparoscopic surgery, while the envisioned application of the latter is multi-port laparoscopic surgery. The design and fabrication of these systems have been detailed. The conducted testing demonstrated how the features of the Inflatable Arm, such as stiffness controllability, body poses redundancy, ample internal routing space, shrinkability, steerability and high dexterity, can be particularly beneficial for MIS applications, both in traditional and robotic-assisted scenarios. Tests have been performed simulating the envisioned workspace of these systems, i.e., the human abdomen, to assess their performance, producing highly encouraging results for both the Inflatable Tentacle and the Inflatable Endoscope. The use of fabric and latex as the main structural elements, rather than metal, makes the proposed systems inexpensive and therefore easily disposable, both of which are desirable features for the proposed applications in the area of surgery. The author has explored how the use of a double fabric layer to create tendon channels by the means of two parallel machine-sewn seam lines as well as machine-sewn tendon fixtures facilitate the industrialisation of the production process. The future work related to the two systems presented in this chapter is discussed in Chapter 7. A video demonstrating the navigation capabilities of the Inflatable Arm when inserted through a trocar port in the same human torso replica illustrated in Figure 60 is available for download and streaming at the following link: https://youtu.be/4fA_Ljpzhc4. The video also provides an overview of the overall system.

Chapter 6

6 The AirExGlove for Adaptive Hand Rehabilitation

This chapter is the second of the two chapters dedicated to the applications of the bio-inspired antagonistic system presented in Chapter 4. Here the author introduces a light-weight, inflatable soft exoskeleton for hand rehabilitation called the AirExGlove, which is based on the actuation principle of the Inflatable Arm. The application focus for this system is on patients affected by a pathology called clenched fist deformity, typical for post-stroke patients. This chapter focuses on the design and testing of the AirExGlove. Experts in the field of rehabilitation from a partner institution, the Rehabilitation Centre IRCCS "Don Carlo Gnocchi", part of the Don Carlo Gnocchi Foundation (Via di Scandicci 269, 50143, Florence, Italy), have assisted the author in the clinical assessment of the proposed system, also involving a patient affected by clenched fist deformity to perform preliminary testing.

6.1 Introduction

Despite the advancements in modern medicine, stroke is still one of the leading causes of disability worldwide [269]. The hospitalization, rehabilitation and long-term care of post-stroke patients account for a considerable amount of human and financial resources that are usually born by the healthcare system, affecting transversely high [270], [271], middle and low income countries [272]. People who survive a stroke are often left with long-term problems due to motion disabilities in the upper and lower limbs. A number of robotic assistive devices have been developed for rehabilitation therapies in the past decades [273], [274]. Both exoskeletons and end-effector devices can provide additional support during physiotherapy [275]. The effectiveness of robotic-assisted therapy has shown significant impact in a number of studies [276], [277]; in particular, these systems have outperformed standard rehabilitation routines in case of upper limb extremities [278], resulting in the growing development of hand rehabilitation devices in the past years. Focussing on hand rehabilitation, a number of rigid linkage systems have been proposed: e.g., the fixed platform proposed by Ito et al. [279] for fine motion assistance of the fingers and the wrist, or the HEXORR robotic platform for full hand range of motion [280]. More portable solutions have been explored as well, such as the HANDEXOS multi-phalanges device [281], the HandSOME spring operated exoskeleton [282] and a low-cost adaptable system presented in [283]. These systems have been widely used for hand exoskeletons with embedded pneumatic-, hydraulic- or tendon-driven actuation to impose trajectories to the fingers [284]. The rigidity of the links allows high power to be transmitted from the actuators to the fingers, following accurately-predefined trajectories. The encumbrance on the back of the hand and on the side of the fingers, as well as the size of the actuation system, however, limit portability and usability in everyday life tasks. For instance, the systems presented in [285] utilise a three-section linkage and gear system with a section height on the back side of the finger equal to two times the diameter of the corresponding phalanx. The solution presented in [286] has similar drawbacks.

The use of Bowden cables in tendon-driven systems to move the weight of the actuation system away from the hand has been also explored in [287]; the use of Bowden cable-based series elastic actuators to provide accurate torque control of the hand digits has also been investigated [288]. However, even though the weight of the actuation is significantly reduced on the hand side in this design, these systems have the same encumbrance issues of the rigid-linked systems described previously. The ergonomics of hand exoskeletons have been significantly improved by the emerging field of soft robotics: a number of systems have been developed using soft materials such as elastomers [274] (see also Figure 61 (c), [275] and fabric [106], [291] (see also Figure 62 (b)), making use of pneumatic and tendon actuation, respectively. The use of Bowden cables has also been explored for soft systems [292]. However, the majority of systems based on elastomers provide only a single direction actuation; the systems presented in [275] (see also Figure 61 (a), [278], for example, can only assist when closing but not when opening the hand. In this case, intermediate positions can be only achieved through a challenging interplay between a certain pressure value and the opposing muscle activity of the fingers. These exoskeletons inspired by soft materials are usually pneumatically actuated, with the actuation system mounted on the back of the hand; if mounted on the palm instead, the system would pose an obstacle to most manipulation tasks.

(a)   (b)   (c)

Figure 61 – Elastomer-based soft exoskeleton systems for the hand: (a) the system developed by the research team from Harvard (Cambridge, MA, USA) based on PneuNets [290], (b) a development of the same system reinforced with fabric sleeves [34], (c) the MRC-Glove, an MRI compatible solution developed by the research team from the National University of Singapore (Singapore) [289].

Figure 62 – Fabric-based soft exoskeleton systems for the hand: (a) a fluidically actuated system using flexible plastic actuators embedded in fabric pouches developed by the research team from the National University of Singapore (Singapore) [295]*; (b) the palm and the back side of the tendon-driven system developed by the research team from the Worcester Polytechnic Institute (Worcester, MA, USA)* [291]*.*

On the other hand, systems based on fabric structures using tendon actuation such as those presented in [106], [291], [294] can support both the closing and opening of the hand. In these fabric-based systems the tendons can easily be guided along both sides of the hand, thanks to their low diameter. To help post-stroke patients suffering from the clenched fist deformity with their hand-opening rehabilitation tasks, an alternative solution based on a fabric structure and a plastic actuator has been proposed in [14], [295] (see also Figure 62 (a)). However, similar to the hand-closing pneumatic actuators presented in [290], achieving intermediate stable finger positions poses a challenge.

In this chapter, the author introduces the AirExGlove – an innovative Air-actuated Exoskeleton Glove. The proposed system shares design features, such as tendon-actuation on the palm side and pressure actuation using pneumatic chambers with its predecessors. Some examples are shown in shown in Figure 62: (a) a fluidically actuated system using flexible plastic actuators embedded in fabric pouches on the dorsal side of the hand developed by the research team from the National University of Singapore (Singapore) [295] and (b) a soft robotic tendon-actuated exomusculature from the research team from Worcester Polytechnic Institute (MA, USA) [291]. Building on previous work in the field as well as on the research outcome of companies developing assistive systems in the field, such as the SEM™ Glove (Bioservo Technologies AB,

Kista, Sweden) [296] the author aimed at finding the best tendon configuration to maximize the ergonomics and the portability of the system. The proposed system makes use of the bio-inspired antagonistic actuation principle of the Inflatable Arm to control the stiffness of a system over a wide range. This hybrid solution combines the benefits of both pneumatic and tendon-driven actuation and is applied here in the exoskeletal system to deliver gradual rehabilitation therapy to patients with hand-opening disabilities, such as clenched fist in post-stroke patients; pneumatic actuators are located on the back of the hand to assist the user during hand-opening tasks. Tendons are guided along the palm of the device and can be used to limit the opening to the desired level. This antagonistic actuation allows for the achievement of infinite intermediate stable configurations between a fully open and closed hand, thus facilitating the delivery of a patient-specific rehabilitation therapy.

This chapter is organized as follows: the working principle and the design of the AirExGlove are described in Section 6.2, where the fabrication method as well as the control system are also presented. The experimental setup and the results of the investigation related to mechanical characterization and a thorough clinical assessment are presented in Section 6.3. The experimental results related to the finger trajectories with different tendon tensions are presented in Section 6.4. In Section 6.5, the results of a preliminary clinical study with a single patient are presented. Section 6.6 summarises the work presented in this chapter.

Throughout all the experiments conducted in the research detailed in this chapter, with the exception of the tests presented in Section 6.5, all the exoskeleton systems developed were solely worn by a healthy subject (female, 25, 171 mm wrist-to-index-finger-tip length, 75 mm palm width, hand S size). The first publication related to the AirExGlove has been accepted for publication in the 2018 IEEE-RAS International Conference on (RoboSoft), the first monothematic conference from IEEE dedicate to Soft Robotics and it will be

presented as: A. Stilli, A. Cremoni, M. Bianchi, A. Ridolfi, F. Gerli, F. Vannetti, H.A. Wurdemann, B. Allotta and K. Althoefer. "AirExGlove - A Novel Pneumatic Exoskeleton Glove for Adaptive Hand Rehabilitation in Post-Stroke Patients".

6.2 Design and Methodology

The AirExGlove final design is the result of an investigation intended to optimize patient comfort and the ergonomics of the system. A number of design iterations have been developed in the context of this research, and the most relevant ones are reported in this section. In the design process, the author intended the AirExGlove to include the following characteristics:

- To deliver gradual rehabilitation therapy to patients affected by hand-opening disabilities.
- To be portable and lightweight, using fabric material for the majority of the exoskeleton structure.
- To be unobtrusive, particularly on the palm side in order to provide natural grasping.
- To be scalable, thanks to the use of a fabric-based system that allows for the size of the glove to be easily adjusted to fit any hand size.

The AirExGlove, as with the Inflatable Arm from which it takes the antagonistic actuation, has been conceived to be intrinsically and extrinsically actuated: the pneumatic actuation system is mounted on the back of the hand (intrinsic) to enable assisted hand-opening, while the tendon-driven system is located inside the hand palm (extrinsic) to enable assisted hand-closure and to mechanically limit the hand-opening when a partial opening is requested. The straightening effect, previously highlighted in Section 4.3.1 and generated by the pneumatic actuation, is used to extend the fingers. The idea is to align the phalanxes of the fingers with the dorsal side of the hand; therefore, the pneumatic actuators need

to run through the full length of the fingers and also extend far enough on the dorsal side of the hand to provide the needed torque. The users targeted in this investigation are patients affected by clenched fist deformity, a pathology typical of post-stroke patients, where the subject is able to close the hand but not to open it. For this reason, even though the possibility of delivering assisted hand-closure has been considered and a dedicated mechanism has been embedded in the presented system, the focus of this research is on design optimization for assisted hand-opening.

6.2.1 Single-chamber solution

At the beginning of the investigation related to the design of the pneumatic actuators to be embedded on the dorsal side of the system, a single-chamber solution for each finger was proposed, similar to the work presented in [295]. This work was developed in the context of the system presented in this thesis. To initially test the proposed design, a commercially-available sport glove was used as a base for embedding the single-chamber actuators, with an external fabric layer of Nylon PU (55 g/m², [297]) and a commercially-available latex balloon added to the design. A professional sewing machine (PFAFF Creative 3.0, [298]) was used to create all the systems presented in this chapter. The first prototype of the proposed system is presented in Figure 63 (c), where a single-chamber is embedded on the back of the thumb. The thumb was selected to perform the initial worst-case-scenario testing, as it is the strongest among the five digits of the human hand in terms of closure force. If a pneumatic actuator covering the entire length of the thumb is able to extend it, an actuator of the same section covering the length of any of the four fingers would be able to produce an equal or greater level of extension. Because the lengths of both the thumb and the pneumatic chamber are limited, both by the thumb length and the hand-back size, the only geometric parameter that can be changed to modify the exerted straightening torque is the section area of the chamber.
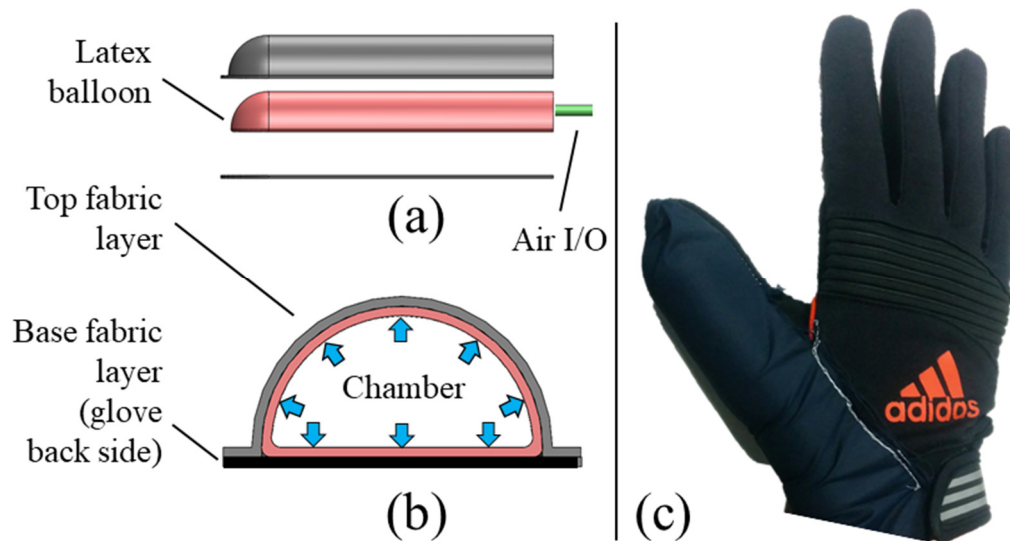
Figure 63 – Single-chamber solution: CAD drawings of the thumb pneumatic actuator (a) in exploded view and (b) section view with the azure arrows showing the force distribution due to the pressurized air; single-chamber prototype assembled using a commercially available glove.

This modification is performed under the assumption that the chamber length is already maximised, by using all the space available on the back of the hand. Pressure can also be increased; however, the pressure range used should be also considered in relation to the intended application: with a fixed rehabilitation platform, high pressure can be provided, while with a portable rehabilitation platform, low pressure is preferable. The system in Figure 63 (c), makes use of a commercially-available glove, female size S. Preliminary results on this system indicate that full thumb extension can be achieved at 100 kPa. However, though the device fulfilled the requirements in terms of exertable forces, the subject experienced a significant compression force on the dorsal side of the thumb, resulting in discomfort and blood flow reduction after few minutes of use. This is largely due to a design issue shared by the system presented in [295]; as shown in the section view in Figure 63 (b), the wall of the chamber base consists of the back-side of the glove. When a deformable chamber with a non-circular section is pressurised, due to the hydrostatic force distribution of the air, it tends to deform to reach equilibrium. As a result, once the chamber is inflated, it tends to change its shape from the semi-cylindrical shape illustrated in Figure 63 (a) to a

cylindrical one. This change results in a force distribution on the base wall that generates a compression force on the thumb. This design solution, even though it maximises the space available on the back of the hand, creates a significant discomfort for the user and results in a significant encumbrance on the back of the hand once pressurized air is supplied to the actuators. In order to solve this issue, a different solution has been implemented and is presented in the next sub-section.

6.2.2 Multi-chamber solution

To overcome the compression issue and design limitations of a single-chamber solution, a multi-chamber, fully-external solution has been explored, as demonstrated in Figure 64. While in the previous design one wall of the chamber was shared with the back-side of the glove, in this new design all the chambers are completely external and share only a seam line with the back of the glove, as illustrated in the cross-section view in Figure 64 (a). Furthermore, this design offers ease of customization; the diameter of the chambers can be adjusted according to the desired force output for a given pressure level.
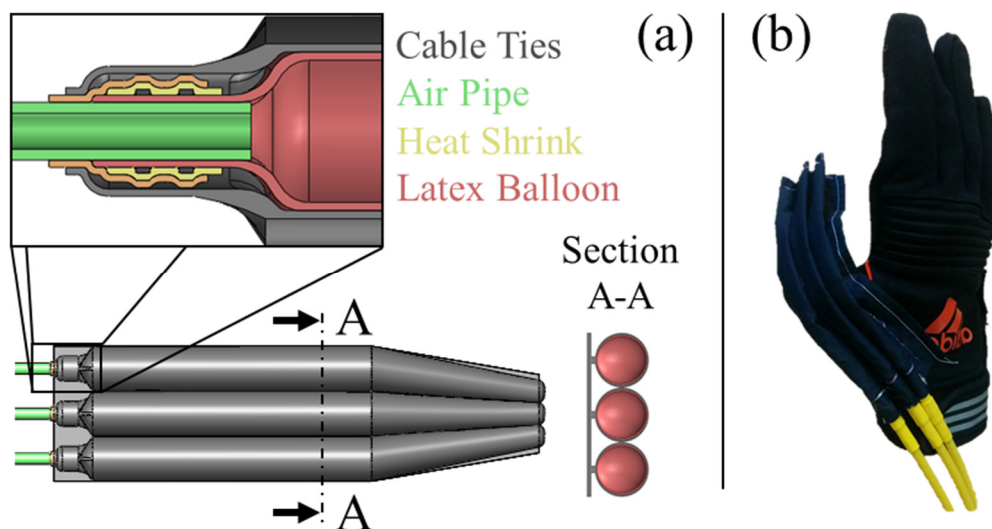
Figure 64 – Multi-chamber solution: (a) CAD drawings of the thumb pneumatic actuator with three chambers, including a longitudinal section view in correspondence of the air I/O showing the components used to seal the chambers and a cross section view showing the three chambers inflated without compressing the back of the thumb; (b) the actuator prototype assembled on the glove.

The number of chambers can be also adjusted in order to find the best balance between dorsal encumbrance, chamber diameter, exertable force and pressure used. A single-chamber external solution could have been considered as well to solve the discomfort problem; however, the encumbrance on the back of the hand would have been significantly larger. As the new design requires smaller chambers, a different type of commercially-available latex balloon has been used, with a circular (8-mm diameter) non-inflated cross section and a length of 300 mm. The connection between the balloon and the 4-mm plastic pipe used as air input/output has been sealed using a combination of cable ties, heat-shrink tube and super-glue, all inexpensive, commercially-available components. A detail of the longitudinal section of the sealed connection is displayed in Figure 64 (a). Heat-shrink tubes have many desirable properties when it comes to sealing, including the ability to conform around irregular shapes and rapid installation. The sealing was tested without leakages up to 350 kPa. The inflated diameter of the chamber, i.e., the dorsal encumbrance of the pneumatic actuation, is 13.5 mm for the presented system. In order to test the performance of the multi-chamber design, the pneumatic actuator has been sewn on the glove and pressurised while worn, providing a full thumb extension for 190 kPa, therefore also satisfying for the fingers. During preliminary tests on this system, it has been noted that a sudden pressure decrease can lead to the balloon displacing inside the chamber. In the absence of a constraining element, the balloon is free to move, twist and rotate inside the fabric sleeve. Since this significantly affects the reliability of the system and enhances the probability of the balloon intertwining and therefore breaking, a solution to solve this problem is required. A shape coupling in the distal section of the actuators has been implemented; an 8-mm diameter plastic sphere has been inserted in each balloon and moved to the distal end. A seam line perpendicular to the longitudinal axis of the chamber has been added to reduce its cross section, trapping the sphere in the distal end and providing the required constraint to prevent the displacement of the latex balloon inside the fabric chamber.
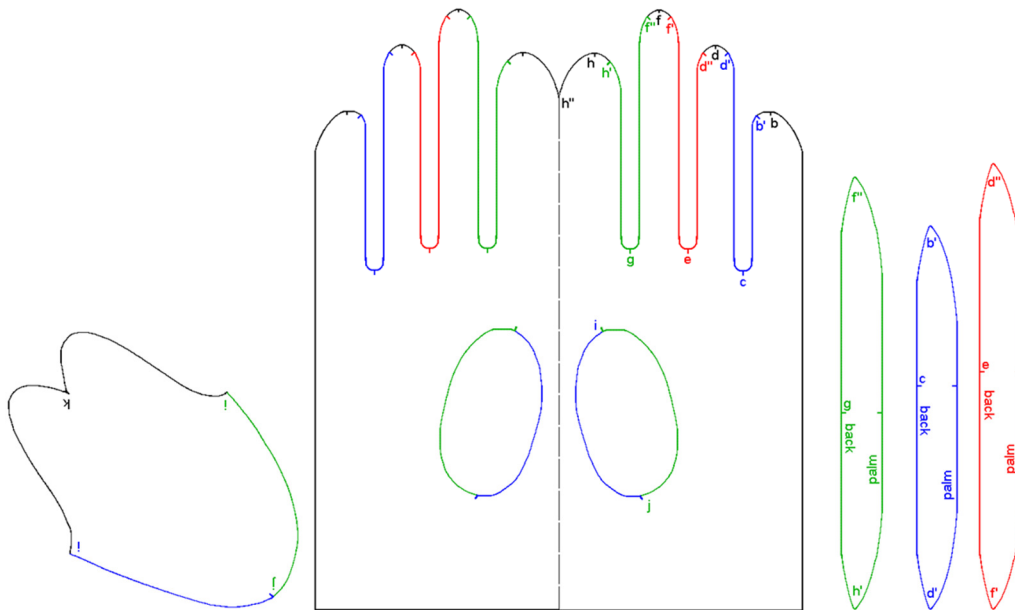
Figure 65 – Sewing template for glove, size S, female, right hand, used to create the main structure of the AirExGlove.

To improve the usability of the glove while interacting with the environment, particularly during in-hand manipulation tasks, the encumbrance of the pneumatic actuators has been reduced in proximity to the tips of the fingers and thumb, where the contact with objects takes place. Therefore, the initial cylindrical structure has been modified into a truncated cone and a cylinder, as indicated in the top view in Figure 64, by folding the fabric at the end of each chamber and fixing the shape with an additional seam line. The chambers have been also joined together at their distal extremities using an extra seam line in order to further reduce the overall encumbrance.

6.2.3 The AirExGlove Integrated System

The multi-chamber solution was implemented in the final design of the AirExGlove. In contrast to the prototypes presented in the previous sections, where a commercially-available glove has been used as the base in which to embed the actuators, in this design a customized glove was created using the female hand size S template shown in Figure 65 as the base structure of the

proposed system. This customization also allowed to use the same material for all the fabric elements of the glove. A double layer of fabric has been used on the palm side, allowing the routing of the tendons to be guided along two parallel seam lines for each tendon channel, similar to the procedure used in 5.2.1. Figure 66 illustrates different views of the first complete prototype of the AirExGlove. The system is composed of four main elements: a customized fabric glove made of Nylon PU (55 g/m², [297]), an inclusive wristband with an adjustable Velcro closure, a set of pneumatic actuators (mounted on the hand's dorsal side) and a set of tendons (fixed on the palm). The fabric used for the glove is flexible but not stretchable and thus provides a good force transmission between the exoskeleton and the hand without reducing dexterity. Inextensibility of the fabric is also a critical requirement for the embedded actuators in order to ensure the required forces and stiffness. The working principle and design of the system for one of the long fingers are presented in Figure 67 (a) and (b); a long-finger schematic illustrating the bone/joint chain is also depicted in Figure 67 (a).
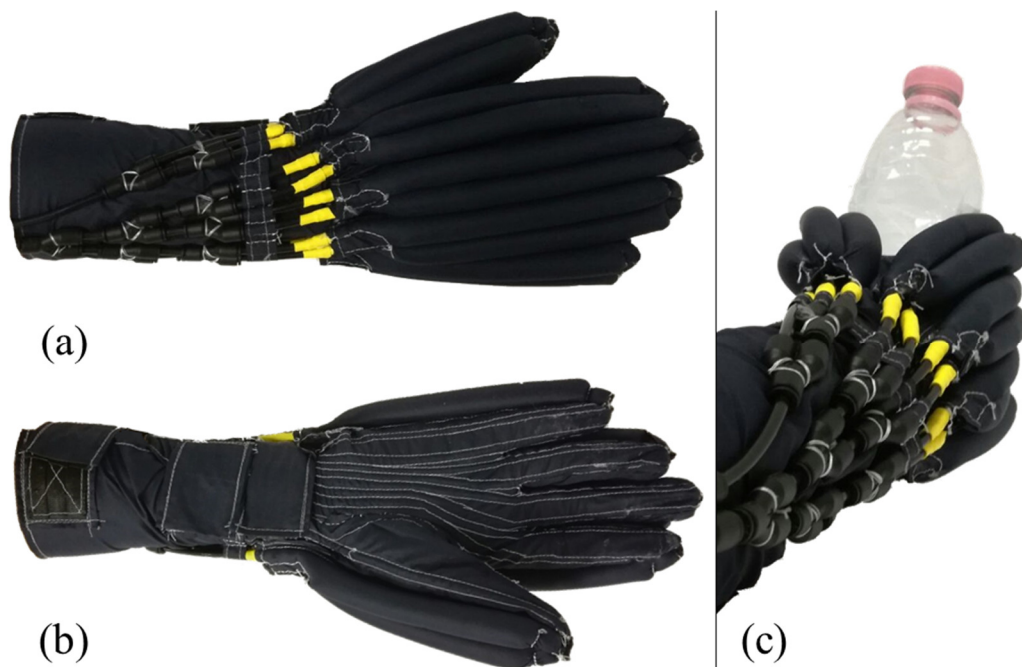
Figure 66 – Overview of the AirExGlove: (a) hand dorsal side of the system (pneumatic chambers pressurized), (b) hand palm side (tendon channel seams visible in white) and (c) side view of the system (thumb side) when grasping a plastic bottle.

Each finger is composed of the following bones (base-to-tip): proximal, middle and distal phalanx. The thumb is composed only of two phalanxes (proximal and distal). The names of the joints between the finger bones (base-to-tip) are the metacarpophalangeal (MCP), proximal interphalangeal (PIP) and distal interphalangeal (DIP). Inside the palm, each finger is connected to a metacarpal bone through the carpometacarpal joint (CMC). Abbreviations are listed in Figure 67 (a) next to the respective joint numbers. Each pneumatic actuator chamber is composed of an airtight latex bladder pressurised through an input/output channel (see Figure 67 (b) Air I/O), fitted inside a fabric sleeve. Seam lines along the tendon channels are also visible in Figure 67 (b). Once a positive air pressure is applied to the bladder, the chamber inflates.
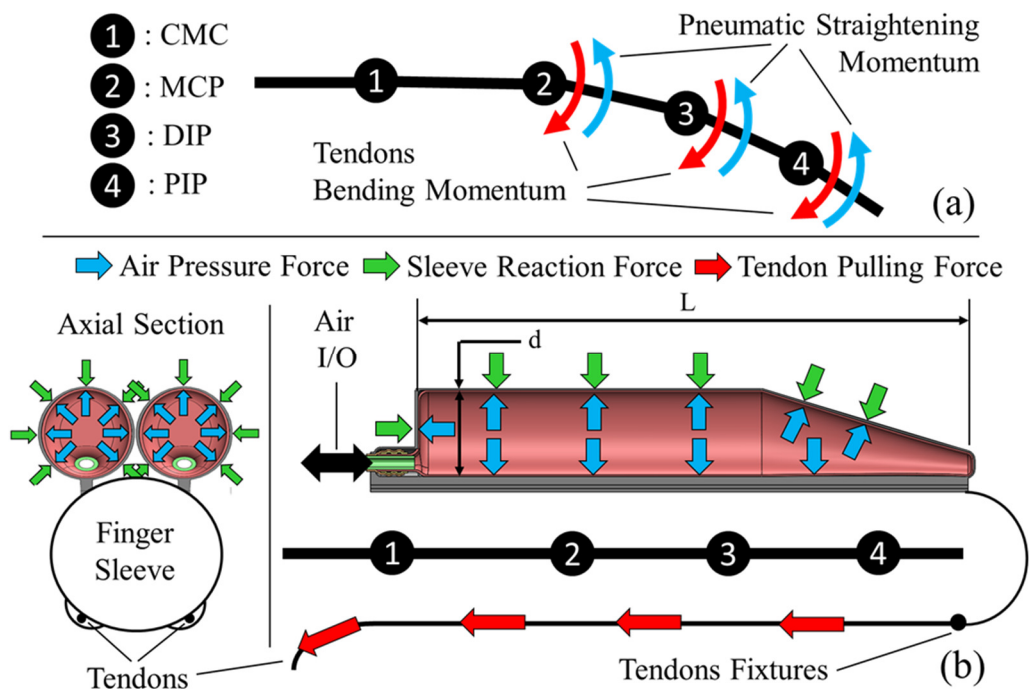
Figure 67 – AirExGlove actuation principle: (a) a schematic of the long fingers is depicted, showing the joints names and the active momentum provided by the pneumatic and tendon driven actuation system. (b) From left to right, a radial and a longitudinal section view of a single chamber are shown. Different arrows are used to illustrate the distribution of the air pressure forces (azure), the reaction forces produced by the sleeve (green), the pulling forces exerted by the tendons (two tendons per finger and for thew thumb, running on the palm side) (red). The double-headed arrow indicates the input/output channel for the pressurized air. Geometrical parameters of the chambers d (diameter) and L (length) are also indicated.

The fabric sleeve, due to its inextensibility, limits the inflation to a predefined cylindrical shape as indicated by the section in Figure 67 (b). The balance between the air pressure force (azure-coloured arrows in Figure 67 [b]) and the reaction force of the fabric sleeve (green-coloured arrows in Figure 67 [b]) generates the straightening momentum shown by the azure-coloured arrows in Figure 67 (a). As highlighted in the previous section, thanks to the external arrangement of the chambers on the dorsal side of the hand, no compression force is perceived by the user, assuring his or her comfort. As shown in Figure 66, the pneumatic actuators cover the whole length of the fingers and their respective metacarpal sections. The straightening momentum indicated in Figure 67 (a) tends to align each finger group of three (two for the thumb) phalanxes with its respective metacarpal bone. In contrast, by controlling the tendon displacement, a bending/reaction momentum opposite to the one provided by the pneumatic actuators can be provided. The equilibrium between these two momenta allows the fingers to be positioned in an infinite number of intermediate stable configurations, ranging from the full hand opening to the full closure. Each finger is actuated by a pair of tendons, both fixed at the fingertip in Figure 67 (a). Each pair of tendons is controlled by the same actuator; hence they experience the same displacement. The use of two tendons for each finger and for the thumb is redundant; however, this tendon configuration allows the tendons to be routed on the side of the finger pads rather than along the middle; thus, they hardly interfere during grasping tasks. The design of the glove enables high customizability both in regard to the hand size and the forces exerted on the fingers by the pneumatic actuation. Tailored gloves can be manufactured according to the user's hand shape, and by virtue of modularity of the pneumatic actuators, the number and sizes (diameter, length) of the chambers can be defined based on the user's needs and pre-existing medical conditions.

6.2.4 Control System Architecture

In Figure 68, the envisioned control system for the AirExGlove is presented. Actuators are located in a box fixed on a belt, while tendons are routed using Bowden cables along the back, shoulder and arm to the user's wrist. The same structure applies to the flexible, 4-mm-diameter rubber pipes used to supply pressurised air to the pneumatic actuators. The weight of the envisioned actuation system is estimated to be less than 2 kg for the configuration presented in Figure 68 (five motors and five pressure regulators), and less than 1 kg for an under-actuated configuration with only one motor to pull all the tendons together and one pressure regulator for all the chambers; these weights satisfy the weight requirements for a backpack/belt solution for the actuators as indicated in [34] and compare with similar systems, e.g. for the SEM™ Glove [296], where only three fingers are actuated purely for closure, the belt-mounted motor/battery pack weights 600 g.
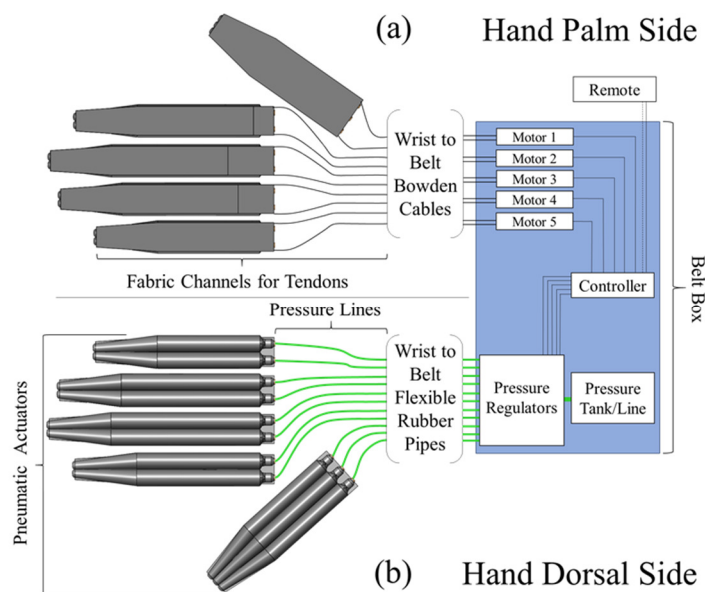
Figure 68 – AirExGlove chambers arrangement and intended control scheme: the system comprises independent actuation for each finger (two chambers for the long fingers, three chambers for the thumb and two tendons for each finger). The pressure regulators, the motors to actuate the tendons, the controller, the pressure tank (or the connection to the pressure line) and the battery are embedded in a box on a belt to be worn by the patient. Tendons are routed using Bowden cables from the belt to the wrist, hard rubber pipes are used for the routing of the pressure lines.

Independent finger or whole-hand actuation can be performed according to needs. As illustrated in Figure 68 and Figure 66, the system is comprised of five pneumatic actuators. Each of the four actuators on the dorsal side of the fingers is composed of two pneumatic chambers. The pneumatic actuator of the thumb makes use of three rather than two pneumatic chambers due to its higher grasping-force-to-length ratio. Furthermore, the number of chambers for the thumb is larger than the that of the fingers in order to keep the same dorsal encumbrance for all the fingers. Applying this antagonistic actuation principle for an exoskeleton, not only it is possible to control the maximum finger opening generated by the pneumatic actuators (and thus, deliver gradual rehabilitation therapy to patients with hand-opening disabilities), but also to use the same system to assist patients with different pathologies during hand closure tasks. The novelty of the work presented in this thesis lies in the design of the proposed system, the AirExGlove. The design of the actuation system (motor pack, pulleys and Bowden cable system mounted in a backpack) is not novel, being already used for grasping reinforcement in several other portable tendon-driven systems, even commercially-available ones such as the SEM™ Glove [296]. Therefore, the author focused his investigation on system design rather than actuation design.

6.3 Characterization of the System

A set of experiments has been conducted to evaluate the performance of the AirExGlove when a subject affected by clenched fist deformity is wearing it. However, no patients were available for testing at the moment of this investigation; therefore, a different approach was chosen by the author. A healthy subject has been used, simulating the clenched fist condition by tensioning the tendons with springs, mimicking the contraction force experienced by an unhealthy subject. Consequently, during all the tests detailed in this and in the following section (6.4), the glove was worn by a healthy subject (female, 25, 171 mm wrist-to-index-finger-tip length, 75 mm palm width, hand

S size). The healthy subject wearing the glove was asked not to exert any force on the system, being passively guided in the movements by the actuators. Sensors such as load cells, dynamometers and magnetic trackers were mounted on the exoskeleton system (rather than the subject's skin) to obtain measurements. Independent measurements were performed on all the fingers when grasping tasks are performed (single-finger power grasping with the thumb in opposition). In general, in all the experiments detailed in this chapter, the data collected showed a high degree of similarity for the index, middle, ring and little finger. For this reason, only the experimental data set for the index finger are reported in this thesis. Ethical approval has been obtained by King's College London Board of Ethics – Faculty of Natural and Mathematical Sciences to perform the testing of the AirExGlove on healthy subjects, as per the tests described in this chapter. This approval does not apply to the qualitative tests conducted on a patient affected by clenched fist deformity presented in Section 6.5. Dedicated information about ethical requirements for this testing have been provided within Section 6.5. The study has been submitted to the board of ethics with the following title: Experimental evaluation of the grasping performance of a novel soft exoskeleton for human hand rehabilitation and empowering. The application reference is: LRS-16/17-3631. A confirmation letter is available in the Appendix VII.

In the first part of this section, the author describes the set of experiments conducted to characterize the mechanical response of the system when a force is applied to the tendon actuation to simulate a contraction, investigating the correlation between this force and the grasping force produced. The normal force applied under the finger pad on objects of different sizes is measured.

In the second part of this section the simulated clenched fist condition is clinically assessed. This procedure is used to correlate the mechanical characterization of the system with the clinical condition of the user, hence, to

evaluate the patient-specific needs and tailor the system accordingly. The level of hand spasticity of post-stroke patients can be clinically assessed by trained physicians or physiotherapists by manually stretching the fingers of the subject in the whole range of motion of the hand, thus evaluating the level of contraction experienced by assigning a score from 0 to 4 on the Ashworth Scale. The Ashworth Scale, first introduced in [299] and later extended by Bohannon and Smith in [300] into the Modified Ashworth Scale (MAS), has been proven to be a reliable method for this assessment [301]. The scale assigns numerical values from 0 to 4 to grade the level of spasticity measured, where "0 = no increase in muscle tone, 1/1+ = slight increase in muscle tone [...], 2 = more marked increase in the muscle tone [...], but affected part(s) easily moved, 3 = considerable increase in muscle tone, passive movement difficult and 4 = affected part(s) rigid in flexion or extension" [300]. The score on the MAS generated by the physical simulations is reported in this section.

6.3.1 Mechanical Characterization

To understand how the force applied to the tendons relates to the grasping force exerted, a set of experiments has been conducted using objects of different diameters and a customised benchmark platform. In Figure 69, the experimental setup is presented.
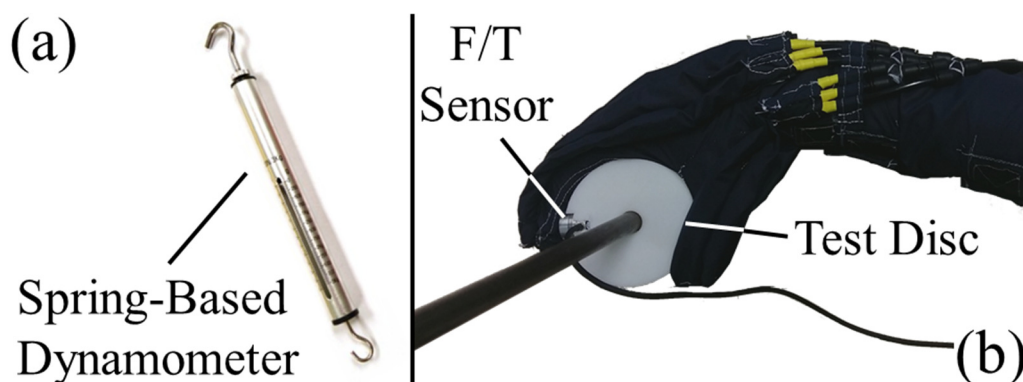
Figure 69 – Experimental setup for mechanical characterization of the AirExGlove: (a) the dynamometer used to load the tendons and contextually measure the force applied, (b) the healthy user wearing the AirExGlove grasping a 3d printed disc with dedicated housing for ATI Nano17 force torque sensor to measure forces under the fingertip.

The tendon pair of the index finger is loaded using the dynamometer (spring-based, 0 – 30 N scale) presented in Figure 69 (a). The loading procedure is as follows: the top eyelet of the instrument is connected to a hook bonded to a linear module, while the movable bottom eyelet of the instrument is connected to the tendon pair. The dynamometer is then moved so to achieve the desired tension on the tendon pair; once the desired pre-load is achieved, the linear module is fixed in position. The user grasps a 3D-printed disc fixed on a pole with an embedded ATI Nano17 Force/Torque sensor (see Figure 69 [b]). In all of the conducted tests, the subject keeps the thumb in opposition to the finger that interacts with the F/T sensor. All the tested disks have a thickness of 27 mm, so there is only one finger at any time in opposition to the thumb. All other fingers were free to move and were not actuated during these tests. As a result, the 1-digit grasping force exerted by the user wearing the glove is obtained by the z-axis force readings of the F/T sensor. Grasping data was collected for test disks of different diameters (Ø40 mm, Ø55 mm, Ø70 mm, Ø85 mm, Ø100 mm). To measure the finger pose, magnetic markers of an Aurora Electromagnetic Tracking System (Northern Digital Inc., Waterloo, Ontario, Canada [213]) are mounted along the finger in correspondence to the fingertip and the DIP, PIP and MCP joints, as demonstrated in the side view of the AirExGlove worn by the subject in Figure 70.
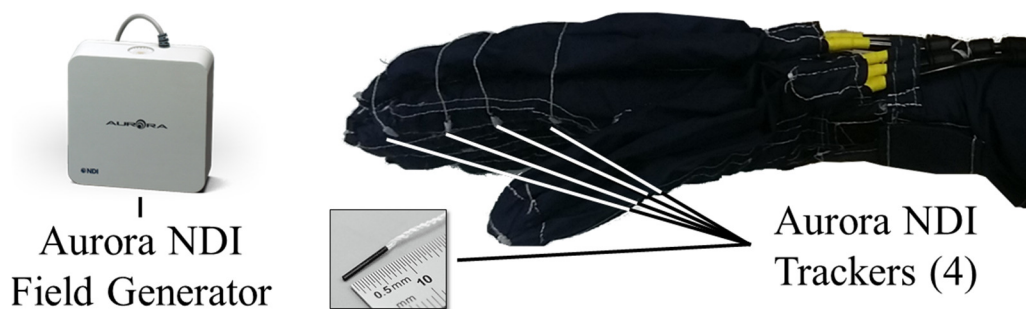
Figure 70 – Magnetic trackers and magnetic field generator Aurora Electromagnetic Tracking System (Northern Digital Inc., Waterloo, Ontario, Canada): markers placed in correspondence of the fingertip, the PIP, the DIP and the MCP for trajectory data acquisition.
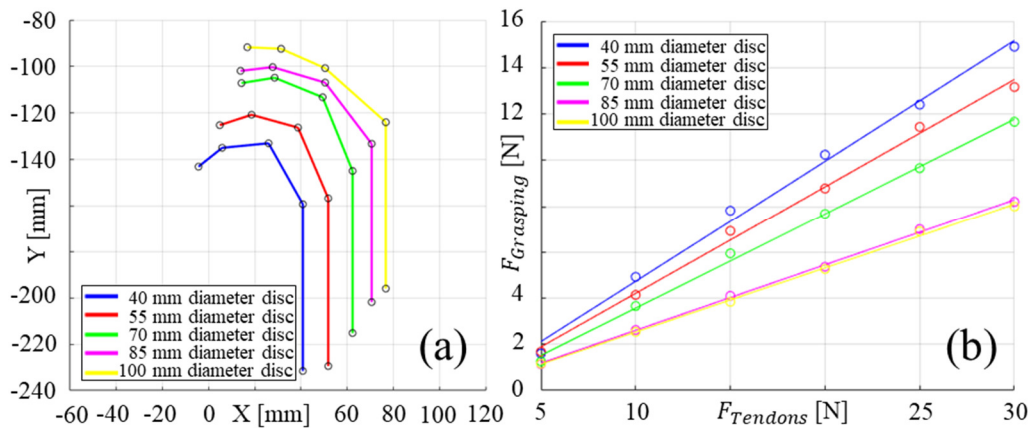
Figure 71 – (a) Positions of the index joints and tip when grasping objects of different diameter (data collected using Aurora Electromagnetic Tracking System (Northern Digital Inc., Waterloo, Ontario, Canada) with magnetic markers placed on the MCP, DIP, PIP joints, at the fingertip and at the base reference in correspondence of the CMC); (b) dependence between forces applied on the tendons ($F_{Tendons}$) using a dynamometer and normal forces measured under the fingertip ($F_{Grasping}$) using an ATI Nano17 F/T sensor. The force sensor has been mechanically coupled with the discs during the tests. The discs have been positioned so to have the F/T sensor in correspondence of the finger pad of the index, hence, to measure the normal component of the contact force between the index and the disc.

The processed data are presented in Figure 71. Looking at Figure 71 (a), the finger pose is displayed when the five discs of different diameters are grasped. The *xy*-plane depicted is the plane where the finger lies, normal to the phalanxes joint axes. Figure 71 (b) shows the dependence between the force applied to the tendons (in steps of 5 N) and the measured grasping force measured under the finger pad. Each load curve corresponds to a disc of a different diameter. A first-order-best-fit function of the data is displayed for each data set. The presented data indicate a growing linear trend between the tension applied to the tendons and the exerted grasping force. Furthermore, the slope of the line decreases with the increase of the diameter of the grasped object. The grasping force results are inversely proportional to the object's size given the same force applied to the tendon pair.

6.3.2 Clinical Assessment

To clinically assess the (equivalent) MAS score of the AirExGlove when a load is applied to the tendons, simulating a clenched fist deformity, a trained physiotherapist, Mr. Gerli from the Rehabilitation Centre IRCCS "Don Carlo Gnocchi", part of the Don Carlo Gnocchi Foundation (Via di Scandicci 269, 50143, Florence, Italy), partner institution of King's College London, has been involved. The procedure for the MAS score assessment of the hand has been detailed in the Introduction of this chapter. A spring-based dynamometer (1 – 10 N scale, spring constant k = 100 N/m) has been used to load the tendons of each finger. The use of a spring-based dynamometer (rather than a load-cell-based one) is critical for this assessment, because it provides the needed flexibility when the fingers are manually extended. It is important to note that the results here presented are dependent on the spring constant of the dynamometer used. The results are reported in Table 5.

Table 5 – Mapping between $F_{Tendons}$ [N], force applied to load the tendons of the fingers, and the score on the Modified Ashworth Scale [-].

$F_{Tendons}$ [N]	0.25	0.5	0.75	1	1.25	1.5	1.75	2	2.25	2.75	3 - 5
MAS Score	1	1	1+	2	2	2	2	2	2+	2+	3

As the data show, applying forces in the range of 0 N – 5 N makes it possible to simulate all the MAS scores in the range 0 – 3, which will cover all the cases in which a rehabilitation device as the AirExGlove can be employed (for MAS scores over 3, the deformity is usually so advanced and the closure force so intense that minimal passive movements are possible).

6.4 Workspace

A comprehensive analysis of the workspace of the AirExGlove is presented in this section and examines two different scenarios, without and with pre-load on the tendons. In both cases, data are collected about the trajectories of the joints

of the index finger when different pressures are applied to the pneumatic actuators.

6.4.1 No pre-load on the tendons

In this section, the workspace of the AirExGlove is evaluated when no pre-load is applied to the tendons, i.e. when it is used by a patient with no or minimal spasticity. In the first phase of this set of experiments, the subject is asked to perform a complete hand opening to provide a reference trajectory. Measurements are obtained with the Aurora Electromagnetic Tracking System (Northern Digital Inc., Waterloo, Ontario, Canada) demonstrated in Figure 70 (b) (markers in correspondence of MCP, DIP, PIP and the fingertip;
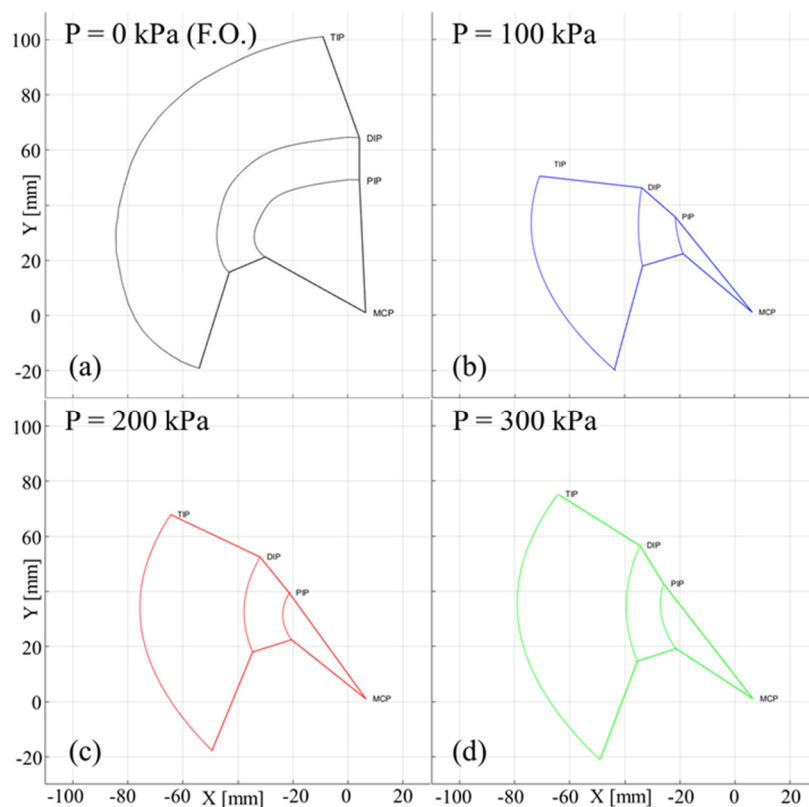
Figure 72 – Trajectories of the index in case of free-opening (a) and when different pressures are applied to the pneumatic actuators: 100 kPa (b), 200 kPa (c) and 300 kPa (d). Tendons are kept loose (no pre-load). (data collected using Aurora Electromagnetic Tracking System (Northern Digital Inc., Waterloo, Ontario, Canada) with magnetic markers placed on the MCP, DIP, PIP joints, at the fingertip and at the base reference in correspondence of the CMC).

The base reference is measured on the CMC). In the second phase, the subject is asked to close the hand. The system is then pressurised applying 100 kPa, 200 kPa and 300 kPa. The subject is asked not to intentionally resist neither assist the system during the movement. Tendons are kept loose during these tests. The processed data collected by the magnetic tracker system during the four tests are presented in Figure 72, showing the three pressure levels considered. The trajectories described by the fingertip and the joints in the pressure-actuated case follow those in the free hand-opening case, providing a natural movement to the user. As shown in subfigure (d), when 300 kPa are applied, the opening gesture achieved by the system is still less than the one achieved by a healthy subject (subfigure (a) free-opening case) when requested to open the hand. Even though the system has been successfully tested (when not worn) at higher pressure levels, the author decided to avoid pressures higher than 300 kPa when worn for the same safety concerns expressed in section 3.3.3. Furthermore, as shown in Figure 73 where the maximum diameter of the objects graspable for the three pressure levels tested, is displayed, the AirExGlove at the pressures considered already allows for a hand opening sufficient for most common grasping tasks, e.g., grasping a glass (70 mm – 90 mm ø) or a bottle (90 mm – 100 mm ø), even at low pressure.
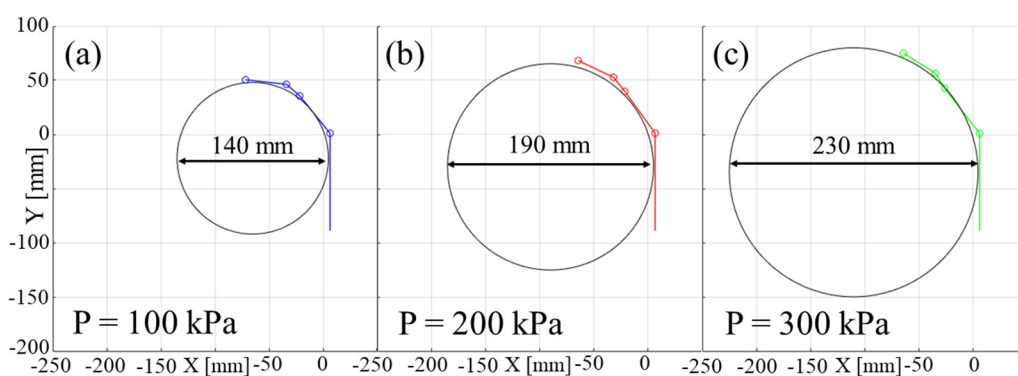
Figure 73 – Maximum diameter of graspable objects with no pre-load on the tendons for different pressure levels.
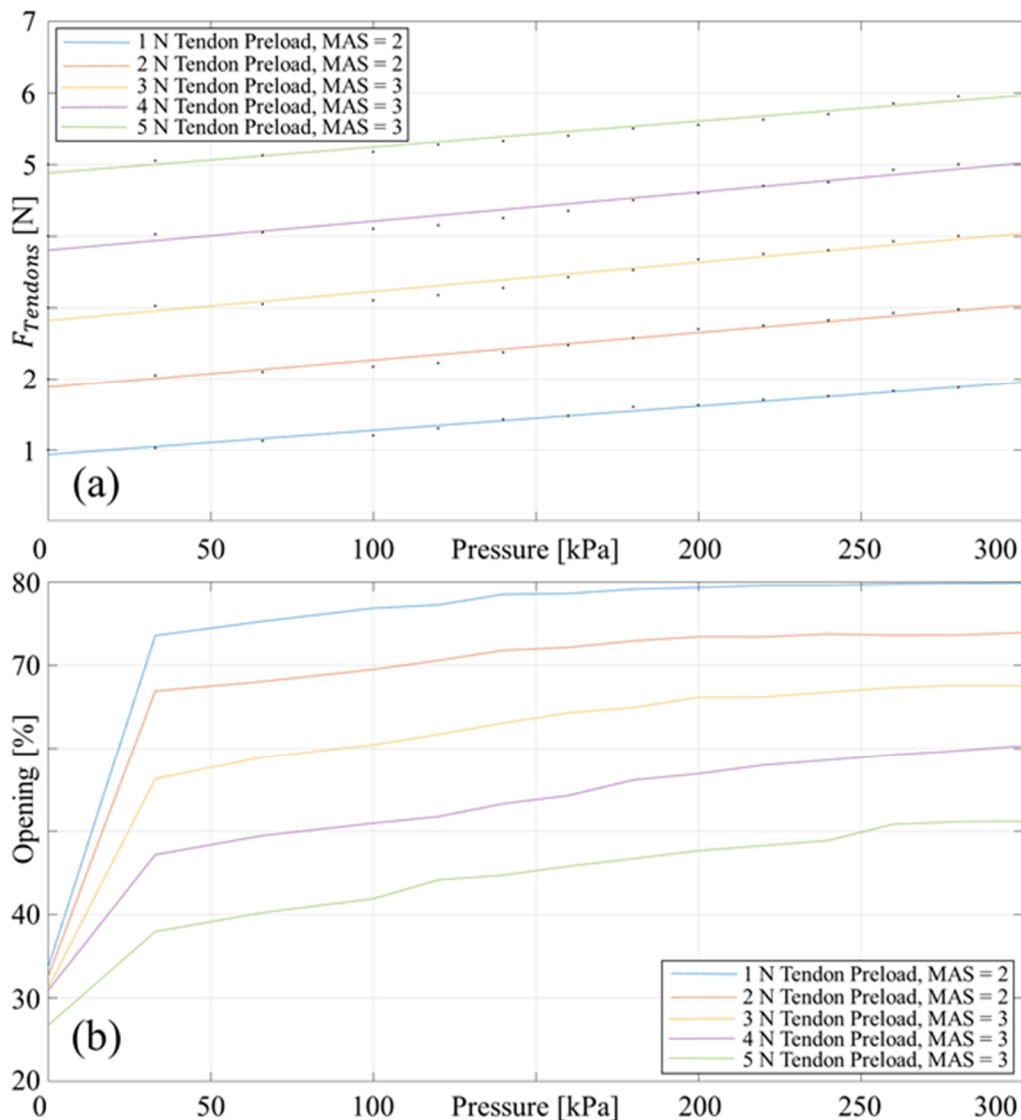
Figure 74 – Index finger system characterization for hand opening using pneumatic actuators with tendon pre-load applied (clenched fist simulation): (a) pre-load on the tendons $F_{Preload}$ [N] and (b) opening percentage [%] for different pre-loads, in the pressure range 0 kPa to 300 kPa.

6.4.2 Pre-load on the tendons

In this section, the data related to the workspace analysis of the AirExGlove when a pre-load is applied to the tendons are presented: these scenarios are equivalent to common hand contractions of patients affected by clenched fist deformity. In this set of experiments, the force on the tendons, the pressure in the pneumatic chambers and the pose of the finger are simultaneously measured. Also in this case, only the data for the index finger are presented. The

experiments have been conducted as follows: 1) the subject is requested to close and then relax the hand; 2) a pre-load is imposed on the index tendon pair (using the same spring-based dynamometer employed during the clinical assessment of the system, 1 N – 10 N scale, spring constant k = 100 N/m), inducing a certain closure level on the hand; 3) the pneumatic actuator is gradually pressurised up to 300 kPa, inducing the desired opening gesture, consequently increasing the tension on the tendon pair. This procedure is repeated for each pre-load level from 1 N – 5 N. According to the data of the first experimental set, the system exerts a normal force on the finger pad in the range of 3 N – 5 N. Figure 74 illustrates the dependence between the pressure applied to the pneumatic actuators and the force measured on the tendon pair. Each curve corresponds to a different pre-load condition (1 N – 5 N range, 1 N steps). Pressure is measured and increased by steps of 0.33 bar in the range of 0 kPa – 100 kPa and steps of 20 kPa in the range of 100 kPa – 300 kPa. A linear approximation is provided for each data set in Figure 74 (a). To quantify the opening gesture, a percentage is calculated based on the opening gesture in the free-hand-opening case. These values are included for all discrete points in Figure 74. The dependence between the opening percentage values, the force acting on the tendons and the pressure inside the pneumatic actuators are presented for the pre-load range 1 – 5 N in the graph of Figure 74 (b). Consequently, it is possible to define the requested pressure and achieve a desired opening gesture for a patient experiencing a certain contraction on the hand. These data refer to the tested subject (female, hand S size). Similar curves can be derived for any hand size for both male and female subjects. The system was able to provide an opening of up to 79% for 1 N of pre-load (MAS = 2) and up to 51% for 5 N of pre-load (MAS = 3) at 300 kPa.

6.5 Clinical testing

In order to validate the results presented in the previous section about the characterization of the AirExGlove and to test its performance in a real

application scenario, a subject affected by clenched fist deformity has been involved. Non-quantitative tests of the AirExGlove with a 54-year-old male subject (hand length: 17.5 cm, hand width: 6 cm) have been performed using the prototype developed at the Rehabilitation Centre IRCCS "Don Carlo Gnocchi", under the supervision of Mr. Gerli, the same trained physiotherapist who clinically assessed the performance of the AirExGlove

The subject in question is affected by type 2 spinal muscular atrophy. Generally, subjects affected by this pathology exhibit a low muscle tone, especially in their limbs; this situation is the opposite of that of post-stroke patients, where involuntary permanent muscular contraction affects the patient's limbs. However, this particular subject exhibits a tendon retroaction in the forearm that induces the same clenched fist deformity of post-stroke patients. Therefore, it is also possible to assign an equivalent MAS score to the patient. Mr. Gerli assessed this score in the patient; the MAS score measured is 1+. A number of tests were conducted to validate the usability and ergonomics of the AIREXGlove on the subject. These qualitative tests are presented in the video available for download and streaming at the following link: https://youtu.be/iZaq4SEZW7Q. The test subject is a long-term collaborator with the research institute, which has given him extensive experience in testing new rehabilitation devices. After the testing conducted in May of 2017, the subject gave enthusiastic feedback about the AirExGlove, particularly appreciating its great ergonomics, natural movement, unobtrusiveness during interactions with the environment and low weight.

According to the rules of the institution that hosted the tests, i.e., the Rehabilitation Centre IRCCS "Don Carlo Gnocchi", ethical approval is not required for the one-time qualitative tests conducted. Written confirmation of this rule has been also obtained from the director of the Rehabilitation Centre IRCCS "Don Carlo Gnocchi", Professor Carlo Macchi. This confirmation document was prepared for the submission to the Soft Robotics journal and can

be found in Appendix VIII. Written informed consent was obtained from the patient in compliance with the *World Medical Association Declaration of Helsinki – Ethical principles for medical research involving human subjects* (2013) [302]. The informed consent and the information sheet for the subject can be found in Appendix IX of this thesis.

6.6 Summary

In this chapter, the AirExGlove, a novel exoskeleton for hand rehabilitation in post-stroke patients who are affected by the clenched fist deformity, has been presented. A thorough literature review of the current state of hand rehabilitation devices that make use of rigid and soft robotic systems has been presented. The most relevant design iterations investigated to achieve the final design of the proposed system have also been explored. A customised system embedding eleven pneumatic actuators and five pairs of tendon actuators has been developed. Extensive testing has been conducted to characterise the AirExGlove's mechanical behaviour. A trained physiotherapist has been consulted to assess the performance of the system when its tendon actuators are used to simulate the clenched fist condition. The results suggest that the system is suitable to deliver high-dosage hand rehabilitation therapy to patients affected by muscle spasticity that scores up to 3 in the MAS scale. The author demonstrated how the AirExGlove, thanks to its design, is also significantly lighter and less bulky than both its analogue rigid-linked exoskeleton systems and their silicone-based counterparts. Preliminary testing on a single patient scoring 1+ on the MAS scale has been successfully conducted and the results have also been presented in this chapter. The limitations of this system as well as recommendations for future work are discussed in Chapter 7.

Chapter 7

7 Conclusions

This chapter summarises the research contributions and outcomes of this thesis, discussing also the limitations of the presented works. Recommendations for future work are provided; future work aims to overcome the remaining limitations of created systems and to extend beyond the achieved contributions.

7.1 Conclusions

This thesis has investigated the development of a novel design paradigm to enable on demand stiffness controllability in soft robotics structures. The following conclusions are drawn:

Creation of a novel variable stiffness robotic system

1. A novel variable stiffness system (VSS), the Variable Stiffness Link (VSL) has been proposed in this thesis. Based on the classification detailed in the background chapter, as seen also in [44], the proposed system is an Active VSS that works in Active-Passive antagonistic configuration, where the active actuation means is the pneumatic actuation and the passive means is realised by a structure based on silicone elements, meshes and fabric. The VSL is a stiffness-controllable structural element that can be embedded in soft robots or be used to replace rigid components in conventional robots. The VSL benefits of a simple, cost-effective and scalable design, as well as of a low weight-to-load ratio. The VSL design is modular by nature and has been conceived as a novel base structural element for soft and conventional robotic systems. The robust design of the VSL allows for the use of high pressures on the pneumatic actuation side (up to 300 kPa tested without leakages or any damage occurring). Hence, high stiffness levels can be achieved, thanks to its multi-material design which combines meshes and fabrics for internal and external braiding, respectively. The author has demonstrated how the VSL can overcome the pressure and stiffness limitations of conventional soft silicone-based systems. The pneumatic actuation of the VSL is used to provide on-demand stiffening. The pressure level signal is used for the closed-loop control of the VSL's internal pressure. This pressure signal, if appropriately processed, can also be used to detect pressure variations generated as a result of

deformations through undesired interactions/collisions with the environment.

2. A novel bio-inspired design for a soft continuum manipulator, the Inflatable Arm, has been proposed. Building on the design paradigm of the VSL, the author proposed a novel system not only stiffness-controllable but also endowed with shape-shifting and shape-locking capabilities. Based on the classification detailed in the background chapter, firstly presented in [44], the proposed system is an Active VSS that works in Active-Active antagonistic configuration, where the first active actuation means is the pneumatic actuation and the second one is based on tendon-driven actuation. A flexible latex membrane and a flexible, yet inextensible, fabric sleeve are used to enable stiffness controllability. The Inflatable Arm, as the VSL, benefits of a simple, cost-effective and scalable design, with an even smaller weight-to-load ratio, being only composed of extremely light-weight components. The use of foldable flexible materials allows the system to almost completely shrink or even squeeze through narrow openings, being still fully functional. Thus, a novel highly dexterous hyper-redundant design for continuum robotic manipulators has been created.

Investigation of new applications for soft stiffness-controllable structures

3. A novel hybrid design concept combining soft and rigid elements, the VSL Robot, for human-robot collaborative applications has been proposed in Section 3.4. A proof-of-concept anthropomorphic manipulator embedding two VSLs and three rotational joints has been presented and tested, to show the feasibility of this design and test its performance. The author demonstrated that the VSL is a suitable active replacement for the main structural elements of conventional robotic systems, the links. When it comes to the integration of the VSL in a

conventional robotic manipulator, its design allows for ease of internal cable routing, without affecting its stiffness controllability. The author demonstrated also how the VSL's pneumatic actuation can be used to endow the manipulator with collision detection and reaction capabilities. Collision detection algorithms have been tested based on pressure feedback, implementing articulate reactions, such as: collision detection, movement interruption, stiffness reduction and movement away from the point of collision. To the best of the author's knowledge, this is the first time a stiffness adjustment mechanism has been added to the links of an industrial-like collaborative robot, allowing for additional safety for the human operator in the shared workspace. The effectiveness of the VSL has been demonstrated in a robotic arm system employing on conventional rotational joints actuated by electric motors. This approach can be used to enhance safe HRI in manipulators based on these kind of joints, as well as to further increase the safety of those manipulators based on Variable Stiffness Actuators/Joints.

4. A novel entirely soft bio-inspired design concept for highly dexterous laparoscopic tools to be used in Minimally Invasive Surgical applications has been proposed. The author demonstrated how this design is suitable both for single-port and multi-port laparoscopic surgery scenarios, introducing the Inflatable Tentacle for the former and the Inflatable Endoscope for the latter. The author showed how this design concept is suitable for robotic actuated manipulators, with the Inflatable Tentacle, and for hand-held devices similar to traditional laparoscopic tools, with the Inflatable Endoscope. In both cases the author demonstrated how the bio-inspired antagonistic actuation can be effectively used to achieve complex body shapes, leading to a significant increase in the workspace of such systems, as compared to conventional mechanisms. The design features of the proposed systems have been proven to be extremely useful in the laparoscopic surgical scenario: the absence of rigid components

allows for ease of access through narrow openings, i.e. trocar ports here, by squeezing the manipulator body and deploying it past the narrowing, without impairing its manoeuvrability. The author has shown how the use of tendon-driven and pneumatic actuation allows for completely remote actuation, minimising the encumbrance of the actuators inside the manipulator body. Lastly, the author created systems that are inherently safe with regards to the interaction with delicate tissues inside the human body, thanks to the use of soft materials and to their stiffness tuning capabilities. Thus, a novel design concept with the potential of significantly improving on the current approach of traditional and robotic-assisted laparoscopic tools has been presented.

5. A novel soft rehabilitation device for patients affected by hand disabilities, the AirExGlove, has been presented. The fabrication process of this system has been detailed, a working prototype has been extensively tested and an integrated actuation architecture for independent-finger and full-hand control has been presented. The proposed system is based on the actuation principle of the Inflatable Arm (Chapter 4), employing tendon-driven and pneumatic actuation to enable stiffness-tuning, shape-shifting and shape-locking capabilities. The proposed system has been conceived to assist patients affected by clenched fist deformity, a dysfunction that impairs subjects disabling their capability to open their hands. It is noted that, with the proposed system, assisted hand closure can also be performed. The pneumatic actuation assists the patient during the opening movement: tendon-driven actuation can be concurrently used to limit the opening gesture to deliver a rehabilitation therapy that adapts to the changing abilities of the recovering patient. The author has shown how tendon-driven actuation can also be used to simulate the clenched fist condition by loading the tendons, hence, the system can be calibrated and its behaviour modelled, without the need of clinical trials. Thus, the AirExGlove can be tailored

to the patient's condition and hand geometry, optimising the user experience. The author demonstrated how the actuation mechanism of the proposed device can be used to deliver high-dosage and high-power rehabilitation therapy to patients affected by clenched fist deformity, scoring up to 3 on the Modified Ashworth Scale (MAS). Lastly, the author has tested the AirExGlove on a patient affected by clenched fist deformity with an equivalent MAS score of 1+: the patient provided enthusiastic feedback about the proposed system, highlighting in particular the naturalness of the opening gesture, the comfort and the ergonomics. Hence, the effectiveness and the potential of this design concept has been demonstrated.

7.2 Recommendations for Future Work

This thesis contributes a novel design paradigm allowing soft robotic devices to change stiffness over a wide range. Having designed, created and experimentally tested multiple novel design concepts enabling on-demand stiffness for soft robotic structures, it is evident that there are also a number of limitations which serve to provide a basis for future work. These include:

1. The fabrication processes presented in this thesis have shown that the proposed soft, stiffness-controllable structures can be easily developed across different scales allowing applications in minimally invasive surgery as well as applications where these robots are utilised to work closely together with humans in industrial settings. The design simplicity of these systems has the potential to allow their industrialisation. For fabrication, these prototypes effectively undergo a crafting process combining multiple materials such as fabric meshes and silicone materials inside moulds in a number of procedural steps to finally create a new robotic structure. During these fabrication processes, the used moulds have been made by latest state-of-the-art 3D additive

manufacturing. However, there is a large number of steps that require manual work, including preparing and sewing meshes and textiles, that are of paramount importance to the structure and, hence, to the behaviour of these robotic devices. There is a need to industrialise the fabrication steps to allow precise reproducibility, in particular, when these soft, stiffness-controllable robots are working in interaction with humans. Hence, the proposed fabric-based systems need to be optimised to meet the design requirements of weaving and knitting machines.

2. Resulting from inconsistent fabrication methods among other things, modelling is hugely challenging for soft robotic structures. Researchers have widely investigated model-based approaches and Finite Element Methods to describe the kinematics of these systems. Struggling to achieve real-time capability, generally heavy from the computational point of view, efforts have been for instance, dedicated towards the optimisation of FEM models. To overcome the limitations of these approaches, it is suggested that future work should focus on deep learning and machine learning approaches – methods that have become attractive for applications with complex models affected by high uncertainty, such as the systems at the centre of the investigation of this thesis. This is particularly the case when the proposed systems are in interaction with objects or humans, as learning algorithms seem to be most effective when exposed to unexpected behaviours and able to respond quicker than complex model-based algorithms.

3. It was successfully demonstrated that the proposed VSL can act as an actuator and distributed sensor at the same time. The pressure controller continuously measures the pressure inside the link and detects immediate pressure change. Hence, it is possible to determine if a collision between the link and the environment has occurred. However, the challenge remains to return information about the magnitude of the interaction, as the present algorithm only detects the collision's occurrence. Improved

filtering of the pressure feedback and more advanced algorithms needs to be investigated to accurately evaluate also the magnitude of the interaction.

4. The exact location of the collision is also undetected when using the present method. Future work could concentrate on creating structures that are made of arrays of soft stiffness-controllable pouches. This solution would allow the accurate identification of the location of collision.

5. Though each pneumatically actuated robotic structure returns real-time pressure data, it would be challenging to make distinct classification between a collision and a load applied at the end effector (either through guided interaction by a human as in the case of kinaesthetic teaching or through a pick and place task). The modification of the soft robotic structure mentioned above and more effective modelling approaches could overcome these challenges.

6. Collision detection algorithms have been tested only with the VSL. The same sensing principle can be applied to the Inflatable Arm and to its design derivations, the Inflatable Tentacle and the Inflatable Endoscope. Thus, valuable feedback can be provided to the surgeon and automatic reactions could be implemented to prevent any damage to the soft tissues of the patient body during surgical interventions. In a surgical scenario, even minimal interaction forces can create significant damages and, due to their magnitude, their detection could be even more challenging with this method. Hence, considering the design differences between these systems, the use of this sensing approach should be investigated and tested, to validate its functionality and applicability in the case of the Inflatable Arm.

7. As shown for the application in MIS, the Inflatable Arm can be deployed and can elongate by multiple times its initial size, due to its antagonistic actuation principle and its foldable and flexible design. During the linear

deployment process, an outer bellow-shaped sleeve made of crimped fabric could significantly enhance the unidirectionality of the movement. Further developments in terms of design will also focus on creating a multi-chamber system allowing for individual adjustments of the stiffness of small sections, enabling a modular design, similar to the approach proposed with the VSL. Hydraulic actuation should be also investigated in order to evaluate the pros and cons of the usage of an uncompressible fluid on the mechanical behaviour of the system.

8. Another application area in which these inflatable systems could prove superior to standard robotic arms is underwater robotics; the capability of the manipulator to adjust its stiffness by increasing the pressure in the inner chamber of its body could be used to compensate for the external water pressure. This use would allow for the significant counteraction the compression effects of deep water, thus preserving the manipulator's functionality and prevent damage to the mechanical structure of the system. A large-scale version of this system could also be explored in the context of space applications: the deployability and shrinkability of this design could be particularly beneficial for space transportation. In both these cases for different reasons, closed hydraulic circuits rather than pneumatics should be considered. Even though these applications have not been explored in this thesis, the author acknowledges the potential of the proposed design for them.

9. The use of the inflatable fabric-based systems presented in this thesis in surgical applications can significantly improve the performance of state-of-the-art laparoscopic systems, both in robotic and traditional surgery. However, the translation of robotic technologies into commercial products is extremely challenging in medical applications, and in particular in surgical scenarios. In this regard, one of the major challenges is to create systems that can be sterilised according to medical standards [303]. Even after sterilisation, the same tool can only be used

a limited amount of times, e.g. the tools of the da Vinci Surgical System® from Intuitive Surgical Inc. should be disposed after 10 uses in most of the cases. Future work should focus on the investigation of materials suitable for one of the standard sterilisation processes. Given the low-cost of the proposed system, the creation of disposable tools should also be considered.

10. The AirExGlove has proven to be a valuable tool for robotic assisted rehabilitation of the hand, even in the under-actuated configuration that makes use of a single pressure line to actuate all the pneumatic actuators and a single actuator to pull all the tendons simultaneously. However, with the current design, only extension and flexion of the hand extremities can be controlled. This degree of freedom is generally sufficient to control the fingers in their whole workspace, but is not enough to control both degrees of freedom (extension and rotation) of the thumb, as highlighted by the grasping tests conducted with the patient. Here the thumb was not able to reach the natural opposition configuration used for pinch and power grasp, as also shown in the last part of the video (see Section 6.5 for the link to the video). This limitation should be addressed to unlock the full potential of the proposed system. A dedicated pneumatic or tendon-driven actuator can be added to provide the missing degree of freedom on the thumb.

11. Both the INFLEXGlove and the VSL Robot are systems designed to last and to be re-used, however, the prototypes built in the context of this research have been tested for a time-span significantly shorter than their envisioned product life. A dedicated study about the effects of fatigue on fabric-based pneumatic actuators should be considered to better assess the effectiveness of the proposed systems in real-life applications.

12. The use of pneumatic actuators comes with a number of useful design features such as the remote location of the pressure source, inexpensive light-weight commercially available components (tubes, connectors and

pressure regulators) and accurate pressure control. However, one of the main shortcomings of pneumatic actuation is the need of a source of pressurized air which can be a limitation to the usability of the system in certain applications. In the case of the VSL Robot presented in Section 3.4, the author is looking at application of the envisioned system in industrial settings. In such settings, pressure lines up to 1000 kPa are commonly available for use. Similarly, in the case of the medical robotic systems discussed in Chapter 5, pressure lines are generally available in all the major hospital facilities, supplying medical air at 345-380 kPa with a minimum flow of 100 l/minute [304], a pressure level suitable to actuate both the Inflatable Arm and the Inflatable Tentacle. Furthermore, portability is not a typical design priority in medical robotics: most of the commercially available medical robots, e.g. the da Vinci Surgical System® from Intuitive Surgical Inc., present bulky actuation systems. Thus, even embedding a dedicated compressor can be considered a design solution where no pressure lines are available. This is different in the case of the hand rehabilitation device proposed in Chapter 6, the AirExGlove, where portability can be extremely beneficial. To enable this, the only viable options are the use of high-pressure tanks to store compressed air or the use of small portable compressors in combination with batteries. In both cases to enable portability these systems need to be embedded in a backpack worn by the user, where also the actuators of the tendons are located, together with the power source of the motors. In consideration of the current trend in the development of batteries (fast recharging, high efficiency and large storage capability) as well as of the not demanding pressure requirements of the proposed system (300 kPa – 500 kPa), the author considers the latter option more suitable for the application. Hydraulic closed circuits and pumps can also be considered; the weight of the fluid, however, could significantly increase the weight of the system at the end effector, i.e. the glove, hence, reducing the

usability of the whole system. Further investigation in this context is required to find the best trade-off between battery life, portability and usability.

Appendix

In this Appendix datasheets and other relevant technical information are made available to allow the readers to recreate the systems and reproduce the experiments presented in this thesis are provided. In cases where the length of the information material is excessive to fit this document and such material is available online, website references are provided in the text.

I. Smooth Inc. Silicones Comparison

Product Name	Ecoflex® 00-30	Ecoflex® 00-50	OOMOO® 25	OOMOO® 30	Dragon Skin® 20	Dragon Skin® 30
100% Modulus	10 psi	12 psi	—	—	49 psi	86 psi
Colour	Translucent	Translucent	Light Blue	Lavender	Translucent	Translucent
Cure Time	4 hours	3 hours	75 minutes	6 hours	4 hours	16 hours
Die B Tear Strength	38 pli	50 pli	40 pli	40 pli	120 pli	108 pli
Elongation @ Break	900 %	980 %	250 %	250 %	620 %	364 %
Mix Ratio By Volume	1A:1B	1A:1B	1A:1B	1A:1B	1A:1B	1A:1B
Mix Ratio By Weight	1A:1B	1A:1B	100A:130B	100A:130B	1A:1B	1A:1B
Pot Life	45 minutes	18 minutes	15 minutes	30 minutes	25 minutes	45 minutes
Shore A Hardness	00-30	00-50	25	30	20	30
Shrinkage	<.001 in. / in.	<.001 in. / in.	0.0025 in. / in.	0.0025 in. / in.	<.001 in. / in.	<.001 in. / in.
Specific Gravity	1.07 g/cc	1.07 g/cc	1.34 g/cc	1.34 g/cc	1.08 g/cc	1.08 g/cc
Specific Volume	26.0 cu. in./lb.	25.9 cu. in./lb.	20.6 cu. in./lb.	20.6 cu. in./lb.	25.6 cu. in./lb.	25.7 cu. in./lb.
Useful Temperature (max)	450 °F	450 °F	400 °F	400 °F	450 °F	—
Useful Temperature (min)	-65 °F	-65 °F	-65 °F	-65 °F	-65 °F	—
Tensile Strength	200 psi	315 psi	240 psi	240 psi	550 psi	500 psi
Mixed Viscosity	3,000 cps	8,000 cps	4,250 cps	4,250 cps	20,000 cps	30,000 cps

Figure 75 – Comparison between the datasheets of Ecoflex® 00-30, Ecoflex® 00-50, OOMOO® 25, OOMOO® 30, Dragon Skin® 20 and Dragon Skin® 30; retrieved from [195].

II.   SMC ITV00(1/3)0-3BS-Q Specifications
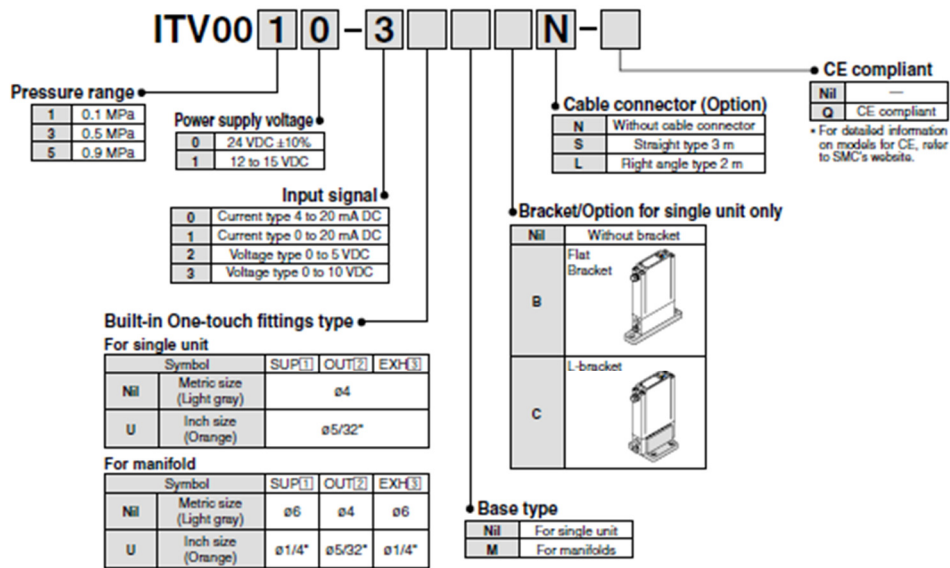
Model		ITV001□	ITV003□	ITV005□
Minimum supply pressure		Set pressure +0.1 MPa		
Maximum supply pressure		0.2 MPa	1.0 MPa	
Set pressure range		0.001 to 0.1 MPa	0.001 to 0.5 MPa	0.001 to 0.9 MPa
Maximum flow rate		3.5 ℓ/min(ANR) (Supply pressure: 0.2 MPa)	6 ℓ/min(ANR) (Supply pressure: 0.6 MPa)	6 ℓ/min(ANR) (Supply pressure: 0.6 MPa)
Power supply	Voltage	24 VDC ±10%, 12 to 15 VDC		
	Current consumption	Power supply voltage 24 VDC type: 0.12 A or less Power supply voltage 12 to 15 VDC type: 0.18 A or less		
Input signal	Voltage type	0 to 5 VDC, 0 to 10 VDC		
	Current type	4 to 20 mA DC, 0 to 20 mA DC		
Input impedance	Voltage type	Approximately 10 kΩ		
	Current type	Approximately 250 Ω		
Output signal	Analog output	1 to 5 VDC (Load impedance: 1 kΩ or more) Output accuracy: Within ±6% (Full span)		
Linearity		Within ±1% (Full span)		
Hysteresis		Within 0.5% (Full span)		
Repeatability		Within ±0.5% (Full span)		
Sensitivity		Within 0.2% (Full span)		
Temperature characteristics		Within ±0.12% (Full span)/°C		
Operating temperature range		0 to 50°C (No condensation)		
Enclosure		Equivalent to IP65 *		
Connection type		Built-in One-touch fittings		
Connection size	For single unit	Metric size	①, ②, ③: ø4	
		Inch size	①, ②, ③: ø5/32"	
	Manifold	Metric size	①, ③: ø6, ②: ø4	
		Inch size	①, ③: ø1/4", ②: ø5/32"	
Weight		100 g or less (without option)		

Figure 76 – Datasheet of the pressure regulator SMC ITV0010-3BS-Q and SMC ITV0030-3BS-Q used in the VSL Robot presented in 3.4, in the Inflatable Arm presented in 4.1; retrieved from [197].

III. Soyo Unipolar Stepper Motor Specifications

Item	Specifications
Step Angle	1.8°
Step Angle Accuracy	±5% (full step, no load)
Resistance Accuracy	±10%
Inductance Accuracy	±20%
Temperature Rise	80℃ Max.(rated current,2 phase on)
Ambient Temperature	-20℃~+50℃
Insulation Resistance	100M Ω Min. ,500VDC
Dielectric Strength	500VAC for one minute
Shaft Radial Play	0.02Max. (450 g-load)
Shaft Axial Play	0.08Max. (450 g-load)
Max. radial force	75N (20mm from the Flange)
Max. axial force	10N
Rotation	CW(See from Front Flange)

Model No.	Rated Voltage	Current /Phase	Resistance /Phase	Inductance /Phase	Holding Torque	# of Leads	Rotor Inertia	Weight	Detent Torque
Single Shaft	V	A	Ω	mH	Kg-cm		g-cm²	kg	g-cm
SY57ST76-0686B	12	0.68	17.7	30	9	6	200	0.72	0.72

Figure 77 – Datasheet of stepper motor SY57ST76/0686B used in the VSL Robot presented in 3.4. Retrieved from [201].

IV. HS-7954SH Servomotor Specifications

Operating Voltage Range (Volts DC)	6.0V ~ 7.4V
Speed (Second @ 60°)	0.15 ~ 0.12
Maximum Torque Range oz. / in.	333 ~ 403
Maximum Torque Range kg. / cm.	24.0 ~ 29.0
Current Draw at Idle	9 mA
No Load Operating Current Draw	240 mA
Stall Current Draw	3,000 mA
Dead Band Width	1 µs
Dimensions (Inches)	1.57 x 0.78 x 1.45
Dimensions (Metric)	40.0 x 20.0 x 37.0
Weight (Ounces)	2.40
Weight (Gram)	68.0
Circuit Type	G2 Programable Digital
Motor Type	Coreless Metal Brush
Gear Material	Steel
Bearing Type	Dual Ball Bearing
Output Shaft (type / Ømm)	Standard 24
Case Material	Plastic / Aluminum
Dust / Water Resistance	Splash Proof
Connector Gauge (AWG) / Strand Count	22 / 60

Figure 78 – Datasheet of servomotor HS-7954SH used in the VSL Robot presented in 3.4. Retrieved from [202].

V. Circuit diagram of the control board of the VSL Arm
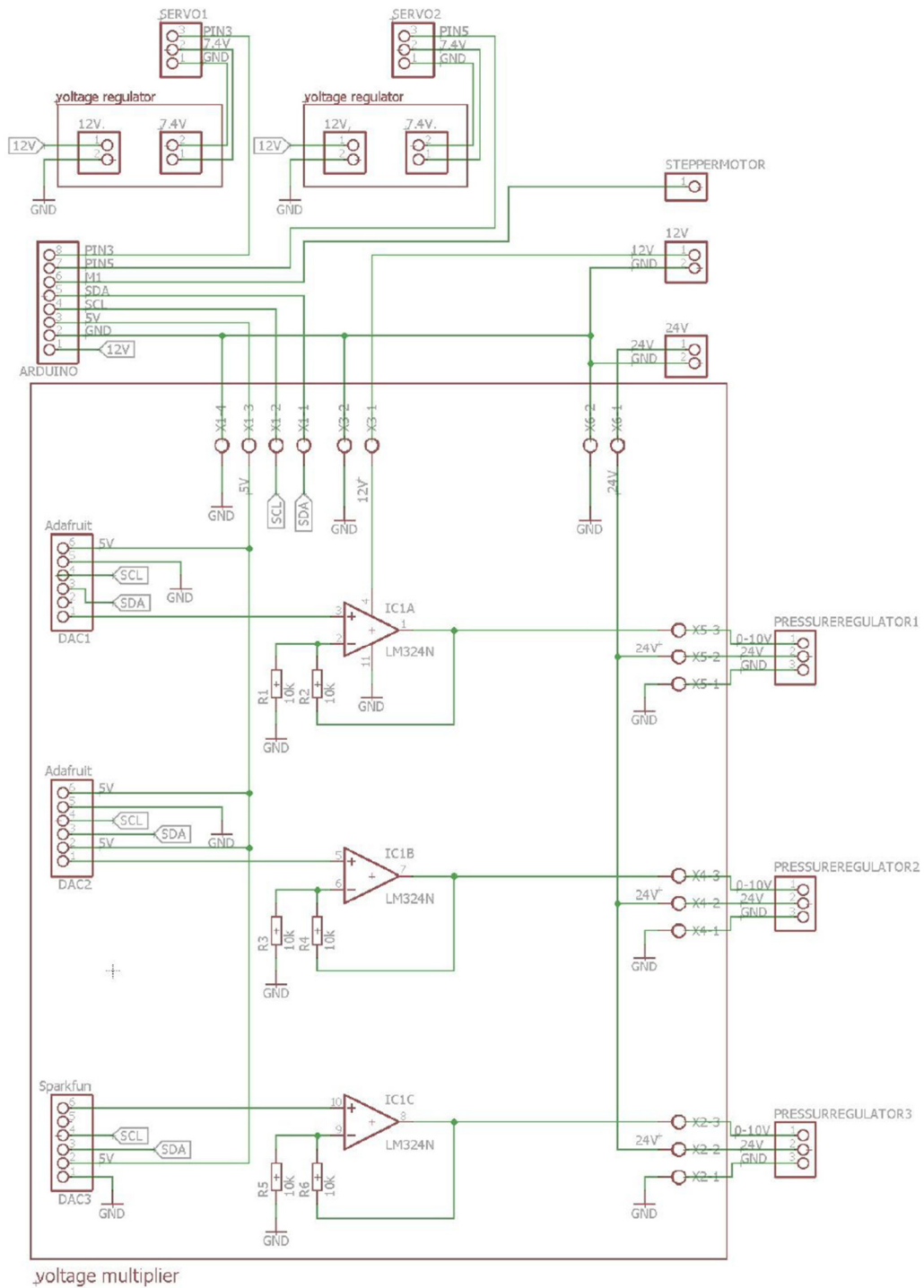
Figure 79 – Circuit diagram of the control board of the VSL Robot presented in 3.4.1 showing the connections between the Arduino board, the pressure regulators, the servomotors and the stepper motor, the voltage regulators and the DACs.

VI.   Arduino Code Collision VSL Robot Controller

```cpp
#include <Servo.h>
#include <Wire.h>
#include <Adafruit_MotorShield.h>
#include "utility/Adafruit_MS_PWMServoDriver.h"

#define servo1_pin 3
#define servo2_pin 5
#define servo_min 900
#define servo_max 2100
#define pressure_max 2
#define operating_pressure 1
// Voltage regulator 1 (red) A3
#define regulator_1 A3
// Voltage regulator 2 (black) A2
#define regulator_2 A2
#define read_cycles 100

Adafruit_MotorShield        AFMS        =
Adafruit_MotorShield();
Adafruit_StepperMotor       *myMotor    =
AFMS.getStepper(200, 2);

Servo servo1;
Servo servo2;

// Pressure
int sensorValue1 = 0;
int sensorValue2 = 0;
float voltageSensor1 = 0;
float voltageSensor2 = 0;
uint16_t voltage_ = 0;

// Kinematics
int mode = 0;
float degree_alpha = 0;
float degree_betha = 0;
float degree_gamma = 0;
float degree_old = 0;
float y = 0;
float alpha = 0;
float betha = 0;
float gamma = 0;

void setup()
{
    Serial.begin(9600);
    AFMS.begin();
    setbothpressure(operating_pressure);
    StartPosition();
    info();
}

void loop()
{
  if (Serial.available() > 0)
  {
    mode = Serial.parseInt();

    if (mode == 1 || mode == 2 || mode == 3)
    {
        Serial.print("Input the pressure: ");
        while (mode != 0)
        {
            if (Serial.available() > 0)
            {
                float voltage = Serial.parseFloat();
                if (mode == 1)
                {
                    set_pressure1(voltage);
                }
                if (mode == 2)
                {
                    set_pressure2(voltage);
                }
                if (mode == 3)
                {
                    setbothpressure(voltage);
                }
                mode = 0;
            }
        }
    }
    else if (mode == 4)
    {
        read_pressure(2);
    }
```

```
    else if (mode == 5)
    {
       set_pressure2(0);
       delay(2000);

    workspaceTest2Link_MinToMax();
    }
    else if (mode == 6)
    {
       set_pressure2(0.5);
       delay(2000);

    workspaceTest2Link_MinToMax();
    }
    else if (mode == 7)
    {
       set_pressure2(1);
       delay(2000);

    workspaceTest2Link_MinToMax();
    }
    else if (mode == 8)
    {
       set_pressure2(1.5);
       delay(2000);

    workspaceTest2Link_MinToMax();
    }
    else if (mode == 9)
    {
       set_pressure2(2);
       delay(2000);

    workspaceTest2Link_MinToMax();
    }
   mode = 0;
   info();
  }
}

void info(void)
{
 Serial.println();
 Serial.println("1: Set pressure link 1");
 Serial.println("2: Set pressure link 2");
```

```
 Serial.println("3: Set pressure link 1 and 2");
 Serial.println("4: Read Pressure Link 2");
 Serial.println("5: Test Link 2 - 0.0 Bar");
 Serial.println("6: Test Link 2 - 0.5 Bar");
 Serial.println("7: Test Link 2 - 1.0 Bar");
 Serial.println("8: Test Link 2 - 1.5 Bar");
 Serial.println("9: Test Link 2 - 2.0 Bar");
 Serial.println();
}
// -------- KINETIC ---------
void StartPosition(void)
{
   // Step-Motor
   degree_alpha = 0;
   alpha = degree_alpha;
   // Servo 1
   degree_betha = 90;
   betha = degree_betha;
   // Servo 2 - this will move from 0 to 180
   degree_gamma = 90;
   gamma = degree_gamma;

   // Servo 1
   degree_betha = (((float)1200 / 180) * betha) + 900;
   servo1.attach(servo1_pin, servo_min, servo_max);
   servo1.writeMicroseconds(degree_betha);

   delay(100);
   servo1.detach();

   // Servo 2
   degree_gamma = (((float)1200 / 180) * gamma) +
900;
   servo2.attach(servo2_pin, servo_min, servo_max);
   servo2.writeMicroseconds(degree_gamma);

   delay(100);
   servo2.detach();

   if (degree_old <= 1 && y < 0)
   {
   degree_old = 3200;
   }

   if (degree_old >= 3198 && y > 0)
```

```
  {
  degree_old = 0;
  }


  // Step-Motor
  degree_alpha = (((float)3200 / 360) * alpha);

  if (degree_alpha > degree_old)
  {
  for (int x = degree_old  ; x < degree_alpha ; x++ )
  {
    myMotor->onestep(FORWARD,
MICROSTEP);
  }
  }
  else if (degree_alpha < degree_old)
  {
  for (int x = degree_old  ; x > degree_alpha ; x-- )
  {
    myMotor->onestep(BACKWARD,
MICROSTEP);
  }
  }
  degree_old = degree_alpha;
}


void workspaceTest2Link_MinToMax(void)
{
  Serial.println("Test started - writeMicroseconds");
  servo2.attach(servo2_pin, servo_min, servo_max);
  gamma = 180;
  degree_gamma = (((float)1200 / 180) * gamma) +
900;
  servo2.writeMicroseconds(degree_gamma);
  servo2.detach();
  Serial.println("Test ended.");

  Serial.println("Test started - Write");
  servo2.attach(servo2_pin, servo_min, servo_max);
  gamma = 0;
  degree_gamma = (((float)1200 / 180) * gamma) +
900;
  //servo2.writeMicroseconds(degree_gamma);
  servo2.write(0);
  servo2.detach();
```

```
  Serial.println("Test ended.");

}

// -------- PRESSURE ---------
// Average pressure in bar
// regulator == 1 for pressure regulator 1
// regulator == 2 for pressure regulator 2
float avgpressure(int regulator)
{
  float avg_pressure = 0;
  int cycles = 50;
  if (regulator == 1)
  {
    for (int i=0; i < cycles; i++)
    {
      sensorValue1 = analogRead(regulator_1);
      voltageSensor1  =  ((5.0  /  810.0)  *
(sensorValue1 - 213));
      avg_pressure  =  avg_pressure  +
voltageSensor1;
    }
  }
  else if (regulator == 2)
  {
    for (int i=0; i < cycles; i++)
    {
      sensorValue2 = analogRead(regulator_2);
      voltageSensor2  =  ((5.0  /  810.0)  *
(sensorValue2 - 213));
      avg_pressure  =  avg_pressure  +
voltageSensor2;
    }
  }
  avg_pressure = avg_pressure / cycles;
  if (avg_pressure <= 0)
  {
    Serial.println("Error - The average pressure is
zero or below");
    Serial.println(avg_pressure);
  }
  return avg_pressure;
}

// Set the pressure, in bar, of link #1 and #2
```

```
void setbothpressure(float volt)
{
    set_pressure1(volt);
    set_pressure2(volt);
}


// Set the pressure in bar of the link #1
// The control of the input of the function is done here
void set_pressure1(float volt)
{
    if (volt > pressure_max)
    {
        volt = pressure_max;
        Serial.println("The bar must be between 0 and
the maximum.");
        Serial.println("It is now the maximum.");
    }
    else if (volt < 0)
    {
        volt = 0;
        Serial.println("The bar must be between 0 and
5.");
        Serial.println("It is now 0.");
    }
    voltage_ = ((float)(4095 / 5) * (volt));
    Wire.beginTransmission(0x61);
    Wire.write(64);
    Wire.write(voltage_ / 16);
    Wire.write(voltage_ % 16);
    Wire.endTransmission();
}


// Set the pressure in bar of the link #2
// The control of the input of the function is done here
void set_pressure2(float volt)
{
    if (volt > pressure_max)
    {
        volt = pressure_max;
        Serial.println("The bar must be between 0 and
the maximum.");
        Serial.println("It is setted to the max.");
    }
    else if (volt < 0)
    {
        volt = 0;
        Serial.println("The bar must be between 0 and
the maximum.");
        Serial.println("It is setted to 0.");
    }

    voltage_ = ((float)(4095 / 5) * (volt));
    Wire.beginTransmission(0x63);
    Wire.write(64);
    Wire.write(voltage_ / 16);
    Wire.write(voltage_ % 16);
    Wire.endTransmission();

}

// Read the preossure in bar of the link #2 for 5 sec
void read_pressure(int regulator)
{
    byte tmp[read_cycles];
    byte pressureLink2 = 0;
    byte pressureLink1 = 0;
    float printValue = 0;
    float tmp2[read_cycles];
    Serial.println("Start!");
    if (regulator == 1)
    {
        for (int i=0; i < read_cycles; i++)
        {
            sensorValue1 = analogRead(regulator_1);
            pressureLink1 = ((sensorValue1 - 213 + 2) /
4);
            tmp[i] = pressureLink1;
        }
    }
    else if (regulator == 2)
    {
        for (int i=0; i < read_cycles; i++)
        {
            sensorValue2 = analogRead(regulator_2);
            voltageSensor2 = ((5.0 / 810.0) *
(sensorValue2 - 213));
            pressureLink2 = ((sensorValue2 - 213 + 2) /
4);
            tmp[i] = pressureLink2;
            tmp2[i] = voltageSensor2;
```

```
          }
      }
      else
      {
          Serial.println("Error! Undefined regulator");
      }
    Serial.println("The results are:");
    for (int i=0; i < read_cycles; i++)
    {
          Serial.println(tmp[i]);
    }
     Serial.println("The results are:");
    for (int i=0; i < read_cycles; i++)
    {
          printValue = ((5.0 / 810.0) * (4 * tmp[i] - 2));
          Serial.println(printValue);
    }
     Serial.println("The OLD results are:");
    for (int i=0; i < read_cycles; i++)
    {
          Serial.println(tmp2[i]);
    }


    // Test time
 unsigned long    start = micros();
    for (int i=0; i < 1000; i++)
    {
          sensorValue2 = analogRead(regulator_2);
          voltageSensor2 = ((5.0 / 810.0) * (sensorValue2
- 213));
          //Serial.println(voltageSensor2);
    }

    unsigned long end = micros();
    unsigned long delta = end - start;
    Serial.println("Total time in microseconds:");
    Serial.println(delta);

    unsigned long deltaAvg = delta/1000;
    Serial.println("Average      total      time      in
microseconds:");
    Serial.println(deltaAvg);
}
```

VII.   King's College London – Ethical Approval – Confirmation Letter

Research Ethics Office

Franklin Wilkins Building
5.9 Waterloo Bridge Wing
Waterloo Road
London SE1 9NH
Telephone 020 7848 4020/4070/4077
rec@kcl.ac.uk

KING'S
College
LONDON

Agostino Stilli

28 February 2017

Dear Agostino

LRS-16/17-3631 - Experimental evaluation of the grasping performance of a novel soft exoskeleton for human hand rehabilitation and empowering

I am pleased to inform you that full approval for your project has been granted by the BDM Research Ethics Panel

- Ethical approval is granted for a period of **three years** from 28 February 2017 . You will not receive a reminder that your approval is about to lapse. It is your responsibility to apply for an extension prior to the project lapsing.
- You should report any untoward events or unforeseen ethical problems to the panel Chair, via the Research Ethics Office, within a week of occurrence. Information about the panel may be accessed at: http://www.kcl.ac.uk/innovation/research/support/ethics/committees/sshl/reps/index.aspx
- If you wish to change your project or request an extension of approval, please complete and submit a Modification Request to crec-lowrisk@kcl.ac.uk. Please quote your ethics reference number, found at the top of this letter, in all correspondence with the Research Ethics Office. Details of how to complete a modification request can be found at: http://www.kcl.ac.uk/innovation/research/support/ethics/applications/modifications.aspx
- All research should be conducted in accordance with the King's College London *Guidelines on Good Practice in Academic Research* available at: http://www.kcl.ac.uk/college/policyzone/assets/files/research/good%20practice%20Sept%2009%20FINAL.pdf

Please note that we may, for auditing purposes, contact you to ascertain the status of your research.

We wish you every success with your research.

Best wishes,

BDM Research Ethics Panel REP Reviewers

Page 1 of 1

VIII. Letter from the Director of the Rehabilitation Centre IRCCS "Don Carlo Gnocchi", Florence, Italy

S.O.D. Complessa di Riabilitazione Generale
A.O.U. Careggi - Firenze
Unità di Riabilitazione Intensiva ad Alta Specializzazione
Fondazione Don Carlo Gnocchi - I.R.C.C.S.
Direttore Prof. Claudio Macchi

Coordinatrice Centri UGCA
Fondazione Don Gnocchi
Prof.ssa Anna Mazzucchi
Caposala
Sig. Mirka Greczyn
Staff medico di reparto
Dr. Barbara Binazzi
Dr.ssa Bahia Hakiki
Dr. Andrea Marella
Dr. Emilio Portaccio
Dr.ssa Annamaria Romoli
Dr. Ariela Tofani
Coordinatore Fisioterapisti
Carla Castellani
Logoterapisti
Loredana Croci
Irene Galli
Azzurra Morrocchesi
Maria Pia Taglioli
Medici Psicologi Clinici
Prof. Stefano Lera
Dr.ssa Rosanna Intini
Neuropsicologo
Dr. Marco Borsotti
Consulente Nutrizionista
Dr. Maria Luisa Eliana Luisi
Consulente
Neurofisiopatologia
Dr. Antonello Grippo

Florence 17.8.2017

To whom it may concern in the Editorial Office of the Soft Robotics Journal,
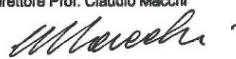
I, Professor Claudio Macchi, Director of the Rehabilitation Centre IRCCS "Don Carlo Gnocchi", part of the Don Carlo Gnocchi Foundation, Via di Scandicci 269, 50143, Florence, Italy, am writing this letter to confirm that the one-time qualitative tests conducted on the patient Massimo Bianchini in May 2017 using the exoskeleton system called "INFLEXOGlove", in compliance with the institute regulations, did not require approval from the board of ethics. The tests were conducted and supervised by trained physicians and written informed consent was obtained from the patient, who regularly collaborates with our research centre

Best regards

Professor. Claudio Macchi

Mail: cmacchi@dongnocchi.it

Centro di Riabilitazione Don Gnocchi - Firenze
Istituto di Ricovero e Cura a Carattere Scientifico
Dipartimento di Riabilitazione
Direttore Prof. Claudio Macchi

Istituto di Ricovero e Cura a Carattere Scientifico
Via di Scandicci, 269 • 50143 Firenze
DIREZIONE tel. 055.7393701 • fax 055.7393001
EMAIL: direzione.polotoscana@dongnocchi.it
CENTRALINO tel. 055.73931

CSQ
IQNet
SISTEMA QUALITA' CERTIFICATO
UNI EN ISO 900

MSC-UGCA-161 Rev 1 Sett.15

IX. Informed Consent Signed by the Massimo Bianchini, Male, 54 y/o, Affected by Type 2 Spinal Muscular Atrophy with Clenched Fist Deformity (Forearm Tendon Retroaction).

Studio: Test ergonomico di un sistema di movimentazione per la mano con attuazione pneumatica
Centro: **IRCCS Centro di Riabilitazione Don Carlo Gnocchi - Firenze**
Documento: Foglio Informativo e Consenso Informato - Versione: 24/05/2017

MODULO DI CONSENSO INFORMATO per la partecipazione allo studio:

Test ergonomico di un sistema di movimentazione per la mano con attuazione pneumatica

PER I SOGGETTI ADULTI

Io sottoscritto/a: ___MASSIMO BIANCHINI___
Cognome e Nome in stampatello del soggetto adulto partecipante.

nato/a a, il: ___12-06-1963 FIRENZE___
Luogo e data di nascita del soggetto adulto partecipante.

DICHIARO QUANTO SEGUE:

1. ho letto e compreso il foglio informativo di cui questo modulo è parte integrante;

2. ho avuto la possibilità di porre domande e di chiedere spiegazioni al/alla Dr./D.ssa _____ dal/dalla quale ho ricevuto risposte soddisfacenti;

3. mi sono state illustrate la natura, lo scopo e la durata dello studio, le procedure che saranno seguite, il trattamento previsto per i partecipanti e il tipo di collaborazione che ad essi sarà richiesta;

4. ho compreso che la mia partecipazione allo studio è libera e volontaria e che in qualsiasi momento posso decidere di ritirarmi dallo studio senza essere in alcun modo privato/a delle cure e dell'assistenza di cui ho bisogno e dell'eventuale accesso a nuove prospettive diagnostiche e/o terapeutiche e senza che siano compromessi i miei diritti e il mio rapporto con il medico e con gli operatori sanitari;

5. ai sensi del Decreto Legislativo n.196/2003 e successive modificazioni, acconsento al trattamento dei miei dati personali e sensibili raccolti nell'ambito di questo studio nei termini e nei modi indicati nel presente documento.

Tutto ciò premesso, nella mia piena capacità di intendere e di volere e senza alcuna forma di condizionamento o coercizione, accetto la proposta di partecipare allo studio descritto nel presente documento.

Luogo e data: ___CNR 25-05-2017___   Firma: ___Massimo Biel___

PARTE RISERVATA ALL'OPERATORE CHE HA PRESENTATO L'INFORMATIVA

Io sottoscritto/a Dr/D.ssa ___GERLI FILIPPO___ *(Cognome e Nome in stampatello)*
DICHIARO:

a. di avere spiegato alla persona sopraindicata la natura e lo scopo dello studio, nonché le procedure che saranno adottate e il tipo di collaborazione che sarà richiesta;

b. di non avere cercato di influenzare o di costringere in alcun modo la persona sopra indicata per indurla a manifestare il suo consenso alla partecipazione allo studio;

c. di rilasciare alla persona sopraindicata una copia firmata e datata del presente modulo insieme al foglio informativo.

Luogo e data: ___CNr 25-05-2017___   Firma: _____

- 4 -

.

Bibliography

[1]   C. Laschi, "Soft Robotics: from scientific challenges to technological applications," in *SPIE Defense+ Security*, 2016, p. 983626.

[2]   J. Rossiter and H. Hauser, "Soft robotics—the next industrial revolution," *IEEE Robot. Autom. Mag*, vol. 23, pp. 17–20, 2016.

[3]   B. Trimmer, "A Journal of Soft Robotics: Why Now?," *Soft Robot.*, vol. 1, no. P, pp. 1–4, Jul. 2013.

[4]   M. T. Tolley *et al.*, "A resilient, untethered soft robot," *Soft Robot.*, vol. 1, no. 3, pp. 213–223, 2014.

[5]   R. V Martinez *et al.*, "Robotic tentacles with three-dimensional mobility based on flexible elastomers.," *Adv. Mater.*, vol. 25, no. 2, pp. 205–12, Jan. 2013.

[6]   J. E. Kresta, D. M. Rojas, R. Moliner, C. Jayakody, and D. Myers, "High resilient silicone foam and process for preparing same." Google Patents, 01-Jul-2008.

[7]   H. Sun and D. Rigby, "Polysiloxanes: ab initio force field and structural, conformational and thermophysical properties," *Spectrochim. Acta Part*

A Mol. Biomol. Spectrosc., vol. 53, no. 8, pp. 1301–1323, 1997.

[8] L. G. Hanu, G. P. Simon, and Y.-B. Cheng, "Thermal stability and flammability of silicone polymer composites," *Polym. Degrad. Stab.*, vol. 91, no. 6, pp. 1373–1379, 2006.

[9] D. E. Cagliostro, "Waterproof silicone coatings of thermal insulation and vaporization method." Google Patents, 17-Aug-1999.

[10] S. Kumagai and N. Yoshimura, "Influence of single and multiple environmental stresses on tracking and erosion of RTV silicone rubber," *IEEE Trans. Dielectr. Electr. Insul.*, vol. 6, no. 2, pp. 211–225, 1999.

[11] S. Seok, C. D. Onal, R. Wood, D. Rus, and S. Kim, "Peristaltic locomotion with antagonistic actuators in soft robotics," in *Proceedings - IEEE International Conference on Robotics and Automation*, 2010, vol. 60, pp. 1228–1233.

[12] C. Laschi, M. Cianchetti, B. Mazzolai, L. Margheri, M. Follador, and P. Dario, "Soft Robot Arm Inspired by the Octopus," *Adv. Robot.*, vol. 26, no. 7, pp. 709–727, Jan. 2012.

[13] K. C. Galloway, P. Polygerinos, C. J. Walsh, and R. J. Wood, "Mechanically programmable bend radius for fiber-reinforced soft actuators," *2013 16th Int. Conf. Adv. Robot. ICAR 2013*, 2013.

[14] H. K. Yap *et al.*, "A Fully Fabric-Based Bidirectional Soft Robotic Glove for Assistance and Rehabilitation of Hand Impaired Patients," *IEEE Robot. Autom. Lett.*, vol. 2, no. 3, pp. 1383–1390, 2017.

[15]   Y.-L. Park *et al.*, "Design and control of a bio-inspired soft wearable robotic device for ankle–foot rehabilitation," *Bioinspir. Biomim.*, vol. 9, no. 1, p. 16007, 2014.

[16]   M. D. Grissom *et al.*, "Design and experimental testing of the OctArm soft robot manipulator," in *Defense and Security Symposium*, 2006, p. 62301F–62301F.

[17]   M. Cianchetti *et al.*, "Soft Robotics Technologies to Address Shortcomings in Today's Minimally Invasive Surgery: The STIFF-FLOP Approach," *Soft Robot.*, vol. 1, no. 2, pp. 122–131, 2014.

[18]   K. Suzumori, S. Endo, T. Kanda, N. Kato, and H. Suzuki, "A bending pneumatic rubber actuator realizing soft-bodied manta swimming robot," in *Robotics and Automation, 2007 IEEE International Conference on*, 2007, pp. 4975–4980.

[19]   E. Brown *et al.*, "Universal robotic gripper based on the jamming of granular material," *Proc. Natl. Acad. Sci.*, vol. 107, no. 44, pp. 18809–18814, 2010.

[20]   www.pneubotics.com, "Pneubotics." [Online]. Available: http://www.pneubotics.com/. [Accessed: 23-Jun-2017].

[21]   www.festo.com, "FESTO." [Online]. Available: www.festo.com. [Accessed: 23-Jun-2017].

[22]   www.imdb.com/title/tt2245084/, "Big Hero 6." [Online]. Available: http://www.imdb.com/title/tt2245084/. [Accessed: 13-Aug-2017].

[23] T. Arnold and M. Scheutz, "The Tactile Ethics of Soft Robotics: Designing Wisely for Human–Robot Interaction," *Soft Robot.*

[24] R. Cieślak and A. Morecki, "Elephant trunk type elastic manipulator - a tool for bulk and liquid materials transportation," *Robotica*, vol. 17, no. 1. pp. 11–16, 1999.

[25] G. Immega and K. Antonelli, "The KSI tentacle manipulator," *Proc. 1995 IEEE Int. Conf. Robot. Autom.*, vol. 3, pp. 3149–3154, 1995.

[26] C. Laschi, B. Mazzolai, V. Mattoli, M. Cianchetti, and P. Dario, "Design of a biomimetic robotic octopus arm.," *Bioinspir. Biomim.*, vol. 4, no. 1, p. 15006, 2009.

[27] R. Buckingham, "Snake arm robots," *Ind. Robot An Int. J.*, vol. 29, no. 3, pp. 242–245, 2002.

[28] S. Hirose, "Biologically Inspired Robots: Snake-Like Locomotors and Manipulators," *Appl. Mech. Rev.*, vol. 48, no. 3, pp. B27–B27, 1995.

[29] H. F. Schulte, "The characteristic of the McKibben artificial muscle," *Appl. Extern. power prosthetics Orthot.*, pp. 94–115, 1962.

[30] B. Mosadegh *et al.*, "Pneumatic networks for soft robotics that actuate rapidly," *Adv. Funct. Mater.*, vol. 24, no. 15, pp. 2163–2170, 2014.

[31] D. G. Caldwell, G. A. Medrano-Cerda, and M. Goodwin, "Control of pneumatic muscle actuators," *IEEE Control Systems Magazine*, vol. 15, no. 1. pp. 40–48, 1995.

[32]   R. Kang, D. T. Branson, T. Zheng, E. Guglielmino, and D. G. Caldwell, "Design, modeling and control of a pneumatically actuated manipulator inspired by biological continuum structures.," *Bioinspir. Biomim.*, vol. 8, no. 3, p. 36008, Sep. 2013.

[33]   R. K. Katzschmann, A. D. Marchese, and D. Rus, "Hydraulic autonomous soft robotic fish for 3D swimming," in *Experimental Robotics*, 2016, pp. 405–420.

[34]   P. Polygerinos, Z. Wang, K. C. Galloway, R. J. Wood, and C. J. Walsh, "Soft robotic glove for combined assistance and at-home rehabilitation," *Rob. Auton. Syst.*, vol. 73, pp. 135–143, 2015.

[35]   F. Renda, M. Cianchetti, M. Giorelli, a Arienti, and C. Laschi, "A 3D steady-state model of a tendon-driven continuum soft manipulator inspired by the octopus arm.," *Bioinspir. Biomim.*, vol. 7, no. 2, p. 25006, Jun. 2012.

[36]   W. McMahan, B. a. Jones, and I. D. Walker, "Design and implementation of a multi-section continuum robot: Air-Octor," *2005 IEEE/RSJ Int. Conf. Intell. Robot. Syst.*, pp. 2578–2585, 2005.

[37]   A. Ataollahi *et al.*, "3-DOF MR-Compatible Multi-Segment Cardiac Catheter Steering Mechanism.," *IEEE Trans. Biomed. Eng.*, no. c, Aug. 2013.

[38]   A. Loeve, P. Breedveld, and J. Dankelman, "Scopes too flexible...and too stiff.," *IEEE Pulse*, vol. 1, no. 3, pp. 26–41, 2010.

[39]   Y. Bar-Cohen, "Electroactive polymers as artificial muscles-reality and

challenges," 2001.

[40]   B. Liu, S. A. Boggs, and M. T. Shaw, "Electrorheological properties of anisotropically filled elastomers," *IEEE Trans. Dielectr. Electr. Insul.*, vol. 8, no. 2, pp. 173–181, 2001.

[41]   C. Majidi and R. J. Wood, "Tunable elastic stiffness with microconfined magnetorheological domains at low magnetic field," *Appl. Phys. Lett.*, vol. 97, no. 16, p. 164104, 2010.

[42]   M. Follador, M. Cianchetti, A. Arienti, and C. Laschi, "A general method for the design and fabrication of shape memory alloy active spring actuators," *Smart Materials and Structures*, vol. 21, no. 11. p. 115029, 2012.

[43]   H. Lipson, "Challenges and opportunities for design, simulation, and fabrication of soft robots," *Soft Robot.*, vol. 1, no. 1, pp. 21–27, 2014.

[44]   M. Manti, V. Cacucciolo, and M. Cianchetti, "Stiffening in soft robotics: A review of the state of the art," *IEEE Robot. Autom. Mag.*, vol. 23, no. 3, pp. 93–106, 2016.

[45]   G. Gerboni, T. Ranzani, A. Diodato, G. Ciuti, M. Cianchetti, and A. Menciassi, "Modular soft mechatronic manipulator for minimally invasive surgery (MIS): overall architecture and development of a fully integrated soft module," *Meccanica*, vol. 50, no. 11, pp. 2865–2878, 2015.

[46]   Y. Elsayed *et al.*, "Finite element analysis and design optimization of a pneumatically actuating silicone module for robotic surgery

applications," *Soft Robot.*, vol. 1, no. 4, pp. 255–262, 2014.

[47] N. Cheney, J. Bongard, and H. Lipson, "Evolving soft robots in tight spaces," in *Proceedings of the 2015 annual conference on Genetic and Evolutionary Computation*, 2015, pp. 935–942.

[48] R. Deimel and O. Brock, "A Novel Type of Compliant , Underactuated Robotic Hand for Dexterous Grasping," *Proc. Robot. Sci. Syst.*, p. p18, 2014.

[49] R. Ham, T. Sugar, B. Vanderborght, K. Hollander, and D. Lefeber, "Compliant actuator designs," *IEEE Robot. Autom. Mag.*, vol. 16, no. 3, 2009.

[50] S. Wolf *et al.*, "Variable Stiffness Actuators: Review on Design and Components," *IEEE/ASME Trans. Mechatronics*, vol. 21, no. 5, pp. 2418–2430, 2016.

[51] C. Laschi, B. Mazzolai, and M. Cianchetti, "Soft robotics: Technologies and systems pushing the boundaries of robot abilities," *Sci. Robot.*, vol. 1, no. 1, p. eaah3690, 2016.

[52] P. Beyl, M. Van Damme, R. Van Ham, B. Vanderborght, and D. Lefeber, "Pleated pneumatic artificial muscle-based actuator system as a torque source for compliant lower limb exoskeletons," *IEEE/ASME Trans. Mechatronics*, vol. 19, no. 3, pp. 1046–1056, 2014.

[53] C.-P. Chou and B. Hannaford, "Measurement and modeling of McKibben pneumatic artificial muscles," *IEEE Trans. Robot. Autom.*, vol. 12, no. 1, pp. 90–102, 1996.

[54] M. Mori, K. Suzumori, M. Takahashi, and T. Hosoya, "Very high force hydraulic McKibben artificial muscle with a p-phenylene-2, 6-benzobisoxazole cord sleeve," *Adv. Robot.*, vol. 24, no. 1–2, pp. 233–254, 2010.

[55] B. Tondu and P. Lopez, "Modeling and control of McKibben artificial muscle robot actuators," *IEEE Control Syst.*, vol. 20, no. 2, pp. 15–38, 2000.

[56] M. Luo, W. Tao, F. Chen, T. K. Khuu, S. Ozel, and C. D. Onal, "Design improvements and dynamic characterization on fluidic elastomer actuators for a soft robotic snake," in *Technologies for Practical Robot Applications (TePRA), 2014 IEEE International Conference on*, 2014, pp. 1–6.

[57] A. D. Marchese, R. K. Katzschmann, and D. Rus, "A recipe for soft fluidic elastomer robots," *Soft Robot.*, vol. 2, no. 1, pp. 7–25, 2015.

[58] R. Deimel and O. Brock, "A compliant hand based on a novel pneumatic actuator," *Proc. - IEEE Int. Conf. Robot. Autom.*, pp. 2047–2053, 2013.

[59] C. D. Onal and D. Rus, "A modular approach to soft robots," in *Biomedical Robotics and Biomechatronics (BioRob), 2012 4th IEEE RAS & EMBS International Conference on*, 2012, pp. 1038–1045.

[60] M. Cianchetti, T. Ranzani, G. Gerboni, I. De Falco, C. Laschi, and A. Menciassi, "STIFF-FLOP surgical manipulator: Mechanical design and experimental characterization of the single module," *IEEE Int. Conf. Intell. Robot. Syst.*, pp. 3576–3581, 2013.

[61] F. Ilievski, A. D. Mazzeo, R. F. Shepherd, X. Chen, and G. M. Whitesides, "Soft Robotics for Chemists," *Angew. Chemie*, vol. 123, no. 8, pp. 1930–1935, Feb. 2011.

[62] R. F. Shepherd *et al.*, "Multigait soft robot," *Proc. Natl. Acad. Sci.*, vol. 108, no. 51, pp. 20400–20403, 2011.

[63] A. Ölander, "An electrochemical investigation of solid cadmium-gold alloys," *J. Am. Chem. Soc.*, vol. 54, no. 10, pp. 3819–3833, 1932.

[64] K. Otsuka and C. M. Wayman, *Shape memory materials*. Cambridge university press, 1999.

[65] L. B. Vernon and H. M. Vernon, "Process of manufacturing articles of thermoplastic synthetic resins." Google Patents, 18-Mar-1941.

[66] L. C. Chang and T. A. Read, "Behavior of the elastic properties of AuCd," *Trans Met Soc AIME*, vol. 191, p. 47, 1951.

[67] O. Nittono and Y. Koyama, "Cubic-Tetragonal Transformation and Shape Memory Behavior in Indium-Thallium and Indium-Cadmium Alloys," *Trans. Japan Inst. Met.*, vol. 23, no. 6, pp. 285–295, 1982.

[68] T. A. Schroeder and C. M. Wayman, "The formation of martensite and the mechanism of the shape memory effect in single crystals of Cu-Zn alloys," *Acta Metall.*, vol. 25, no. 12, pp. 13751383–13811391, 1977.

[69] G. Clement, P. Nandot, and J.-M. Welter, "The Cu--Al--Ni Shape Memory Alloys," *Mater. Tech.(Paris)*, vol. 81, no. 6, pp. 65–76, 1993.

[70] K. E. Wilkes and P. K. Liaw, "The fatigue behavior of shape-memory alloys," *JOM*, vol. 52, no. 10, pp. 45–51, 2000.

[71] W. J. Buehler, J. V Gilfrich, and R. C. Wiley, "Effect of low-temperature phase changes on the mechanical properties of alloys near composition TiNi," *J. Appl. Phys.*, vol. 34, no. 5, pp. 1475–1477, 1963.

[72] G. B. Kauffman and I. Mayo, "The story of nitinol: the serendipitous discovery of the memory metal and its applications," *Chem. Educ.*, vol. 2, no. 2, pp. 1–21, 1997.

[73] J. M. Jani, M. Leary, A. Subic, and M. A. Gibson, "A review of shape memory alloy research, applications and opportunities," *Mater. Des.*, vol. 56, pp. 1078–1113, 2014.

[74] J. A. Walker, K. J. Gabriel, and M. Mehregany, "Thin-film processing of TiNi shape memory alloy," *Sensors Actuators A Phys.*, vol. 21, no. 1–3, pp. 243–246, 1990.

[75] M. Ehrlich *et al.*, "Endovascular stent graft repair for aneurysms on the descending thoracic aorta," *Ann. Thorac. Surg.*, vol. 66, no. 1, pp. 19–24, 1998.

[76] Y.-S. Kim *et al.*, "Nitinol spring rod dynamic stabilization system and Nitinol memory loops in surgical treatment for lumbar disc disorders: short-term follow up," *Neurosurg. Focus*, vol. 22, no. 1, pp. 1–9, 2007.

[77] Y. Fu, H. Du, W. Huang, S. Zhang, and M. Hu, "TiNi-based thin films in MEMS applications: a review," *Sensors Actuators A Phys.*, vol. 112, no. 2, pp. 395–408, 2004.

[78] J. Ma, I. Karaman, and R. D. Noebe, "High temperature shape memory alloys," *Int. Mater. Rev.*, vol. 55, no. 5, pp. 257–315, 2010.

[79] K. Ullakko, J. K. Huang, V. V Kokorin, and R. C. O'handley, "Magnetically controlled shape memory effect in Ni2MnGa intermetallics," *Scr. Mater.*, vol. 36, no. 10, pp. 1133–1138, 1997.

[80] J. Tellinen, I. Suorsa, A. Jääskeläinen, I. Aaltio, and K. Ullakko, "Basic properties of magnetic shape memory actuators," in *8th international conference ACTUATOR*, 2002, pp. 566–569.

[81] O. Heczko and L. Straka, "Temperature dependence and temperature limits of magnetic shape memory effect," *J. Appl. Phys.*, vol. 94, no. 11, pp. 7139–7143, 2003.

[82] A. Lendlein and S. Kelch, "Shape-memory polymers," *Angew. Chemie Int. Ed.*, vol. 41, no. 12, pp. 2034–2057, 2002.

[83] A. Lendlein and R. Langer, "Biodegradable, elastic shape-memory polymers for potential biomedical applications," *Science (80-.).*, vol. 296, no. 5573, pp. 1673–1676, 2002.

[84] G. Li and N. Uppu, "Shape memory polymer based self-healing syntactic foam: 3-D confined thermomechanical characterization," *Compos. Sci. Technol.*, vol. 70, no. 9, pp. 1419–1427, 2010.

[85] I. Bellin, S. Kelch, R. Langer, and A. Lendlein, "Polymeric triple-shape materials," *Proc. Natl. Acad. Sci.*, vol. 103, no. 48, pp. 18043–18047, 2006.

[86] T. Pretsch, "Triple-shape properties of a thermoresponsive poly (ester urethane)," *Smart Mater. Struct.*, vol. 19, no. 1, p. 15006, 2009.

[87] R. Mohr, K. Kratz, T. Weigel, M. Lucka-Gabor, M. Moneke, and A. Lendlein, "Initiation of shape-memory effect by inductive heating of magnetic nanoparticles in thermoplastic polymers," *Proc. Natl. Acad. Sci. U. S. A.*, vol. 103, no. 10, pp. 3540–3545, 2006.

[88] A. Lendlein, H. Jiang, O. Jünger, and R. Langer, "Light-induced shape-memory polymers," *Nature*, vol. 434, no. 7035, pp. 879–882, 2005.

[89] H. Lv, J. Leng, Y. Liu, and S. Du, "Shape-memory polymer in response to solution," *Adv. Eng. Mater.*, vol. 10, no. 6, pp. 592–595, 2008.

[90] A. Lai, Z. Du, C. L. Gan, and C. A. Schuh, "Shape memory and superelastic ceramics at small scales," *Science (80-.).*, vol. 341, no. 6153, pp. 1505–1508, 2013.

[91] C. Keplinger, M. Kaltenbrunner, N. Arnold, and S. Bauer, "Röntgen's electrode-free elastomer actuators without electromechanical pull-in instability," *Proc. Natl. Acad. Sci.*, vol. 107, no. 10, pp. 4505–4510, 2010.

[92] C. K. Chiang *et al.*, "Electrical conductivity in doped polyacetylene," *Phys. Rev. Lett.*, vol. 39, no. 17, p. 1098, 1977.

[93] K. Kaneto, "Research trends of soft actuators based on electroactive polymers and conducting polymers," in *Journal of Physics: Conference Series*, 2016, vol. 704, no. 1, p. 12004.

[94] G. Kovacs, P. Lochmatter, and M. Wissler, "An arm wrestling robot

driven by dielectric elastomer actuators," *Smart Mater. Struct.*, vol. 16, no. 2, p. S306, 2007.

[95]   A. J. Lovinger, "Ferroelectric polymers," *Science (80-.).*, vol. 220, no. 4602, pp. 1115–1121, 1983.

[96]   E. Fukada, "History and recent progress in piezoelectric polymers," *IEEE Trans. Ultrason. Ferroelectr. Freq. Control*, vol. 47, no. 6, pp. 1277–1290, 2000.

[97]   R. Vertechy, G. Berselli, V. Parenti Castelli, and M. Bergamasco, "Continuum thermo-electro-mechanical model for electrostrictive elastomers," *J. Intell. Mater. Syst. Struct.*, vol. 24, no. 6, pp. 761–778, 2013.

[98]   Z. Suo, "Theory of dielectric elastomers," *Acta Mech. Solida Sin.*, vol. 23, no. 6, pp. 549–578, 2010.

[99]   S. Ahn, R. M. Kasi, S.-C. Kim, N. Sharma, and Y. Zhou, "Stimuli-responsive polymer gels," *Soft Matter*, vol. 4, no. 6, pp. 1151–1157, 2008.

[100] S. Nemat-Nasser, "Micromechanics of actuation of ionic polymer-metal composites," *J. Appl. Phys.*, vol. 92, no. 5, pp. 2899–2915, 2002.

[101] Y. Bahramzadeh and M. Shahinpoor, "A review of ionic polymeric soft actuators and sensors," *Soft Robot.*, vol. 1, no. 1, pp. 38–52, 2014.

[102] B. J. Akle, M. D. Bennett, and D. J. Leo, "High-strain ionomeric–ionic liquid electroactive actuators," *Sensors Actuators A Phys.*, vol. 126, no. 1, pp. 173–181, 2006.

[103] M. Shahinpoor, Y. Bar-Cohen, J. O. Simpson, and J. Smith, "Ionic polymer-metal composites (IPMCs) as biomimetic sensors, actuators and artificial muscles-a review," *Smart Mater. Struct.*, vol. 7, no. 6, p. R15, 1998.

[104] T. Fukushima, K. Asaka, A. Kosaka, and T. Aida, "Fully Plastic Actuator through Layer-by-Layer Casting with Ionic-Liquid-Based Bucky Gel," *Angew. Chemie Int. Ed.*, vol. 44, no. 16, pp. 2410–2413, 2005.

[105] J. Ru, Y. Wang, L. Chang, H. Chen, and D. Li, "Preparation and characterization of water-soluble carbon nanotube reinforced Nafion membranes and so-based ionic polymer metal composite actuators," *Smart Mater. Struct.*, vol. 25, no. 9, p. 95006, 2016.

[106] H. In, B. B. Kang, M. Sin, and K. J. Cho, "Exo-Glove: A wearable robot for the hand with a soft tendon routing system," *IEEE Robot. Autom. Mag.*, vol. 22, no. 1, 2015.

[107] D. B. Camarillo, C. F. Milne, C. R. Carlson, M. R. Zinn, and J. K. Salisbury, "Mechanics Modeling of Tendon-Driven Continuum Manipulators," *IEEE Trans. Robot.*, vol. 24, no. 6, pp. 1262–1273, Dec. 2008.

[108] A. T. Asbeck, S. M. M. De Rossi, I. Galiana, Y. Ding, and C. J. Walsh, "Stronger, smarter, softer: next-generation wearable robots," *IEEE Robot. Autom. Mag.*, vol. 21, no. 4, pp. 22–33, 2014.

[109] I. Galiana, F. L. Hammond, R. D. Howe, and M. B. Popovic, "Wearable soft robotic device for post-stroke shoulder rehabilitation: Identifying misalignments," in *Intelligent Robots and Systems (IROS), 2012*

IEEE/RSJ International Conference on, 2012, pp. 317–322.

[110] R. Pelrine, F. Carpi, D. De Rossi, R. Kornbluh, R. Pelrine, and P. Sommer-Larsen, "Variable stiffness mode: devices and applications," in *Dielectric elastomers as electromechanical transducers: fundamentals, materials, devices, models and applications of an emerging electroactive polymer technology*, Oxford, Elsevier, 2008.

[111] Q. Pei, M. Rosenthal, R. Pelrine, S. Stanford, and R. Kornbluh, "Multifunctional electroelastomer roll actuators and their application for biomimetic walking robots," SRI INTERNATIONAL MENLO PARK CA, 2003.

[112] F. Carpi, G. Frediani, C. Gerboni, J. Gemignani, and D. De Rossi, "Enabling variable-stiffness hand rehabilitation orthoses with dielectric elastomer transducers," *Med. Eng. Phys.*, vol. 36, no. 2, pp. 205–211, 2014.

[113] K. Jung, J. C. Koo, J. Nam, Y. K. Lee, and H. R. Choi, "Artificial annelid robot driven by soft actuators.," *Bioinspir. Biomim.*, vol. 2, no. 2, pp. S42–S49, 2007.

[114] I. A. Anderson, T. A. Gisby, T. G. McKay, B. M. O'Brien, and E. P. Calius, "Multi-functional dielectric elastomer artificial muscles for soft and smart machines," *J. Appl. Phys.*, vol. 112, no. 4, p. 41101, 2012.

[115] J. D. Greer, T. K. Morimoto, A. M. Okamura, and E. W. Hawkes, "Series pneumatic artificial muscles (sPAMs) and application to a soft continuum robot," in *Robotics and Automation (ICRA), 2017 IEEE International Conference on*, 2017, pp. 5503–5510.

[116] T. Doi, S. Wakimoto, K. Suzumori, and K. Mori, "Proposal of flexible robotic arm with thin McKibben actuators mimicking octopus arm structure," in *Intelligent Robots and Systems (IROS), 2016 IEEE/RSJ International Conference on*, 2016, pp. 5503–5508.

[117] N. Correll, Ç. D. Önal, H. Liang, E. Schoenfeld, and D. Rus, "Soft autonomous materials—using active elasticity and embedded distributed computation," in *Experimental Robotics*, 2014, pp. 227–240.

[118] K. Suzumori, S. Wakimoto, K. Miyoshi, and K. Iwata, "Long bending rubber mechanism combined contracting and extending tluidic actuators," in *Intelligent Robots and Systems (IROS), 2013 IEEE/RSJ International Conference on*, 2013, pp. 4454–4459.

[119] S. Wakimoto, I. Kumagai, and K. Suzumori, "Development of large intestine endoscope changing its stiffness," in *Robotics and Biomimetics (ROBIO), 2009 IEEE International Conference on*, 2009, pp. 2320–2325.

[120] I. Kumagai, S. Wakimoto, and K. Suzumori, "Development of large intestine endoscope changing its stiffness-2nd report: Improvement of stiffness change device and insertion experiment," in *2010 IEEE International Conference on Robotics and Biomimetics*, 2010.

[121] J. Nagase, S. Wakimoto, T. Satoh, N. Saga, and K. Suzumori, "Design of a variable-stiffness robotic hand using pneumatic soft rubber actuators," *Smart Mater. Struct.*, vol. 20, no. 10, p. 105015, 2011.

[122] Y. Shan *et al.*, "Variable stiffness structures utilizing fluidic flexible matrix composites," *J. Intell. Mater. Syst. Struct.*, vol. 20, no. 4, pp. 443–456, 2009.

[123] M. Cianchetti, M. Calisti, L. Margheri, M. Kuba, and C. Laschi, "Bioinspired locomotion and grasping in water: the soft eight-arm OCTOPUS robot," *Bioinspir. Biomim.*, vol. 10, no. 3, p. 35003, 2015.

[124] B. Mazzolai, L. Margheri, M. Cianchetti, P. Dario, and C. Laschi, "Soft-robotic arm inspired by the octopus: II. From artificial requirements to innovative technological solutions," *Bioinspir. Biomim.*, vol. 7, no. 2, p. 25005, 2012.

[125] M. Cianchetti, A. Licofonte, M. Follador, F. Rogai, and C. Laschi, "Bioinspired soft actuation system using shape memory alloys," in *Actuators*, 2014, vol. 3, no. 3, pp. 226–244.

[126] M. Henke and G. Gerlach, "A multi-layered variable stiffness device based on smart form closure actuators," *J. Intell. Mater. Syst. Struct.*, vol. 27, no. 3, pp. 375–383, 2016.

[127] T. Umedachi, V. Vikas, and B. A. Trimmer, "Highly deformable 3-d printed soft robot generating inching and crawling locomotions with variable friction legs," in *Intelligent Robots and Systems (IROS), 2013 IEEE/RSJ International Conference on*, 2013, pp. 4590–4595.

[128] W. Wang, H. Rodrigue, and S.-H. Ahn, "Smart soft composite actuator with shape retention capability using embedded fusible alloy structures," *Compos. Part B Eng.*, vol. 78, pp. 507–514, 2015.

[129] M. Henke, J. Sorber, and G. Gerlach, "Multi-layer beam with variable stiffness based on electroactive polymers," in *SPIE Smart Structures and Materials+ Nondestructive Evaluation and Health Monitoring*, 2012, p. 83401P–83401P.

[130] A. Orita and M. R. Cutkosky, "Scalable Electroactive Polymer for Variable Stiffness Suspensions," *IEEE/ASME Trans. Mechatronics*, vol. 21, no. 6, pp. 2836–2846, 2016.

[131] W.-B. Li, W.-M. Zhang, H.-X. Zou, Z.-K. Peng, and G. Meng, "A Novel Variable Stiffness Mechanism for Dielectric Elastomer Actuators," *Smart Mater. Struct.*, 2017.

[132] S. Shian, K. Bertoldi, and D. R. Clarke, "Dielectric elastomer based 'grippers' for soft robotics," *Adv. Mater.*, vol. 27, no. 43, pp. 6814–6819, 2015.

[133] Y. Yan *et al.*, "Electroactive Ionic Soft Actuators with Monolithically Integrated Gold Nanocomposite Electrodes," *Adv. Mater.*, vol. 29, no. 23, 2017.

[134] J. L. C. Santiago, I. S. Godage, P. Gonthina, and I. D. Walker, "Soft Robots and Kangaroo Tails: Modulating Compliance in Continuum Structures Through Mechanical Layer Jamming," *Soft Robot.*, vol. 3, no. 2, pp. 54–63, 2016.

[135] M. E. Giannaccini *et al.*, "A variable compliance, soft gripper," *Auton. Robots*, vol. 36, no. 1–2, pp. 93–107, 2014.

[136] J. Amend, N. Cheng, S. Fakhouri, and B. Culley, "Soft Robotics Commercialization: Jamming Grippers from Research to Product," *Soft Robot.*, vol. 3, no. 4, pp. 213–222, 2016.

[137] S. Licht, E. Collins, D. Ballat-Durand, and M. Lopes-Mendes, "Universal jamming grippers for deep-sea manipulation," in *OCEANS 2016*

MTS/IEEE Monterey, 2016, pp. 1–5.

[138] J. Hughes and F. Iida, "Localized differential sensing of soft deformable surfaces," in *Robotics and Automation (ICRA), 2017 IEEE International Conference on*, 2017, pp. 4959–4964.

[139] A. Jiang, G. Xynogalas, P. Dasgupta, K. Althoefer, and T. Nanayakkara, "Design of a variable stiffness flexible manipulator with composite granular jamming and membrane coupling," *2012 IEEE/RSJ Int. Conf. Intell. Robot. Syst.*, pp. 2922–2927, Oct. 2012.

[140] Y. J. Kim, S. Cheng, S. Kim, and K. Iagnemma, "A novel layer jamming mechanism with tunable stiffness capability for minimally invasive surgery," *IEEE Trans. Robot.*, vol. 29, no. 4, pp. 1031–1042, 2013.

[141] J. Rabinow, "The magnetic fluid clutch," *Electr. Eng.*, vol. 67, no. 12, p. 1167, 1948.

[142] J. D. Carlson, D. M. Catanzarite, and K. A. St. Clair, "Commercial magneto-rheological fluid devices," *Int. J. Mod. Phys. B*, vol. 10, no. 23n24, pp. 2857–2865, 1996.

[143] N. K. Petek, D. J. Romstadt, M. B. Lizell, and T. R. Weyenberg, "Demonstration of an automotive semi-active suspension using electrorheological fluid," SAE Technical Paper, 1995.

[144] J.-S. Oh and S.-B. Choi, "State of the Art of Medical Devices Featuring Smart Electro-rheological and Magneto-rheological Fluids," *J. King Saud Univ.*, 2017.

[145] Z. Varga, G. Filipcsei, and M. Zrínyi, "Magnetic field sensitive functional elastomers with tuneable elastic modulus," *Polymer (Guildf).*, vol. 47, no. 1, pp. 227–233, 2006.

[146] R. H. Ewoldt, "Extremely soft: design with rheologically complex fluids," *Soft Robot.*, vol. 1, no. 1, pp. 12–20, 2014.

[147] A. Pettersson, S. Davis, J. O. Gray, T. J. Dodd, and T. Ohlsson, "Design of a magnetorheological robot gripper for handling of delicate food products with varying shapes," *J. Food Eng.*, vol. 98, no. 3, pp. 332–338, 2010.

[148] J. D. Carlson and M. R. Jolly, "MR fluid, foam and elastomer devices," *mechatronics*, vol. 10, no. 4, pp. 555–569, 2000.

[149] N. G. Cheng, A. Gopinath, L. Wang, K. Iagnemma, and A. E. Hosoi, "Thermally Tunable, Self-Healing Composites for Soft Robotic Applications," *Macromol. Mater. Eng.*, vol. 299, no. 11, pp. 1279–1284, 2014.

[150] J. Shintake, B. Schubert, S. Rosset, H. Shea, and D. Floreano, "Variable stiffness actuator for soft robotics using dielectric elastomer and low-melting-point alloy," in *Intelligent Robots and Systems (IROS), 2015 IEEE/RSJ International Conference on*, 2015, pp. 1097–1102.

[151] B. E. Schubert and D. Floreano, "Variable stiffness material based on rigid low-melting-point-alloy microstructures embedded in soft poly (dimethylsiloxane)(PDMS)," *Rsc Adv.*, vol. 3, no. 46, pp. 24671–24679, 2013.

[152] A. Tonazzini, S. Mintchev, B. Schubert, B. Mazzolai, J. Shintake, and D. Floreano, "Variable Stiffness Fiber with Self-Healing Capability," *Adv. Mater.*, vol. 28, no. 46, pp. 10142–10148, 2016.

[153] P. V. C. Handbook, "www. parasethylene-kish. com," 2005.

[154] N. M. Alves, J. F. Mano, E. Balaguer, J. M. M. Dueñas, and J. L. G. Ribelles, "Glass transition and structural relaxation in semi-crystalline poly (ethylene terephthalate): a DSC study," *Polymer (Guildf).*, vol. 43, no. 15, pp. 4111–4122, 2002.

[155] A. Balasubramanian, M. Standish, and C. J. Bettinger, "Microfluidic thermally activated materials for rapid control of macroscopic compliance," *Adv. Funct. Mater.*, vol. 24, no. 30, pp. 4860–4866, 2014.

[156] J. R. Capadona, K. Shanmuganathan, D. J. Tyler, S. J. Rowan, and C. Weder, "Stimuli-responsive polymer nanocomposites inspired by the sea cucumber dermis," *Science (80-.).*, vol. 319, no. 5868, pp. 1370–1374, 2008.

[157] K. Shanmuganathan, J. R. Capadona, S. J. Rowan, and C. Weder, "Bio-inspired mechanically-adaptive nanocomposites derived from cotton cellulose whiskers," *J. Mater. Chem.*, vol. 20, no. 1, pp. 180–186, 2010.

[158] M. A. McEvoy and N. Correll, "Thermoplastic variable stiffness composites with embedded, networked sensing, actuation, and control," *J. Compos. Mater.*, vol. 49, no. 15, pp. 1799–1808, 2015.

[159] J. Fryman and B. Matthias, "Safety of industrial robots: From conventional to collaborative applications," in *Robotics; Proceedings of*

ROBOTIK 2012; 7th German Conference on, 2012, pp. 1–5.

[160] ISO Copyright Office, "ISO 10218:2011 'Robots and robotic devices – Safety requirements for industrial robots', with parts 1 ('Robots') and 2 ('Robot systems and integration')." ISO Copyright Office, Geneva, 2011.

[161] T. Jacobs and G. S. Virk, "ISO 13482-The new safety standard for personal care robots," in *ISR/Robotik 2014; 41st International Symposium on Robotics; Proceedings of*, 2014, pp. 1–6.

[162] ISO Copyright Office, "ISO TS 15066:2016 'Robots and robotic devices – Collaborative robots.'" ISO Copyright Office, Geneva, 2016.

[163] X. Tong and W. Lei, "A Systematic Analysis of Functional Safety Certification Practices in Industrial Robot Software Development," in *MATEC Web of Conferences*, 2017, vol. 100, p. 2011.

[164] S. Oberer-Treitz, T. Dietz, and A. Verl, "Safety in industrial applications: From fixed fences to direct interaction," in *2013 44th International Symposium on Robotics, ISR 2013*, 2013.

[165] A. J. Baerveldt, "A safety system for close interaction between man and robot," *Saf. Comput. Control Syst. SAFECOMP*, vol. 92, pp. 25–29, 2014.

[166] O. Khatib, "Robots in Human Environments: Basic Autonomous Capabilities," *Int. J. Rob. Res.*, vol. 18, pp. 684–696, 1999.

[167] S. Haddadin, A. Albu-Schaffer, and G. Hirzinger, "Requirements for Safe Robots: Measurements, Analysis and New Insights," *Int. J. Rob. Res.*, vol. 28, no. 11–12, pp. 1507–1527, 2009.

[168] www.kuka.com, "KUKA Robots." [Online]. Available: www.kuka.com. [Accessed: 21-Jul-2017].

[169] "ABB Robotics website (retrieved on 14.09.16)." .

[170] A. De Santis, B. Siciliano, A. De Luca, and A. Bicchi, "An atlas of physical human-robot interaction," *Mechanism and Machine Theory*, vol. 43, no. 3. pp. 253–270, 2008.

[171] H. A. Yanco and J. L. Drury, "A Taxonomy for Human-Robot Interaction," *Engineering*, p. 9, 2002.

[172] www.universal-robots.com, "Universal Robots website (retrieved on 14.09.2016)." [Online]. Available: https://www.universal-robots.com. [Accessed: 13-Aug-2017].

[173] www.ferrobotics.com, "FerRobotics Compliant Robot Technology." [Online]. Available: www.ferrobotics.com. [Accessed: 13-Aug-2017].

[174] www.franka.de, "FRANKA EMIKA." [Online]. Available: www.franka.de. [Accessed: 21-Jul-2017].

[175] www.rethinkrobotics.com, "Rethink Robotics." [Online]. Available: http://www.rethinkrobotics.com/. [Accessed: 21-Jul-2017].

[176] G. A. Pratt and M. M. Williamson, "Series elastic actuators," in *Intelligent Robots and Systems 95.'Human Robot Interaction and Cooperative Robots', Proceedings. 1995 IEEE/RSJ International Conference on*, 1995, vol. 1, pp. 399–406.

[177] G. Tonietti, R. Schiavi, and A. Bicchi, "Design and Control of a Variable Stiffness Actuator for Safe and Fast Physical Human/Robot Interaction," *Robotics and Automation, 2005. ICRA 2005. Proceedings of the 2005 IEEE International Conference on*. pp. 526–531, 2005.

[178] A. De Luca and R. Mattone, "Sensorless robot collision detection and hybrid force/motion control," in *Proceedings of the 2005 IEEE international conference on robotics and automation*, 2005, pp. 999–1004.

[179] P. A. Lasota, T. Fong, and J. A. Shah, "A Survey of Methods for Safe Human-Robot Interaction," *Found. Trends® Robot.*, vol. 5, no. 4, pp. 261–349, 2017.

[180] M. W. Hyun, J. Yoo, S. T. Hwang, J. H. Choi, S. Kang, and S. J. Kim, "Optimal design of a variable stiffness joint using permanent magnets," in *IEEE Transactions on Magnetics*, 2007, vol. 43, no. 6, pp. 2710–2712.

[181] J. Choi, S. Park, W. Lee, and S. C. Kang, "Design of a robot joint with variable stiffness," in *Proceedings - IEEE International Conference on Robotics and Automation*, 2008, pp. 1760–1765.

[182] J. Choi, S. Hong, W. Lee, and S. Kang, "A variable stiffness joint using leaf springs for robot manipulators," in *Proceedings - IEEE International Conference on Robotics and Automation*, 2009, pp. 4363–4368.

[183] D. Silvera-Tawil, D. Rye, and M. Velonaki, "Artificial skin and tactile sensing for socially interactive robots: A review," *Robotics and Autonomous Systems*, vol. 63, no. P3. pp. 230–243, 2015.

[184] R. D. Ponce Wong, J. D. Posner, and V. J. Santos, "Flexible microfluidic normal force sensor skin for tactile feedback," *Sensors Actuators A Phys.*, vol. 179, pp. 62–69, Jun. 2012.

[185] A. Schmitz, P. Maiolino, M. Maggiali, L. Natale, G. Cannata, and G. Metta, "Methods and technologies for the implementation of large-scale robot tactile sensors," *IEEE Trans. Robot.*, vol. 27, no. 3, pp. 389–400, 2011.

[186] D. M. Ebert and D. D. Henrich, "Safe human-robot-cooperation: image-based collision detection for industrial robots," *IEEE/RSJ Int. Conf. Intell. Robot. Syst.*, vol. 2, no. October, pp. 1826–1831, 2002.

[187] www.bluedanuberobotics.com, "Website Blue Danube Robotics." [Online]. Available: http://www.bluedanuberobotics.com/. [Accessed: 19-Jul-2017].

[188] S. Sanan, M. H. Ornstein, and C. G. Atkeson, "Physical human interaction for an inflatable manipulator," in *2011 Annual International Conference of the IEEE Engineering in Medicine and Biology Society*, 2011, pp. 7401–7404.

[189] Y. Noh *et al.*, "A Three-Axial Body Force Sensor for Flexible Manipulators," 2014.

[190] S. Sareh *et al.*, "Bio-Inspired Tactile Sensor Sleeve for Surgical Soft Manipulators," pp. 1454–1459, 2014.

[191] T. Ranzani, M. Cianchetti, G. Gerboni, I. De Falco, G. Petroni, and A. Menciassi, "A modular soft manipulator with variable stiffness," no.

September, pp. 11–14, 2013.

[192] H. A. Wurdemann *et al.*, "Embedded electro-conductive yarn for shape sensing of soft robotic manipulators," in *Engineering in Medicine and Biology Society (EMBC), 2015 37th Annual International Conference of the IEEE*, 2015, pp. 8026–8029.

[193] Y. Noh *et al.*, "A continuum body force sensor designed for flexible surgical robotics devices," *Conf. Proc. ... Annu. Int. Conf. IEEE Eng. Med. Biol. Soc. IEEE Eng. Med. Biol. Soc. Annu. Conf.*, vol. 2014, pp. 3711–3714, 2014.

[194] Y. Noh *et al.*, "Three-Axis Fiber-optic Body Force Sensor for Flexible Manipulators," *IEEE Sens. J.*, vol. 16(6), pp. 1641–1651, 2016.

[195] J. Fras, J. Czarnowski, M. Macias, J. Glowka, M. Cianchetti, and A. Menciassi, "New STIFF-FLOP module construction idea for improved actuation and sensing," *Robotics and Automation (ICRA), 2015 IEEE International Conference on*. pp. 2901–2906, 2015.

[196] A. A. M. Faudzi, M. R. M. Razif, I. N. A. M. Nordin, K. Suzumori, S. Wakimoto, and D. Hirooka, "Development of bending soft actuator with different braided angles," in *IEEE/ASME International Conference on Advanced Intelligent Mechatronics, AIM*, 2012, pp. 1093–1098.

[197] V. Wall, R. Deimel, and O. Brock, "Selective stiffening of soft actuators based on jamming," *Robotics and Automation (ICRA), 2015 IEEE International Conference on*. pp. 252–257, 2015.

[198] A. Stilli, H. A. Wurdemann, and K. Althoefer, "A Novel Concept for Safe

, Stiffness-Controllable Robot Links," *Soft Robot.*, p. soro.2016.0015, 2016.

[199] www.normesh.co.uk, "Normesh Ltd." [Online]. Available: http://www.normesh.co.uk/da/111262. [Accessed: 21-Jul-2017].

[200] www.smooth-on.com, "Smooth-On, Inc." [Online]. Available: www.smooth-on.com. [Accessed: 21-Jul-2017].

[201] A. F. Shore, "Apparatus for measuring the hardness of materials." Google Patents, 08-Jul-1930.

[202] J.-C. Thomas and C. Wielgosz, "Deflections of highly inflated fabric tubes," *Thin-Walled Struct.*, vol. 42, no. 7, pp. 1049–1066, 2004.

[203] S. L. Veldman, O. K. Bergsma, and A. Beukers, "Bending of anisotropic inflated cylindrical beams," *Thin-walled Struct.*, vol. 43, no. 3, pp. 461–475, 2005.

[204] www.smcpneumatics.com, "SMC Pneumatics." .

[205] J. S. Przemieniecki, *Theory of matrix structural analysis*. Courier Corporation, 1985.

[206] www.engineeringtoolbox.com/young-modulus-d_417.html, "Young's Modulus - Tensile and Yield Strength for common Materials." [Online]. Available: www.engineeringtoolbox.com/young-modulus-d_417.html.

[207] P. Polygerinos *et al.*, "Modeling of soft fiber-reinforced bending actuators," *IEEE Trans. Robot.*, vol. 31, no. 3, pp. 778–789, 2015.

[208] A. Stilli, L. Grattarola, H. Feldmann, H. A. Wurdemann, and K. Althoefer, "Variable Stiffness Link (VSL): Toward inherently safe robotic manipulators," in *Robotics and Automation (ICRA), 2017 IEEE International Conference on*, 2017, pp. 4971–4976.

[209] I. Gaiser *et al.*, "Compliant robotics and automation with flexible fluidic actuators and inflatable structures," in *Smart Actuation and Sensing Systems-Recent Advances and Future Challenges*, InTech, 2012.

[210] S. Sanan, J. B. Moidel, and C. G. Atkeson, "Robots with inflatable links," in *Intelligent Robots and Systems, 2009. IROS 2009. IEEE/RSJ International Conference on*, 2009, pp. 4331–4336.

[211] www.robotshop.com, "RobotShop." [Online]. Available: www.robotshop.com. [Accessed: 13-Aug-2017].

[212] www.hitecrcd.com, "HiTech." [Online]. Available: www.hitecrcd.com. [Accessed: 13-Aug-2017].

[213] www.ndigital.com, "Northern Digital Inc. (NDI)." [Online]. Available: www.ndigital.com. [Accessed: 17-Aug-2017].

[214] C. A. Hobbs, P. Gloyns, and S. Rattenbury, "Euro NCAP, Assessment protocol and biomechanical limits," *Euro NCAP*, 1999.

[215] S. Haddadin, A. Albu-Schäffer, and G. Hirzinger, "Safety Evaluation of Physical Human-Robot Interaction via Crash-Testing.," in *Robotics: Science and Systems*, 2007, vol. 3, pp. 217–224.

[216] S. Haddadin, A. Albu-Schaffer, A. De Luca, and G. Hirzinger, "Collision

detection and reaction: A contribution to safe physical human-robot interaction," in *Intelligent Robots and Systems, 2008. IROS 2008. IEEE/RSJ International Conference on*, 2008, pp. 3356–3363.

[217] G. Robinson and J. B. C. Davies, "Continuum robots - a state of the art," *Proc. 1999 IEEE Int. Conf. Robot. Autom. (Cat. No.99CH36288C)*, vol. 4, 1999.

[218] I. D. Walker, "Robot strings: long, thin continuum robots," in *Aerospace Conference, 2013 IEEE*, 2013, pp. 1–12.

[219] I. A. Gravagne, C. D. Rahn, and I. D. Walker, "Large deflection dynamics and control for planar continuum robots," *IEEE/ASME Transactions on Mechatronics*, vol. 8, no. 2. pp. 299–307, 2003.

[220] Z. Li and R. Du, "Design and analysis of a bio-inspired wire-driven multi-section flexible robot," *Int. J. Adv. Robot. Syst.*, vol. 10, no. 4, p. 209, 2013.

[221] S. Sanan, J. Moidel, and C. G. Atkeson, "A continuum approach to safe robots for physical human interaction," in *Int'l Symposium on Quality of Life Technology*, 2011.

[222] R. J. Webster, A. M. Okamura, and N. J. Cowan, "Toward active cannulas: Miniature snake-like surgical robots," in *Intelligent Robots and Systems, 2006 IEEE/RSJ International Conference on*, 2006, pp. 2857–2863.

[223] C. Bedell, J. Lock, A. Gosline, and P. E. Dupont, "Design optimization of concentric tube robots based on task and anatomical constraints," in

Robotics and Automation (ICRA), 2011 IEEE International Conference on, 2011, pp. 398–403.

[224] S. Neppalli *et al.*, "OctArm - A soft robotic manipulator," in *IEEE International Conference on Intelligent Robots and Systems*, 2007, p. 2569.

[225] J. Shang *et al.*, "An articulated universal joint based flexible access robot for minimally invasive surgery," in *Proceedings - IEEE International Conference on Robotics and Automation*, 2011, pp. 1147–1152.

[226] A. Jiang, E. Secco, H. Wurdemann, T. Nanayakkara, and K. Althoefer, "Stiffness-controllable octopus-like robot arm for minimally invasive surgery," no. Cras, pp. 4–5, 2013.

[227] A. Jiang, T. Aste, P. Dasgupta, K. Althoefer, and T. Nanayakkara, "Granular Jamming With Hydraulic Control," in *Volume 6A: 37th Mechanisms and Robotics Conference*, 2013, vol. 6 A, p. V06AT07A021.

[228] www.theverge.com, "Ant-Roach Robot." [Online]. Available: https://www.theverge.com/2011/11/23/2582645/otherlab-ant-roach-inflatable-robot. [Accessed: 02-Aug-2017].

[229] B. Jones, W. McMahan, and I. Walker, "Design and analysis of a novel pneumatic manipulator," *Proc. 3rd IFAC …*, 2004.

[230] Y. Gutfreund, T. Flash, G. Fiorito, and B. Hochner, "Patterns of arm muscle activation involved in octopus reaching movements.," *J. Neurosci.*, vol. 18, no. 15, pp. 5976–5987, 1998.

[231] M. Cianchetti, A. Arienti, M. Follador, B. Mazzolai, P. Dario, and C. Laschi, "Design concept and validation of a robotic arm inspired by the octopus," *Mater. Sci. Eng. C*, vol. 31, no. 6, pp. 1230–1239, 2011.

[232] A. Stilli, H. A. Wurdemann, and K. Althoefer, "Shrinkable, stiffness-controllable soft manipulator based on a bio-inspired antagonistic actuation principle," in *IEEE International Conference on Intelligent Robots and Systems*, 2014, pp. 2476–2481.

[233] H. A. Wurdemann, A. Stilli, and K. Althoefer, "Lecture notes in computer science: An antagonistic actuation technique for simultaneous stiffness and position control," in *International Conference on Intelligent Robotics and Applications*, 2015, pp. 164–174.

[234] A. Stilli, F. Maghooa, H. Wurdemann, and K. Althoefer, "A new bio-inspired, antagonistically actuated and stiffness controllable manipulator," in *Workshop on Computer/Robot Assisted Surgery (CRAS)*, 2014.

[235] M. Hatzinger, S. T. Kwon, S. Langbein, S. Kamp, A. Häcker, and P. Alken, "Hans Christian Jacobaeus: Inventor of human laparoscopy and thoracoscopy," *J. Endourol.*, vol. 20, no. 11, pp. 848–850, 2006.

[236] T. Schollmeyer, A. S. Soyinka, M. Schollmeyer, and I. Meinhold-Heerlein, "Georg Kelling (1866–1945): the root of modern day minimal invasive surgery. A forgotten legend?," *Arch. Gynecol. Obstet.*, vol. 276, no. 5, pp. 505–509, 2007.

[237] G. S. Litynski, "Laparoscopy-The Early Attempts: Spotlighting Georg Kelling and Hans Christian Jacobaeus," *JSLS J. Soc. Laparoendosc.*

Surg., vol. 1, no. 1, p. 83, 1997.

[238] G. S. Litynski, *Highlights in the history of laparoscopy: the development of laparoscopic techniques--a cumulative effort of internists, gynecologists, and surgeons*. Barbara Bernert Verlag, 1996.

[239] R. M. Satava, "Surgical robotics: the early chronicles: a personal historical perspective," *Surg. Laparosc. Endosc. Percutaneous Tech.*, vol. 12, no. 1, pp. 6–16, 2002.

[240] Y. S. Kwoh, J. Hou, E. A. Jonckheere, and S. Hayati, "A robot with improved absolute positioning accuracy for CT guided stereotactic brain surgery," *IEEE Trans. Biomed. Eng.*, vol. 35, no. 2, pp. 153–160, 1988.

[241] Q. Mei *et al.*, "PROBOT—A computer integrated prostatectomy system," in *Visualization in biomedical computing*, 1996, pp. 581–590.

[242] W. L. Bargar, A. Bauer, and M. Börner, "Primary and Revision Total Hip Replacement Using the Robodoc (R) System.," *Clin. Orthop. Relat. Res.*, vol. 354, pp. 82–91, 1998.

[243] P. Gomes, "Surgical robotics: Reviewing the past, analysing the present, imagining the future," *Robot. Comput. Integr. Manuf.*, vol. 27, no. 2, pp. 261–266, 2011.

[244] J. D. Schmitto, S. A. Mokashi, and L. H. Cohn, "Minimally-invasive valve surgery," *J. Am. Coll. Cardiol.*, vol. 56, no. 6, pp. 455–462, 2010.

[245] M. Jakopec, F. R. y Baena, S. J. Harris, P. Gomes, J. Cobb, and B. L. Davies, "The hands-on orthopaedic robot' Acrobot': Early clinical trials

of total knee replacement surgery," *IEEE Trans. Robot. Autom.*, vol. 19, no. 5, pp. 902–911, 2003.

[246] A. G. Harrell and B. T. Heniford, "Minimally invasive abdominal surgery: Lux et veritas past, present, and future," *Am. J. Surg.*, vol. 190, no. 2, pp. 239–243, 2005.

[247] Vranic A., "New developments in surgery," *Radiol. Oncol.*, vol. 142, pp. 295–297, 2011.

[248] P. J. Schuler, M. Scheithauer, N. Rotter, J. Veit, U. Duvvuri, and T. K. Hoffmann, "A single-port operator-controlled flexible endoscope system for endoscopic skull base surgery," *HNO*, vol. 63, no. 3, pp. 189–194, 2015.

[249] A. Degani, H. Choset, B. Zubiate, T. Ota, and M. Zenati, "Highly articulated robotic probe for minimally invasive surgery.," *Conf. Proc. IEEE Eng. Med. Biol. Soc.*, vol. 2008, pp. 3273–6, Jan. 2008.

[250] G. G. Ginsberg, "Colonoscopy with the variable stiffness colonoscope," *Gastrointest. Endosc.*, vol. 58, no. 4, pp. 579–584, 2003.

[251] C. A. Seneci *et al.*, "Design and evaluation of a novel flexible robot for transluminal and endoluminal surgery," in *Intelligent Robots and Systems (IROS 2014), 2014 IEEE/RSJ International Conference on*, 2014, pp. 1314–1321.

[252] N. Patel *et al.*, "Evaluation of a novel flexible snake robot for endoluminal surgery," *Surg. Endosc.*, vol. 29, no. 11, pp. 3349–3355, 2015.

[253] P. Dario *et al.*, "A novel mechatronic tool for computer-assisted arthroscopy," *IEEE Trans. Inf. Technol. Biomed.*, vol. 4, no. 1, pp. 15–29, 2000.

[254] Z. Li *et al.*, "Design of a novel flexible endoscope—cardioscope," *J. Mech. Robot.*, vol. 8, no. 5, p. 51014, 2016.

[255] E. V Mangan, D. A. Kingsley, R. D. Quinn, and H. J. Chiel, "Development of a peristaltic endoscope," *Robot. Autom. 2002. Proceedings. ICRA '02. IEEE Int. Conf.*, vol. 1, no. FEBRUARY 2002, pp. 347–352 vol.1, 2002.

[256] H. S. Yoon and B. J. Yi, "A 4-DOF flexible continuum robot using a spring backbone," *2009 IEEE Int. Conf. Mechatronics Autom. ICMA 2009*, pp. 1249–1254, 2009.

[257] A. Jiang, K. Althoefer, P. Dasgupta, and T. Nanayakkara, "The Core Snake, the variable stiffness laparoscopic camera," in *The Hamlyn Symposium on Medical Robotics, London, United Kingdom*, 2013.

[258] F. Maghooa, A. Stilli, Y. Noh, K. Althoefer, and H. A. Wurdemann, "Tendon and pressure actuation for a bio-inspired manipulator based on an antagonistic principle," *Robotics and Automation (ICRA), 2015 IEEE International Conference on*. pp. 2556–2561, 2015.

[259] R. J. Webster and B. a. Jones, "Design and Kinematic Modeling of Constant Curvature Continuum Robots: A Review," *Int. J. Rob. Res.*, vol. 29, no. 13, pp. 1661–1683, Jun. 2010.

[260] Sparkfun, "Sparkfun Big Easy Driver ROB-11876 - Datasheet." [Online].

Available: https://cdn.sparkfun.com/datasheets/Robotics/A4988-Datasheet.pdf. [Accessed: 25-Aug-2017].

[261] F. Cianchi, F. Staderini, and B. Badii, "Single-Incision Laparoscopic Colectomy: A New Era in the Treatment of Colorectal Cancer?," J. S. B. T.-C. C.-S. Khan Diagnostics and Treatment, Ed. Rijeka: InTech, 2014, p. Ch. 06.

[262] H. J. Lee and I. H. Derweesh, "LESS Partial Nephrectomy," *Atlas Laparosc. Robot. Single Site Surg.*, p. 87, 2017.

[263] A. Cestari, A. C. Galli, M. N. Sangalli, M. Zanoni, M. Ferrari, and G. Roviaro, "Totally extraperitoneal (TEP) bilateral hernioplasty using the Single Site® robotic da Vinci platform (DV-SS TEP): description of the technique and preliminary results," *Hernia*, vol. 21, no. 3, pp. 383–389, 2017.

[264] A. Stilli, H. A. Wurdemann, and K. Althoefer, "A Novel Flexible Endoscope for Minimally Invasive Surgery (1 page paper)," in *Annual International Conference of the IEEE Engineering in Medicine and Biology Society (EMBC)*, 2016.

[265] A. Stilli, A. Cremoni, H. A. Wurdemann, and K. Althoefer, "A new antagonistically actuated endoscope: Towards an inherently safe minimally invasive examination," in *Hamlyn Symposium on Medical Robotics*, 2016.

[266] A. Stilli, H. A. Wurdemann, and K. Althoefer, "A Novel Inflatable and Flexible Endoscope for Inherently Safe Minimally Invasive Examination," in *Workshop on Computer/Robot Assisted Surgery*

(CRAS), 2016.

[267] www.olympus-global.com, "Olympus." [Online]. Available: www.olympus-global.com. [Accessed: 13-Aug-2017].

[268] www.karlstorz.com, "Karl Storz." [Online]. Available: www.karlstorz.com. [Accessed: 13-Aug-2017].

[269] H. Wang *et al.*, "Global, regional, and national life expectancy, all-cause mortality, and cause-specific mortality for 249 causes of death, 1980–2015: a systematic analysis for the Global Burden of Disease Study 2015," *Lancet*, vol. 388, no. 10053, pp. 1459–1544, 2016.

[270] D. Epstein, A. Mason, and A. Manca, "The hospital costs of care for stroke in nine European countries," *Health Econ.*, vol. 17, no. S1, pp. S21–S31, 2008.

[271] X. Tong, M. G. George, C. Gillespie, and R. K. Merritt, "Trends in Hospitalizations and Cost Associated with Acute Ischemic Stroke by Age, United States 2003-2012," *Stroke*, vol. 47, no. Suppl 1, pp. A183–A183, 2016.

[272] D. O. Abegunde, C. D. Mathers, T. Adam, M. Ortegon, and K. Strong, "The burden and costs of chronic diseases in low-income and middle-income countries," *Lancet*, vol. 370, no. 9603, pp. 1929–1938, 2007.

[273] I. Díaz, J. J. Gil, and E. Sánchez, "Lower-limb robotic rehabilitation: literature review and challenges," *J. Robot.*, vol. 2011, 2011.

[274] B. R. Brewer, S. K. McDowell, and L. C. Worthen-Chaudhari,

"Poststroke Upper Extremity Rehabilitation: A Review of Robotic Systems and Clinical Results," *Top. Stroke Rehabil.*, vol. 14, no. 6, pp. 22–44, 2007.

[275] J. Mehrholz and M. Pohl, "Electromechanical-assisted gait training after stroke: a systematic review comparing end-effector and exoskeleton devices," *J. Rehabil. Med.*, vol. 44, no. 3, pp. 193–199, 2012.

[276] V. S. Huang and J. W. Krakauer, "Robotic neurorehabilitation: a computational motor learning perspective.," *J. Neuroeng. Rehabil.*, vol. 6, p. 5, 2009.

[277] P. S. Lum, C. G. Burgar, P. C. Shor, M. Majmundar, and M. Van der Loos, "Robot-assisted movement training compared with conventional therapy techniques for the rehabilitation of upper-limb motor function after stroke," *Arch. Phys. Med. Rehabil.*, vol. 83, no. 7, pp. 952–959, 2002.

[278] W. H. Chang and Y.-H. Kim, "Robot-assisted therapy in stroke rehabilitation," *J. stroke*, vol. 15, no. 3, p. 174, 2013.

[279] S. Ito, H. Kawasaki, Y. Ishigure, M. Natsume, T. Mouri, and Y. Nishimoto, "A design of fine motion assist equipment for disabled hand in robotic rehabilitation system," *J. Franklin Inst.*, vol. 348, no. 1, pp. 79–89, 2011.

[280] C. N. Schabowsky, S. B. Godfrey, R. J. Holley, and P. S. Lum, "Development and pilot testing of HEXORR: hand EXOskeleton rehabilitation robot," *J. Neuroeng. Rehabil.*, vol. 7, no. 1, p. 1, 2010.

[281] A. Chiri, N. Vitiello, F. Giovacchini, S. Roccella, F. Vecchi, and M. C. Carrozza, "Mechatronic design and characterization of the index finger module of a hand exoskeleton for post-stroke rehabilitation," *IEEE/ASME Trans. Mechatronics*, vol. 17, no. 5, pp. 884–894, 2012.

[282] E. B. Brokaw, I. Black, R. J. Holley, and P. S. Lum, "Hand Spring Operated Movement Enhancer (HandSOME): A portable, passive hand Exoskeleton for stroke rehabilitation," *IEEE Trans. Neural Syst. Rehabil. Eng.*, vol. 19, no. 4, pp. 391–399, 2011.

[283] B. Allotta, R. Conti, L. Governi, E. Meli, A. Ridolfi, and Y. Volpe, "Development and experimental testing of a portable hand exoskeleton," in *IEEE International Conference on Intelligent Robots and Systems*, 2015, vol. 2015–Decem, pp. 5339–5344.

[284] P. Heo, G. M. Gu, S. jin Lee, K. Rhee, and J. Kim, "Current hand exoskeleton technologies for rehabilitation and assistive engineering," *International Journal of Precision Engineering and Manufacturing*, vol. 13, no. 5. pp. 807–824, 2012.

[285] T. T. Worsnopp, M. A. Peshkin, J. E. Colgate, and D. G. Kamper, "An actuated finger exoskeleton for hand rehabilitation following stroke," in *2007 IEEE 10th International Conference on Rehabilitation Robotics, ICORR'07*, 2007, pp. 896–901.

[286] N. S. K. Ho *et al.*, "An EMG-driven exoskeleton hand robotic training device on chronic stroke subjects: Task training system for stroke rehabilitation," *IEEE Int. Conf. Rehabil. Robot.*, 2011.

[287] A. Wege and G. Hommel, "Development and control of a hand

exoskeleton for rehabilitation of hand injuries," in *2005 IEEE/RSJ International Conference on Intelligent Robots and Systems*, 2005, pp. 3046–3051.

[288] P. Agarwal, J. Fox, Y. Yun, M. K. O'Malley, and A. D. Deshpande, "An index finger exoskeleton with series elastic actuation for rehabilitation: Design, control and performance characterization," *Int. J. Rob. Res.*, vol. 34, no. 14, pp. 1747–1772, 2015.

[289] H. K. Yap, J. H. Lim, F. Nasrallah, F. Z. Low, J. C. H. Goh, and R. C. H. Yeow, "MRC-glove: A fMRI compatible soft robotic glove for hand rehabilitation application," *IEEE Int. Conf. Rehabil. Robot.*, vol. 2015–Septe, no. 65, pp. 735–740, 2015.

[290] P. Polygerinos *et al.*, "Towards a soft pneumatic glove for hand rehabilitation," *IEEE Int. Conf. Intell. Robot. Syst.*, pp. 1512–1517, 2013.

[291] M. A. Delph, S. A. Fischer, P. W. Gauthier, C. H. M. Luna, E. A. Clancy, and G. S. Fischer, "A soft robotic exomusculature glove with integrated sEMG sensing for hand rehabilitation," *IEEE Int. Conf. Rehabil. Robot.*, 2013.

[292] M. Xiloyannis, L. Cappello, D. B. Khanh, S.-C. Yen, and L. Masia, "Modelling and design of a synergy-based actuator for a tendon-driven soft robotic glove," in *Biomedical Robotics and Biomechatronics (BioRob), 2016 6th IEEE International Conference on*, 2016, pp. 1213–1219.

[293] H. K. Yap, J. H. Lim, F. Nasrallah, J. C. H. Goh, and R. C. H. Yeow, "A soft exoskeleton for hand assistive and rehabilitation application using

pneumatic actuators with variable stiffness," in *Proceedings - IEEE International Conference on Robotics and Automation*, 2015, vol. 2015–June, no. June, pp. 4967–4972.

[294] D. Popov, I. Gaponov, and J.-H. Ryu, "Portable Exoskeleton Glove With Soft Structure for Hand Assistance in Activities of Daily Living," *IEEE/ASME Trans. Mechatronics*, vol. 22, no. 2, pp. 865–875, 2017.

[295] H. K. Yap, J. H. Lim, J. C. H. Goh, and C.-H. Yeow, "Design of a Soft Robotic Glove for Hand Rehabilitation of Stroke Patients with Clenched Fist Deformity using Inflatable Plastic Actuators," *J. Med. Device.*, no. c, 2016.

[296] http://bioservo.com/wp-content/uploads/2016/12/BSTQ0160_13-User-Guide-ENG.pdf, "The SEM Glove Data Sheet." [Online]. Available: http://bioservo.com/wp-content/uploads/2016/12/BSTQ0160_13-User-Guide-ENG.pdf. [Accessed: 17-Aug-2017].

[297] www.ukfabricsonline.com, "UK Fabrics online." [Online]. Available: ukfabricsonline.com. [Accessed: 17-Aug-2017].

[298] www.pfaff.com, "PFAFF." [Online]. Available: http://www.pfaff.com. [Accessed: 17-Aug-2017].

[299] B. ASHWORTH, "Preliminary trial of carisoprodol in multiple sclerosis.," *Practitioner*, vol. 192, pp. 540–542, 1964.

[300] R. W. Bohannon and M. B. Smith, "Interrater reliability of a modified Ashworth scale of muscle spasticity," *Phys ther*, vol. 67, no. 2, pp. 206–207, 1987.

[301] J. M. Gregson, M. Leathley, A. P. Moore, A. K. Sharma, T. L. Smith, and C. L. Watkins, "Reliability of the Tone Assessment Scale and the modified Ashworth scale as clinical tools for assessing poststroke spasticity," *Arch. Phys. Med. Rehabil.*, vol. 80, no. 9, pp. 1013–1016, 1999.

[302] W. M. Association, "Declaration of Helsinki: Ethical principles for medical research involving human subjects. 64th WMA General Assembly, Fortaleza, Brazil." 2016.

[303] W. A. Rutala and D. J. Weber, "Guideline for disinfection and sterilization in healthcare facilities, 2008," 2008.

[304] www.ecri.org, "Medical Air Standard." [Online]. Available: http://www.mdsr.ecri.org/summary/detail.aspx?doc_id=8279. [Accessed: 26-Aug-2017].

[305] www.advancedsurgical.ie, "Advanced Surgical Concepts." [Online]. Available: www.advancedsurgical.ie. [Accessed: 13-Aug-2017].

[306] www.medtronic.com, "Medtronic." [Online]. Available: http://www.medtronic.com. [Accessed: 13-Aug-2017].